GEOPHYSICAL STUDIES OF THE CRUST AND UPPERMOST MANTLE OF SOUTHERN AFRICA

By

Eldridge M. Kgaswane

GEOPHYSICAL STUDIES OF THE CRUST AND UPPERMOST MANTLE OF SOUTHERN AFRICA

Eldridge Maungwe Kgaswane

Degree of Doctor of Philosophy:

A thesis submitted to the Faculty of Science, University of the Witwatersrand, in fulfillment of the requirements for the degree of Doctor of Philosophy in Geophysics

Johannesburg, 2013

Declaration

I declare that this thesis is my own, unaided work. It is being submitted for the Degree of Doctor of Philosophy in the University of the Witwatersrand, Johannesburg. It has not been submitted before for any degree or examination in any other University.

____

E. M. Kgaswane

__________ day of ___________________ 2013

Abstract

The general aim of this thesis is to investigate heterogeneity in the structure of the crust and uppermost mantle of Archaean and Proterozoic terrains in southern Africa and to use the findings to advance our understanding of Precambrian crustal genesis. Teleseismic, regional and local seismic recordings by the broadband stations of the Southern African Seismic Experiment (SASE), Kimberley array, South African National Seismograph Network (SANSN) and the Global Seismic Network (GSN) are used in the inversion procedures to address the aim of this thesis.

In the first part of the thesis, the nature of the lower crust across the southern African shield is investigated by jointly inverting receiver functions and Rayleigh wave group velocities. The resultant Vs models show that much of southern Africa has a lower crust that is mafic in composition, whereas the western parts of the Kaapvaal and Zimbabwe Cratons have a lower crust that is intermediate-to-felsic in composition probably due to rifting. The second part of the thesis evaluates the "dipping-sheet" and "continuous-sheet" models of the Bushveld Complex using better-resolved seismic models derived in a two-step approach, employing high-frequency Rayleigh wave group velocity tomography and the joint inversion of high-frequency receiver functions and 2–60 sec Rayleigh wave group velocities. The resultant seismic models favor a "continuous-sheet" model of the Bushveld Complex, although detailed modelling near the centre of the Complex shows that the subsurface mafic layering could be disrupted.

The third part of the thesis, is focused on jointly inverting high-frequency teleseismic receiver functions and 10–60 sec Rayleigh wave group velocities to place shear wave velocity constraints on the source of the Beattie Magnetic Anomaly (BMA) at depth and to evaluate existing geophysical models of the BMA source. The resultant Vs models across the BMA suggest the BMA source to be at upper to middle crustal depths (5–20 km) with high velocity layers ($\geq$ 3.5 km/s). Further to this, is a lower crust that is highly mafic (Vs $\geq$ 4.0 km/s) and a crust beneath the BMA that is on average thicker than 40 km. Plausible models of the BMA source are massive sulphide ore bodies and/or mineralized granulite-facies mid-crustal rocks and/or mineralized Proterozoic anorthosites.

Overall, the findings in this research project are consistent with the broad features of a previous model of Precambrian lithospheric evolution but allows for refinements of that model.

Dedication

In memory of my late grandmother, Alinah Majohanna Miya,

1923 – 2005

Acknowledgments

I am indebted to the Council for Geoscience, AfricaArray program, National Science Foundation (NSF) in the USA and the National Research Foundation (NRF) for having provided me with the opportunity to carry out this research project. Without this financial support this project would have been impossible.

I am very grateful to the supervision team, Profs Andrew Nyblade (USA), Paul Dirks (Australia), Ray Durrheim (South Africa) and Jordi Julià (Brazil), for their invaluable guidance and assistance with the conceptual understanding of this research project. I received assistance from Profs Charles Ammon, Rick Brazier, Mulugeta Dugda and Yongcheol Park (either at or formerly at Pennsylvania State University, USA) with the computer aspects of this research project. The LSQR and joint inversion codes, developed by Profs Charles Ammon and Jordi Julià, respectively, were used in the research project. Several people in the Spatial Data and Central Regions units (Council for Geoscience) provided assistance and advice with the use of ArcGis (including the digitization of terrain boundaries) and the construction of geological cross-sections, respectively. My colleagues, Tarzan Kwadiba and Stephanie Scheiber, assisted with the regional earthquake catalogues and IGRF corrections of the magnetic field, respectively. Dr. Susan Webb was willing to share some of her terrain boundaries and diagrams used in two of the peer-reviewed publications of this project. I am also grateful to all those who assisted with the Southern African Seismic Experiment.

Finally, I am thankful to the staff in the Department of Geosciences at Pennsylvania State University (USA) for having provided assistance and resources for the time I spent in the USA as a visiting scholar.

Contents

Lists of figures and tables

Tables	Page

Chapter 1

Introduction

1.1 Overview and motivation

The overall aim of this thesis is to investigate heterogeneity in the composition and structure of the crust and uppermost mantle of Archaean and Proterozoic terrains in southern Africa and to use these findings to advance our understanding of the genesis and evolution of the lithosphere. In this introductory chapter (Chapter 1) I briefly review the state of knowledge prior to this study and the problems to be addressed by this research study. I also give an outline of the thesis.

Since this thesis comprises separate chapters/papers that use similar methodologies and study the same tectonic region, the description of geodynamic settings and methodology has not been repeated in each chapter. Wherever the descriptions are not exactly identical, a full description has been provided. For example, the joint inversion method has been implemented in different ways and therefore pertinent descriptions have been provided. Chapters 2 and 3 are essentially a summary of the two peer-reviewed papers included in this thesis, while chapter 4 describes research work that has not yet been published.

Chapters 2, 3 and 4 each begin with a review of literature, geology, data sources, and modelling methods. The review is followed by a description of the results achieved. Subsequent to this, there will be an interpretation and summary of the findings in each of the chapters. The thesis concludes with Chapter 5, which provides an overall summary of the findings, recommendations for further studies, and the tectonic implications of the findings.

Each chapter has its own reference list. The content of the Appendices (included at the end of the thesis) are described in each of the central chapters.

1.1.1 The southern African shield

The Precambrian lithosphere making up the southern African shield is primarily comprised of the Kaapvaal and Zimbabwe Cratons surrounded by belts of various ages: the Proterozoic Namaqua-Natal Belt (NNB) and the Phanerozoic Cape Fold Belt (CFB) to the south; and the Proterozoic Kheis and Okwa-Magondi Belts to the west and northwest, respectively (e.g. de Wit et al., 1992; Eglington and Armstrong, 2004). Figure 1.1 is a simplified tectonic map of southern Africa showing major Precambrian terrains. Terrain names and boundaries shown in Figure 1.1 are taken from Eglington and Armstrong (2004) and Jelsma and Dirks (2002). Tectonic structures not shown in Figure 1.1 are the Archaean-ProterozoicRehobothProvince and the Neoproterozoic Damara Belt (both mainly exposed in Namibia, but also extending further into the western parts of Botswana) located further west of both cratons, and the Pan-African belts on the eastern border of the Zimbabwe Craton (ZC). The RehobothProvince was recently geochronologically determined to have Archaean remnants, in addition to its known Proterozoic rocks (e.g. Hartnady et al., 1985; Cornell et al., 1998; Van Schijndel, 2013). The eastern margin of the Kaapvaal Craton (KC) is characterized by a sequence of N-S striking Jurassic Karoo volcanics called the Lebombo Monocline (see Figure 1.2). The cratons have been modified by several well-known tectonomagmatic events (e.g. the Ventersdorp, the Great Dyke, the Bushveld) and a meteorite impact (e.g. the Vredefort). Figure 1.2 shows a simplified geological version of the tectonic map in Figure 1.1.

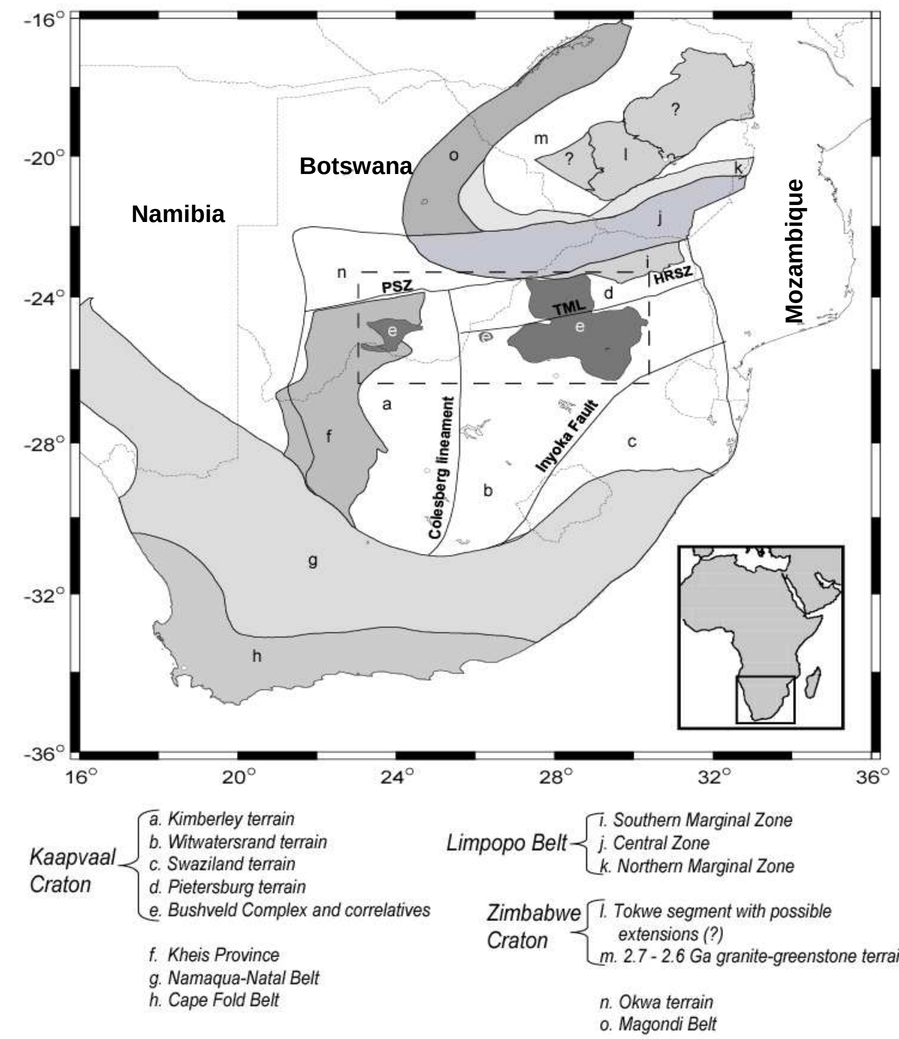

Figure 1.1 Tectonic map of southern Africa showing major Precambrian terrains. Political boundaries are shown with thin dashed lines. The box shown with bold dashed lines encloses the region affected by the Bushveld magmatic event. TML, Thabazimbi Murchison Lineament; PSZ, Palala Shear Zone and HRSZ, Hout River Shear Zone.Figure 1.1 has been slightly modified from Kgaswane et al. (2009).

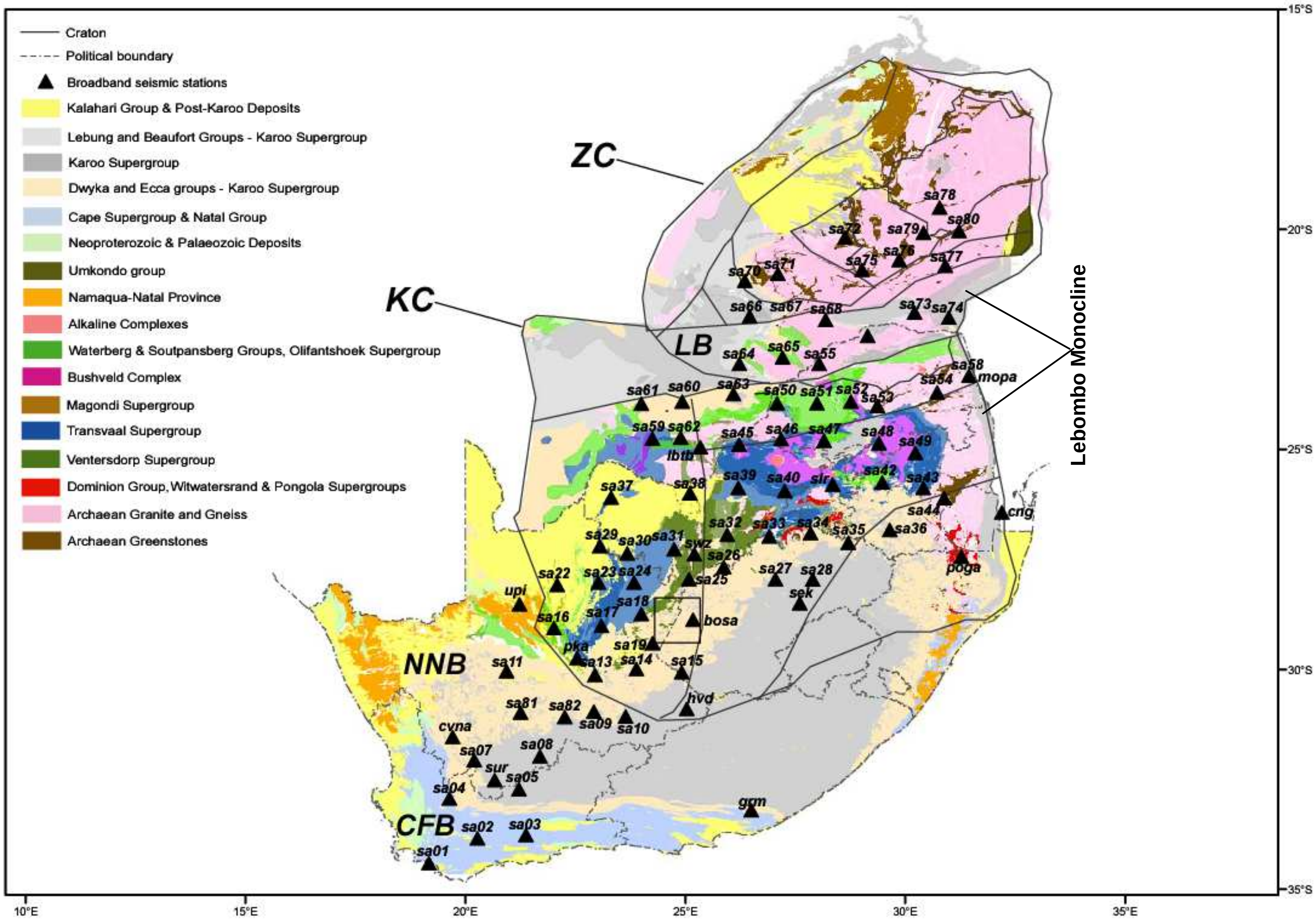

Figure 1.2 Map showing a simplified surface geology of southern Africa. Map has been modified from the 1:1,000,000 geology maps of South Africa and SADEC (Southern African Development Community). The legend on the left shows the younging of the rocks to be from bottom to top. Positions of the broadband seismic stations used in this research project, are superimposed on the map and the square encloses the five of the broadband seismic stations of the Kimberley array. Further details on the broadband seismic stations are elaborated in Chapter 2. KC – Kaapvaal Craton; ZC – Zimbabwe Craton; LB – Limpopo Belt; NNB – Namaqua-Natal Belt; and CFB – Cape Fold Belt.

Figure 1.2 shows that the early formation of both the KC and ZC were characterized by the emplacement of greenstones, granites and gneisses [e.g. Tokwe Gneiss (~ 3.6 Ga) in central Zimbabwe, Ngwane Gneiss (> 3.6 Ga) in eastern Kaapvaal, Barberton Supergroup (> 3.1 Ga) in eastern Kaapvaal]. The KC stabilized around 2.7 Ga whilst the ZC stabilized around 2.6 Ga. The two cratons were subsequently fused circa 2.6 Ga by the collisional orogen called the Limpopo Belt (3.5–2.0 Ga) (de Wit et al., 1992; Jelsma and Dirks, 2002; Kramers et al., 2006). Both the KC and the ZC, together with the surrounding mobile belts, have attracted many geoscientific investigations, of which the Southern African Seismic Experiment (SASE) deployment (1997 – 1999) (Carlson et al., 1996) has been the most notable in terms of size and multidisciplinary attention.

1.1.2 Crustal structure

This research project aims to build on the studies (including SASE) of the crustal structure of southern Africa (e.g. Green and Durrheim, 1990; Durrheim and Green, 1992; Harvey et al; 2001; Nguuri et al., 2001; Stankiewicz et al., 2002; Niu and James, 2002; James et al., 2003; Kwadiba et al., 2003; Wright et al., 2003; de Wit and Tinker, 2004; Webb et al., 2004, 2010; Nair et al., 2006; Gore et al., 2009). The findings from these studies show that the Moho is quite variable across the Archaean and Proterozoic terrains in southern Africa, with the undisturbed cratonic areas having a Moho depth of 35–40 km, most of the adjacent Proterozoic regions with a crustal thickness in the range of 40–50 km and Phanerozoic regions with a crustal thickness around 36–45 km. A seismic refraction study of the central parts of the KC shows a felsic upper crystalline crust and an intermediate-felsic lower crust (Durrheim and Green, 1992). It was further noted by de Wit and Tinker (2004) in a seismic reflection study that the lowermost crust in the central parts of the KC is of trondhjemite-tonalite-granodiorite

(TTG) composition and was probably partially melted by the Ventersdorp magmatic event (~2.7 Ga) resulting in a flat Moho. A seismological study of the Kimberley area (within the Kimberley region) in the western part of the KC indicates the prevalence of an intermediate-felsic lower crust above a flat Moho. A gravity model by Webb et al. (2004, 2010) postulates the continuity of the mafic layering at upper crustal depths across the centre of the Bushveld Complex (BC) (northern part of the KC), with the mafic layer isostatically compensated by a thickened Moho (~50 km) in the centre of the BC. Geophysical studies of the Beattie Magnetic Anomaly (BMA) across the Namaqua-Natal Belt (NNB) (south of the KC) constrain it to be located at upper to middle crustal depths (~5–20 km) and also show the BMA body to have compressional velocities of 6.6–7.0 km/s (i.e., shear wave velocities of ~3.8–4.0 km/s) (e.g. Harvey et al., 2001; Lindeque et al., 2007, 2011; Loots, 2012; Quesnel et al., 2009; Stankiewicz et al., 2007, 2008; Weckmann et al., 2007a,b).

While previous studies have provided important results and constraints, much remains unknown. For example: the variation in the composition of the lower crust and uppermost mantle of the southern African shield, the continuity (or otherwise) of the BC, and the origin of the Beattie Magnetic Anomaly (BMA). These questions are addressed in this thesis using new data acquired by an extensive broadband network of seismic stations spread across southern Africa.

1.1.3 Studies of mantle anisotropy

The geodynamic model derived from mantle studies of southern Africa is that Neo-Archaean collisional orogenesis was responsible for generating a mantle fabric that subsequently controlled the magmatic history of southern Africa and produced much of the deformation seen on surface (e.g. Fouch et al., 2004; Silver et al., 2001, 2004, 2006; Adam and Lebedev, 2012). According to Silver et al. (2004, 2006), there were four major magmatic events: the Great Dyke (~2.57 Ga) in the ZC, the Ventersdorp tectonomagmatic event (~2.7 Ga) in the southwestern part of the Kaapvaal Craton (KC), the Bushveld magmatic event (~2.06 Ga) in the northern part of the KC, and the Soutpansberg rifting event (~1.88 Ga) around the northern boundary of the KC and the Limpopo Belt (LB).

Shear wave splitting and surface wave observations (e.g. Silver et al., 2001, 2004, 2006; Adam and Lebedev, 2012) provide evidence of mantle anisotropy with fast polarization orientations that coincide and are sub-parallel to crustal features e.g. the Great Dyke, the Thabazimbi Murchison Lineament in the northern part of the KC, the Colesburg Lineament in the western part of the KC, and the Palala and Triangle Shear Zones that cross-cut the LB. The SKS studies further show strong mantle anisotropy in the western parts of the KC and the ZC, and weak anisotropy in the eastern part of the KC and ZC. There is weak anisotropy in the Kheis Belt and few localities on the western part of the BC. Figure 1.3 shows the magnitude and distribution of mantle anisotropy based on SKS observations. This study seeks to establish the correlation if any, between deformation in the crust and uppermost mantle.

1.1.4 Sn velocities

Based on 1-D surface wave inversions, past seismic studies generally show Sn velocities that vary from 4.5–4.7 km/s within the KC between Moho depths of 60–70 km (e.g. Freybourger et al., 2001; Larson et al., 2006). Recent surface wave tomographic studies (e.g. Li and Burke, 2006; Adam and Nyblade, 2011) generally show Sn velocities of 4.5–4.7 km/s between Moho and 60 km depth beneath the KC, and Sn velocities that are slightly > 4.7 km/s beneath the adjacent Proterozoic belts at similar depths.

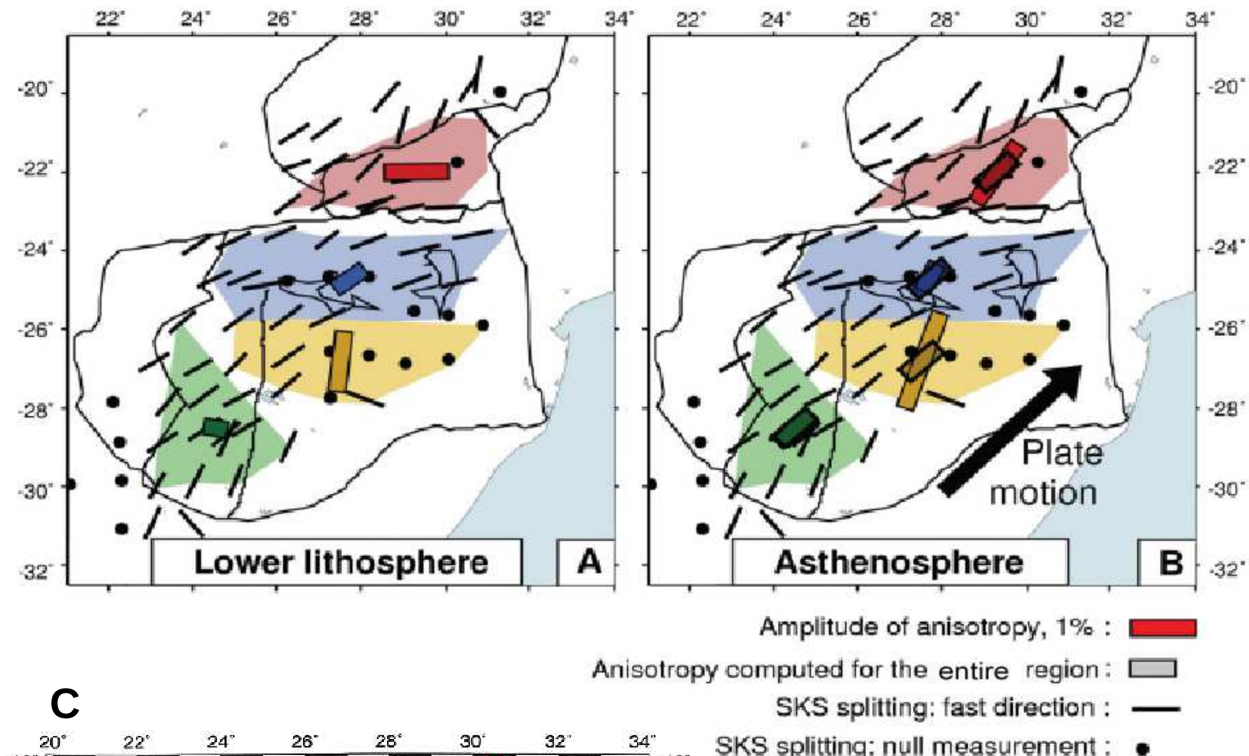

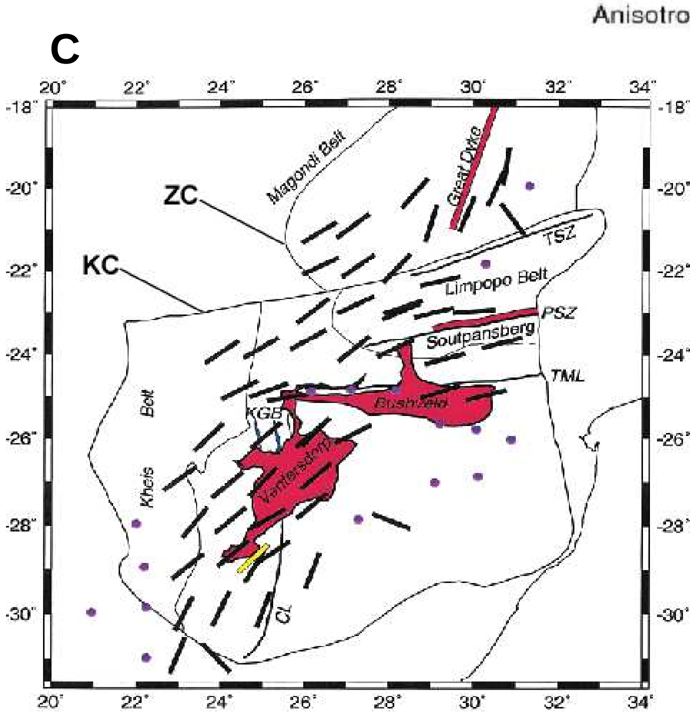

Figure 1.3 **A** and **B.** Shear wave splitting observations showing magnitude and orientation of anisotropy in the lower lithosphere and asthenosphere. Weak anisotropy is represented by the black solid dots. Both diagrams were reproduced from Adam and Lebedev (2012). **C.** Shear wave splitting observations at mantle depth. The purple dots represent weak anisotropy. The diagram was reproduced from Silver et al. (2004). TSZ – Triangle Shear Zone, PSZ – Palala Shear Zone, TML – Thabazimbi Murchison Lineament, CL – Colesburg Lineament, KGB – Kraaipan Greenstone Belt, ZC – Zimbabwe Craton and KC – Kaapvaal Craton.

These Sn velocities do not show significant variations across the different terrains. It is therefore one of the aims of this research project to reconcile the Vs results of the uppermost mantle from this study with the findings of the above-mentioned studies.

1.2 Thesis outline

The research program that is described in this thesis is divided into three parts. Detailed description follows below.

1.2.1 Vs structure of the southern African lithosphere

The first part of the thesis (Chapter 2) examines the variability of the lower crust and uppermost mantle across southern Africa using 89 broadband seismic stations, including the SASE. A joint inversion technique (e.g. Julià et al., 2000, 2003) was used to invert teleseismic P-wave receiver functions and the Rayleigh wave group velocity dispersions to obtain 1-D shear wave velocity models. Previous studies for southern Africa have focused on the independent inversion of either the receiver functions (Midzi and Ottemöller, 2001) or surface wave dispersions (e.g. Yang et al., 2008). This investigation jointly inverts both data sets, which places new constraints and improves the resolution of the Vs–depth models. This study seeks to determine the distribution of mafic lithologies in the lower crust throughout southern Africa and deduce the implications of the evolution of Precambrian crust. Past seismological studies have either concentrated on a small area of the southern African shield or placed insufficient constraints on the lower crust for some of the terrains within the southern Africa shield. As a result, they did not produce a systematic description of the presence of mafic lithologies in the lower crust of the Archean craton and the adjacent mobile belts (e.g.

Durrheim and Green, 1992; Niu and James, 2002; Nguuri et al., 2001; Kwadiba et al., 2003; Nair et al., 2006).

Mafic lithologies have been shown to exist in the lower crust in regions such as the Tanzanian craton (Juliá et al., 2005) and in most Proterozoic crustal regions. The joint inversion results in this study show evidence of the presence of mafic lithologies in the lower crust in most Archaean and Proterozoic terrains in southern Africa. Exceptions include regions in the western parts of the KC and ZC. The crustal thicknesses derived from the joint inversion further show a good correlation with crustal thickness estimates from other studies. A further examination of the joint inversion results show that there is no clear relationship between the average Vs in the lowermost crust (below 30 km depth) and crustal thickness throughout southern Africa. The joint inversion results show Sn velocities varying from 4.5 to 4.8 km/s in the uppermost mantle region (i.e., from Moho to 60 km depth) of southern Africa. The above velocity range indicates that Sn variations do not deviate more than 0.3 km/s. This implies that there are no significant Sn variations in the uppermost mantle across the Precambrian tectonic terrains of southern Africa. These results are also consistent with previous findings. The material in this chapter was published in a peer-reviewed article (appended to this thesis) with the following citation: ***Kgaswane, E.M., Nyblade, A.A., Julià, J., Dirks, P.H.G.M., Durrheim, R.J., Pasyanos, M.E., 2009. Shear wave velocity structure of the lower crust in southern Africa: Evidence for compositional heterogeneity within Archaean and Proterozoic terrains. Journal of Geophysical Research, 114, B12304.doi:10.1029/2008JB006217.***

My contribution in the above-mentioned publication is that I compiled a catalogue of 100 teleseismic earthquakes that I used to compute receiver functions. I then used the joint inversion code developed by Prof. Jordi Julià (co-author) to obtain Vs profiles for 101 broadband seismic stations. I assembled a preliminary draft of the text, figures, and tables, with the exception of Figure 4, which was contributed by Prof. Michael Pasyanos (co-author). The supervision team (Profs. Andy Nyblade, Paul Dirks and Ray Durrheim) including the other two co-authors (indicated above) helped in reviewing the publication during its drafting phase and conceptually guided the different aspects of the publication. I have also partly assisted with the maintenance and removal of the SASE (1997–1999) temporary broadband deployment which formed a huge observational component (81%) of the seismic network used in this study.

1.2.2 Continuity of the Bushveld Complex

The second part of the thesis (Chapter 3) aims to evaluate the "dipping-sheet" (Meyer and De Beer, 1987) and "continuous-sheet" (e.g. Webb et al., 2004, 2010) models of the Bushveld Complex (BC) using seismic models with greater resolution than that used in the first part of the thesis. The "dipping-sheet" model of Meyer and De Beer (1987) predicts a BC that is discontinuous with no compensation at the Moho. The "continuous-sheet" model of Webb et al. (2004) predicts a BC that is connected at depth and compensated by thickening at the Moho. I have placed the new constraints on the seismic models by first tomographically obtaining Rayleigh wave group velocity maps between periods of 2–15 s. Vs variations with depth and distance were not definitive due to lack of resolution and therefore did not yield publishable results. Second, I extended the Rayleigh wave group velocities in the 2–15 s period range to periods of 60 s using the dispersions from the revised Pasyanos and Nyblade (2007) model. I then jointly inverted the composite Rayleigh wave group velocity dispersions with high-frequency receiver functions for 16 broadband stations distributed across the BC.

The newly constrained seismic models indicate a mafic layering between the BC outcrops that is spatially heterogeneous and more complexly distributed than that predicted by the "continuous-sheet" model and further show evidence of a thickened crust beneath the centre of the BC. The joint inversion results on the uppermost mantle region (Moho–60 km depth) beneath the BC show no systematic differences with past studies. The material in this chapter was published in a peer-reviewed article (appended to this thesis) with the following citation: ***Kgaswane, E.M., Nyblade, A.A., Durrheim, R.J., Julià, J., Dirks, P.H.G.M., and Webb, S.J., 2012. Shear wave velocity structure of the Bushveld Complex, South Africa. Tectonophysics 554–557, 83–104, doi:10.1016/j.tecto.2012.06.003.***

My contribution in the publication indicated above is that I used the inversion code developed by Prof. Charles Ammon (Department of Geosciences, Penn State University, USA) to obtain Rayleigh wave group velocity maps using 197 mining-related and tectonic earthquakes recorded by 45 seismic broadband stations (which included SASE seismic stations) located across the BC. Part of the mining and tectonic earthquake catalogue was contributed by my colleague, Tarzan Kwadiba. I then used the joint inversion code to obtain 16 Vs profiles for broadband seismic stations located within an area of best resolution. The receiver functions (which I computed) used in the joint inversions came from the catalogue of telesismic earthquakes I had already compiled for the work described in Chapter 2. I assembled a preliminary draft of the text, figures, and tables, with the exception of Figures 2a and b which were contributed by Dr. Sue Webb (co-author). The supervision team (Profs. Andy Nyblade, Paul Dirks and Ray Durrheim) including the co-authors helped in reviewing the publication during its drafting phase and conceptually guided the different aspects of the paper.

1.2.3 The Beattie Magnetic Anomaly

The third part of the thesis (Chapter 4) aims to place shear wave velocity constraints on the source of the Beattie Magnetic Anomaly (BMA) within the Namaqua-Natal Belt (NNB) and to evaluate the merits of the existing geophysical models of the BMA source. The crustal source of the BMA has been much debated (e.g. Corner, 1989; Pitts et al., 1992; Harvey et al., 2001; Weckmann et al., 2007a,b; Quesnel et al., 2009; Lindeque et al., 2011). I jointly inverted the high-frequency receiver functions with recently available Rayleigh wave group velocities (Raveloson et al., 2012) that are better resolved than the group velocities used in the first part of the thesis. The resulting seismic models suggest that the source of the BMA lies at upper to middle crustal depths with high Vs ($\geq$ 3.5 km/s) layers. The seismic models further show evidence of a crust that is thick (i.e., $\geq$ 40 km) and a mafic lower crust beneath the area occupied by the BMA. Physical parameter estimates of the crustal host of the BMA suggest that the BMA source could either be an NNB mid-crust with massive sulphide ore bodies, and/or granulite-facies mid-crustal rocks enriched with iron bearing mineralization, and/or massif anorthosites enriched with iron bearing mineralization. These are all plausible models of the BMA source. The joint inversion results on the uppermost mantle (i.e., Moho–60 km depth) are consistent with the findings in Chapter 2 and also consistent with past studies.

My contribution in the chapter described above is that I used the joint inversion code to obtain Vs profiles for the three SASE broadband seismic stations distributed along the Beattie Magnetic Anomaly. I assembled a preliminary draft on text, figures and tables of this chapter. The IGRF versions of the magnetic field shown in Figure 4.9 were contributed by my colleague, Stephanie Scheiber. The supervision team (Profs Andy Nyblade and Ray Durrheim) helped in reviewing this chapter during its drafting phase and conceptually guided the different aspects of the chapter.

References

Adams, A., and Nyblade, A., 2011. Shear wave velocity structure of the southern African upper mantle with implications for the uplift of southern Africa. *Geophysical Journal International*, 186, 808 – 824.

Adam, J.M.-C., and Lebedev, S., 2012.Azimuthal anisotropy beneath southern Africa from very broad-band surface-wave dispersion measurements.*Geophysical Journal International*, 191, 155 – 174.

Corner, B., 1989. The Beattie anomaly and its significance for crustal evolution within the Gondwana framework, paper presented at First Technical Meeting. *South African Geophysical Association*, Johannesburg.

Cornell, D.H., Armstrong, R.A., and Walraven, F., 1998. Geochronology of the Proterozoic Hartley Basalt Formation, South Africa: constraints on the Kheis tectogenesis and the Kaapvaal Craton's earliest Wilson cycle. *Journal of African Earth Sciences*, 26, 5 – 27.

De Wit, M.J., Roering, C., Hart, R.J., Armstrong, R.A., Ronde, C.E.J., Green, R.W.E., Tredoux, M., Peberdy, E., Hart, R.A., 1992.Formation of an Archaean continent.*Nature*, 357, 553 – 562.

De Wit, M.J., and Tinker, J. 2004. Crustal structures across the central Kaapvaal Craton from deep-seismic reflection data. *South African Journal of Geology*, 107, 185 – 206.

Durrheim, R.J. and Green, R.W.E., 1992. A seismic refraction investigation of the Archaean Kaapvaal Craton, South Africa, using the mine tremors as the energy source.*Geophysical Journal International*, 108, 812 – 832.

Eglington, B.M., and Armstrong, R.A., 2004. The Kaapvaal Craton and adjacent orogens, southern Africa: a geochronological database and overview of the geological development of the craton. *South African Journal of Geology*, 107, 13 – 32.

Fouch, M.J., Silver, P.G., Bell, D.R., and Lee, J.N., 2004. Small-scale variations in seismic anisotropy near Kimberley, South Africa.*Geophysical Journal International*, 157, 764 – 774.

Freybourger, M., Gaherty, J.B., Jordan, T.H., and the Kaapvaal Seismic Group, 2001.Structure of the Kaapvaal craton from surface waves.*Geophysical Research Letters*, 28, 13, 2489 – 2492.

Gore, J., James, D.E., Zengeni, T.G., and Gwavava, O., 2009. Crustal structure of the Zimbabwe Craton and the Limpopo Belt of southern Africa: new constraints from seismic data and implication for its evolution. *South African Journal of Geology*, 112, 213 – 228. doi:10.2113/gssajg.112.3-4.213.

Green, R.W.E., and Durrheim, R.J., 1990. A seismic refraction investigation of the Namaqualand Metamorphic Complex, South Africa.*Journal of Geophysical Research*, 95, No.B12, 19927– 19932.

Hartnady, C.J.H., Joubert, P., and Stowe, C.W., 1985. Proterozoic crustal evolution in southwestern Africa.*Episodes*, 8, 49 – 50.

Harvey, J.D., de Wit, M.J., Stankiewicz, J., and Doucouré, C.M., 2001. Structural variations of the crust in the SouthwesternCape, deduced from seismic receiver functions. *South African Journal of Geology*, 104, 231 – 242.

James, D. E., Niu, F., & Rokosky, J. 2003. Crustal structure of the Kaapvaal Craton and its significance for early crustal evolution; A tale of two cratons; the Slave-Kaapvaal workshop. *Lithos*, *71*(2-4), 413-429.

Jelsma, H. A. and Dirks, P.H.G.M., 2002.Neoarchaean tectonic evolution of the Zimbabwe Craton. In C.M.R. Fowler, C.J. Ebinger and C.J. Hawkesworth (Editors), *The Early Earth: Physical, Chemical and Biological Development. Geological Society of London, Special Publications,* 199, 183 – 211.

Julià, J., Ammon, C. J., Hermann, R. B. and Correig, A. M., 2000.Joint inversion of receiver functions and surface-wave dispersion observations.*Geophysical Journal International*, 143, 99 – 112.

Julià, J., Ammon, C. J. and Hermann, R. B., 2003.Lithospheric structure of the Arabian Shield from the joint inversion of receiver functions and surface-wave group velocities.*Tectonophysics*, 371, 1 -21.

Julià, J., Ammon, C. J. and Nyblade, A. A., 2005.Evidence for mafic lower crust in Tanzania, East Africa from joint inversion of receiver functions and Rayleigh wave dispersion velocities.*Geophysical Journal International*, 162, 555 – 569.

Kgaswane, E.M., Nyblade, A.A., Julià, J., Dirks, P.H.G.M., Durrheim, R.J., and Pasyanos, M.E., 2009.Shear wave velocity structure of the lower crust in southern Africa: Evidence for compositional heterogeneity within Archaean and Proterozoic terrains. *Journal of Geophysical Research*, 114, B12304.doi:10.1029/2008JB006217.

Kramers, J.D., McCourt, S., and van Reenen, D.D., 2006. The Limpopo Belt, *In*: M. R. Johnson, C. R. Anhaeusser, R. J. Thomas (Editors) *TheGeology of South Africa*, Geological Society of South Africa, Johannesburg/ Council for Geoscience, Pretoria, 209 – 236.

Kwadiba, M.T.O., Wright, C., Kgaswane, E.M., Simon, R. E., & Nguuri, T. K., 2003. Pn arrivals and lateral variations of Moho geometry beneath the Kaapvaal Craton; A tale of two cratons; the Slave-Kaapvaal workshop. *Lithos, 71*(2-4), 393-411.

Larson, A.M., Snoke, J.A., James, D.E., 2006. S-wave velocity structure, mantle xenoliths and the upper mantle beneath the Kaapvaal craton.*Geophysical Journal International*, doi: 10.1111/j.1365-246X.2006.03005.x

Li, A., and Burke, K., 2006. Upper mantle structure of southern Africa from Rayleigh wave tomography.*Journal of Geophysical Research*, 111, B10303, doi:10.1029/2006JB004321.

Lindeque, A.S., Ryberg, T., Stankiewicz, J., Weber, M.H., and de Wit, M.J., 2007.Deep crustal seismic reflection experiment across the Southern Karoo Basin, South Africa.*South African Journal of Geology*, 110, 419 – 438.

Lindeque, A., de Wit, M.J., Ryberg, T., Weber, M., and Chevalier, L., 2011. Deep crustal profile across the southern KarooBasin and Beattie Magnetic Anomaly, South Africa: an integrated interpretation with tectonic implications. *South African Journal of Geology*, 114, 3 – 4, 265 – 292, doi:10/2113/gssajg.114.3-4.265.

Loots, L., 2012.Investigation of the crust in the southern Karoo using the seismic reflection technique. MSc (*in preparation*), University of the Witwatersrand, Johannesburg, South Africa.

Meyer, R., and De Beer, J.H., 1987. Structure of the Bushveld Complex from resistivity measurements.*Nature*, 325, 610 – 612.

Midzi, V., and Ottemöller, L., 2001.Receiver function structure beneath three southern Africa seismic broadband stations.*Tectonophysics*, 339, 443 – 454.

Nair, S.K., Gao, S.S., Kelly, H.L. and Silver, P.G., 2006. Southern African crustal evolution and composition: Constraints from receiver function studies. *Journal of Geophysical Research*, 111, B02304, doi:10.1029/2005JB003802.

Nguuri, T.K., Gore, J., James, D.E., Webb, S. J., Wright, C., Zengeni, T.G., Gwavava, O., Snoke, J.A., and Kaapvaal Seismic Group, 2001. Crustal structure beneath southern africa and its implications for the formation and evolution of the Kaapvaal and Zimbabwe Cratons. *Geophysical Research Letters*, *28*, 13, 2501 – 2504.

Niu, F and James, D. E., 2002. Fine structure of the lowermost crust beneath the Kaapvaal Craton and its implications for crustal formation and evolution.*Earth and Planetary Science Letters*, 200, 121 – 130.

Pasyanos, M.E., and Nyblade, A.A., 2007.A top to bottom lithospheric study of Africa and Arabia.*Tectonophysics*, 444, no. 1 – 4, 27 – 44.

Pitts, B., Mahler, M., de Beer, J., Gough, D., 1992. Interpretation of magnetic, gravity and magnetotelluric data across the Cape Fold Belt and Karoo Basin, in *Inversion Tectonics of the Cape Fold Belt, Karoo and Cretaceous Basins of Southern Africa*, edited by M. de Wit and I. Ransome, pp. 27 – 32, A.A. Balkema, Brookfield, Vt.

Quesnel, Y., Weckmann, U., Ritter, O., Stankiewicz, J., Lesur, V., Mandea, M., Langlais, B., Sotin, C., Galdéano, A., 2009.Simple models for the Beattie Magnetic Anomaly in South Africa.*Tectonophysics*, 478, 111 – 118.

Silver, P.G., Gao, S.S., Liu, K.H. and K.S. Group, 2001. Mantle deformation beneath southern Africa.*Geophysical Research Letters*, 28, 2493 – 2496.

Silver, P.G., Fouch, M.J., Gao, S.S., Schmitz, M., and Kaapvaal Seismic Group, 2004. Seismic anisotropy, mantle fabric, and the magmatic evolution of Precambrian southern Africa.*South African Journal of Geology*, 107, 45 – 58.

Silver, P.G., Behn, M.D., Kelly, K., Schmitz, M., and Savage, B., 2006.Understanding cratonic flood basalts.*Earth and Planetary Science Letters*, 245, 190 – 201.

Stankiewicz, J., Chevrot, S., van der Hilst, R. D. and de Wit, M. J., 2002. Crustal thickness, discontinuity depth, and upper mantle structure beneath southern Africa: constraints from body wave conversions. *Physics of the Earth and Planetary Interiors*, 130, 235 – 251.

Stankiewicz, J., Ryberg, T., Schulze, A., Lindeque, A., Weber, M., de Wit, M., 2007.Initialresults from wide-angle seismic refraction lines in the Southern Cape.*South African Journal of Geology*, 110, 407 – 418.

Stankiewicz, J., Parsiegla, N., Ryberg, T., Gohl, K., Weckmann, U., Trumbull, R., Weber, M., 2008. Crustal structureof the southern margin of the African continent: Results from geophysical experiments. *Journal of Geophysical Research*, 113, B10313,doi:10.1029/2008JB005612.

Van Schijndel, V., 2013.Precambrian crustal evolution of the Rehoboth Province, South Africa.Ph.D. thesis, University of Gothenburg, Sweden (unpublished).

Webb, S.J., R.G. Cawthorn, T.K. Nguuri, and James, D.E., 2004. Gravity modelling of Bushveld Complex connectivity supported by Southern African Seismic Experiment results.*South African Journal of Geology*, 107, 207 – 218.

Webb, S.J., Ashwal, L.D., Cawthorn, R.G., 2010. Continuity between eastern and western Bushveld Complex, South Africa, confirmed by xenoliths from kimberlite.*Contributions to Mineralogy and Petrology*, 162, 101 – 107, doi:10.1007/s00410-010-0586-z.

Weckmann, U., Ritter, O., Jung, A., Branch, T., de Wit, M., 2007a.Magnetotelluric measurements across the Beattie magnetic anomaly and the Southern Cape Conductive Belt, South Africa.*Journal of Geophysical Research*, 112, doi:10.1029/2005JB003975.

Weckmann, U., Jung, A., Branch, T., Ritter, O., 2007b.Comparison of electrical conductivity structures and 2D magnetic modelling along two profiles crossing the Beattie Magnetic Anomaly, South Africa.*South African Journal of Geology*, 110, 449 – 464.

Wright, C., Kgaswane, E.M., Kwadiba, M.T.O., Simon, R.E., Nguuri, T.K., and McRae-Samuel, R., 2003.South African seismicity, April 1997 – April 1999, and regional variations in the crust and uppermost mantle of the Kaapvaal Craton, *Lithos*, 71, 369 – 392.

Yang, Y., Li, A., Ritzwoller, M.H., 2008. Crustal and uppermost mantle structure in southern Africa revealed from ambient noise and teleseismic tomography. *Geophysical Journal International* 174, 235 – 248, doi:10.1111/j.1365-246X.2008.03779x.

Chapter 2

Structure of the lower crust of southern Africa

Abstract

In this study, P-wave teleseismic receiver functions and Rayleigh wave group velocities are jointly inverted to investigate the nature of the lower crustal structure across southern Africa. The investigation entailed the use of teleseismic recordings by 89 broadband seismic stations located in Botswana, South Africa and Zimbabwe. The 1-D shear wave velocity models obtained from the joint inversion show that most of the Archaean and Proterozoic terrains in southern Africa have a lower crust (below 20–30 km depths) with velocities ≥ 4.0 km/s, implying a lower crust that is mafic in composition. This is in contrast to a greater portion of the Kimberley terrain (including small portions of the adjacent Kheis Province and Witwatersrand terrain) in South Africa and the western part of the Tokwe terrain within the Zimbabwe Craton, which show a lower crust (below 20–30 km depths) with velocities that are ≤ 3.9 km/s, implying a lower crust that is intermediate-to-felsic in composition. The intermediate-to-felsic nature of the lower crust in the Kimberley terrain is attributed to rifting and crustal thinning due to the Ventersdorp tectonomagmatism (~ 2.7 Ga). Similar type of rifting and crustal thinning could have occurred in the western part of the Tokwe terrain.

The material in this chapter is fully described in the peer-reviewed paper with the following citation: ***Kgaswane, E. M., A. A. Nyblade, J. Julià, P. H. G. M. Dirks, R. J.Durrheim, and M. E. Pasyanos (2009), Shear wave velocity structure of the lower crust insouthern Africa: Evidence for compositional heterogeneity within Archaean and Proterozoicterrains, J. Geophys. Res., 114, B12304, doi:10.1029/2008JB006217.***

2.1 Introduction

This study aims to add onto the existing knowledge of the structure and compositional variability of the crust across the southern African shield already gathered by previous seismic studies. The lower crust is one part of the southern African shield that still needs further elucidation. In fact, the composition of the lower crust is still an active research area of global geodynamics (e.g. Christensen and Mooney, 1995; Rudnick and Fountain, 1995; Rudnick and Gao, 2003). In this study the nature of both Archaean and Proterozoic crust in southern Africa is investigated by using 1-D shear wave velocity models obtained by jointly inverting receiver functions and Rayleigh wave group velocities.

Receiver function analysis by Niu and James (2002) found that the lower crust around most parts of the Kimberley region in the western part of the Kaapvaal Craton (KC) has an intermediate-to-felsic composition. From this result, they suggested that the lower crust beneath the KC is dominated by intermediate-to-felsic lithologies. In contrast, receiver function analyses by Nguuri (2004) and Nair et al. (2006), yielded crustal Vp/Vs ratios as high as 1.78 for parts of the KC and the surrounding Proterozoic mobile belts, suggesting the presence of mafic lithologies in the lower crust in certain parts. Crustal velocity models developed using seismic reflection and refraction data also suggest significant variability in lower crustal composition (e.g. Green and Durrheim, 1990; Durrheim and Green, 1992; de Wit and Tinker, 2004). The joint inversion results of data recorded by the array of broadband seismographs (see Figure 2.1) covering a considerable area of the southern African shield indicate conspicuous differences in the lower crustal composition within and between the Archaean and Proterozoic terrains.

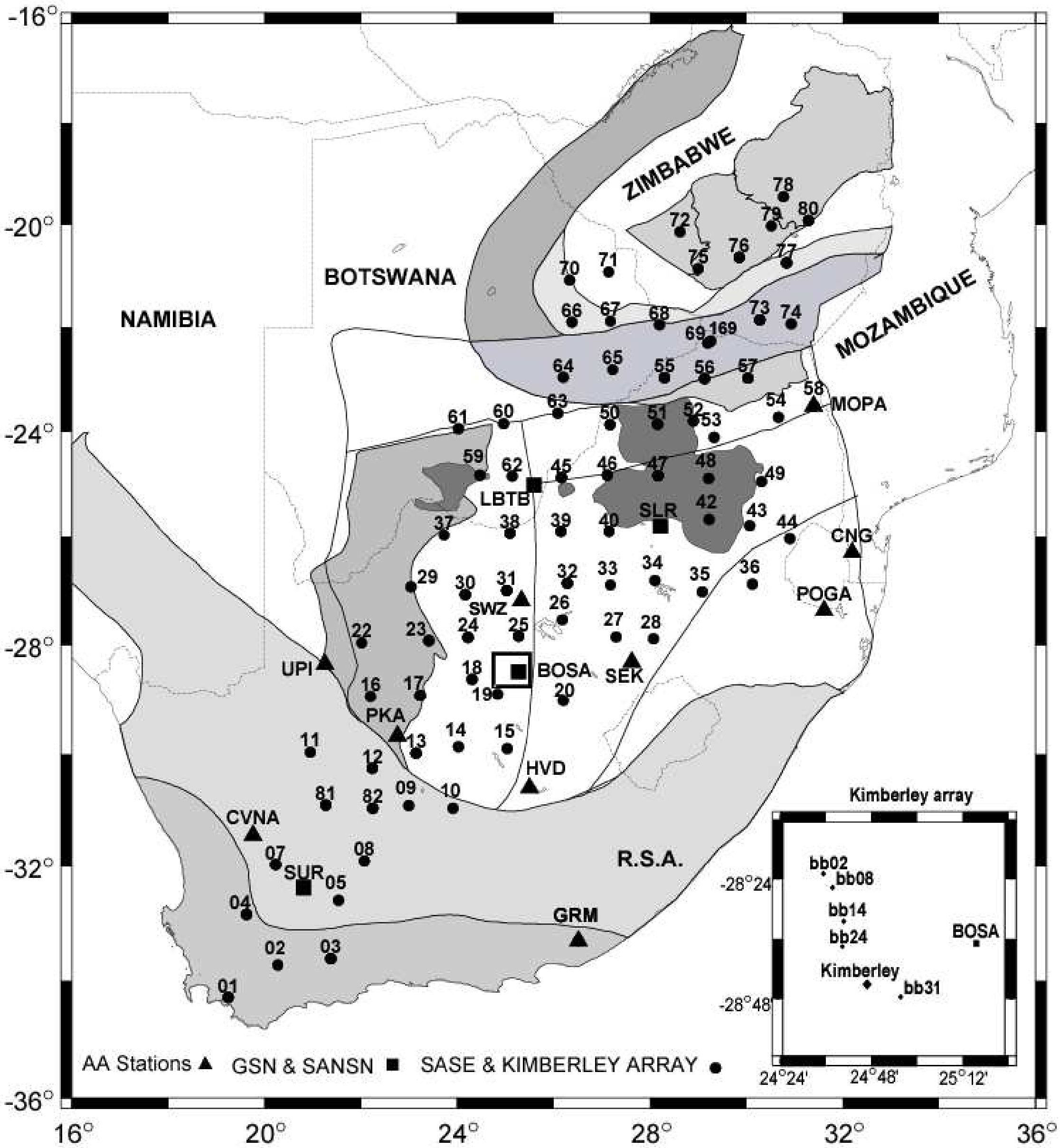

Figure 2.1 Map showing distribution of broadband seismic stations used in this study in relation to the terrain boundaries shown in Figure 1.1. The open square in the central part of the Kimberley terrain shows the location of the Kimberley array. The area within the box is enlarged in the bottom right corner. AA, AfricaArray network; GSN, Global Seismic Network; SANSN, South Africa National Seismic Network; SASE, Southern African Seismic Experiment.

In this chapter, following a brief review of the geological framework of southern Africa, I describe the data sets and technique used for the joint inversions, discuss similarities and differences in the lower crustal composition indicated by the resultant velocity models, and further examine the implications of the lower crustal heterogeneity in terms of the major tectonomagmatic events that affected the Precambrian crustal fabric of the southern African shield.

2.2 Tectonic and geological framework of southern Africa

The Precambrian lithospheric fabric of the southern African shield is mainly comprised of the Archaean KC and Zimbabwe Craton (ZC), which are connected by the Archaean and Palaeoproterozoic Limpopo Belt (LB) (de Wit et al., 1992) (see Figure 1.1). The Archaean KC and ZC together form central piece of the so-called Kalahari Craton, which is rimmed by the Palaeoproterozoic Okwa-Magondi Belt to the northwest, the Mesoproterozoic Namaqua-Natal Belt (NNB) and the Palaeoproterozoic Kheis Province (KP) to the south and southwest, respectively, and the Palaeozoic Cape Fold Belt (CFB) even further to the south (Figure 1.1). The KC (~3.7–2.7 Ga) (de Wit et al., 1992; Eglington and Armstrong, 2004) is basically a granite-greenstone terrain subdivided into four sub-terrains: the Kimberley (3.0–2.8 Ga), Pietersburg (3.0–2.8 Ga), Witwatersrand and Swaziland terrains (both 3.6–3.1 Ga), which are separated by the Thabazimbi-Murchison and Colesburg lineaments and the Inyoka Fault (see Figure 1.1). Throughout geological time, the KC has been subjected to a series of magmatic and deformation events that are responsible for the presence of intracratonic basins including the Dominion (3.1 Ga), Witwatersrand (3.0–2.8 Ga), Ventersdorp (2.7 Ga), and Transvaal (2.6–2.2 Ga) (Eglington and Armstrong, 2004; Johnson et al., 2006).

The ZC (~3.6–2.5 Ga) is also a granite-greenstone terrain that formed in three stages (e.g. Dirks and Jelsma, 2002). The Tokwe Gneiss terrain (3.6–3.3 Ga) was formed in the centre of the craton. A sequence of clastic sediments and greenstones accreted against the western part of this terrain between 3.2 and 2.8 Ga. The Great Dyke was emplaced around 2.58 Ga and marks the last major tectonothermal event to affect the craton (Jelsma and Dirks, 2002). The LB (Figure 1.1) is an east-west trending zone of high-grade metamorphic rocks that separates the KC and ZC (e.g. McCourt and Armstrong, 1998; Kramers et al., 2006) and is subdivided into three domains: the Northern Marginal Zone (NMZ), the Central Zone (CZ), and the Southern Marginal Zone (SMZ), which are separated by major shear zones (Kramers et al., 2006). The Bushveld Complex (BC) (2.06 Ga) (Figure 1.1) is the largest known layered mafic intrusion, extending > 350 km in both north-south and east-west directions across the northern KC. It is divided into the Rustenburg Mafic Layered Suite, the Lebowa Granite Suite, the Rashoop Granophyre Suite, and the volcanic Rooiberg Group (e.g. South African Committee for Stratigraphy, 1980; Hatton and Schweitzer, 1995; Webb et al., 2004; Cawthorn et al., 2006).

The Kalahari Craton is surrounded by Proterozoic to Phanerozoic belts.The Magondi Belt (2.0–1.8 Ga) to the west and northwest of the ZC is dominated by passive margin, shelf sediments of the Magondi Supergroup. These rocks have been correlated with deformed mafic and felsic magmatic rocks of the 2.05 Ga Okwa terrain in central Botswana (Figure 1.1) (Stowe, 1989; McCourt et al., 2001). The NNB (Figure 1.1) to the south and west of the KC is comprised of igneous and supracrustal rocks that accreted against the craton during the Namaqua Orogeny (1.2–1.0 Ga). The NNB is exposed to the southwest (the Namaqua Sector) and southeast (the Natal Sector) of the craton (e.g. Cornell et al., 2006), but the central part of the belt is covered by younger sediments of the Karoo Supergroup. The Kheis Belt (Figure 1.1) rims the western part of the KC and is characterized by the passive margin of the sequence of siliciclastic rocks of the Olifantshoek Supergroup (2.0–1.7 Ga). The belt was formed as a thin-skinned fold-and-thrust belt when the Olifantshoek rocks were thrust eastward onto the craton and coincided with the accretion of the Namaqua Sector of the NNB (1.2–1.0 Ga) to the far west (e.g. Stowe, 1986; Moen, 1999; Eglington and Armstrong, 2004; Cornell et al., 2006). The Palaeozoic to Mesozoic CFB (see Figure 1.1) is located further south of the KC and is comprised of the siliciclastic passive sequence of the Cape Supergroup (500–330 Ma), which deformed in a northeast verging fold-and-thrust belt during the Cape Orogeny (~278–245 Ma). There is ongoing debate as to whether the fold belt formed as a result of a subduction zone on the southern margin of the Gondwana supercontinent or as a result of a south-dipping major crustal shear zone (e.g. Thamm and Newton, 2006 and references therein; Newton et al., 2006 and references therein).

2.3 The crustal structure of southern Africa – literature review

Earthquakes or tremors due to gold mining activities in the Witwatersrand Basin were the energy sources used by early seismological studies of the crustal structure of the KC (e.g. Gane et al., 1949; Willmore et al., 1952; Gane et al., 1956; Hales and Sacks, 1959). Based on their observations, Hales and Sacks (1959) postulated that the crust of the eastern KC had a two-layered structure. This study estimated the upper crust to have P and S wave velocities of 6.0 and 3.6 km/s, respectively, and the rest of the crust to have P- and S-wave velocities that reach 7.2 km/s and 4.2 km/s, respectively. The study further estimated a crustal thickness of ~37 km and P-wave velocity of 8.0 km/s in the uppermost mantle. Pioneering surface wave studies (e.g. Bloch et al., 1969) used seismograms produced by regional earthquakes to invert fundamental and higher mode Rayleigh and Love wave group and phase velocities to derive a shear wave velocity model of the northern KC. The model shows a Poisson's ratio of 0.28 for the lower crust of the northern KC and a crustal thickness in the range of 40–45 km.

Durrheim and Green (1992) conducted the first refraction study of the central KC using mine tremors from the gold mines in the Witwatersrand Basin. The resulting model showed a crustal thickness of 35 km and P-wave velocities in the range of 6.4–6.7 km/s for the lower crust. A similar approach using explosives as energy sources, was carried out for the NNB by Green and Durrheim (1990). Numerous seismological studies in the past decade were based on seismic broadband data collected from the SASE network (Carlson et al., 1996). These studies (e.g. Harvey et al., 2001; Nguuriet al., 2001; Stankiewicz et al., 2002; Niu and James, 2002, James et al., 2003, Kwadiba et al., 2003; Wrightet al., 2003; Webb et al., 2004; Nair et al., 2006; Gore et al., 2009) show crustal thicknesses of 35–45 km and 34–37 km for the KC and ZC, respectively. Thestudies further reported Moho depths for the KP, BC, LB, Okwa/Magondi Belt, NNB and CFB to be 40 km, 40–53 km, 37–55 km, 40–45 km, 40–50 km, and26–45 km, respectively. A seismic refraction study of the Damara Belt (~ 0.55 Ga) and the Archaean-Proterozoic Rehoboth Province indicated that these two tectonic terrains have lower crustal P-wave velocities of ~7.2 km/s (i.e, ~ 4.2 km/s Vs), crustal thicknesses of ~47 km, and a crust-mantle transition zone that is approximately 13 km thick (Baier et al., 1983).

Nguuri (2004) and Nair et al. (2006) reported variableVp/Vs ratios for a number of crustal terrains acrosssouthern Africa (see Table 1 in the attached paper) and interpreted Vp/Vs ratios >1.76 to be indicative of mafic and ultramafic lithologies in the crust. The differences in the Vp/Vs ratio for some terrains, as well as the number of stations used to compute the average ratios, reflect different selections of geographicregions and data in the two studies. Gore et al. (2009) estimated a Poisson's ratio greater than 0.26 for the LB, implying a mafic crust, and Poisson's ratio of ≤ 0.26 for the ZC, suggestive of the lack or absence of mafic layers in the cratonic crust.

Niu and James (2002) used receiver function analysis to investigate the crustal structure beneath a small area in the Kimberley terrain using data from the Kimberley seismic array. They obtained P and S velocities for the lowermost crust of 6.75 and 3.90 km/s, respectively, and a Poisson's ratio of 0.25, indicating an intermediate-to-felsic composition for the lowermost crust.They also found a sharp (i.e., less than 0.5 km wide) and flat (i.e., topographic relief less than 1 km) Moho. Petrologic studies of the Kimberley area by Schmitz and Bowring (2003a, b) show that mafic granulites are absent from lower crustal xenolith suites, consistent with the findings of Niu and James (2002).

2.4 Data sources, data processing and methodology

2.4.1 Data sources

Originally, 101 broadband seismic stations were used to compute receiver functions but after quality control only 89 stations (see Results section) were used for further interpretation. The 101 seismic stations belong to the SASE network (82 stations), the AfricaArray network (10 stations), the South African National Seismograph Network (1 station), the Global Seismic Network (3 stations) and the Kimberley array (5 stations) which was deployed in 1999 as a high resolution extension of the SASE network (Niu and James, 2002). The AfricaArray network (consisting of seismic stations covering a substantial portion of the African continent) began operation in 2006 and only more than 1 year of data from the AfricaArray stations in southern Africa were used for this study (see Figure 2.1). A total of 89 teleseismic earthquakes with epicentral distances between 30° and 99° recorded by the stations were selected for computing receiver functions (Figure 2.2a). The earthquakes have moment magnitudes ranging from 5.8 to 9.0.

Appendix A describes the full details of the earthquakes. Rayleigh wave group velocities used in this study for periods of 10–90 s were taken from a revised version of the model presented by Pasyanos and Nyblade (2007). In the revised Pasyanos and Nyblade (2007) model, group velocity measurements from 39 broadband seismic stations spread across southern Africa were combined with the measurements used to construct the original Pasyanos and Nyblade (2007) model (Figure 2.2b). The group velocity measurements were made using single station measurements (event to station) and the inversion method used to obtain group velocity maps is based on ray approximation. For periods of 100–175 s, group velocities were taken from the Harvard model (Larson and Ekström, 2001). A single dispersion curve for each station was obtained by first joining the group velocities from 10–90 s and 100–175 s and then smoothing the composite curve using a 3-point running average. The group velocity measurements from the Harvard model were included in the composite curve so that the 1-D models obtained from the inversions would show mantle structure that is regionally representative of southern Africa.

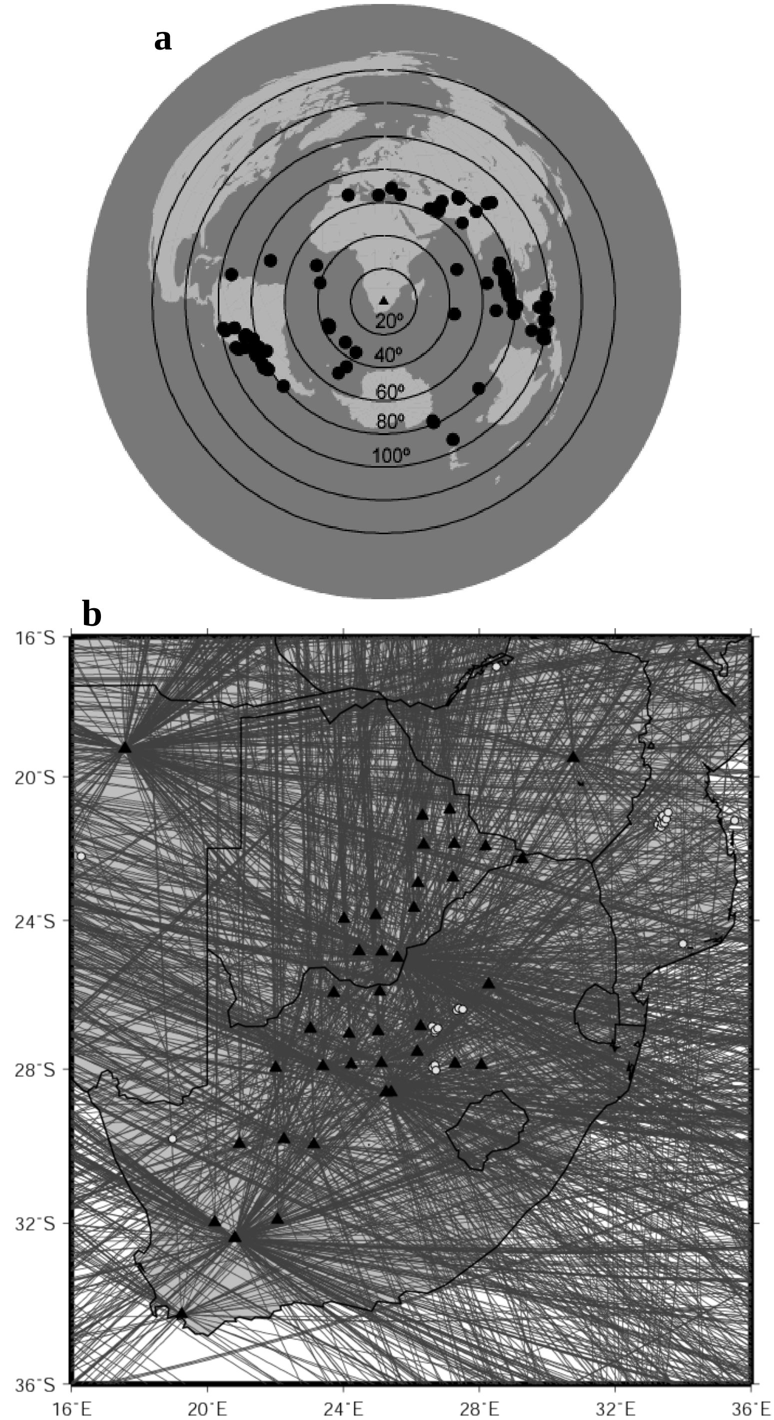

Figure 2.2 (**a).** Distribution of teleseismic earthquakes used for this study (small solid circles). The triangle shows the center of the SASE network. Concentric circles show distance in 20° increments from the center of the network. (**b).** Map showing raypath coverage for 20 s Rayleigh waves used in the revised Pasyanos and Nyblade (2007) group velocity model. Station locations are shown with solid triangles, and event locations are shown with white circles. Most of the events are located outside of the area shown in the map.

2.4.2 Data processing and methodology

2.4.2.1 Receiver functions

A receiver function is a time series waveform computed from three-component seismograms and shows the relative response of Earth structure beneath or near the receiver site (Ammon et al, 1990; Ammon, 1997). Receiver functions in this study were computed using the iterative deconvolution method of Ligorría and Ammon (1999). In computing a receiver function response, the deconvolution procedure removes effects associated with near-source structure, source time function, and instrumental effects from the time series waveforms (Langston, 1979). Only the radial receiver functions were used in the joint inversion with the Rayleigh wave group velocity curves. The transverse receiver functions are identically zero for isotropic and laterally homogeneous media, and were computed to verify that this is the case for crust and upper mantle structure under each station.

To properly account for the phase move out due to varying incidence angles (Cassidy, 1992; Gurrola and Minster, 1998), receiver functions are grouped according to ray parameter. For each station, receiver functions were binned in ray parameter groups from 0.04 to 0.049 s/km, 0.05 to 0.059 s/km, and 0.06 to 0.069 s/km. Receiver function averages were then computed for each ray parameter bin. For each teleseismic event, receiver functions were computed at two overlapping frequency bands: a low frequency band of $f \leq 0.5$ Hz (Gaussian bandwidth of 1.0 s), and a high frequency band of $f \leq 1.25$ Hz (Gaussian bandwidth of 2.5 s). The low frequency bandwidth provides a better constraint on longer wavelength features in the subsurface, while the high frequency bandwidth provides a better constraint on shorter wavelength features. The combination of low and high frequency receiver functions helps in discriminating sharp versus gradational transitions in the subsurface (Owens and Zandt, 1985; Julià, 2007).

2.4.2.2 Joint inversion method

The joint inversion of receiver functions and fundamental-mode surface wave dispersions makes use of a linearized inversion procedure and provides 1-D shear wave depth-velocity profiles for each recording station (Julià et al., 2000, 2003). The application of the joint inversion method assumes that both the receiver functions and surface wave dispersions sample the same portion of the Earth structure and the medium is plane-layered, isotropic, and laterally homogeneous. The advantage of jointly inverting receiver functions and surface wave dispersion measurements is that better resolution of the subsurface shear wave velocity structure can be obtained compared to when either data set is inverted independently (Julià et al., 2000, 2003). The linearized inversion procedure minimizes an objective function consisting of a weighted combination of the L2 norm of the vector residuals corresponding to each data set and a model vector difference norm (smoothness constraint) of the second order differences between adjacent layers (Ammon et al., 1990; Julià et al., 2000). The weights consist of a normalization constant that accounts for the different number of data points and different physical units in each data set, as well as an influence factor that controls the relative influence of each data set on the inverted model (Julià et al., 2000). The model vector difference norm helps in stabilizing the inversion procedure by placing smoothness constraint on the resulting 1-D depth-velocity profiles.

The resulting Vs models are, therefore, a compromise between fitting observations, model simplicity, and *a priori* constraints (Julià et al., 2005). Appendix B provides a theoretical basis for the linearized form of the joint inversion scheme as developed by Julià et al. (2000, 2003). The joint inversion technique has been widely used to investigate crustal and upper mantle structure in other continental regions, the Arabian shield (Julià et al., 2003), the Tanzania Craton (Julià et al., 2005), and the Ethiopian Plateau (Dugda et al., 2007). Influence factors and smoothing parameters (in this study) were selected for each tectonic domain in order to obtain smooth depth-velocity profiles that match the observations. For most of the stations, a good fit to the data was obtained for an influence factor of 0.5 and a smoothness parameter from zero to 0.2. The smoothness parameter had to be raised as high as 0.3 for some of the stations within the mobile belts, suggesting a greater degree of small-scale heterogeneity.

The parameterization of the starting model consisted of 74 layers extending to a depth of 532 km. Layer thicknesses of 1 and 2 km were used for the first and second layer, 2.5 km for layers between 3 and 60.5 km depth, 5 km for layers between 60.5 and 255.5 km depth, and 17 to 40 km for layers below 255.5 km depth. The increase in layer thicknesses with depth corresponds to a decrease in the resolving power of the dispersion velocities with increasing period. The starting model used for the inversions is the PREM model (Dziewonski and Anderson, 1981) modified for continental structure above 60.5 km depth (see Figure 5 of attached paper). Poisson's ratio in the starting model was set at 0.25 in the crust and mantle to a depth of 86 km, 0.28 between depths of 86–230 km, 0.29 between depths of 230 and 374 km, 0.30 between depths of 374–430 km, and 0.29 between depths of 430–532 km. Densities were obtained from P-wave velocities using the empirical relationship of Berteussen (1977).

2.4.2.3 Starting model dependence and trade-offs

The sensitivity of the inversion results towards the starting model can be tested using a range of regional models as starting models for the inversion (Qiu et al., 1996; Zhao et al., 1999; Simon et al., 2002; Li and Burke, 2006). P-wave velocities were computed using the same Vp/Vs ratio as for the starting model. The results of this test (see Figure 5 of attached paper) indicate inversion results in the 0–60 km depth range that produce the same or similar inversion results and this confirms the inversion results of the joint inversion algorithm are not sensitive to the starting models.

Since long-period group velocities constrain average velocity structure within relatively large depth ranges in the upper mantle, a trade-off exists between shallow and deep structure (e.g. Julià et al., 2005). This trade-off can be constrained by forward modelling structure below 200 km depth using a trial-and-error process to find models that best fit the 140–175 s period group velocities. This was done by fixing velocities below 200 km between a range of –5 and +5% of the PREM velocities and then inverting for the velocity structure above 200 km depth. The best fitting model for each station was selected when the predicted group velocities in the 140–175 s period range matched the observed group velocities. As an example, station SA55 with velocities of PREM and –2, –3, –5% of PREM below 200 km depth was forward modelled and the best fitting model for this station is –3% PREM (see Figure 6 of attached paper). For most of the stations, it was found that a –2% PREM model tends to fit the 140–175 s period group velocities best. However, a –3% PREM model was used for the stations in the KP, LB, Okwa terrain, and ZC, and a –5% PREM model was used for both the NNB and CFB.

2.4.2.4 Model Uncertainties

The uncertainties in the Vs models at crustal depths were determined by a selection of model parameters for the inversions, as well as by the group velocities taken from the revised Pasyanos and Nyblade (2007) model. Following the approach by Julià et al. (2005), the uncertainties in the inversion results from parameter selection were estimated by repeating inversions for each station using a range of weighting parameters, constraints, and Poisson's ratio. The uncertainties in the shear wave velocities for the crust obtained from this procedure are around 0.1 km/s. Resolution tests of the revised Pasyanos and Nyblade (2007) group velocity model indicate that the spatial resolution at periods most sensitive to crustal structure (10–50 s) is 3 to 4 degrees, and thus the revised Pasyanos and Nyblade (2007) group velocity model has sufficient resolution to image differences in group velocities between regions that are 300 to 400 km wide.

Uncertainties in crustal velocities introduced by the group velocity measurements were assessed by selecting two dispersion curves from the revised Pasyanos and Nyblade (2007) model showing ‘‘end-member’’ high and low group velocities. The high group velocities from one station were replaced with the low ones from another station (and vice versa) and subsequently the joint inversions were performed for each station with the newly acquired group velocities. This approach was repeated for many stations using the approach indicated above. The results are illustrated for two stations, BOSA and SA81 (shown in Figure 2.3). For station BOSA in the middle of the KC, group velocities in the 10–50 s range are lower than for station SA81 in the NNB, and the 1-D inversions for these stations show a very different lower crustal structure (Figures 2.3a and 2.3c).

When the 1-D inversion is performed for station BOSA using the higher group velocities for SA81, the shear wave velocities increase by 0.1 to 0.2 km/s (Figure 2.3b). When the 1D inversion is performed for SA81 using the lower group velocities for BOSA, the shear wave velocities decrease by 0.1 to 0.2 km/s (Figure 2.3d). In all four models, the dispersion curves and receiver functions are fit equally well (Figure 2.3). This exercise indicates that even for regions less than 300 to 400 km wide, at most an uncertainty of 0.1 to 0.2 km/s in shear wave velocity is introduced by using the group velocities from the revised Pasyanos and Nyblade (2007) model. According to these assessments, the overall uncertainty in the shear wave velocities is no more than 0.2 km/s for any given crustal layer in the model. This uncertainty in the shear wave velocity translates into an uncertainty of no more than 2 to 3 km in Moho depth for most stations where a velocity discontinuity can be seen between the crust and mantle, and no more than 5 km where a smoothly varying shear wave velocity profile is found, indicating a gradational Moho.

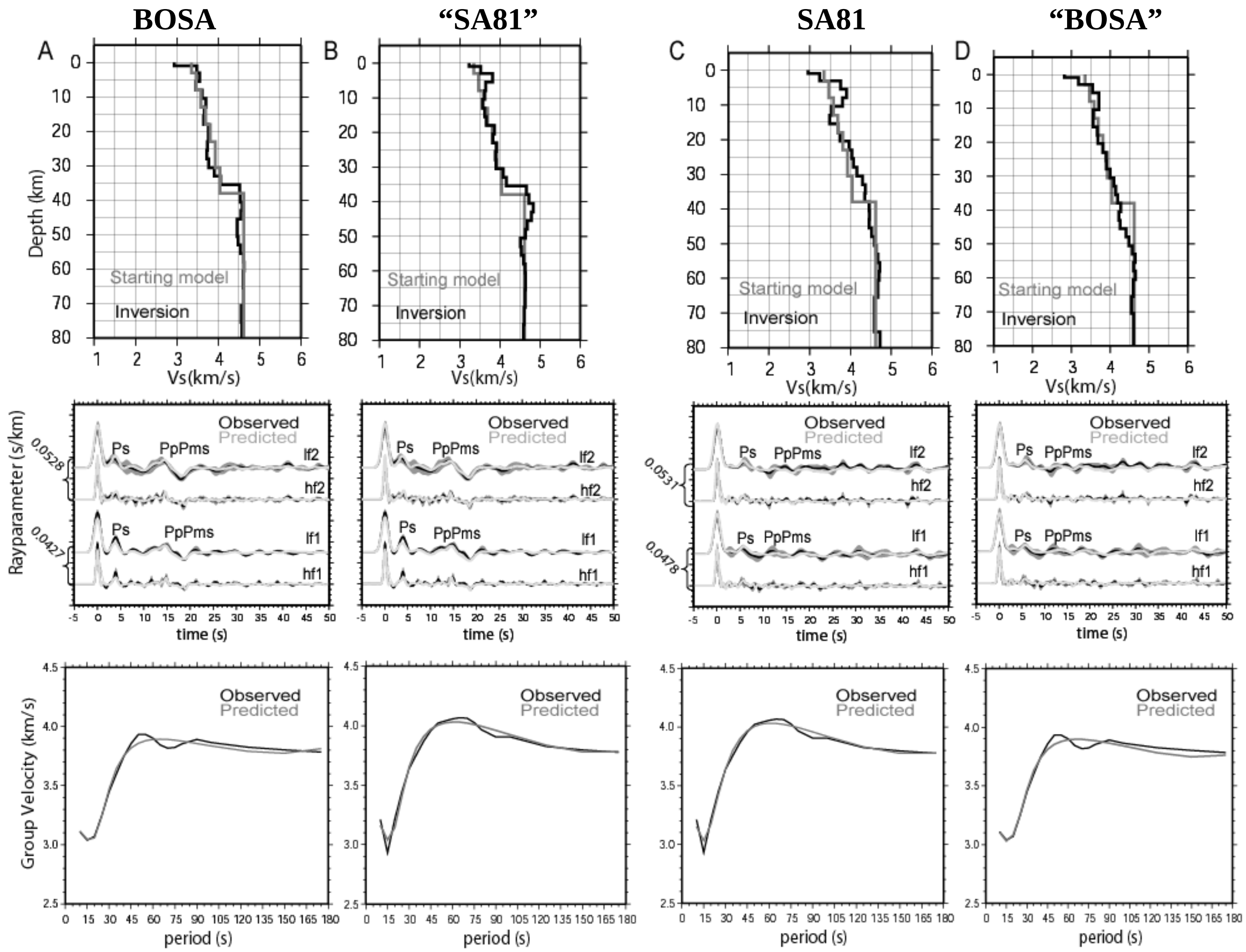

Figure 2.3 Assessment of uncertainties in the joint inversion results using two stations, BOSA and SA81, with different group velocity curves. (**a**). Normal inversion results for BOSA using the group velocities for the location of BOSA from the revised Pasyanos and Nyblade (2007) model. (**b**). Inversion results similar to Figure 2.3a but obtained with the group velocities replaced with those of SA81. (**c**). Normal inversion results for SA81 using the group velocities for the location of SA81 from the revised Pasyanos and Nyblade (2007) model. (**d**). Inversion results similar to Figure 2.3c but obtained with the group velocities replaced with those of BOSA.The top plots show 1-D Vs models from the joint inversion using the receiver functions shown in the middle plots and the group velocities are shown in the bottom plots. For the receiver functions, 1s error bounds are shown with gray shading around the average observed receiver functions (black line) and the predicted receiver functions (light gray line). The high (hf1, hf2) and low (lf1, lf2) frequency receiver functions are grouped in different ray-parameter bins.

2.5 Results

The inversion yielded poor results for twelve of the 101 stations and therefore interpretations were not made for these stations. The inversion results for these twelve stations either showed a poor signal-to-noise ratio, leading either to poor waveform fits (e.g. stations SA01, SA02, SA03, SA58, SA69,SA82, SA139, SA155, CNG), or the Moho Ps conversion was indistinct (e.g. stations SA07, SA08, SA12). The results for the remaining 89 stations are summarized in Figure 2.4a–d. The velocity profiles for 10 stations (SA10, SA22, SA43, SA44, SA66, SA73, SA169, GRM, MOPA, POGA) show two depths where there is an increase in shear wave velocity above 4.3 km/s with a region of velocity less than 4.3 km/s in between.

Detailed modelling of the receiver functions and Rayleigh wave group velocities associated with the joint inversion results in Figure 2.4 are shown in Appendix C. Figure 2.4 shows the shear wave velocity profilesgrouped by tectonic terrain, and Table 2.1 provides a summaryof key crustal parameters derived from these profiles. The crustal thickness beneath each station was determined by picking the Moho at the depth where Vs exceeds 4.3 km/s (e.g. Christensen and Mooney, 1995; Christensen, 1996). Shear wave velocity ranges fortypical lower crustal lithologies obtained by using experimentallydetermined P-wave velocities and Vp/Vs ratios (e.g. Christensen and Mooney, 1995; Christensen, 1996) show that shear wave velocities in the lower crust cannot be higher than 4.3km/s. Shear wave velocities above 4.3 km/s have therefore been assumed to indicate the presence of lithologies with mantle compositions, and therefore the Moho has been picked where the shear wave velocities exceed that value. Many of the stations show a clear Moho discontinuity where Vs increases from < 4.3 km/s to > 4.3 km/s, but for other stations the change in shear wave velocity is gradational.

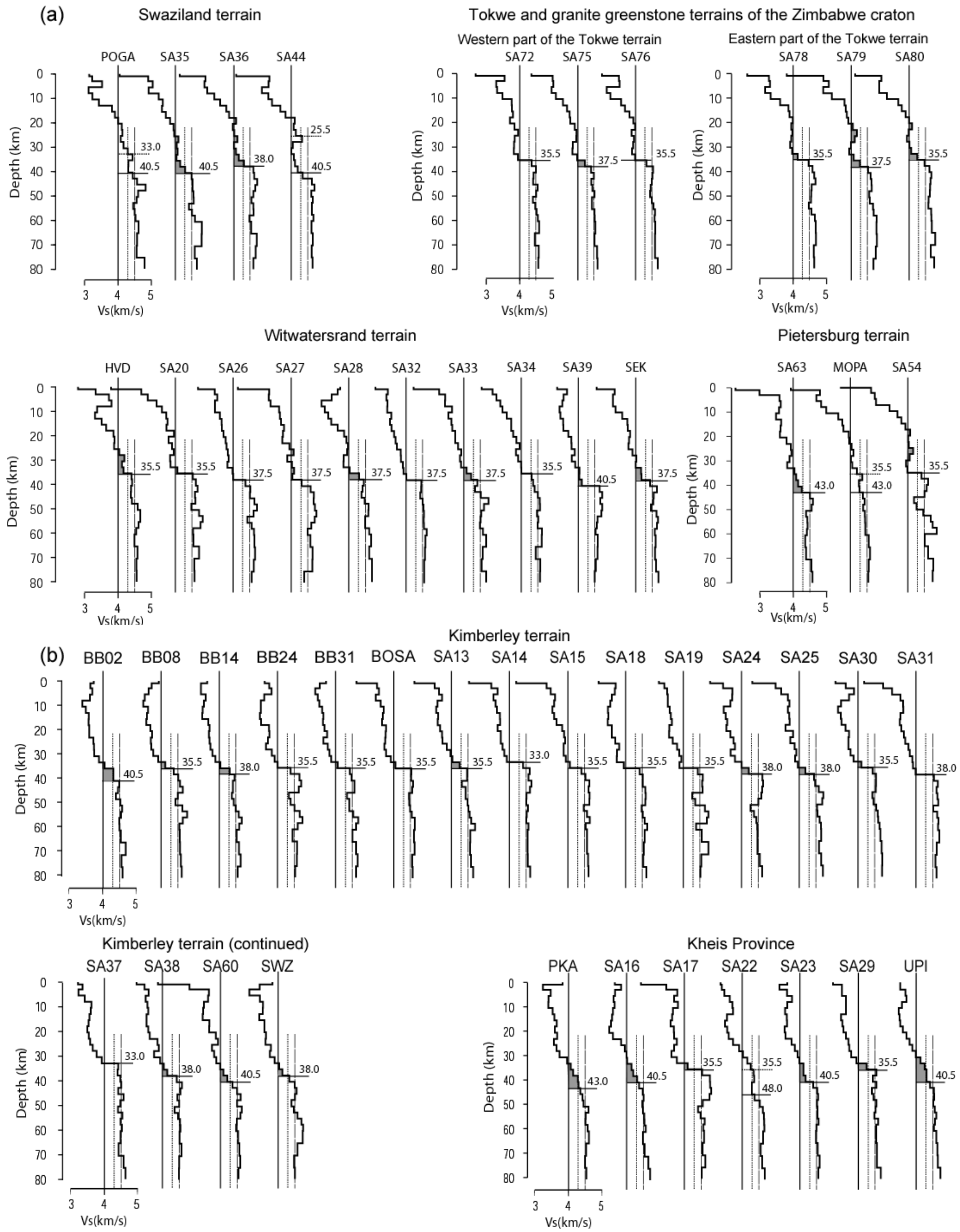

Figure 2.4 (a–d) Shear wave velocity profiles grouped by tectonic terrain. Moho depths are indicated with horizontal lines and numbers in km. Lower crustal layers with Vs ≥ 4.0 km/s are shaded, and reference lines at 4.0 km/s (solid), 4.3 km/s (dotted), and 4.5 km/s (dashed) are shown in each profile. See text for explanation of profiles where two horizontal lines (one dotted and one solid) are shown.

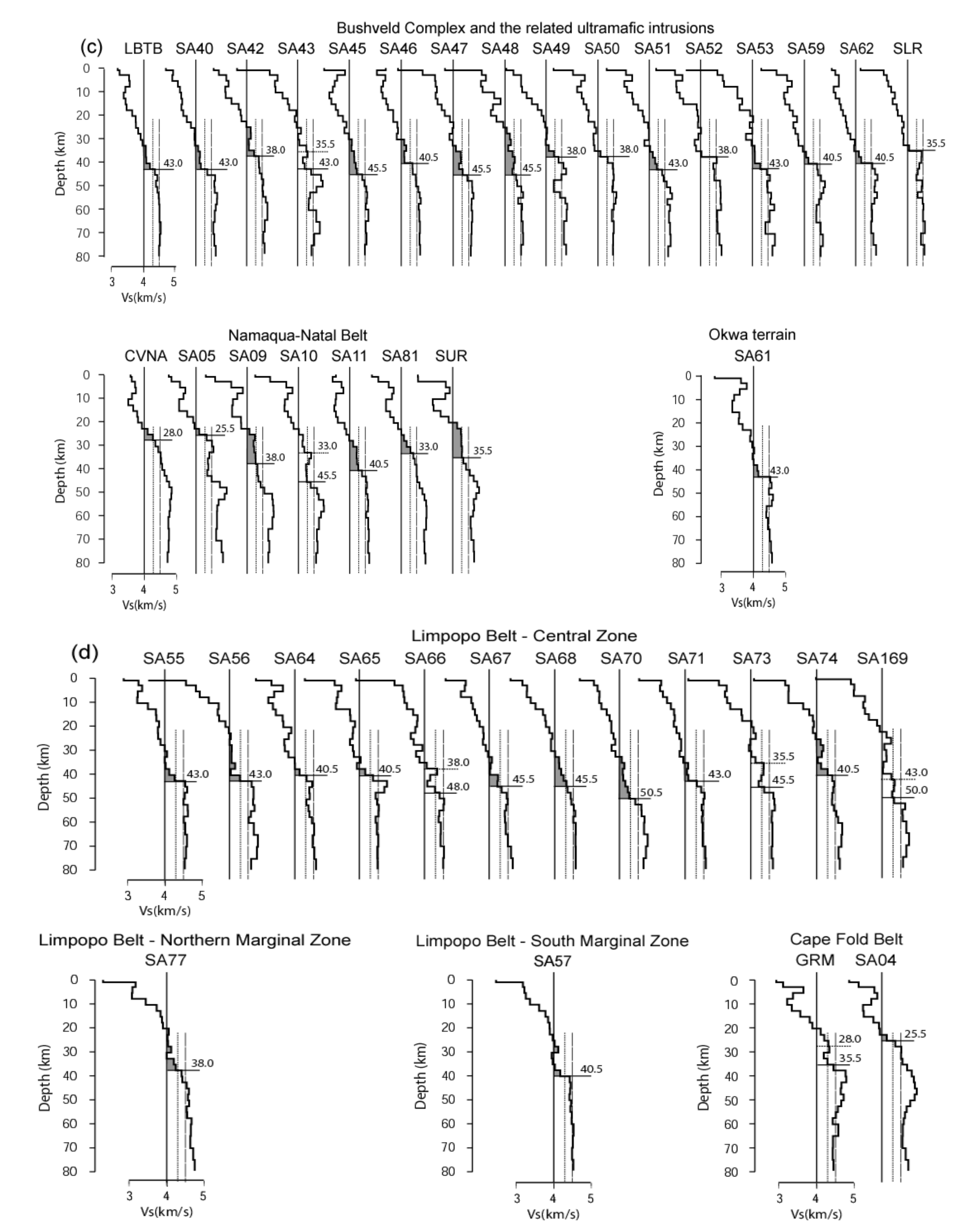

Figure 2.4 (Continued)

Table 2.1 Summary of crustal structure by geological terrains shown in Figures 2.4 and 2.5

Regime	Terrain	Average Moho depth ± standard deviation (km)	Number of stations	Sn (km/s)	Average Vs of the crust ± standard deviation (km)	Average Vs below 20 km depth (km/s)	Average Vs below 30 km depth (km/s)	Average thickness of layers in the lower crust with Vs ≥ 4.0 km/s (km)
KC	**Witwatersrand**	37 ± 3	11	4.6	3.7 ± 0.1	3.9	4.0	11
	Swaziland	39 ± 2	4	4.7	3.7 ± 0.1	4.1	4.2	22
	Pietersburg	39 ± 2	4	4.6	3.7 ± 0.1	4.0	4.0	14
	Kimberley							
	Kimberley (central)	36 ± 1	17	4.6	3.6 ± 0.1	3.8	3.8	2
	Kimberley (N-S margins)	39 ± 1	4	4.6	3.7 ± 0.1	3.9	4.0	6
ZC	**Western part of the Tokwe terrain**	36 ± 1	3	4.5	3.7 ± 0.0	3.9	3.9	4
	Eastern part of the Tokwe terrain	41 ± 3	4	4.5	3.8 ± 0.0	4.0	4.0	15
BC		42 ± 5	13	4.6	3.7 ± 0.1	4.0	4.1	15
NNB		45 ± 4	8	4.7	3.9 ± 0.1	4.2	4.3	22
LB	**SMZ**	40 ± 0	1	4.5	3.7 ± 0.0	4.0	4.0	17
	CZ	47 ± 5	10	4.6	3.8 ± 0.0	4.0	4.1	21
	NMZ	38± 0	1	4.6	3.7 ± 0.0	4.1	4.1	23
KP		39 ± 3	6	4.5	3.8 ± 0.1	4.0	4.2	15
Okwa terrain		43± 0	2	4.5	3.7 ± 0.0	3.9	4.0	11
CFB		26 ± 2	1	4.7	3.8 ± 0.1	4.2	4.4	19

N.B. *KC – Kaapvaal Craton; ZC – Zimbabwe Craton; BC – Bushveld Complex; NNB – Namaqua-Natal Belt; LB – Limpopo Belt; KP – Kheis Province; CFB – Cape Fold Belt; Sn – shear wave refracted by the uppermost mantle layer.*

The velocity profiles for 10 stations (SA10, SA22, SA43, SA44, SA66, SA73, SA169, GRM, MOPA, POGA) show two depths where there is an increase in shear wave velocity above 4.3 km/s with a region of velocity less than 4.3 km/s in between. This high-low-high velocity structure is indicated in Figure 2.4 for these 10 stations by showing the first increase in velocity above 4.3 km/s with a dotted line and the second increase with a solid line. These 10 stations have been excluded from further interpretation of Moho.

There is a 1-to-1 correlation within the reported uncertainties between Moho estimates obtained in this study and estimates by Nguuri et al. (2001), Nguuri (2004) and Nair et al. (2006), except for a handful of stations, shown in Figure 2.5 (Figure 9 in the attached paper) with solid symbols. Moho estimates for five stations (SA05, SA09, SA49, SA81, SUR) lie more than 5 km above the 1-to-1 correlation line (Figure 2.5), and are less than those reported by Nguuri et al. (2001), Nguuri (2004), and Nair et al. (2006).

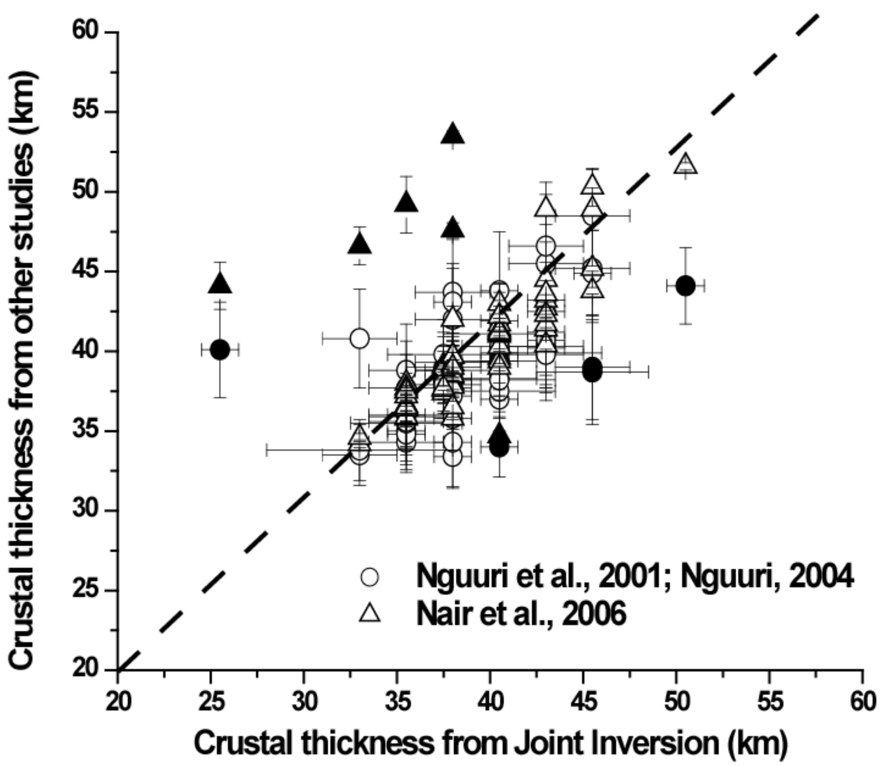

Figure 2.5 Comparison of crustal thickness estimates from this study with crustal thickness estimates from previous studies. The dashed line shows the 1-to-1 correlation, and the solid symbols show stations that do not fall close (≥ 5 km) to the 1-to-1 line.

Moho estimates for four stations (SA16, SA47, SA48, SA70) lie more than 5 km below the 1-to-1 correlation line, and are greater than those reported by Nguuri et al. (2001), Nguuri (2004) and Nair et al. (2006). The velocity profiles for these stations show a complicated lowermost crustal structure commonly associated with a gradational Moho. These differences in Moho estimates could therefore either be attributed to difficulty in identifying the crust-mantle boundary when the velocity structure across this boundary is gradational or the criterion by which the Moho was identified is different from that adopted by other studies.

A further examination done on the results was to verify if there was any relationship between the average velocities in the lowermost crust (below 30 km depth) and crustal thickness. The outcome of this investigation is shown in Figure 2.6. Figure 2.6 shows two differing linear trends suggesting a high gradient for the thin crust (< 41 km) (presumably related to Archaean crust) and low gradient for the thick crust (≥ 41 km) (presumably related to Proterozoic crust). The two linear trends in Figure 2.6 suggest a bimodal distribution for the Precambrian crust. Figure 2.6 assumes 41 km to be the crustal thickness threshold distinguishing thinner Archaean from thicker Proterozoic (above it) crust. However, Figure 2.4 suggest that there are localities within the Archaean craton that have a thick crust (i.e., ≥ 41 km) e.g. Pietersburg terrain with average Vs of ≥ 4.0 km/s in the lowermost crust. On the other hand, there are localities within Proterozoic terrains (e.g. SA16, SA17, SA23, SA29, and UPI in the KheisProvince, SA77 in the LB) that are < 41 km.

Incorporating these type of localities in the trends shown in Figure 2.6 would mean that there is no clear correlation between crustal thickness and the average Vs in the lowermost crust relating to both Archaean and Proterozoic crust. Therefore the linear trends illustrated in

Figure 2.6 are apparent and for the relationship between the two parameters to be meaningful, a very lucid explanation as to under what conditions should certain terrains similar to the ones indicated above be included or excluded from such analysis is required.

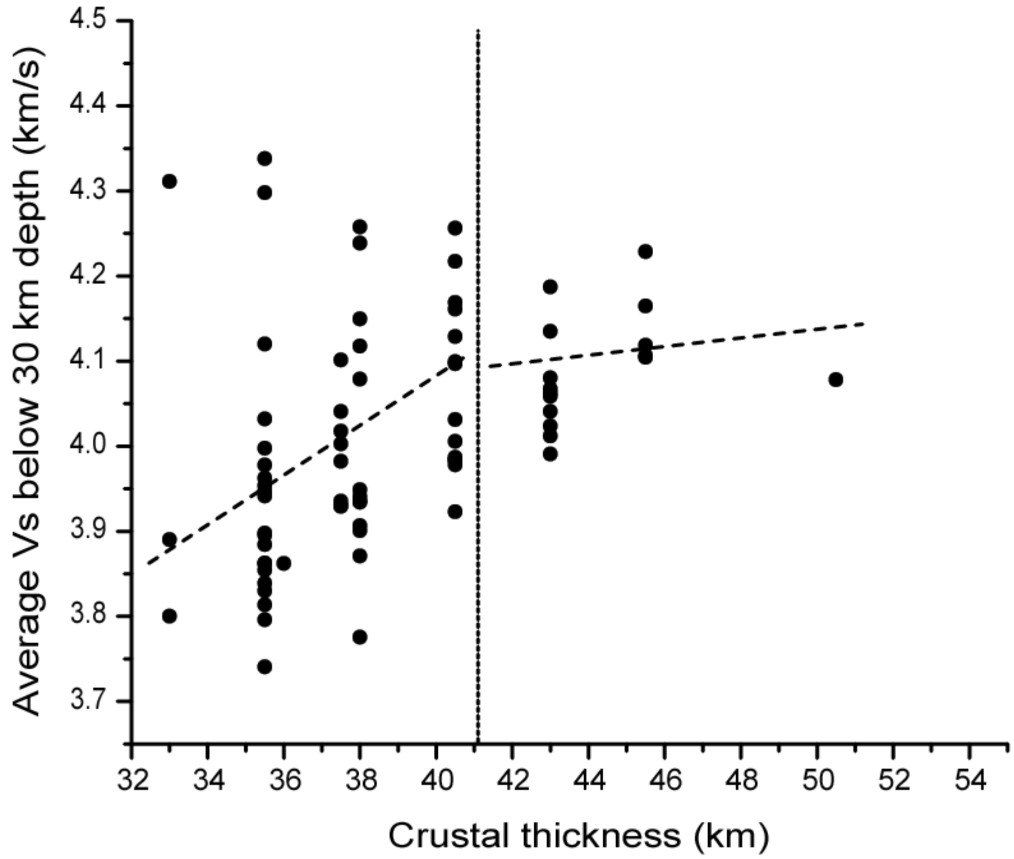

Figure 2.6 Average velocity below 30 km depth as a function of crustal thickness for southern Africa (shown by the solid circles). The dashed lines through the solid circles are the best lines. The relationship between average velocity below 30 km depth and crustal thickness shows two linear trends where the linearity changes around 41 km (marked by the dotted vertical line). See text for further explanation.

The global study by Rudnick and Fountain (1995) suggest a crustal thickness threshold of 43 km distinguishing Archaean crust below it and Proterozoic crust above it. Assuming that the 41 km threshold can statistically be shown to have a standard deviation of ±2 km, therefore at most the 41 km threshold could be increased to 43 km. A 43 km threshold is compatible with crustal thicknesses for localities within the Archaean craton e.g. SA63 in the Pietersburg terrain (see Figure 2.4). However, this threshold is also incompatible with localities within Proterozoic terrains which have crustal thicknesses below 43 km. Therefore, the linear trends in Figure 2.6 require further research investigations and do not yet yield publishable results in this regard.

2.5.1 Lower crustal structure

Table 2.1 clearly shows that most terrains have shear wave velocities of 4.0 km/s or higher over a significant part of the lower crust. However, for the Kimberley terrain and the western part of the Tokwe terrain, average velocities of ≤ 3.9 km/s occur in the lower part of the crust (see Table 2.1). These terrains also have, on average, less than 5 km of high velocity (Vs ≥ 4.0 km/s) rock within the lower part of the crust. Figures 2.7a and b (see Figures 10 and 11 in the attached paper) illustrate the spatial variability of the mean shear wave velocity below 30 km depth in the lower crustal structure for 1 x 1 degree blocks across southern Africa. Superimposed on Figure 2.7a are boxes with different shades illustrating the variability of the average thickness of lower crustal layers with Vs ≥ 4.0 km/s. It can be seen from both Figures 2.4 and 2.7a that the base of the crust in the Kimberley terrain lacks a high velocity rock and the crust is typically that of an evolved Archaean crust and deviates from an original or normal Archaean setting. This anomalous pattern seen in the Kimberley terrain extends into the western part of the Witwatersrand terrain and the eastern part of the KP. It can also be seen in the western part of the Tokwe terrain in the ZC.

2.5.2 Upper crustal structure

A number of stations in the Okwa and NNB terrains show high Vs zones in the upper 15 km of the crust (see Figure 2.4c). However the poor resolution of the revised Pasyanos and Nyblade (2007) group velocity model could mean that these isolated features are not well imaged in the Okwa terrain since they are only shown by station SA61. In contrast, these features are seen over a wide area in the NNB (see Figure 2.4c) and most probably the size of the area can be resolved by the revised Pasyanos and Nyblade (2007) model. Shear wave velocities within these zones vary between 3.7 and 4.0 km/s and tend to decrease to 3.5–3.7 km/s below these zones, implying the presence of a low velocity layer in the midcrust. However, the focus is primarily on the upper crustal velocities (see Chapter 4) since they imply an anomalous upper crustal structure.

2.5.3 Mantle structure

Most terrains within both the cratonic areas and mobile belts show an average Vs from the Moho to depths of ~60 km that varies between 4.5 and 4.7 km/s (i.e., uppermost mantle; Table 2.1). Even though some terrains show an average Sn velocity slightly higher than 4.6 km/s, Table 2.1 shows that there is little evidence for systematic differences in the uppermost mantle (i.e., the top 10–20 km of the mantle) velocities across southern Africa. These results are in agreement with the findings from recent studies of the mantle (e.g. Li and Burke, 2006; Adam and Nyblade, 2011) which indicate that there are no significant differences in the uppermost mantle structure between the cratonic and the adjacent Proterozoic regions. Mantle structure below 60 km might be inadequately resolved since the group velocity dispersions were extended to periods > 90 s using the global Harvard model.

2.6 Discussion

The Karoo flood magmatism (ca. 183 Ma) was the last major tectonothermal event to have affected the lithospheric structure of southern Africa and therefore it could be assumed that the lithosphere has stabilized since then and the variability reflected in Figure 2.7 could be attributed to compositional differences rather than thermal ones.

Many laboratory studies have established that mafic lithologies commonly found in the lower continental crust, such as amphibolite, garnet-bearing and garnet-free mafic granulite, and mafic gneiss, have higher shear wave velocities (> 3.9 km/s), while intermediate-to-felsic lithologies have lower shear wave velocities (< 3.9 km/s) (e.g. Holbrook et al., 1992; Christensen and Mooney, 1995; Rudnick and Fountain, 1995; Christensen and Stanley, 2003; Rudnick and Gao, 2003). The average shear wave velocities (i.e., 4.5–4.7 km/s) in the uppermost mantle region (Moho–60 km depth) indicate only slight differences across southern Africa and therefore suggest the presence of ultramafic rocks of which the common occurrence (e.g. peridotite) is either in varying co-existences with other ultramafic rock types throughout southern Africa, or it has a bulk composition that is the same but perhaps with varying proportions of secondary mineral compositions across southern Africa. Most probably the Archaean cratons would have garnet lherzolite in their uppermost mantle regions given the relatively stable thermal and pressure conditions within the subcratonic mantle roots.

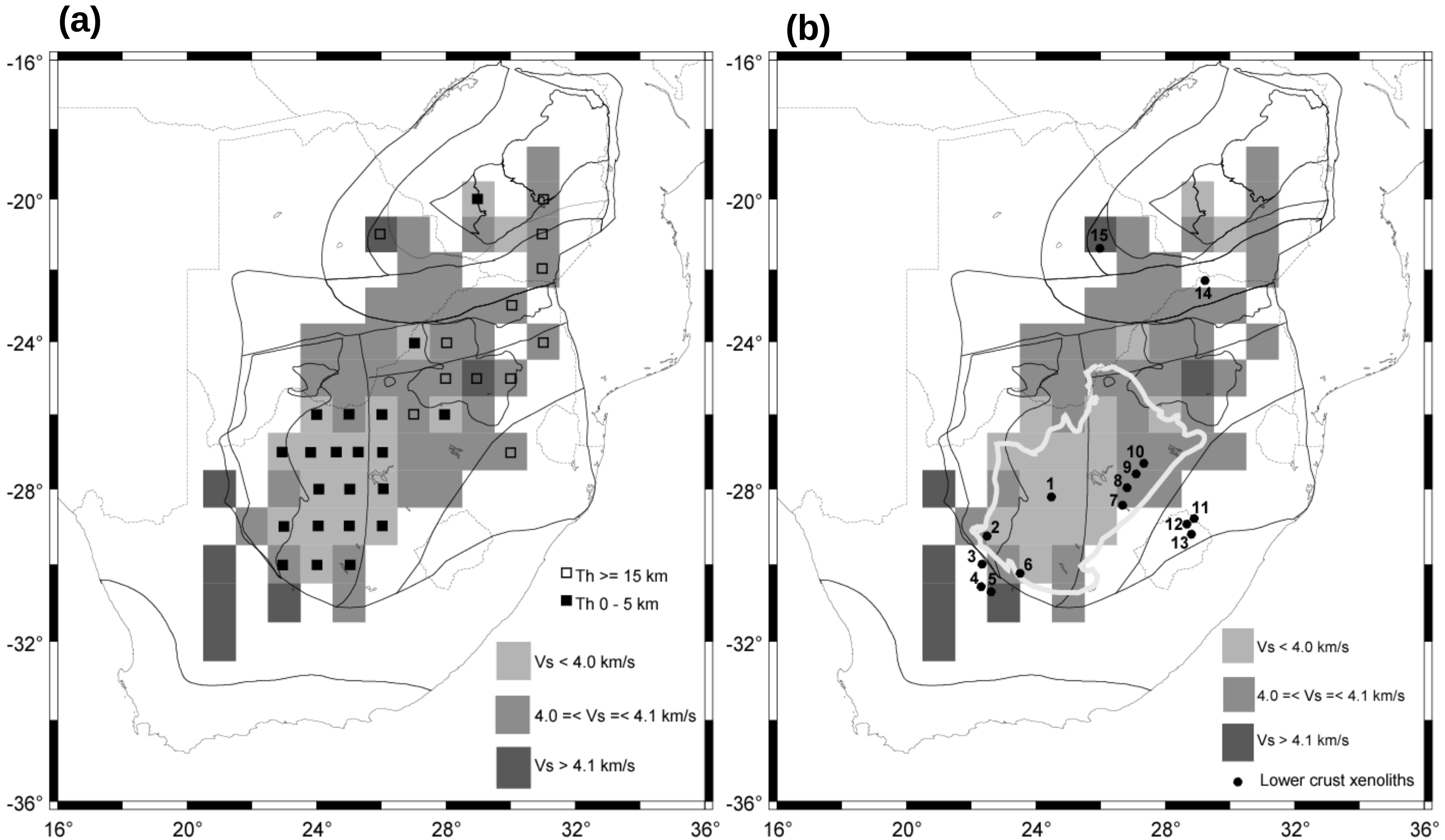

Figure 2.7 (**a).** Map showing the average Vs below 30 km (gray shading) and the average total layer thickness with Vs ≥ 4.0 km/s (shown as open and solid squares and denoted as ''Th'') for 1 x 1 degree blocks. The blocks without symbols are areas where the average total layer thickness with Vs ≥ 4.0 km/s is between 5 and 15 km. (**b).** Map showing the average Vs below 30 km (gray shading), with distribution of the Ventersdorp Supergroup (white line) taken from van der Westhuizen et al. (2006) and the location of lower crust xenoliths obtained from Pretorius and Barton (2003) and Schmitz and Bowring (2003a). The number labels 1–15 represent the names of the kimberlites: 1, Newlands; 2, Markt; 3, Uintjiesberg; 4, Klipfontein-08; 5, Beyersfontein; 6, Lovedale; 7, Star Mine; 8, Kaalvallei; 9, Lace; 10, Voorspoed; 11, Mothae; 12, Letseng-la-Terae; 13, Matsoku; 14, Venetia Mine; and 15, Jwaneng. The solid and dashed lines in both (a) and (b) mark the tectonic and political boundaries, respectively.

2.6.1 Interpretation of higher shear wave velocities in the lower crust

The crustal layers in the velocity models with shear wave velocities of 4.0 km/s or higher imply the presence of mafic lithologies. The lower crust in many Precambrian tectonic settings is characterized by mafic lithologies typically with Vp ~7.0 km/s and Vs ~ 4.0 km/s (e.g. Rudnick and Fountain, 1995; Rudnick and Gao, 2003). Therefore, the suggestion in this study that most terrains within southern Africa have a mafic lower crust is not unusual. Several possibilities have been suggested by Rudnick and Gao (2003) for the genesis of a mafic lower crust in Precambrian tectonic settings: (a) basaltic underplating, (b) magmatic intrusion (basaltic type of magma), and (c) tectonomagmatic processes responsible for the formation of Archaean crust. Given these possibilities, the mafic layer in the lower crust of the BC is likely caused by a combination of magmatic intrusion and underplating.

It has been estimated that the total magma volume that has been added to the Bushveld crust is around 0.6×10^6 km^3 (Von Gruenewaldt et al., 1985), thickening the crust by ~5–10 km. The large (>10 km) thickness of mafic rock in the lower parts of the crust in the NNB, the CZ of the LB, parts of the KP and the CFB can be attributed to suture processes during the formation of these terrains.

In Precambrian terrains elsewhere, suture regions typically with ~5–10 km of crustal thickening are distinguishable [e.g. the Superior Province (Gibb et al., 1983), the Tanzania Craton (Nyblade and Pollack, 1992), the Yilgarn Craton (Mathur, 1974; Wellmann, 1978), the Indian shield (Subrahmanyam, 1978), and the Mann shield (Blot et al., 1962; Louis, 1978; Black et al., 1979)]. The crustal thickening in this type of settings is usually associated with the presence of mafic units in a crust that is commonly affected by granulite-facies metamorphism and extraction of a felsic partial melt component. Both the thicker crust and the large thickness of lower crust with high shear wave velocities found in the NNB, CZ, and KP is consistent with typical ‘‘suture’’ thickened crust found in other Precambrian terrains, and need not be viewed as anomalous. The mafic lower crust estimated in the BC is consistent with Vp/Vs ratios of >1.76, as described by Nguuri (2004) and Nair et al. (2006) (see Table 1 in the attached paper). Similarly, the reported Vp/Vs ratios of 1.78 and 1.84 for the NNB and LB, respectively, are consistent with the findings of this study (Table 2.1).

2.6.2 Interpretation of lower shear wave velocities in the lower crust

Experimental and laboratory studies as indicated above clearly indicate velocity bounds associated with rock type, therefore shear wave velocities below 4.0 km/s (Vs ≤ 3.9 km/s) can be interpreted to be representative of compositions that are primarily intermediate-to-felsic. Figure 2.7a shows several terrains with these velocities and this is more likely to indicate that the lower crust in these terrains is primarily of an intermediate-to-felsic composition. The study by Niu and James (2002) has already noted the lack of mafic material in the lower crust for the Kimberley terrain and moreover, this study has estimated a mean crustal thickness of 37 km for this region. The findings by Niu and James (2002) are consistent with the findings in this study since a larger portion of the Kimberley terrain, as shown in Figure 2.7a, is characterized by a lower crust of an intermediate-to-felsic composition. However, the observation of regions with low shear wave velocities (Vs ≤ 3.9 km/s) in the lower crust extends much further beyond the Kimberley terrain and extends into parts of the adjacent KP and Witwatersrand terrain (Figure 2.7a).

The same trend of low shear wave velocities can be seen in the western part of the Tokwe terrain in the ZC. In explaining the intermediate-to-felsic composition for the lower crust in the Kimberley terrain and the flat topography of the Moho, which are some of the features observed by Niu and James (2002), James et al. (2003) suggested that the crust could have been extensively melted during the Ventersdorp tectonomagmatic event (~2.7 Ga). As a further suggestion to this, I propose that the attenuation of the mafic layer was effected by both melting and crustal thinning associated with the Ventersdorp event. The study by de Wit and Tinker (2004) noted the presence of listric faults in the area overlain by the Ventersdorp Supergroup and proposed that these faults signify thinning of the underlying lower crust.

Figure 2.7b shows the distribution of the Ventersdorp Supergroup superimposed on the shear wave velocity structure of the lower crust. Most of the areas underlain by an intermediate-to-felsic lower crust in South Africa coincide with the region where Ventersdorp rocks have been preserved. The distribution of the Ventersdorp as shown in Figure 2.7b means a substantial portion of the Kimberley terrain underlain by an intermediate-to-felsic lower crust may reflect areas where the mafic lower crust was either thinned or removed during the regional crustal thinning associated with the Ventersdorp event. A similar explanation could be invoked for the low shear wave velocities observed in the lower crust in the western part of the Tokwe terrain, which is overlain by 3.1–2.95 Ga transgressive passive margin and rift sequences (Jelsma and Dirks, 2002).

2.6.3 Crustal Xenoliths

The study by Rudnick and Gao (2003) pointed out that one of the ways by which the composition of the lower crust can be deciphered is by analyzing xenoliths exposed on the surface or at shallow depths and these exposed xenoliths have been shown in many studies to coincide with the presence of mafic lithologies in the lower crust. Jurassic and Cretaceous lower crustal xenoliths in southern Africa are most commonly found within kimberlite pipes (e.g. Dawson, 1980; Nixon, 1987; Schmitz and Bowring, 2003a) (see Figure 2.7b for locations of xenoliths or Figure 11 in the attached paper). Cratonic lower crustal granulite xenoliths from the Kimberley region (location 1), NNB (locations 2, 3, 4, 5, 6), Free State province (locations 7, 8, 9, 10), and northern Lesotho (locations 11, 12, 13) have been described by Schmitz and Bowring (2003a). Off-craton and craton-margin xenoliths come from the CZ of the LB (location 14) (Pretorius and Barton, 2003) and the unexposed extension of the Magondi Belt in north central Botswana (location 15) (Schmitz and Bowring, 2003a).

Xenoliths from kimberlite pipes (e.g. Dawson, 1980; Nixon, 1987; Schmitz and Bowring, 2003a) can be used as an independent check on the composition of the lithosphere through which the pipe ascended. In this way, suites of lower crustal xenoliths collected from kimberlite pipes in the KC and surrounding mobile belts (Schmitz and Bowring, 2003a; Pretorius and Barton, 2003) (Figure 2.7b) can be used to confirm the presence or absence of mafic rocks in the lower crust. Lower crustal xenoliths from the Kimberley terrain are dominated by felsic rocks such as metapelite, and mafic rocks are absent (Schmitz and Bowring, 2003a). Moreover, Cretaceous and Jurassic xenoliths within the Kimberley terrain are a manifestation of mantle metasomatism by highly alkaline mafic silicate melts (e.g. Grégoire et al., 2003; Kobussen et al., 2008).

While the phlogopite-rich xenoliths were uplifted to the upper crustal parts during kimberlitic eruptions, it is possible that felsic rocks such as pegmatites could have been crystallized from the alkaline melts by metamorphic processes and could therefore be forming layering in the lowermost crust and uppermost mantle regions of the Kimberley terrain. However, these felsic layers from the alkaline melts are probably a sporadic overprinting of the lowermost crust and uppermost mantle regions (i.e., appearing mostly below the kimberlite pipes) of the terrain in an area that was already extensively affected by the Ventersdorp volcanism (see section 2.6.2). In contrast, mafic granulite xenoliths are common at all of the other localities (Dawson and Smith, 1987; Dawson et al., 1997; Schmitz and Bowring, 2003a, 2003b) (Figure 2.7b) and are consistent with the variability in the shear wave velocity structure of the lower crust described in this study.

2.7 Conclusions

The 1-D shear wave velocity models from the joint inversion of P-wave receiver functions and Rayleigh wave group velocities for 89 broadband seismic stations indicate and further suggest the following:

1. There is a 1-to-1 correlation within the reported uncertainties between Moho depth estimates from this study and those from previous studies (e.g. Nguuri et al., 2001; Nguuri, 2004; Nair et al., 2006).

2. There is considerable variability in the lower crust across southern Africa and most terrains have shear wave velocities of 4.0 km/s or higher over a significant part of the lower crust.

3. Much of the Kimberley terrain and a fraction of the adjacent KP and the Witwatersrand terrain, as well as the western part of the Tokwe terrain, are characterized by average shear wave velocities of ≤ 3.9 km/s in the lower part of the

crust. The lower shear velocities in the lower crust of the Kimberley terrain are consistent with results from previous studies (Niu and James, 2002; James et al., 2003).

4. The lower crust across much of the southern African shield in both Archaean and Proterozoic terrains has a predominantly mafic composition (i.e., Vs ≥ 4.0 km/s) and this is in contrast to the southwestern part of the KC and western part of the ZC, where the lower crust is intermediate-to-felsic in composition (i.e., Vs < 4.0 km/s). The mafic layer in the lower crust of the BC is likely caused by a combination of magmatic intrusion and underplating. The thick high velocity rock in the lower crustal parts of the NNB, CZ, and Kheis Province are consistent with typical ‘‘suture’’ thickened crust found in Precambrian tectonic settings globally. Most of the areas in the KC that are underlain by an intermediate-to-felsic lower crust and a shallower Moho coincide with the region where Ventersdorp rocks have been preserved. This correlation supports the suggestion by de Wit and Tinker (2004) of crustal extension taking place along listric fault systems during the Ventersdorp tectonomagmatic event (ca 2.7 Ga). A similar explanation could be invoked for the low shear wave velocities observed in the lower crust in the western part of the Tokwe terrain, which is overlain by 3.1–2.95 Ga transgressive passive margin and rift sequences (Jelsma and Dirks, 2002). Overall, these results are consistent with the Precambrian model by Durrheim and Mooney (1994), which suggest that areas of the Archaean crust with a low-velocity base have gone through repeated melting and the crust was further differentiated through recycling processes and therefore this resulted in ultramafic cumulates being part of the mantle. In contrast, the Proterozoic crust has thickened and had undergone underplating which imparted a high-velocity basal layer.

5. The lack of mafic xenoliths in the Kimberley terrain and the presence of mafic xenoliths in the other terrains is consistent with the variability in the shear wave velocity structure of the lower crust found in this study.

6. The shear wave velocity results of the uppermost mantle region (i.e., in the 10–20 km depth below the Moho) indicate average Sn velocities of 4.5–4.7 km/s which do not suggest systematic differences between the different terrains across southern Africa.

References

Ammon, C. J., Randall, G. E., and Zandt, G., 1990. On the nonuniqueness of receiver function inversions. *Journal of Geophysical Research*, 95, 15303–15318, doi:10.1029/JB095iB10p15303.

Ammon, C.J., 1997. Receiver function. http://eqseis.geosc.psu.edu/~cammon/HTML/RftnDocs.

Baier, B., Berckhemer, H., Gajewski, D., Green, R.W., Grimsel, Ch., Prodehl, C., and Vees, R., 1983. Deep seismic sounding in the area of the Damara Orogen, Namibia, In: *Intracontinental Fold Belts*, 887 – 900, eds Martin, H. and Eder, F.W., Springer-Verlag, Berlin.

Berteussen, K. A., 1977. Moho depth determinations based on spectral ratio analysis. *Physics of the Earth and Planetary Interiors*, 31, 313 – 326.

Black, R., Caby, R., Moussine-Pouchkine, A., Bertad, J. M., Boullier, A. M. Fabre, J., and Lesquer, A., 1979. Evidence for late Precambrian plate tectonics in West Africa. *Nature*, 278, 223–227, doi:10.1038/278223a0.

Bloch, S., Hales, A.L. and Landisman, M., 1969. Velocities in the crust and upper mantle of southern Africa from multi-mode surface wave dispersion. *Bulletin of the Seismological*

Society of America, 59, 1599 – 1629.

Blot, C., Crenn,Y. and Rechenmann, R., 1962. Elements apportes par la gravimetrie a la connaissance de la tectonique profonde du Senegal. *C.R. Acad. Sci. Paris*, 254, 1131 – 1133.

Carlson, R.W., Grove, T.L., de Wit, M.J., and Gurney, J.J., 1996. Program to study the crust and mantle of the Archean Craton in southern Africa. *EOS Transactions, American Geophysical Union*, 77, 273 – 277.

Cassidy, J.F., 1992. Numerical experiments in broad-band receiver function analysis. *Bulletin of Seismological Society of America*, 82, 1453 – 1474.

Cawthorn, R.G., Eales, H.V., Walraven, F., Uken, R., and Watkeys, M.K., 2006. The Bushveld Complex, *In*: M. R. Johnson, C. R. Anhaeusser, R. J. Thomas (Editors) *TheGeology of South Africa*, Geological Society of South Africa, Johannesburg/ Council for Geoscience, Pretoria, 261 – 281.

Christensen, N. I., and Mooney, W. D., 1995. Seismic velocity structure and composition of the continental crust: A global view. *Journal of Geophysical Research*, 100, 9761 – 9788.

Christensen, N.I., 1996. Poisson's ratio and crustal seismology. *Journal of Geophysical Research*, 101, 3139 – 3156.

Christensen, N.I., Stanley, D., 2003. Seismic velocities and densities. In: Lee, W.H.K., Kanamori, H., Jennings, P.C., Kisslinger, C., (Eds.) *International Handbook of Earthquake and Engineering*, 81B, 1587 – 1594.

Cornell, D.H., Thomas, R.J., Moen, H.F.G., Reid, D.L., Moore, J.M., and Gibson, R.L., 2006. The Namaqua-Natal Province, *In*: M. R. Johnson, C. R. Anhaeusser, R. J. Thomas (Editors) *The Geology of South Africa*, Geological Society of South Africa, Johannesburg/ Council for Geoscience, Pretoria, 325 – 379.

Dawson, J.B., 1980. *Kimberlites and their Xenoliths*, Springer-Verlag, Berlin.

Dawson, J.B., and Smith, J.V., 1987. Reduced sapphirine granulite xenoliths from the Lace Kimberlite, South Africa: implications for the deep structure of the Kaapvaal Craton.*Contributions to Mineralogy and Petrology*, 95, 376 – 383.

Dawson, J.B., Harley, S.L., Rudnick, R.L., and Ireland, T.R., 1997. Equilibration and reaction in Archaean quartz-sapphirine granulite xenoliths from the Lace kimberlite pipe, South Africa. *Journal of Metamorphic Geology*, 15, 253 – 266.

De Wit, M.J., Roering, C., Hart, R.J., Armstrong, R.A., Ronde, C.E.J., Green, R.W.E., Tredoux, M., Peberdy, E., and Hart, R.A., 1992. Formation of an Archaean continent. *Nature*, 357, 553 – 562.

De Wit, M.J., and Tinker, J. 2004. Crustal structures across the central Kaapvaal Craton from deep-seismic reflection data. *South African Journal of Geology*, 107, 185 – 206.

Dirks, P.H.G.M. and Jelsma, H.A., 2002.Crust-mantle decoupling and the growth of the Archaean Zimbabwe Craton. *Journal of African Earth Sciences*, 34, 157 – 166.

Dugda, M.T., Nyblade, A.A., and Julià, J., 2007. Thin lithosphere beneath the Ethiopian Plateau revealed by a joint inversion of Rayleigh wave group velocities and receiver functions. *Journal of Geophysical Research*, 112, B08305, doi: 10.1029/2006JB004918.

Durrheim, R.J., and Green, R.W.E., 1992. A seismic refraction investigation of the Archaean Kaapvaal Craton, South Africa, using the mine tremors as the energy source. *Geophysical Journal International*, 108, 812 – 832.

Durrheim, R.J., and Mooney, W.D., 1994. Evolution of the Precambrian lithosphere: constraints from seismological and petrochemical constraints. *Journal of Geophysical Research*, 99, B8, 15359 – 15374.

Dziewonski, A.M., and Anderson, D.L., 1981. Preliminary reference Earth model.*Physics of the Earth Planetary Interiors*, 25, S.297 – 356.

Eglington, B.M., and Armstrong, R.A., 2004. The Kaapvaal Craton and adjacent orogens, southern Africa: a geochronological database and overview of the geological development of the Craton. *South African Journal of Geology*, 107, 13 – 32.

Gane, P.G., Logie, H.J., and Stephen, J.H., 1949. Triggered telerecording seismic equipment.*Bulletin of Seismological Society of America*, 39, 117 – 143.

Gane, P.G., Atkins, A.R., Sellschop, J.P.F., and Seligman, P., 1956. Crustal structure in the Transvaal. *Bulletin of Seismological Society of America*, 46, 293 – 316.

Gibb, R. A., Thomas, M.D., Lapointe, P., and Mukhopadhay, M., 1983.Geophysics of proposed Proterozoic sutures in Canada.*Precambrian Research*, 19, 349 – 384.

Gore, J., James, D.E., Zengeni, T.G., and Gwavava, O., 2009. Crustal structure of the Zimbabwe Craton and the Limpopo Belt of southern Africa: new constraints from seismic data and implication for its evolution. *South African Journal of Geology*, 112, 213 – 228. doi:10.2113/gssajg.112.3-4.213.

Green, R.W.E., and Durrheim, R.J., 1990. A seismic refraction investigation of the Namaqualand Metamorphic Complex, South Africa. *Journal of Geophysical Research*, 95, No.B12, 19927– 19932.

Grégoire, M., Bell, D.R., and Le Roex, A.P., 2003. Garnet lherzolites from the Kaapvaal Craton (South Africa): Trace element evidence for a metasomatic history. *Journal of Petrology*, 44, 4, 629 – 657.

Gurrola, H., and Minster, J.B., 1998. Thickness estimates of the upper-mantle transition zone from bootstrapped velocity spectrum stacks of receiver functions. *Geophysical Journal International*, 133, 31 – 43.

Hales, A.L., and Sacks, I.S., 1959. Evidence for an intermediate layer from crustal structure studies in the eastern Transvaal.*Geophysical Journal of the Royal Astronomical Society*, 2, 15–33.

Harvey, J.D., de Wit, M.J., Stankiewicz, J., and Doucouré, C.M., 2001. Structural variations of the crust in the SouthwesternCape, deduced from seismic receiver functions. *South African Journal of Geology*, 104, 231 – 242.

Hatton, C.J. and Schweitzer, J.K., 1995. Evidence for synchronous extrusive and intrusive Bushveld magmatism. *Journal of African Earth Sciences*, 21, 579 – 594.

Holbrook, W.S., Mooney, W.D., and Christensen, N.I., 1992. The seismic velocity structure of the deep continental crust, Chapter 1, *In*: D. M. Fountain, R. Arculus and R. W. Kay (Editors), *Continental Lower Crust*, 1 – 43.

James, D.E., F. Niu, and Rokosky, J., 2003. Crustal structure of the Kaapvaal Craton and its significance for early crustal evolution. *Lithos*, 71, 413 – 429.

Jelsma, H. A. and Dirks, P.H.G.M., 2002.Neoarchaean tectonic evolution of the Zimbabwe Craton. In C.M.R. Fowler, C.J. Ebinger and C.J. Hawkesworth (Editors), *The Early Earth: Physical, Chemical and Biological Development. Geological Society of London, Special Publications*, 199, 183 – 211.

Johnson, M.R., Anhaeusser, C.R., and Thomas, R.J., (Editors), 2006. *The Geology of South Africa*.Geological Society of South Africa, Johannesburg/ Council for Geoscience, Pretoria, 691 pp.

Julià, J., Ammon, C.J., Hermann, R.B., and Correig, A.M., 2000. Joint inversion of receiver functions and surface-wave dispersion observations. *Geophysical Journal International*, 143, 99 – 112.

Julià, J., C.J. Ammon, and Hermann, R.B., 2003. Lithospheric structure of the Arabian Shield from the joint inversion of receiver functions and surface-wave group velocities. *Tectonophysics*, 371, 1 – 21.

Julià, J., Ammon,C.J., and Nyblade, A.A., 2005. Evidence for mafic lower crust in Tanzania, East Africa from joint inversion of receiver functions and Rayleigh wave dispersion velocities. *Geophysical Journal International*, 162, 555 – 569.

Julià, J., 2007. Constraining velocity and density contrasts across the crust-mantle boundary with receiver function amplitudes. *Geophysical Journal International*, 171, 286 – 301.

Kramers, J.D., McCourt, S., and Van Reenen, D.D., 2006. The Limpopo Belt, *In*: M. R. Johnson, C. R. Anhaeusser, R. J. Thomas (Editors) *The Geology of South Africa*, Geological Society of South Africa, Johannesburg/ Council for Geoscience, Pretoria, 209 – 236.

Kobussen, A.F., Griffin, W.L., and O'Reilly, S.Y., 2008. The scale and scope of Cretaceous refertilization of the Kaapvaal lithospheric mantle, Kaapvaal Craton, South Africa. *9th International Kimberlite Conference Extended Abstract*, No. 9IKC-A-00038.

Kreissig, K., Nägler, Th. F., Kramers, J.D., Van Reenen, D.D., and Smit, C.A., 2000. An isotopic and geochemical study of the northern Kaapvaal Craton and the Southern Marginal Zone of the Limpopo Belt: are they juxtaposed terrains? *Lithos*, 50, 1 – 25.

Kwadiba, M.T.O.G., Wright, C., Kgaswane, E.M., Simon, R.E., and Nguuri, T.K., 2003. Pn arrivals and lateral variations of Moho geometry beneath the Kaapvaal Craton. *Lithos*, 71, 393–411.

Langston, C.A., 1979. Structure under Mount Rainier, Washington, inferred from teleseismic body waves. *Journal of Geophysical Research*, 84, 4749 – 4762.

Larson, E.W.F. and Ekström, G., 2001. Global models of surface wave group velocity. *Pure and Applied Geophysics*, 158, no. 8, 1377 – 1400.

Li, A., and Burke, K., 2006. Upper mantle structure of southern Africa from Rayleigh wave tomography.*Journal of Geophysical Research*, 111, B10303, doi:10.1029/2006JB004321.

Ligorría, J.P., and Ammon, C. J., 1999. Iterative deconvolution and receiver function estimation. *Bulletin of Seismological Society of America*, 89, 1359 – 1400.

Louis, P., 1978. Gravimetrie et geologie en Afrique occidentale et centrale. *Mem. Bur. Rech. Geol. Min*., 91, 53 – 61.

Mathur, S.P., 1974. Crustal structure in southwestern Australia from seismic and gravity data. *Tectonophysics*, 24, 151 – 182.

McCourt, S. and Armstrong, R.A., 1998. SIMS U-Pb zircon geochronology of granites from the Central Zone, Limpopo Belt, southern Africa: implications for the age of the Limpopo Orogeny. *South African Journal of Geology*, 101, 329 – 338.

McCourt, S., Hilliard, P., Armstrong, R.A., and Munyanyiwa, H., 2001. Shrimp U-Pb zircon geochronology of the Hurungwe granite northwest Zimbabwe: Age constraints on the timing of the Magondi orogeny and implications for the correlation between the Kheis and Magondi Belts. *South African Journal of Geology*, 104, 39 – 46.

Moen, H.F.G., 1999. The KheisTectonicSubprovince, southern Africa: a lithostratigraphic perspective. *South African Journal of Geology*, 102, 27 – 42.

Nair, S.K., Gao, S.S., Kelly, H.L. and Silver, P.G., 2006. Southern African crustal evolution and composition: Constraints from receiver function studies. *Journal of Geophysical Research*, 111, B02304, doi:10.1029/2005JB003802.

Newton, A.R., Shone, R.W., and Booth, P.W.K., 2006. The Cape Fold Belt, *In*: M. R. Johnson, C. R. Anhaeusser, R. J. Thomas (Editors) *The Geology of South Africa*, Geological Society of South Africa, Johannesburg/ Council for Geoscience, Pretoria, 521 – 530.

Nguuri, T.K., Gore, J., James, D.E., Webb, S. J., Wright, C., Zengeni, T.G., Gwavava, O., Snoke, J.A., and Kaapvaal Seismic Group, 2001. Crustal structure beneath southern Africa and its implications for the formation and evolution of the Kaapvaal and Zimbabwe Cratons. *Geophysical Research Letters, 28*, 13, 2501 – 2504.

Nguuri, T., 2004. Crustal structure of the Kaapvaal Craton and surrounding mobile belts: analysis of teleseismic P waveforms and surface wave inversions, Ph.D. thesis, University of the Witwatersrand (unpublished).

Niu, F., and James, D.E., 2002.Fine structure of the lowermost crust beneath the Kaapvaal Craton and its implications for crustal formation and evolution.*Earth and Planetary Science Letters*, 200, 121 – 130.

Nixon, P. H., 1987. Kimberlitic xenoliths and their cratonic setting, *In*: P. H. Nixon (Editor) *Mantle Xenoliths*, John Wiley and Sons Ltd., 215 – 239.

Nyblade, A.A., and Pollack, H.N., 1992. A gravity model for the lithosphere in western Kenya and northeastern Tanzania. *Tectonophysics*, 212, 257 – 267.

Owens, T.J., and Zandt, G., 1985. The response of the continental crust-mantle boundary observed on broadband teleseismic receiver functions. *Geophysical Research Letters*, 14, 824 – 827.

Pasyanos, M.E., and Nyblade, A.A., 2007. A top to bottom lithospheric study of Africa and Arabia. *Tectonophysics*, 444, no. 1 – 4, 27 – 44.

Pretorius, W., and Barton, J. M. Jr, 2003. Measured and calculated compressional wave velocities of crustal and upper mantle rocks in the Central Zone of the Limpopo Belt, South Africa – implications for lithospheric structure. *South African Journal of Geology*, 106, 205 – 212.

Qiu, X., K. Priestley, and McKenzie, D., 1996. Average lithospheric structure of southern

Africa. *Geophysical Journal International*, 127 (3), 563 – 581.

Ransome, I.G.D. and de Wit, M.J., 1992. Preliminary investigations into a microplate model for the South Western Cape. In: De Wit, M.J. and Ransome, I.G.D. (Eds.), *Inversion Tectonics of the CapeFold Belt, Karoo and CretaceousBasins of Southern Africa*. A.A. Balkema, Rotterdam, 257 – 266.

Rudnick, R.L., and Fountain, D.M., 1995. Nature and composition of the continental crust: a lower crust perspective. *Reviews of Geophysics*, 33 (3), 267 – 309.

Rudnick, R.L., and Gao, S., 2003. Treatise on Geochemistry, vol. 3, 1 – 64.

SACS (South African Committee for Stratigraphy), 1980.Stratigraphy of South Africa.Part 1 (Kent, L.E., Comp.), Lithostratigraphy of the Republic of South Africa, South West Africa/Namibia, and the Republics of Bophuthatswana, Transkei and Venda.*Handbook of Geological Survey of South Africa, 8, 690 pp*.

Schmitz, M.D., and Bowring, S.A., 2003a.Constraints on the thermal evolution of continental lithosphere from U-Pb accessory mineral thermochronometry of lower crustal xenoliths, southern Africa. *Contributions to Mineralogy and Petrology*, 144, 592 – 618.

Schmitz, M.D., and Bowring, S.A., 2003b.Ultrahigh-temperature metamorphism in the lower crust during Neoarchean Ventersdorp rifting and magmatism, Kaapvaal Craton, southern Africa. *Geological Society of America Bulletin*, 115, 533 – 548.

Simon, R.E., Wright, C., Kgaswane, E.M., and Kwadiba, M.T.O., 2002. The P wavespeed structure below and around the Kaapvaal Craton to depths of 800 km, from traveltimes and waveforms of local and regional earthquakes and mining-induced tremors. *Geophysical Journal International*, 151, 132 – 145.

Stankiewicz, J., Chevrot, S., van der Hilst, R.D., and de Wit, M.J., 2002. Crustal thickness, discontinuity depth, and upper mantle structure beneath southern Africa: constraints from body wave conversions. *Physics of the Earth and Planetary Interiors*, 130, 235 – 251.

Stowe, C.W., 1986. Synthesis and interpretation of structures along the north-eastern boundary of the Namaqua Tectonic Province, South Africa.*Transactions of the Geological Society of South Africa*, 89, 185 – 198.

Stowe, C.W., 1989. Discussion on 'The Proterozoic Magondi Belt in Zimbabwe – a review'. *South African Journal of Geology*, 92, 69 – 71.

Subrahmanyam, C., 1978. On the relation of gravity anomalies to geotectonics of the Precambrian terrains of the south Indian shield. *Journal of Geological Society of India*, 19, 251 – 263.

Thamm, A. G., and Johnson, M. R., 2006. The Cape Supergroup, *In*: M. R. Johnson, C. R. Anhaeusser, R. J. Thomas (Editors) *TheGeology of South Africa*, Geological Society of South Africa, Johannesburg/ Council for Geoscience, Pretoria, 443 – 460.

Van der Westhuizen, W.A., de Bruiyn, H., and Meintjes, P.G., 2006. The Ventersdorp Supergroup, *In*: M. R. Johnson, C. R. Anhaeusser, R. J. Thomas (Editors) *TheGeology of South Africa*, Geological Society of South Africa, Johannesburg/ Council for Geoscience, Pretoria, 187 – 208.

Von Gruenewaldt, G., Sharpe, M.R., and Hatton, C.J., 1985. The Bushveld Complex; introduction and review.*Economic Geology*, 80, 803 – 812.

Webb, S.J., Cawthorn, R.G., Nguuri, T.K., and James, D.E., 2004. Gravity modelling of Bushveld Complex connectivity supported by Southern African Seismic Experiment results. *South African Journal of Geology*, 107, 207 – 218.

Wellmann, P., 1978. Gravity evidence for abrupt changes in the mean crustal density at the junction of Australian crustal blocks. *Aust. Bur. Miner. Resour. Geol. Geophys. Bull*., 3, 153–162.

Willmore, P.L., Hales , A.L., and Gane, P.G., 1952. A seismic investigation of crustal structure in the western Transvaal. *Bulletin of Seismological Society of America*, 42, 53 – 80.

Wright, C., Kgaswane, E.M., Kwadiba, M.T.O., Simon, R.E., Nguuri, T.K., and McRae-Samuel, R., 2003.South African seismicity, April 1997 – April 1999, and regional variations in the crust and uppermost mantle of the Kaapvaal Craton. *Lithos*, 71, 369 – 392.

Zhao, M., Langston, C.A., Nyblade, A.A., and Owens, T.J., 1999.Upper mantle velocity structure beneath southern Africa from modelling regional data. *Journal of Geophysical Research*, 104, B3, 4783 – 4794.

Chapter 3

Shear wave velocity structure of the Bushveld Complex, South Africa

Abstract

The crustal structure of the Bushveld Complex is investigated by jointly inverting high-frequency teleseismic receiver functions and 2–90 sec Rayleigh wave group velocities for 16 broadband seismic stations spanning the Bushveld Complex. Group velocities for 2–15 sec periods were obtained from a surface wave tomography using local and regional events, while group velocities for 20–90 sec periods were taken from a published model. The 1-D shear wave velocity models obtained for each station show the presence of a thickened crust in the centre of the Bushveld Complex and that S velocities reach 4.0 km/s or higher over a significant portion of the lower crust (below 30 km depth). The 1-D shear wave velocity models also reveal that the upper crustal structure (above 10 km depth) across the Bushveld Complex is characterized by S velocities as high as ~3.7–3.8 km/s, consistent with the presence of mafic lithologies. These results favour a "continuous-sheet" as opposed to a "dipping-sheet" model for the Bushveld Complex, in which the mafic layers are continuous at depth beneath the centre of the complex. However, detailed modelling of receiver functions at one station within the centre of the complex indicates that the mafic layering maybe locally disrupted by diapirism and metamorphism.

The material in this chapter is fully described in the peer-reviewed paper with the following citation: ***Kgaswane, E.M., Nyblade, A.A., Durrheim, R.J., Julià, J., Dirks, P.H.G.M., and Webb, S.J., 2012. Shear wave velocity structure of the Bushveld Complex, South Africa. Tectonophysics, 554–557, 83–104, doi:10.1016/j.tecto.2012.06.003.***

3.1 Introduction

The Bushveld Complex (BC) (Figure 3.1) was emplaced at ca. 2.06 Ga in the northern part of the Kaapvaal Craton (KC) and is one of the largest mafic layered igneous intrusions in the world. It covers an area of ~ 66 000 km^2 within the northern Kaapvaal Craton, South Africa (e.g. Walraven, 1997; Eglington and Armstrong, 2004; Webb et al., 2004). It has an abundance of platiniferous group metals, as well as large reserves of chromium, titanium, vanadium, nickel, and gold (e.g. Cawthorn et al., 2006). It intruded into the intracratonic sedimentary sequences of the Transvaal Supergroup and is stratigraphically divided into the Rooiberg Group (RG), the Rashoop Granophyre Suite (RGS), the Lebowa Granite Suite (LGS), and the Rustenburg Layered Suite (RLS; e.g. South African Committee for Stratigraphy, 1980; Hatton and Schweitzer, 1995; Cawthorn and Webb, 2001; Cawthorn et al., 2006). Figure 3.1a shows the surface geology of the BC and the different lithologies comprising the entire complex.

The mafic components of the RLS crop out in five geographically distinct areas: the Eastern Limb, the Western Limb, the Far Western Limb, and the two Northern limbs (Figure 3.1; e.g. Webb et al., 2004). A sixth limb, the Southeastern or Bethal Limb (Cawthorn and Webb, 2001), is buried under Karoo sediments. The BC is disrupted in several places by alkaline intrusions (Figure 3.1). Much of the subsurface structure of the BC above 10 km depth is reasonably understood, but the deep structure of the BC and how it was emplaced remains a subject of ongoing research. The BC was originally thought to be a laccolith (Molengraaff, 1901; Jorissen, 1904; Mellor, 1906) or lopolith (e.g. Molengraaff, 1902; Hall, 1932; Du Toit, 1954). However, gravity modelling by Cousins (1959) showed that a Bouguer gravity low associated with the geographic centre of the BC was not consistent with these models.

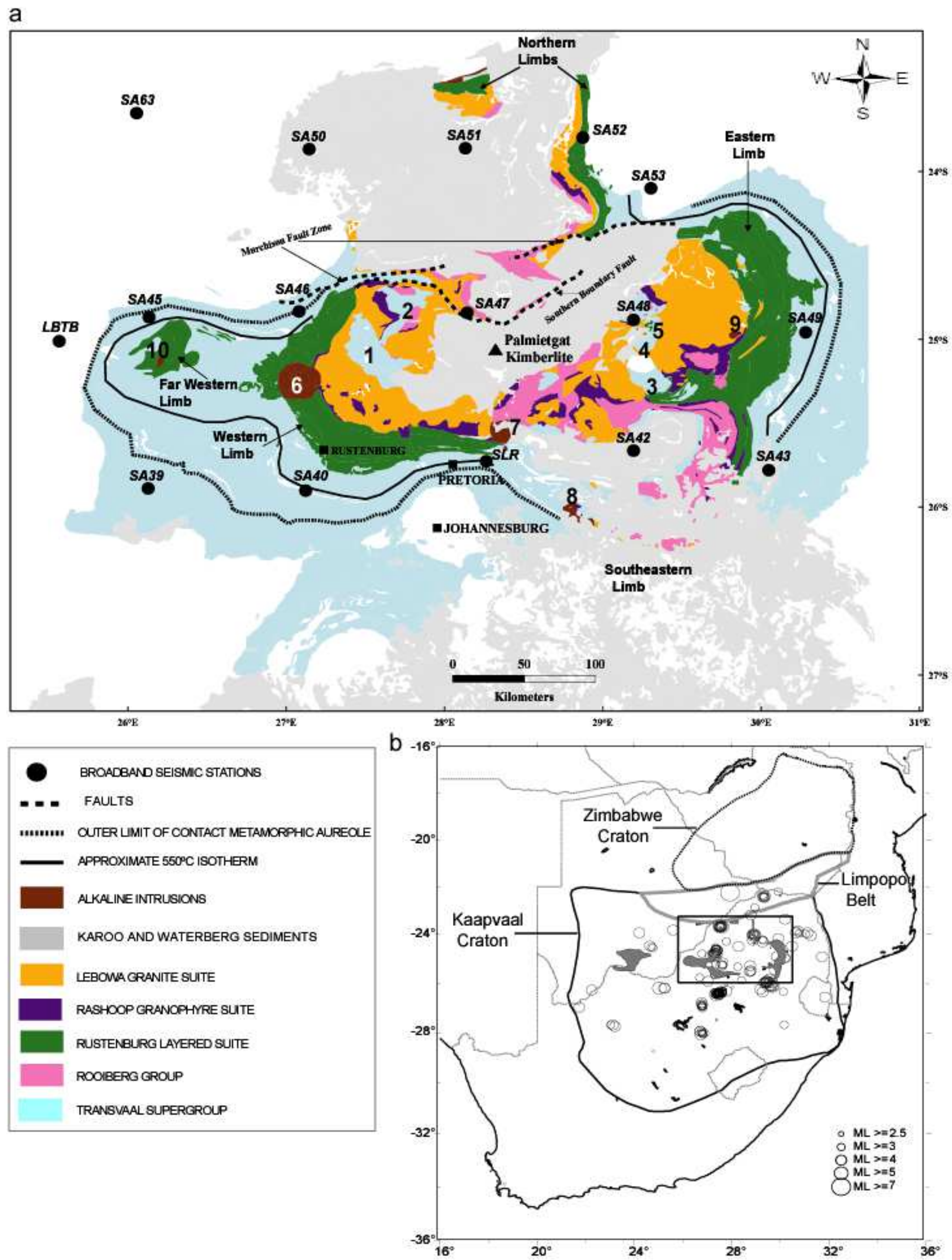

Figure 3.1 (**a**). Map of the Bushveld Complex showing simplified geology and its six limbs – the Eastern, Western, Far Western, Southeastern and the two Northern limbs (map modified from the 1:250,000 geology map of South Africa). The numbers 1, 2, 3, 4 and 5 show the position of some of the domes, and the numbers 6, 7, 8, 9 and 10 show the location of alkaline intrusions. The location of 16 broadband seismic stations for which Vs models are reported are shown. They are the permanent stations, LBTB and SLR and the temporary stations with prefix "SA". **(b).** Map of southern Africa showing the locations of earthquakes (open circles) used in this study. The solid black rectangle encloses the study area. Outcrops of the BC are shown as gray polygons. The outlines of the Kaapvaal Craton, Limpopo Belt and the Zimbabwe Craton are shown in solid black, gray and dotted lines, respectively.

Cousins (1959) suggested that the BC consisted of separate intrusive limbs. This model underwent several refinements, resulting in a model with detached inward dipping bodies (e.g. the "dipping-sheet model"; Biesheuvel, 1970; Van der Merwe, 1976; Walraven and Darracott, 1976; Molyneux and Klinkert, 1978; Du Plessis and Kleywegt, 1987; Meyer and De Beer, 1987). The "dipping-sheet" model was refined by Meyer and De Beer (1987) using gravity modelling and they concluded that the detached limbs extended to depths of 15 km with no compensation at the Moho (Figure 3.2a). Deep electrical soundings and resistivity measurements by Meyer and De Beer (1987), which constrained the gravity modelling, indicated the presence of a conductive layer at depth. Meyer and De Beer (1987) interpreted this conductive layer to be the Silverton shales of the Transvaal Supergroup. However, an alternative interpretation by Webb et al. (2004) suggested that the conductive layer could be the mafic rocks of the RLS following the drilling results by Walraven (1987).

Later geological and geophysical studies (Cawthorn et al., 1998; Cawthorn and Webb, 2001; Webb et al., 2004) have proposed the existence of a continuous mafic layering at depth across the centre of the BC connecting the various limbs (Figure 3.2b). In this model, hereinafter called the "continuous-sheet" model, the continuous mafic layering in the upper crust is isostatically compensated for by a downwarped Moho, consistent with seismic constraints provided by receiver function studies (Nguuri et al., 2001; Nair et al., 2006; Kgaswane et al., 2009). The study by Nguuri et al. (2001) suggests a high shear wave velocity layer ($V_s \sim 4.0$ km/s) within the upper 10 km of the crust for one location near the centre of the BC. More recent findings (see Figure 3.1a; Webb et al., 2010) show the presence of mafic xenoliths in the Palmietgat kimberlite pipe and this further buttressed the hypothesis of a continuous mafic layering in the centre of the BC.

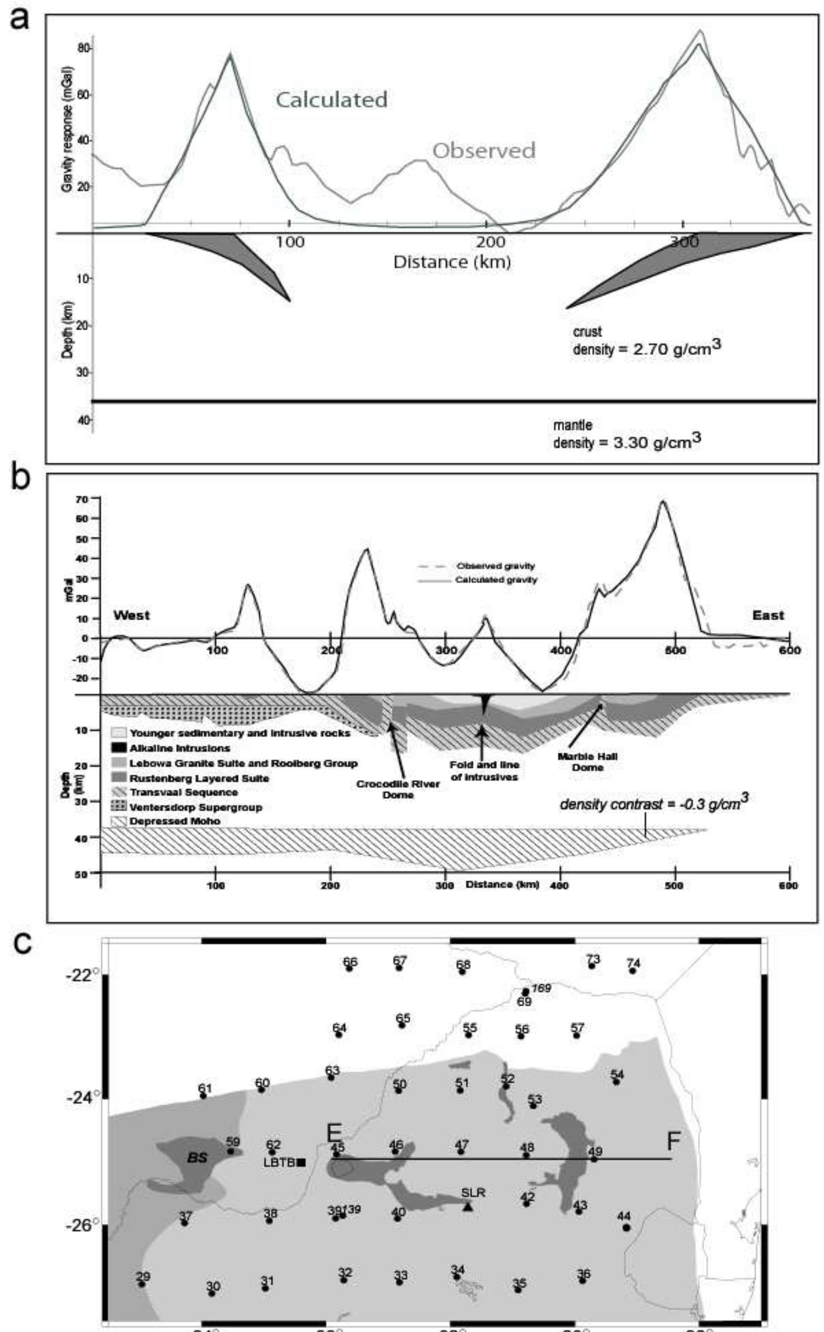

Figure 3.2 (**a).** Meyer and De Beer (1987) gravity model. **(b).** Webb et al. (2004) gravity model. The models in a) and b) have been reproduced from Webb et al. (2004). (**c).** Locations of the SASE (solid circles), GSN (solid square) and SANSN (solid triangle) broadband stations within and surrounding the BC. The profile of the two gravity models is shown by the solid line EF. The area marked BS is the Molopo Farms Complex and represents one of the Bushveld satellites. The background gray-shaded regions show the Kaapvaal Craton. Terrain and political boundaries are shown by dashed black and gray lines, respectively.

The purpose of this study is to use new seismic velocity models of the BC crust to evaluate the "dipping-sheet" and "continuous-sheet" models. The seismic velocity models are obtained by first measuring short-period Rayleigh wave group velocities using locally and regionally recorded seismic events, and then jointly inverting the group velocity measurements with high-frequency receiver functions. The method is similar to Kgaswane et al. (2009), but differs in two ways. Firstly, group velocity maps for short-period Rayleigh waves (2–15 sec) were tomographically developed to improve constraints on the upper crustal velocity structure. Secondly, high-frequency ($f \leq 1.25$ Hz) receiver functions were jointly inverted with Rayleigh wave group velocities to improve resolution of crustal structure. These new constraints provide better resolved shear wave velocity models for locations across the BC and yield new insights into the deep structure of the BC.

3.2 Data sources, data processing and methodology

In this section, the Rayleigh wave tomography method used to obtain group velocity maps for periods between 2 and 15 sec is first described. This is followed by a brief description of the approach adopted to compute receiver functions. Finally an explanation of how the receiver functions and Rayleigh wave group velocity measurements have been jointly inverted.

3.2.1 Group velocity tomography

Rayleigh wave group velocities were measured using 197 mining-related and regional seismic events (see Figure 3.1b) recorded by 45 broadband seismic stations. The seismic events have local magnitudes (ML) greater than 2.5. A detailed event list is shown in Appendix D. The event list is comprised of event catalogues (parameterized in origin time, hypocenters and local magnitudes) compiled from the earthquake bulletins published by the Council for

Geoscience (CGS), by gold mines in the Witwatersrand Basin area, and the Incorporated Research Institutions for Seismology (IRIS). Mining-related earthquakes account for 81% of the total number of earthquakes used for the measurements, the majority of which originated within the gold mining districts of the Witwatersrand Basin. The locations of the 45 broadband seismic stations with respect to the outcrop pattern of the BC are shown in Figure 3.2c. Forty-three of the stations belong to the Southern African Seismic Experiment (SASE) network (Carlson et al., 1996) and two of the stations belong to the Global Seismic Network (GSN) and South African National Seismograph Network (SANSN).

A multiple filter analysis (e.g. Dziewonski et al., 1969; Keilis-Borok, 1989; Claerbout, 1992; Levshin et al., 1992) software developed by Ammon (2001) was used to measure Rayleigh wave group velocities at each period. Figures 3.3 and 3.4 shows the processing of group velocity measurements at station SA31 and the choice of an optimal Gaussian width parameter for the group velocity measurements (using station SA46 as an example), respectively. While all the three Gaussian width parameters tend to show capabilities of optimally constraining group velocity observations, a variable Gaussian width parameter (Figure 3.4b) tends to show a scatter of group velocity measurements that is slightly biased both below and above the theoretical PREM curve. In comparison, the other two parameters (in Figures 3.4a and c) tend to show a scatter that is mostly biased above the theoretical PREM curve.

Figure 3 (in the attached paper) shows the ray coverage (together with the total number of rays) at each period that could be achieved in this study. Ray coverage is greater at shorter periods (2–8 sec) compared to longer periods (10–15 sec).

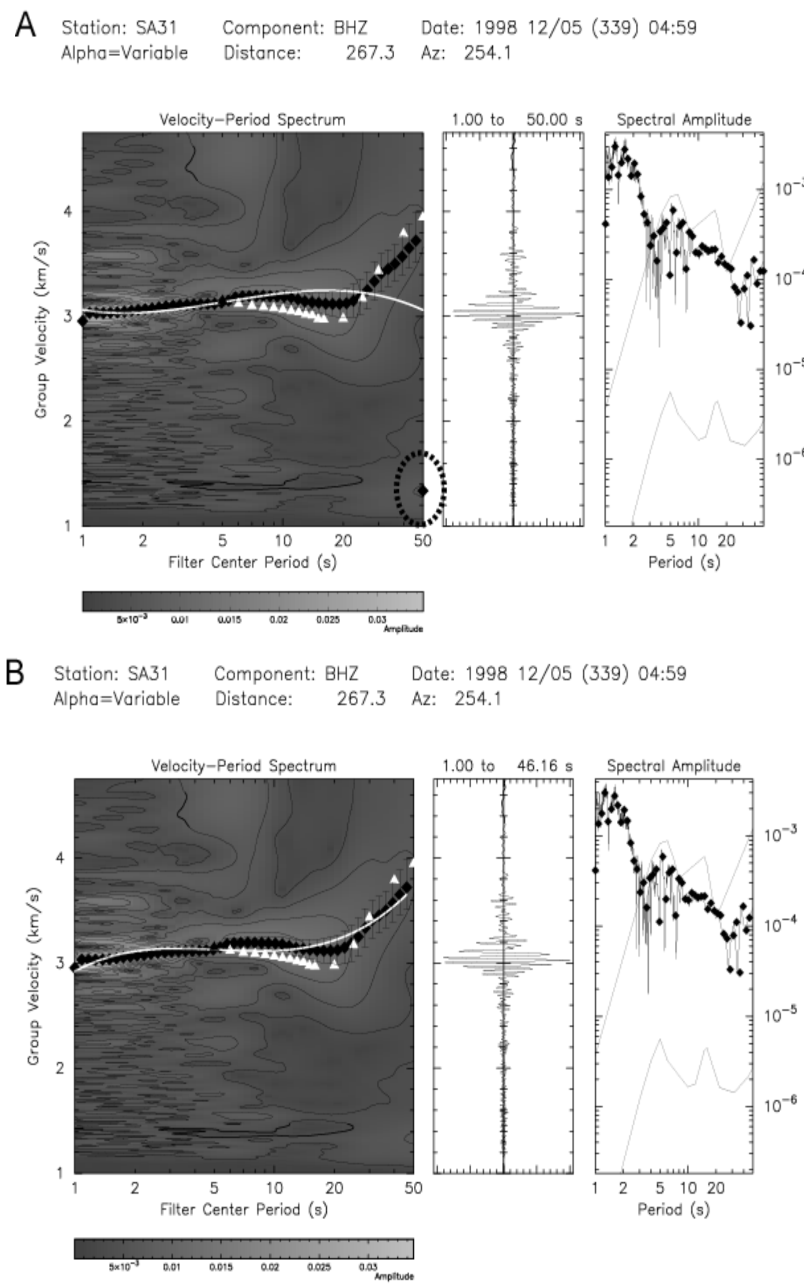

Figure 3.3 Group velocity measurement using station SA31 as an example. **A.** Pre-processing of the Rayleigh wave group velocity curve (black diamonds) and outlying black diamond (enclosed by the dotted ellipse) far below (far left diagram). **B.** Post-processing of the Rayleigh wave group velocity curve showing a group velocity curve fitting a spline curve (white) after a scattered outlying black diamond has been removed (far left diagram). The far left diagram in both A and B is the velocity-period spectrum, the middle diagram is the seismogram along the group velocity axis, and the far right diagram is the amplitude spectrum within the USGS low- and high-noise curves (solid gray lines). The white triangles in the velocity-period spectra represent the theoretical group velocity dispersion from the PREM model.

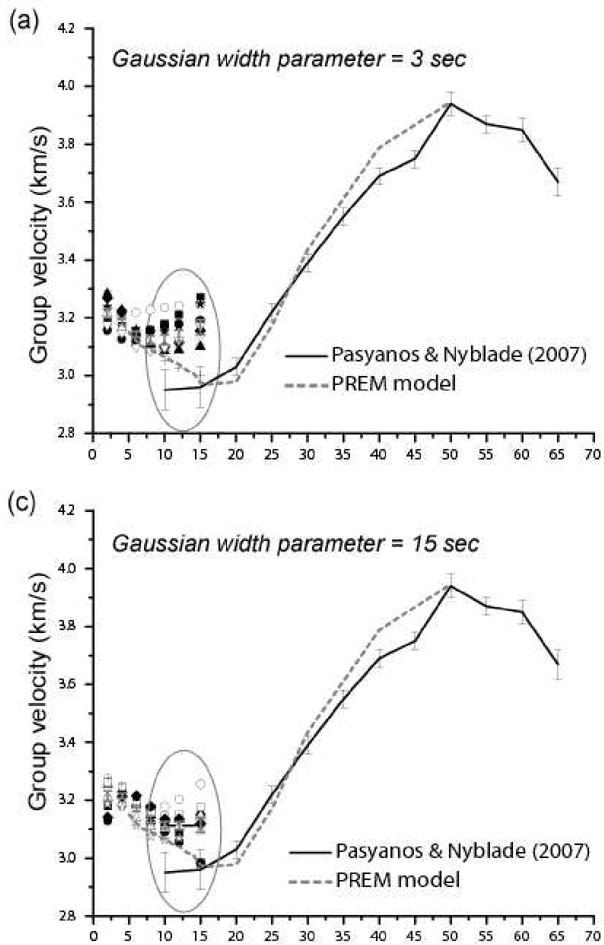

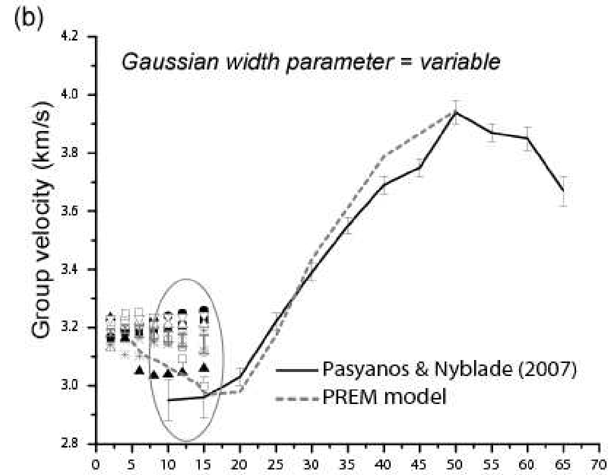

Figure 3.4 Comparison of Gaussian width parameters for station SA46 within the region of 10–15 sec (solid gray ellipse) overlapping measured Rayleigh wave group velocities and those from Pasyanos and Nyblade (2007) model. The measurements between 2–15 sec made from 10 earthquakes originating in the gold mining regions south of the station are shown by the different symbols. (**a).** Gaussian width parameter of 3 sec. (**b).** A variable Gaussian width parameter. (**c).** Gaussian width parameter of 15 sec.

Since the ray paths originate from different source regions, they need to be averaged at each period such that the variability of the measurements in the corresponding averages is assessed and outlying points that could yield spurious features in the resulting inversions are eliminated. Figure 3.5 shows that at each period, the standard deviation of the ensemble of measurements varies by no more than 0.1–0.2 km/s.

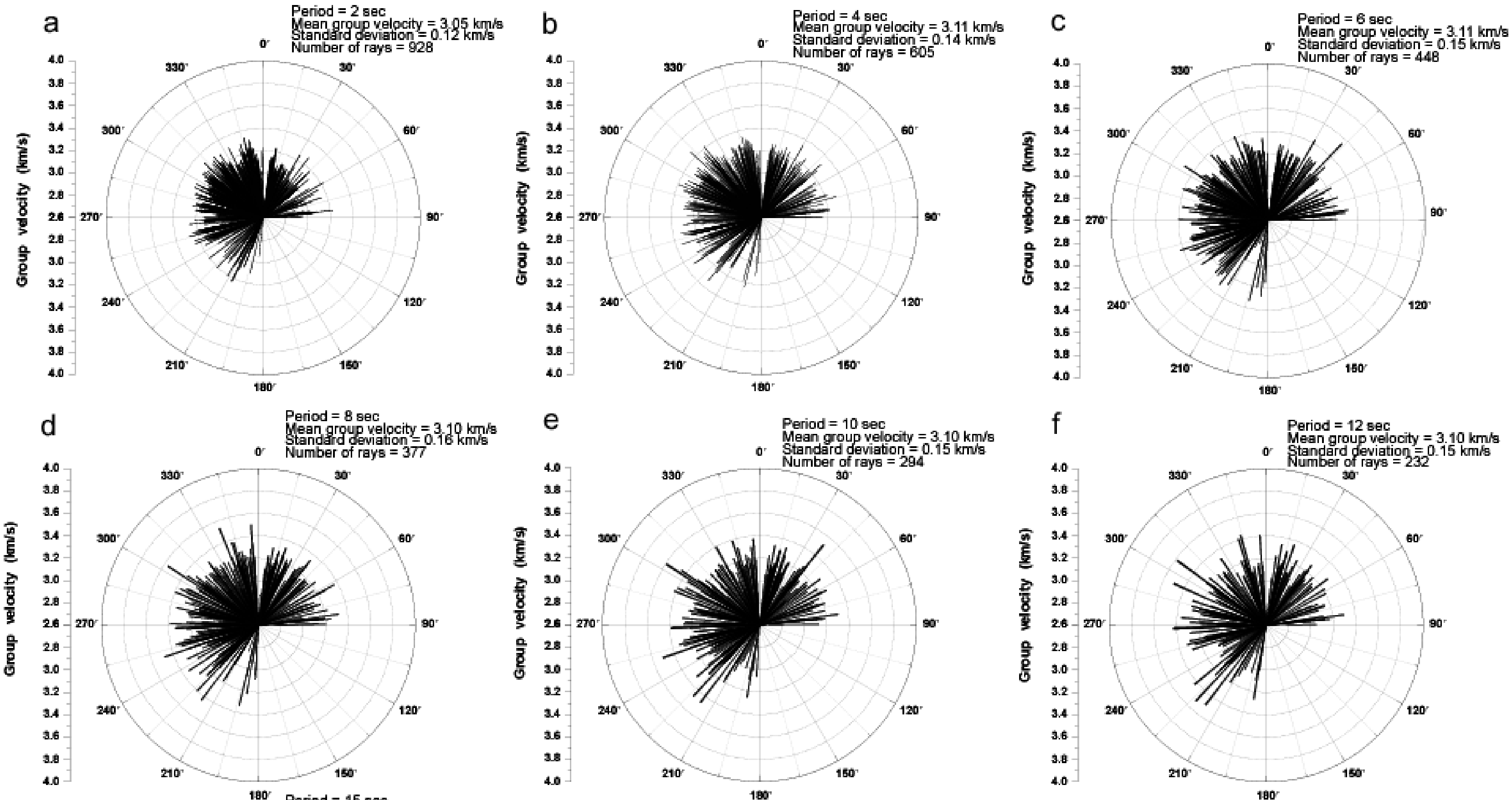

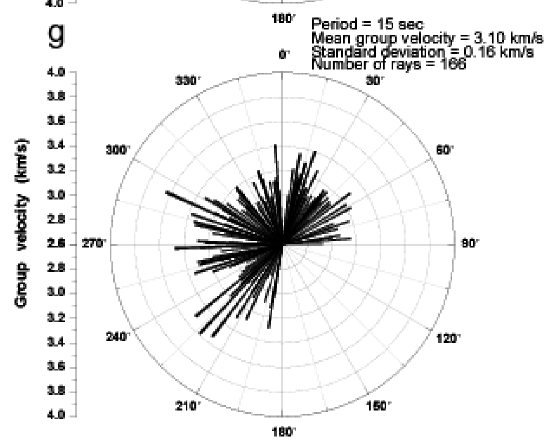

Figure 3.5 **(a–g).** Polar plots illustrating the variability of the group velocity measurements (y-axis) with respect to azimuth at periods of 2, 4, 6, 8, 10, 12 and 15 sec.

The level of uncertainty expected in the measured group velocities at each period should at least be around or less than 0.1 km/s (Ammon, 2001) and so the above-mentioned size of the standard deviation of the ensembles seem to be a reasonable threshold not to permit significant fluctuations in the resulting inverted models.

The group velocity measurements were inverted using a conjugate gradient algorithm (LSQR) based on the method by Paige and Saunders (1982). The LSQR algorithm is based on the following matrix equation:

$$\begin{bmatrix} A \\ \lambda \end{bmatrix} [x] = \begin{bmatrix} b \\ 0 \end{bmatrix} \qquad (3\text{-}1)$$

where A represents a matrix of ray distances in each cell, x is a vector of group velocity perturbations or slownesses, b is a vector of group velocity travel-times (distance/group velocity) and λ is a Laplacian smoothing constraint. A smoothing parameter of 100 was selected as an optimal constraint for the group velocity inversions considering the trade-off in the model smoothness versus travel-time misfit plot (see Figure 4 in the attached paper). Figure 4 only shows results for 2, 4, and 6 sec periods. Further trial-and-error inversions were performed and reveal that a smoothing parameter of 100 provides a better contrast in the inversion results compared to parameters in the range of 0–200. Resolution tests (see Figures 5a and b in the attached paper) using an input model with checkerboard sizes of 100 and 125 km^2 indicate that the 100 x 100 km^2 checkers are not well recovered. The 125 x 125 km^2 checkerboards on the other hand show better recovery of checkers at all periods and this indicates that the velocity variations across the BC are not well resolved at scales less than ~125 km. In addition, at 12 and 15 sec period, only velocity variations within the centre of the BC can be resolved for the 125 x 125 km^2 checkers.

3.2.2 Receiver functions

A total of 17 stations, falling within the area of best resolution as shown in Figure 5 (see attached paper), were used to acquire receiver functions. Only 16 of these stations were ultimately used because they are high quality receiver functions. Figure 3.6 shows examples of receiver functions for stations LBTB and SA47 to illustrate the quality of the data. A total of 100 teleseismic earthquakes (including those used in Chapter 2) were used to compute receiver functions (see Appendix A), the same as used by Kgaswane et al. (2009). The processing of receiver functions is already discussed in section 2.4.2.1 but the only exception in this case is that only receiver functions of $f \leq 1.25$ Hz (Gaussian bandwidth of 2.5 s) were computed for each teleseismic event with a maximum number of 200 iterations using the iterative deconvolution code based on the method by Ligorría and Ammon (1999). These high-frequency receiver functions were stacked according to backazimuth and ray-parameter.

3.2.3 Joint inversion method

The joint inversion of receiver functions and surface wave dispersion measurements yields 1-D Vs models of the structure beneath each recording station (Julià et al., 2000, 2003). The details of this method have already been described in section 2.4.2.2 and further described in the attached papers. In order to create regionally representative dispersions, Rayleigh wave group velocities obtained in this study from 2–15 sec were combined with group velocities from 20 to 90 sec from Pasyanos and Nyblade (2007) to create a composite dispersion curve for each station. The composite dispersion curves were smoothed with a 3-point running average prior to using them in the joint inversions with the receiver functions.

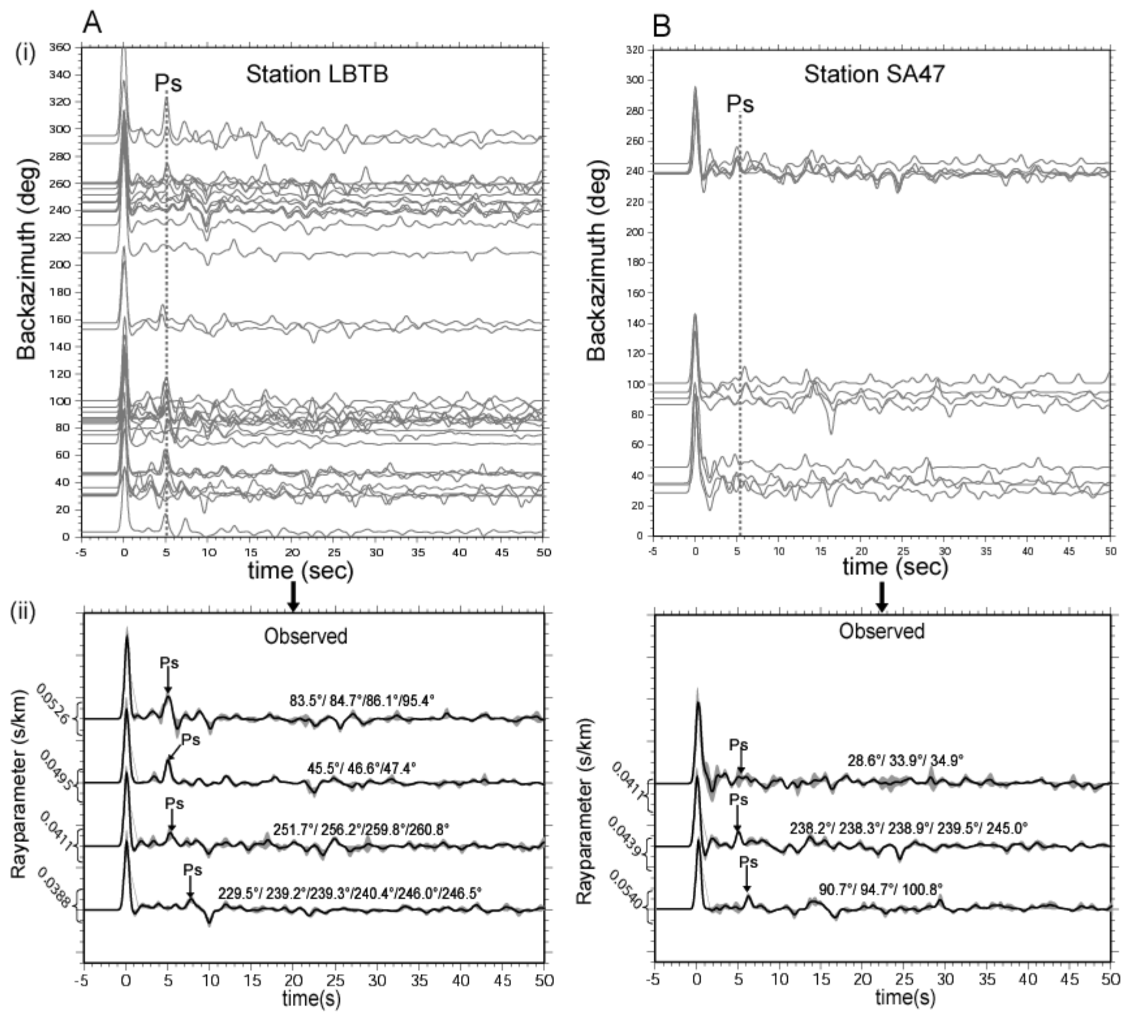

Figure 3.6 **(i).** Individual receiver functions for stations LBTB and SA47 (columns A and B, respectively) plotted using backazimuth as a function of time. The dashed gray lines show the theoretical arrival time of the Moho converted phase (Ps) for the crustal thicknesses and average crustal Vs for stations LBTB and SA47 reported in Table 3.1. The theoretical arrival times were computed using the joint inversion code and assuming the PREM model. **(ii).** Stacked receiver functions grouped according to ray parameter bins and backazimuth. The gray shading around the observed receiver functions shows 1σ error bounds.

For each inversion, the influence factor was set to 0.5 and no smoothing was applied, except for stations SA42, SA43, and SA53, for which smoothing parameters slightly greater than or equal to 0.1 were used. An influence factor of 0.5 equalizes the contribution of the combined misfit from each dataset. Figure 3.7, using stations SA47 and SA53 as examples, shows trade-off curves of (i) waveform misfit versus model roughness and (ii) waveform misfit versus model smoothness, illustrating that using little, if any, smoothing results in rougher velocity models with best resolution. The starting model and its parameterization is similar to what has been described in section 2.4.2.2 with the only exception in this case being that 1 km thick layers were used to a depth of 10 km. The importance of using 1 km thick layers to parameterize the model in the upper 10 km of the crust is illustrated in Figure 9 (see attached paper), where the fits to the data are compared for two models for station SA47, one with 1 km thick layers and the other with 2 km thick layers. The model with 1 km thick layers fits the receiver function stack better than the model with 2 km thick layers.

In assessing the uncertainties in the resulting velocity models, the approach developed by Julià et al. (2005) was used. This involves repeatedly performing the inversions using a range of inversion parameters. This approach is simplistic, but it is effective in developing a sense of the range of variation of the inverted parameters given the observations and the *a priori* constraints. A rigorous statistical approach in estimating the uncertainties will, amongst other things, require that the observations follow a Gaussian distribution and this condition is usually not satisfied. By following the approach of Julià et al. (2005) of repeatedly performing the inversions with a range of inversion parameters, we obtain an uncertainty of approximately 0.1–0.2 km/s for the velocity in each layer, which translates into an uncertainty of ~2–3 km in the depth of any boundary observed in the model, such as the Moho.

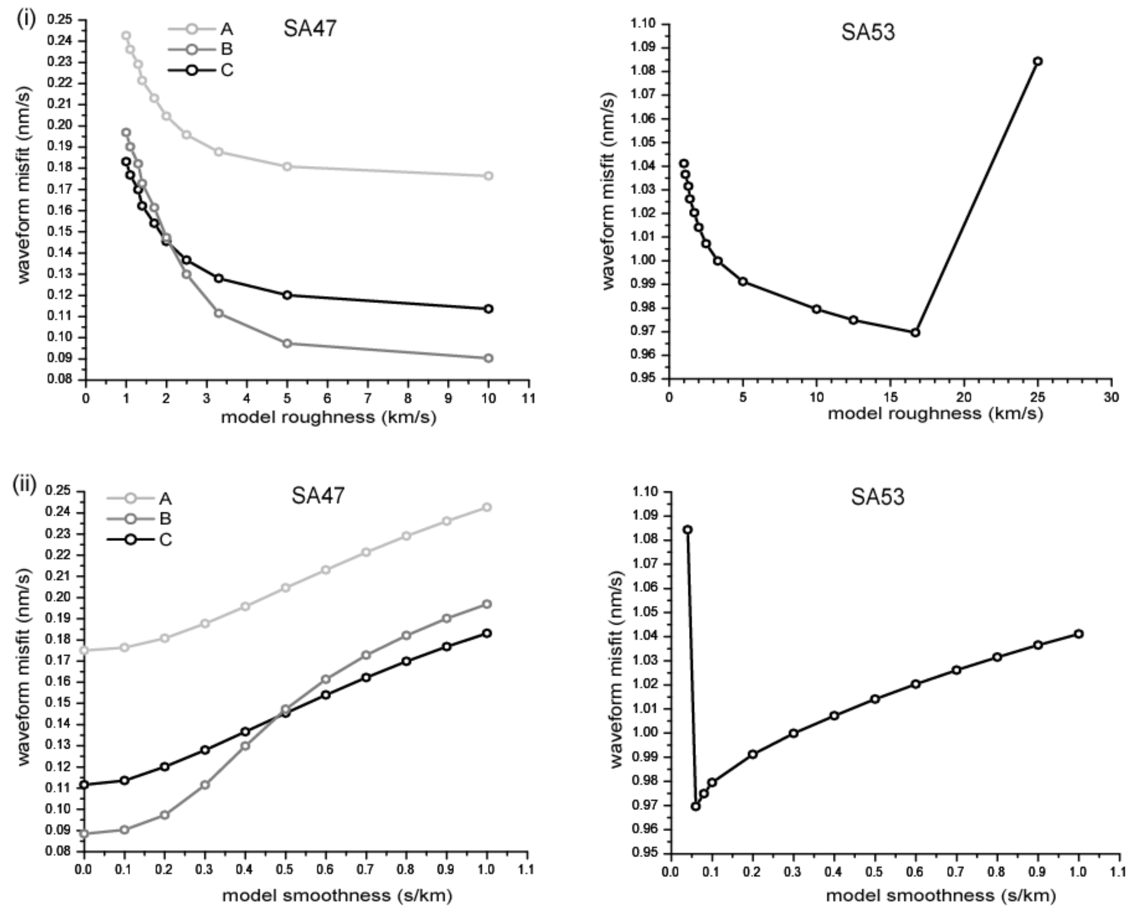

Figure 3.7 Plots of waveform misfit as a function of model roughness and model smoothness (**i** and **ii**, respectively) for stations SA47 and SA53. Labels A, B, C for station SA47 refer to the three receiver function stacks for this station shown in Figure 10 in the attached paper.

3.3 Results

3.3.1 Group velocity tomography

Figures 3.8a–g show the distribution of group velocities at periods 2–15 sec obtained by directly inverting Rayleigh group velocity measurements using the inversion approach as outlined in section 3.2.1.

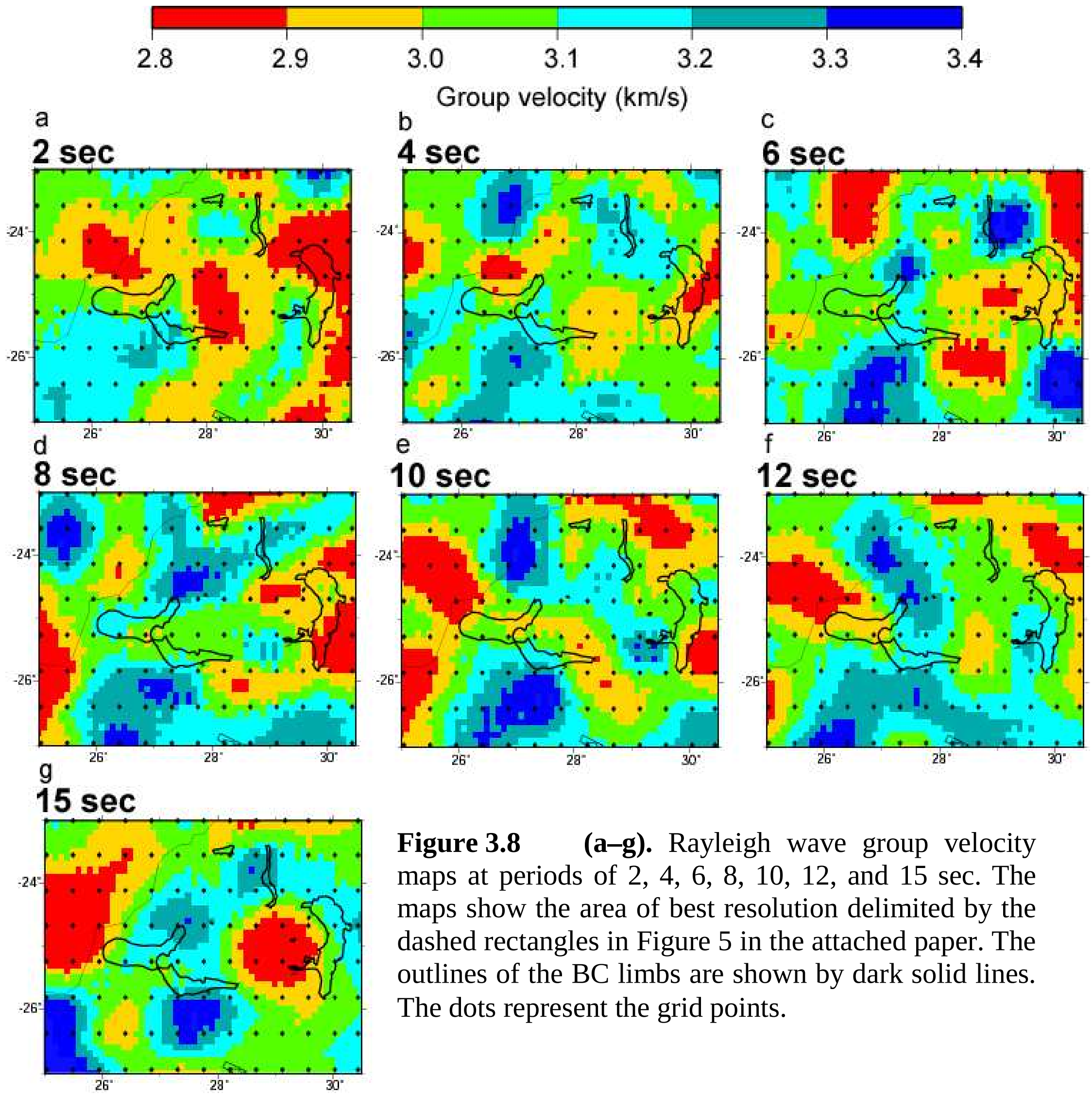

Figure 3.8 (a–g). Rayleigh wave group velocity maps at periods of 2, 4, 6, 8, 10, 12, and 15 sec. The maps show the area of best resolution delimited by the dashed rectangles in Figure 5 in the attached paper. The outlines of the BC limbs are shown by dark solid lines. The dots represent the grid points.

Rayleigh wave group velocities extracted at the grid points (at a grid spacing of 50 km) shown in Figure 3.8 were inverted using the joint inversion method by setting the influence factor for receiver functions to zero. From these inversions, 1-D Vs models were obtained at each grid point. A minimum curvature gridding algorithm (Smith and Wessel, 1990) was used to interpolate between the 1-D Vs models to generate quasi-3D-shear wave velocity images at varying depths from 2 to 15 km (shown in Figure 3.9).

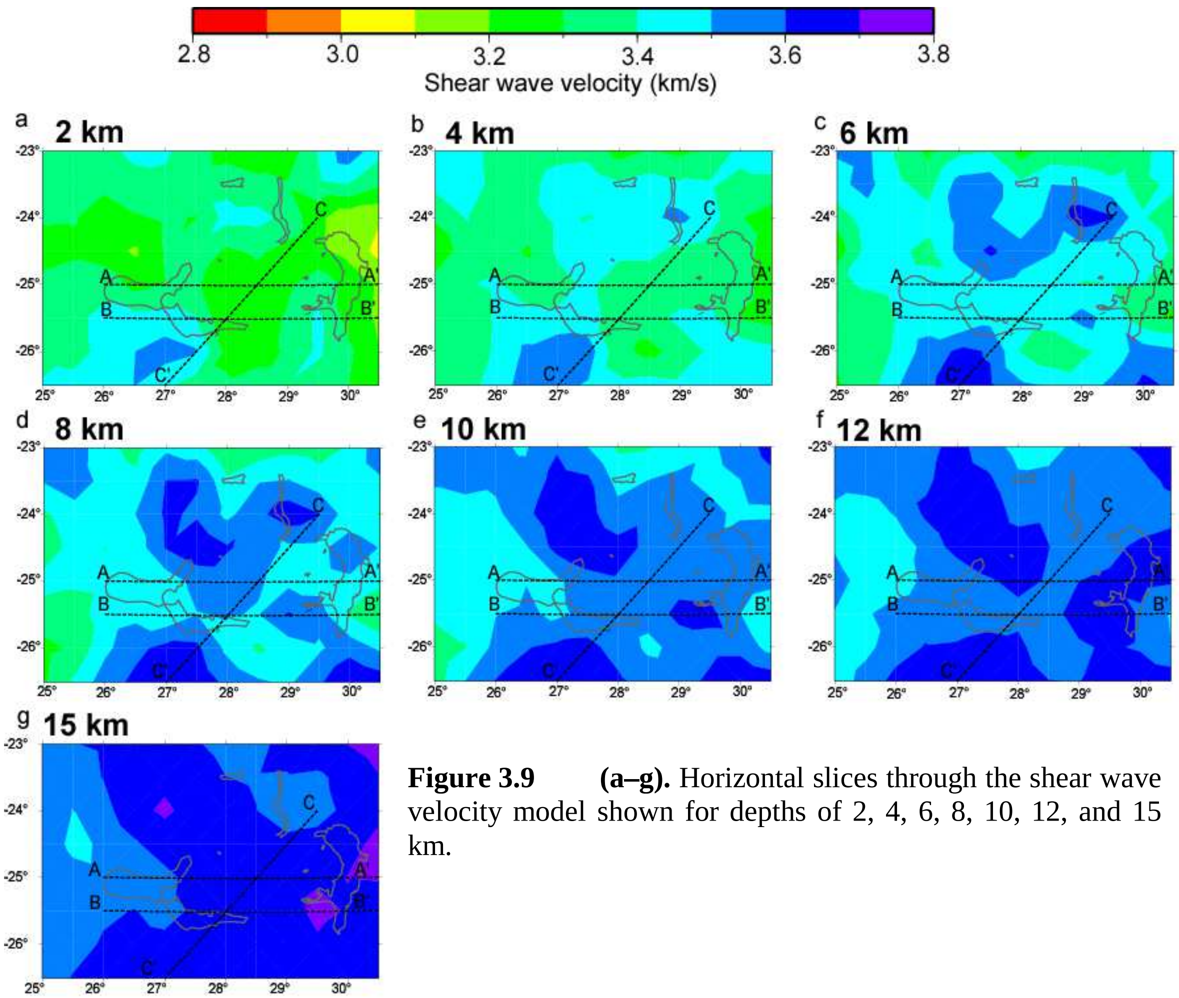

Figure 3.9 **(a–g).** Horizontal slices through the shear wave velocity model shown for depths of 2, 4, 6, 8, 10, 12, and 15 km.

The vertical cross-sections of the three profiles (A–A′, B–B′, C–C′, shown in Figure 3.10) were estimated from the Vs depth slices in Figure 3.9. The dashed rectangles shown in Figures 5a and b (in the attached paper) enclose the area of best resolution and therefore the group velocity tomography results (shown in Figure 3.8) are based on the areas enclosed by the rectangles. The results indicate that across the areas of the BC where velocity variations are best resolved, velocities at all periods vary between 2.8 and 3.2 km/s, but do not show a clear spatial correlation from one period to the next. Whilst Pasyanos and Nyblade (2007) did not report group velocities for periods less than 10 seconds, the group velocities in this study at 10 and 15 sec periods are estimated to be 10–30% greater than those reported by Pasyanos and Nyblade (2007). The ray path coverage reported by Pasyanos and Nyblade (2007) is limited at periods of 10 and 15 sec compared to periods $\geq$ 20 sec. Pasyanos and Nyblade (2007) did not report uncertainties at 10 and 15 sec and further show uncertainties of less than 0.1 km/s at period of 20 sec.

Given the lack of spatial correlation in Figure 3.8, the resolution of the quasi–3D shear wave velocity models shown in Figure 3.9 is coarse and does not clearly expose the outcropping mafic limbs (probably associated with Vs ≥ 3.7 km/s) of the BC seen at surface and subsurface depths (≤ 3 km). The level of spatial resolution needs to be considerably smaller than 125 x 125 km^2 for the subsurface structure of the BC to be mapped accurately. The vertical cross-sections (Figure 3.10) also do not reflect the presence of the outcropping mafic limbs at surface or subsurface depths although there is perhaps a slight indication of a high velocity body (Vs ~3.5–3.6 km/s) towards the southwest on the C–C' profile, probably associated with a portion of the Western Limb. Overall, a definitive interpretation of these results is not possible.

3.3.2 Joint inversion method

In an effort to overcome the lack of resolution associated with the group velocity tomography, joint inversions for 16 stations within the area of best resolution (enclosed by the dashed rectangles in Figures 5a and b of the attached paper) were performed. Figures 10 and 11 (in the attached paper) shows the joint inversion results for all 16 stations, and crustal parameters used in the models are summarized in Table 3.1 shown below. The joint inversion results were generated using composite Rayleigh wave group velocity curves in the period range of 2–90 sec. The 10–60 sec region of the group velocity dispersions are most relevant for the crust and therefore the results shown in Figure 10 of the appended paper have only displayed the dispersions up to 60 sec.

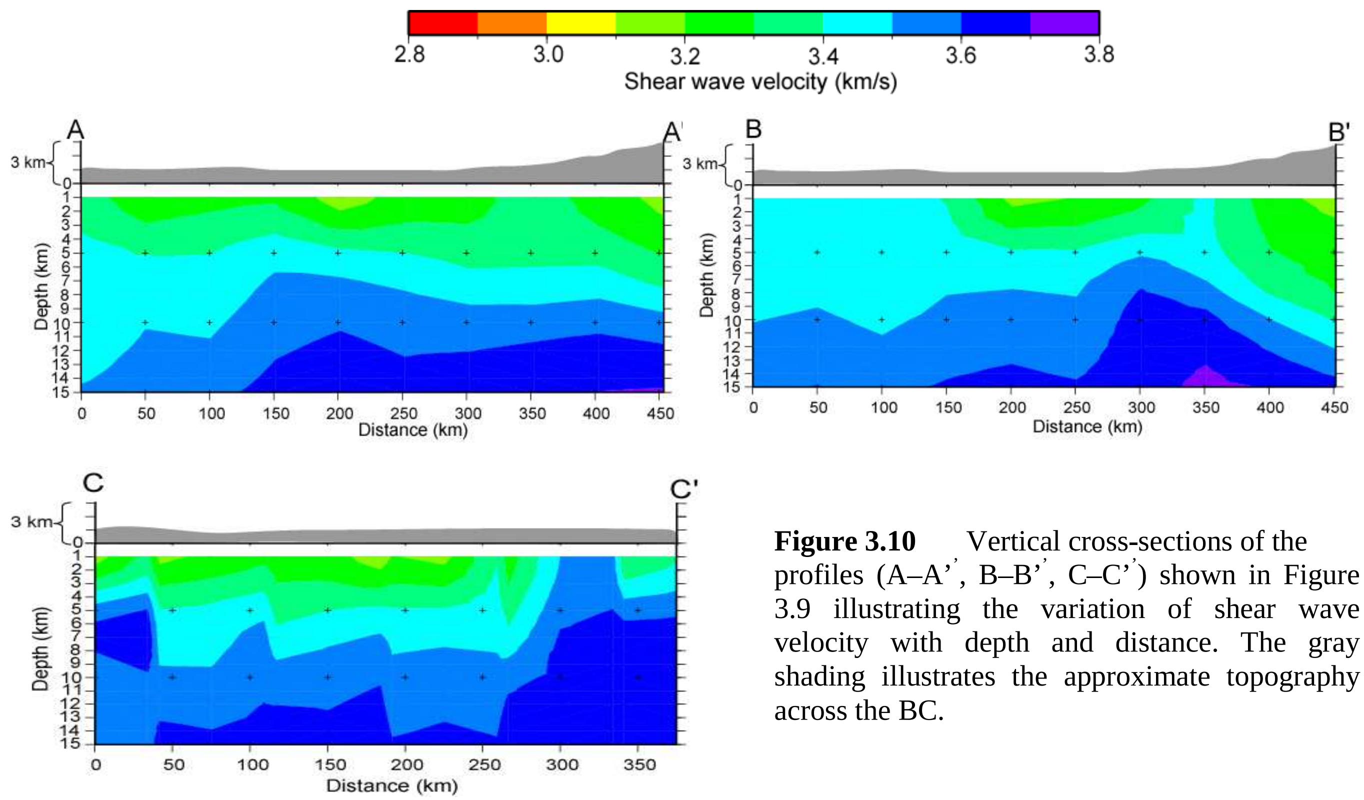

Figure 3.10 Vertical cross-sections of the profiles (A–A'', B–B'', C–C'') shown in Figure 3.9 illustrating the variation of shear wave velocity with depth and distance. The gray shading illustrates the approximate topography across the BC.

Many of the stations show a discontinuity where Vs increases from < 4.3 km/s to > 4.3 km/s, clearly delineating the Moho (see Figure 11 in the attached paper). One of the receiver function stacks for SA47 shows two depths where there is an increase in shear wave velocity above 4.3 km/s with a region of velocity less than 4.3 km/s in between. The Moho depth in this case has been excluded from further interpretation. Some of the stations show a gradational Moho and in such cases the Moho has been placed at the depth where Vs is ≥ 4.3 km/s.

Velocities that are > 4.3 km/s are indicative of mantle lithologies (Christensen and Mooney, 1995; Christensen, 1996). The crustal thicknesses obtained for all 16 stations are similar (i.e., within ~1–3 km) to those reported by Kgaswane et al. (2009).

Figure 3.11 shows three profiles across the BC illustrating that the Moho reaches a maximum depth of 45 km in the centre of the BC, compared to ~37–38 km outside of the BC. In addition to ~5–8 km of crustal thickening, most stations within the BC record a high velocity layer with Vs ≥ 4.0 km/s in the lowermost crust (Table 3.1). For most of the stations, the thickness of this layer exceeds 5 km, but for a few stations (e.g. station SA50), it is less than 5 km thick. With the exception of the gray Vs profiles (included for completeness), the uppermost mantle (Moho–60 km depth) in Figure 3.11 shows shear wave velocities of 4.5–4.6 km/s and this is in agreement with the observations indicated in Chapter 2. Mantle structure below 60 km depth could be insufficiently constrained because of using group velocities up to 90 sec.

The upper crustal velocities above 10 km depth from the joint inversions yield an average Vs of 3.4–3.6 km/s for most localities within the BC (Table 3.1), and these velocities are consistent with those reported by Yang et al. (2008). However, some stations show velocities as high as 3.7–3.8 km/s within the upper crust for layers that are only ±2 km thick (i.e., SA47, SA50 and SA53; see Figure 11 in the attached paper). Stations such as SA47 indicate considerable variability in upper crustal structure as a function of backazimuth and this variability is further examined in section 3.4.

Table 3.1 Summary of crustal parameters beneath the Bushveld Complex

Station	Back-azimuth (deg)	Vs (1 – 5 km depth) ± Std. deviation (km/s)	Vs (6 – 10 km depth) ± Std. deviation (km/s)	Vs below 30 km depth ± Std. deviation (km/s)	Crustal thickness (km)	Thickness of layers with Vs ≥ 4.0 km/s (km)	AverageVs (1 – 10 km depth) (km/s) ± Std. deviation (km/s)	AverageVs Below 30 km Depth (km/s) ± Std. deviation (km/s)	Average Crustal thickness (km)	Average thickness of layers in the lower crust with Vs ≥ 4.0 km/s (km)
LBTB	46.5°	3.5 ± 0.0	3.5 ± 0.1	4.1 ± 0.0	42.5	15	3.5 ± 0.1	4.1 ± 0.1	42.5	11
	87.4°	3.5 ± 0.1	3.5 ± 0.1	4.1 ± 0.1	42.5	10				
	240.2°	3.5 ± 0.1	3.5 ± 0.1	4.0 ± 0.1	40.0	10				
	257.1°	3.5 ± 0.1	3.4 ± 0.1	4.0 ± 0.1	40.0	10				
SA39	37.4°	3.4 ± 0.1	3.5 ± 0.1	4.0 ± 0.1	40.0	5	3.5 ± 0.1	4.0 ± 0.1	40.0	5
SA40	35.0°	3.5 ± 0.0	3.6 ± 0.0	4.0 ± 0.1	45.0	15	3.6 ± 0.1	4.0 ± 0.2	42.5	12
	95.9°	3.6 ± 0.1	3.6 ± 0.1	4.0 ± 0.2	42.5	8				
SA42	86.3°	3.4 ± 0.0	3.6 ± 0.0	4.1 ± 0.1	40.0	13	3.5 ± 0.1	4.1 ± 0.1	40.0	13
SA43	90.0°	3.4 ± 0.2	3.4 ± 0.0	4.1 ± 0.1	42.5	10	3.4 ± 0.1	4.1 ± 0.1	42.5	23
SA45	35.7°	3.4 ± 0.0	3.5 ± 0.1	4.1 ± 0.1	42.5	13	3.5 ± 0.1	4.1 ± 0.0	45.0	15
	96.3°	3.4 ± 0.0	3.5 ± 0.1	4.1 ± 0.1	45.5	16				
SA46	35.0°	3.3 ± 0.1	3.6 ± 0.0	4.1 ± 0.1	42.5	10	3.5 ± 0.1	4.1 ± 0.1	42.5	10
SA47	32.5°	3.5 ± 0.2	3.6 ± 0.2	4.1 ± 0.1	45.0	13	3.6 ± 0.2	4.1 ± 0.1	45.0	11
	95.4°	3.5 ± 0.1	3.6 ± 0.2	-	-	-				
	240.0°	3.5 ± 0.0	3.6 ± 0.1	4.0 ± 0.2	42.5	8				
SA48	244.6°	3.5 ± 0.1	3.3 ± 0.1	4.2 ± 0.1	45.0	18	3.4 ± 0.1	4.2 ± 0.1	45.0	18

SA49	89.1°	3.3 ± 0.1	3.5 ± 0.1	4.1 ± 0.1	37.5	10	3.4 ± 0.1	4.1 ± 0.1	37.5	10
SA50	31.8°	3.5 ± 0.1	3.6 ± 0.1	3.9 ± 0.2	40.0	5	3.6 ± 0.1	3.9 ± 0.1	40.0	4
	157.1°	3.5 ± 0.1	3.6 ± 0.1	3.8 ± 0.1	37.5	0				
	235.9°	3.4 ± 0.1	3.6 ± 0.1	3.9 ± 0.1	40.0	3				
SA51	36.5°	3.3 ± 0.1	3.4 ± 0.1	4.0 ± 0.1	42.5	8	3.4 ± 0.1	4.0 ± 0.1	42.5	8
SA52	31.5°	3.4 ± 0.1	3.4 ± 0.0	4.0 ± 0.2	37.5	6	3.4 ± 0.1	4.0 ± 0.2	37.5	6
SA53	97.2°	3.5 ± 0.1	3.5 ± 0.3	4.1 ± 0.1	40.0	10	3.5 ± 0.1	4.1 ± 0.1	40.0	10
SA63	33.8°	3.5 ± 0.1	3.5 ± 0.1	4.0 ± 0.3	42.5	10	3.5 ± 0.1	4.0 ± 0.2	42.5	9
	241.2°	3.6 ± 0.0	3.5 ± 0.1	4.0 ± 0.1	42.5	8				
SLR	81.1°	3.5 ± 0.2	3.4 ± 0.2	3.9 ± 0.1	37.5	3	3.5 ± 0.2	3.9 ± 0.1	35.0	3
	265.3°	3.5 ± 0.2	3.4 ± 0.1	3.9 ± 0.1	35.0	3				

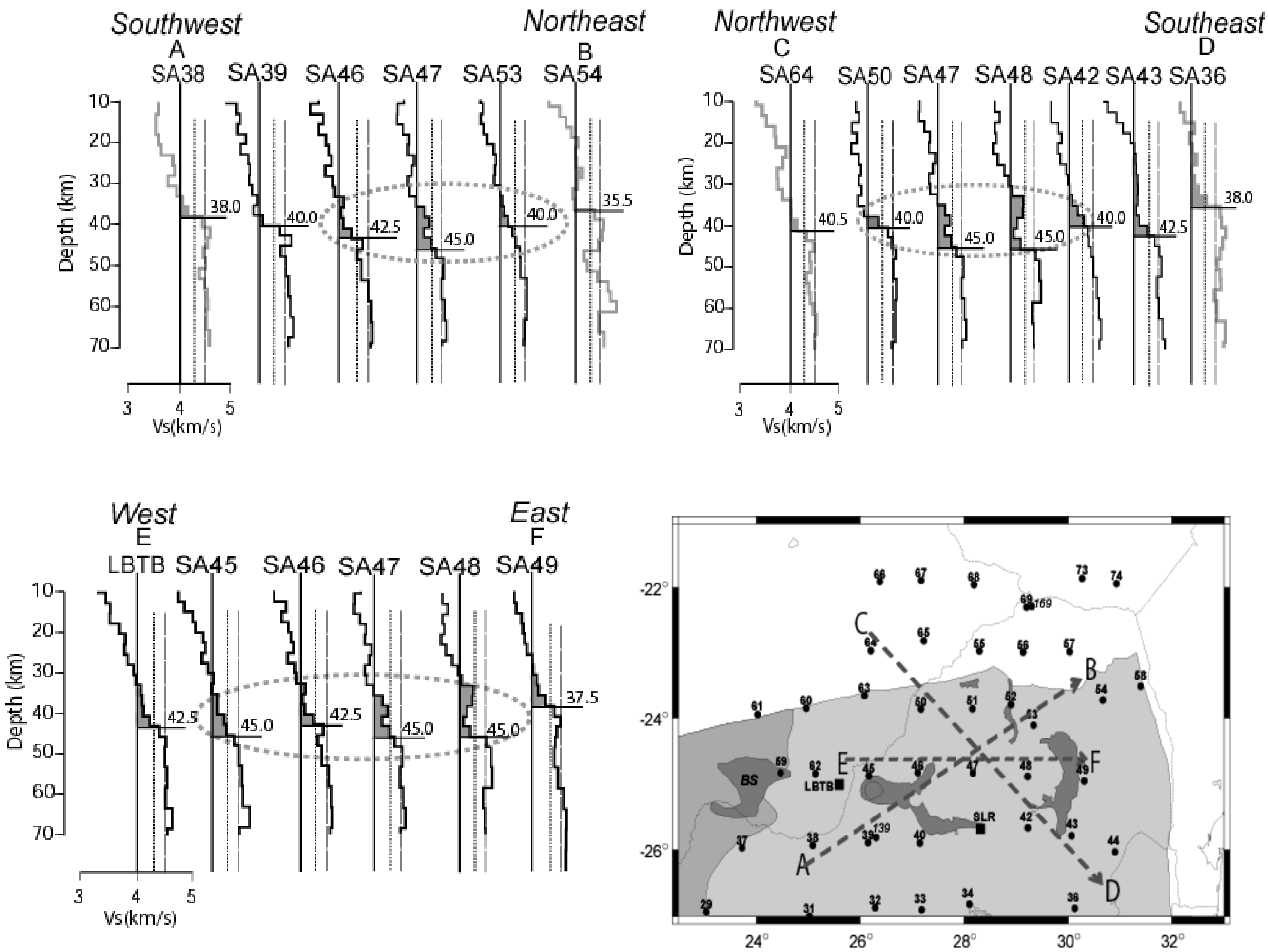

Figure 3.11 Cross-section of the crust across the BC from southwest to northeast (AB), northwest to southeast (CD), and west to east (EF). The shear wave profiles in gray are from Kgaswane et al. (2009). The map (bottom right) shows the location of the profiles (dotted lines) and station locations. The gray shading is the same as in Figure 3.2c.

3.4 Discussion

The main findings of this study are:

a) The BC crust in the centre thickens to a depth of ~ 45 km (e.g. SA45, SA47, SA48) (see Figure 3.11) and a considerable portion of the lower crust (greater than 5 km thickness) across the BC consists of high velocity layers (Vs ≥ 4.0 km/s) (see Figure 11 in the attached paper).

b) Some stations show velocities as high as 3.7–3.8 km/s in the upper crust (e.g. SA47, SA50, SA53). The empirical relation from Christensen and Stanley (2003) is used to convert Vs to density for interpreting the results obtained in this study. The empirical Vs – density (ρ) relation was formulated for both crustal and uppermost mantle lithologies at 200 MPa:

$$Vs = 0.0014\rho - 0.4019 \qquad (3\text{-}2)$$

Using this equation, a lower crustal Vs of 4.0–4.3 km/s and an uppermost mantle Vs of 4.4–4.6 km/s, yields a density contrast for the crustal "root" of ~ –0.2 to –0.3 g/cm^3. Using equation (3-2) and an average Vs of 3.4–3.6 km/s for the top 10 km of the crust, we obtain an average density for the upper crust of 2.7–2.9 g/cm^3. For upper crustal layers with Vs > 3.6 km/s, we obtain densities > 2.9 g/cm^3, which are consistent with the presence of mafic lithologies (Christensen and Stanley, 2003). These findings and density estimates can be used to evaluate the "dipping-sheet" and "continuous-sheet" models for the BC.

3.4.1 "Dipping-sheet" and "continuous-sheet" models

As already indicated in the introductory section, the "dipping-sheet" model by Meyer and De Beer (1987) has a gap between the eastern and western limbs and no compensation at the Moho for the dense upper crustal layers (Figure 3.2a). The findings in this study (i.e., crustal thickening in the centre of the BC (up to 45 km), high Vs layers (Vs ≥ 4.0 km/s) in the lowermost part of the crust (≥ 40 km), and high upper crustal densities beneath the centre of the BC) are not consistent with the features of the "dipping-sheet" model and therefore this model is not supported.

In contrast, the "continuous-sheet" model by Webb et al. (2004) (Figure 3.2b) proposes the presence of a continuous mafic layer in the upper crust across the geographic centre of the BC connecting the eastern and western limbs of the BC. Moreover, the presence of the mafic layer in the upper crust is isostatically compensated by a downwarped Moho which thickens to a depth of ~ 50 km in the centre of the BC. In the “continuous-sheet” model, a density contrast of 0.3 g/cm^3 for each of the upper crust mafic layers is used together with a density contrast of –0.3 g/cm^3 for the lowermost crust or the so-called crustal “root” (> 38 km depth).

The results in this study show that the crust has a thickness of ~ 45 km beneath the centre of the BC (Figure 3.11), consistent with, but somewhat thinner than, the lower crustal structure in the Webb et al. (2004) model. The Webb et al. (2004) model assumes an average density of 2.9 g/cm^3 for the structure above 10 km depth in the centre of the BC, which is equivalent to a Vs of 3.65 km/s using the relation in equation (3-2). The Vs models (Figures 10 and 11 in the attached paper) for some stations show Vs > 3.65 km/s within upper crustal layers, as noted previously, and therefore results in this study are broadly consistent with the upper crustal structure in the Webb et al. (2004) model.

3.4.2 Refinement of the Webb et al. (2004) density model

Figure 3.12 illustrates a revised version of the gravity model by Webb et al. (2004) which allows for a minor adjustment to the thickness of the layers of that model. Similar to the Webb et al. (2004), a background density of 2.7 g/cm^3 for the bulk crust and the same density contrasts for the upper crustal layers were used. Based on the seismic results, we assume a density of 3.3–3.4 g/cm^3 for the uppermost mantle. For the crustal “root” (> 37.5 km depth), a density contrast of –0.2 g/cm^3 was used instead of the –0.3 g/cm^3 density contrast used by Webb et al. (2004). After changing the structure and density of the crustal “root”, we then adjusted the thickness of the upper crustal layers to obtain a good fit to the gravity data.

In the revised density model (Figure 3.12), the mafic layering in the upper crust remains continuous across the BC with a maximum thickness of 4–5 km, similar to Webb et al. (2004). However, the layers of the Transvaal Sequence and younger sediments in the centre of the BC are somewhat thinner than those reported by Webb et al. (2004). This signifies that to accommodate the difference in crustal thickness between the Webb et al. (2004) model and the seismic results obtained in this study, only minor adjustments are required to the Webb et al. (2004) model.

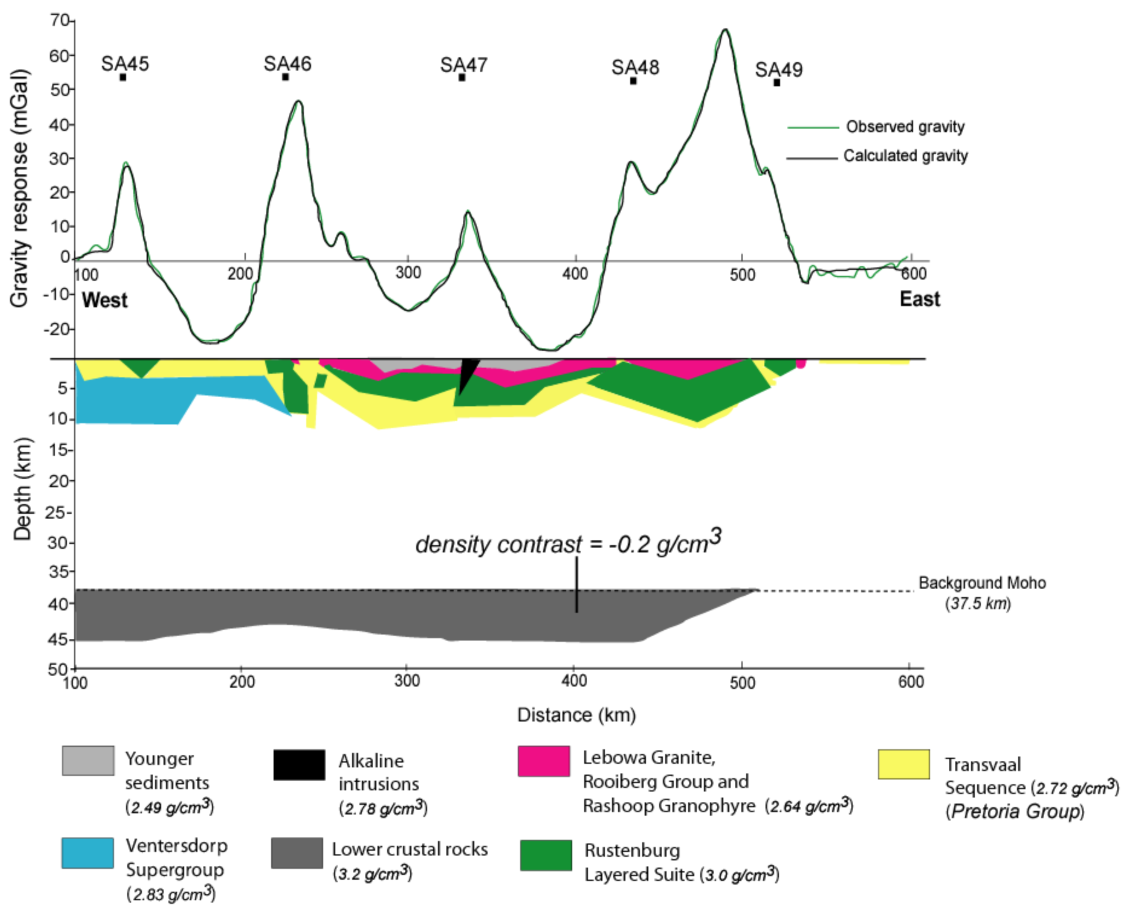

Figure 3.12 Revised Webb et al. (2004) density model based on the Vs models for the five seismic stations indicated. The densities (inside brackets in the legend) for the different crustal layers are taken from Webb et al., 2004.

3.4.3 Structural complexity in the upper crust

Although the seismic models obtained in this study generally concur with the density model by Webb et al. (2004), the Vs models for station SA47 (see Figure 11 in the attached paper) indicate that there could be considerable structural complexity in the centre of the BC. The presence of a uniform mafic layer, as suggested by both the revised (Figure 3.12) and the Webb et al. (2004) density model, could be an idealization of the subsurface centre of the BC which in reality could be more structurally complex and heterogeneous.

The structural complexity can be demonstrated by carefully examining the receiver functions for station SA47, which is located near the centre of the BC (Figure 3.1). The geology immediately around station SA47 is shown in Figure 14 (see attached paper). This figure shows average Ps conversion points at 5 km depth for the three receiver function stacks for SA47 shown in Figure 10 (see attached paper). The Vs profile for SA47 at backazimuth (a) in Figure 11 (see attached paper) corresponds to the conversion point at A in Figure 14 (see attached paper), and similarly the Vs profiles at backazimuths (b) and (c) correspond to conversion points B and C, respectively.

Figure 14 (in the attached paper) shows an overthrust structure just to the south of station SA47, resulting in an anticlinal structure with the receiver functions likely sampling different lithologies (i.e., granites, sandstones, quartzites) depending on backazimuth and depth. Figure 3.13 is a conceptual representation of vertical stratigraphy up to 6 km depth based on the geology in Figure 14 and the Vs results for SA47 in Figure 11. The positions of the Vs profiles at A, B, and C (as shown in Figure 3.13) are based on the assumption that the wavelengths of the teleseismic recordings are greater than 5 km or the correlation lengths of the heterogeneities within the crust (i.e., with high velocity fluctuations) for teleseismic wavefields (~0.3–3 Hz) are of the order of 2–4 km (e.g. Ritter et al., 1998; Ritter and Rothert, 2000).

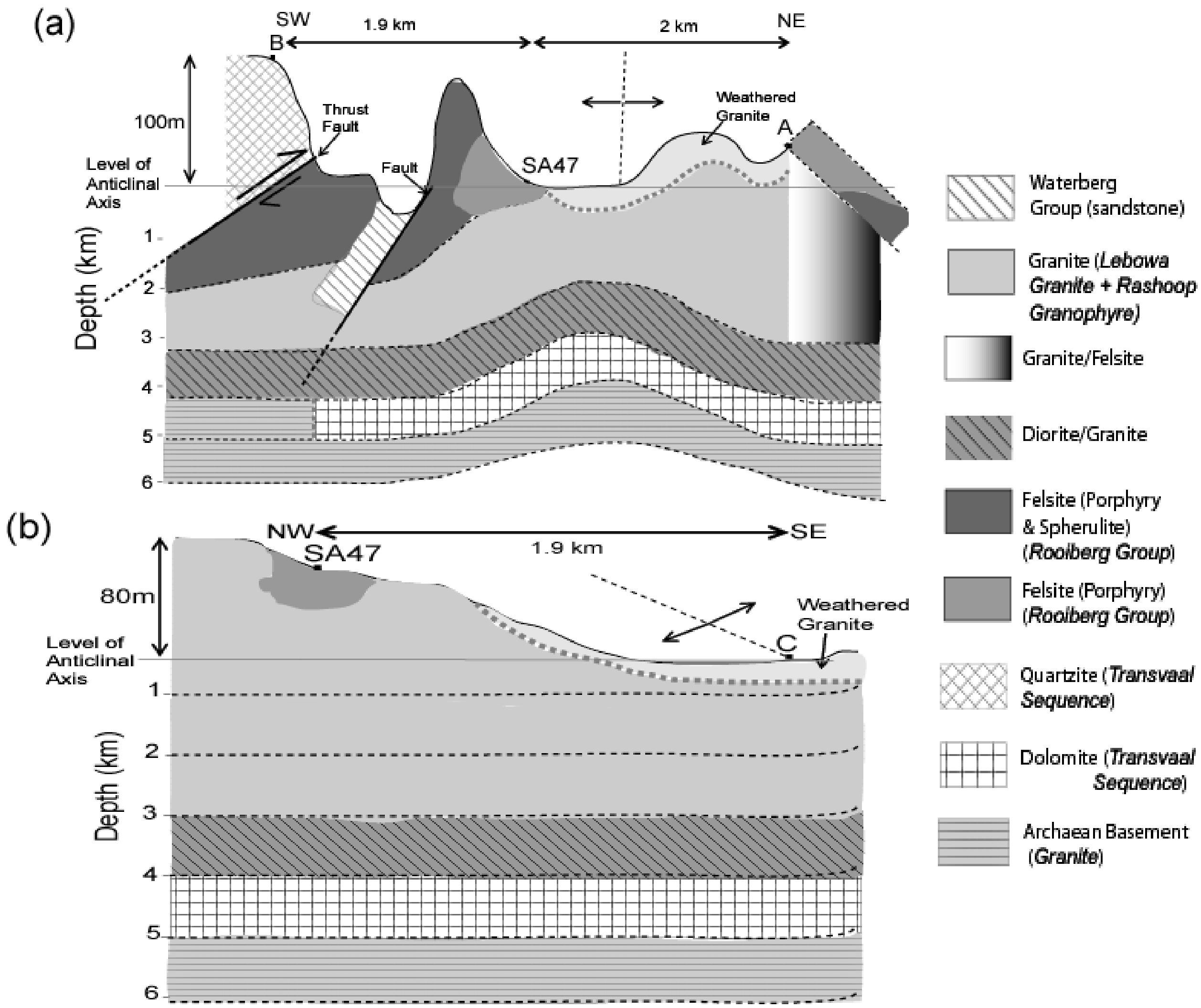

Figure 3.13 Schematic geological cross-sections across station SA47 following: **a.** profile from B to A, **b.** profile SA47 to C, all shown in Figure 14 (see attached paper). Geological contacts are shown as dashed lines since they are inferred from the modelling results. The same applies to fault extensions at depth.

The Vs profiles for the positions indicated in Figure 3.13 are < 3 km from the centre (i.e., station SA47) and therefore the Vs profiles can be assumed to be reasonably representative of subsurface structure at those positions. Figure 3.14 shows the modelling results of the three receiver function stacks for SA47 which aim to reveal the effect of upper crustal structure on the waveforms.

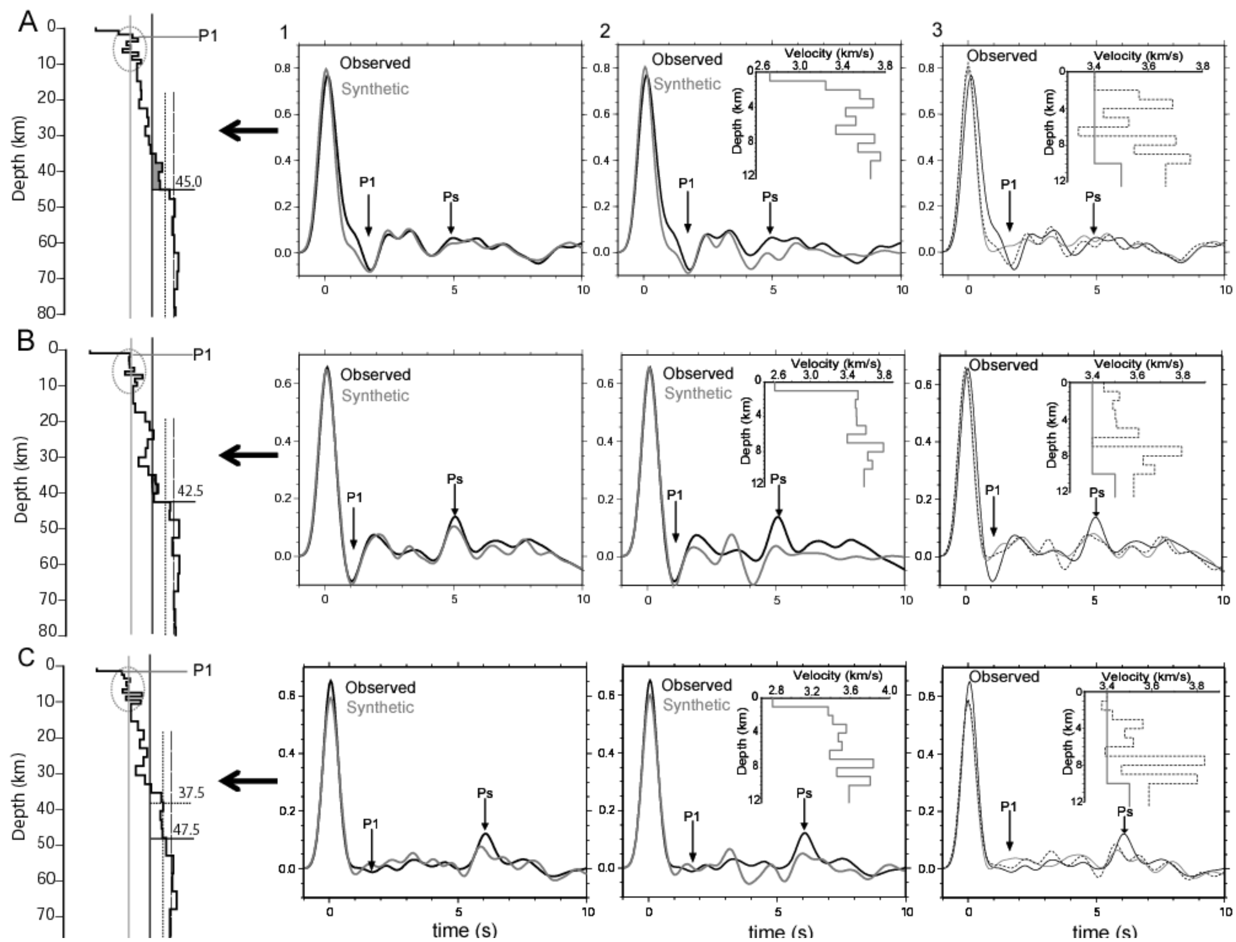

Figure 3.14 Modelling results of the three receiver function stacks for station SA47.

The synthetic receiver functions in the first column of Figure 3.14 were obtained from the joint inversion, whereas those in the second and third columns were generated using a code based on a reflection matrix method by Kennett (1983). The first column of receiver functions (in Figure 3.14) shows the fit between observed and synthetic receiver functions for the models obtained from the joint inversion. The first prominent phase after the direct P arrival within the first two seconds is labelled P1 and is the primary arrival resulting from upper crustal structure.

There is considerable variability in the P1 phase between the three receiver function stacks. For stack A, the phase is characterized by a large down-swing with a peak amplitude at 1.8 sec. For stack B, the phase is characterized by a large down-swing with a peak amplitude at 1.0 sec and for stack C, the phase is characterized by a small down-swing with a peak amplitude around 1.7 sec. The Ps conversion from the Moho is also labelled on each stack.

The second column shows synthetic receiver functions for a velocity model that contains the velocity layering in the upper 10 km of the crust from the joint inversion models (shown at far left on Figure 3.14), and a half space beneath it with a velocity of 3.6 km/s. A comparison between the synthetic and actual receiver functions illustrates that the P1 phase does indeed originate from structure (i.e., thrusted zone) within the top 10 km of the crust.

The third column shows synthetic receiver functions for two velocity models with altered upper crustal layering (structure below 10 km is the same as in the joint inversion models). The aim of this exercise is to isolate which layers within the top 10 km of the crust influence the P1 phase the most. In the first model (dotted line), the low velocity layer in the top 1 km of the model is removed (i.e., the topmost velocity is increased to the velocity in the layer just below it). A comparison of the receiver function fits shows that the earlier arriving P1 phase in stack B is changed significantly (effectively removed), but the fits for stacks A and C are essentially unchanged, indicating that the later arriving P1 phases in those stacks might be influenced by deeper structure.

In the second case (gray line), the velocity structure in the top 10 km is set to a uniform 3.4 km/s, thus removing all of the higher velocity layering in the top 10 km of the crust seen in the joint inversion models. Even though the velocity models (gray lines) in the third column have been set to a uniform 3.4 km/s in the top 10 km of the crust, the corresponding receiver functions are different because of influences from structures below 10 km depth. In this case, the P1 phase in stacks A and C is significantly altered, indicating that the higher velocity layering between 1 and 10 km depth in the joint inversion model is required to fit the P1 phase.

The modelling exercise above shows that the receiver function stacks from two of the three backazimuths (stacks A and C) require higher velocity layers (i.e., Vs of 3.7–3.8 km/s) in the upper crust to obtain a good fit, as compared to stack B. These results suggest that the mafic layering may be better developed to the east and northeast of station SA47 than to the southwest, and hence the upper crustal structure is not as uniform as illustrated by the gravity models (Figure 3.12 and Webb et al., 2004). The non-uniformity could potentially be characteristic of much of the geographic centre of the BC. The suggestions by Uken and Watkeys (1997) indicate there was diapirism and metamorphism across the BC associated with its emplacement. Most probably, this non-uniformity as suggested in this study could primarily be linked with the diapirism and metamorphism as postulated by Uken and Watkeys (1997).

Figure 3.1 shows the position of some of the domes associated with the diapirism triggered by high thermal gradients at the base of the BC. Uken and Watkeys (1997) suggested that the domes were produced by gravitational loading and heating of the sedimentary rocks of the Transvaal Supergroup below the floor of the BC. For areas where temperatures were above 550°C, these floor rocks became unstable and diapirically rose into the overlying units of the RLS. Although the domes are best exposed towards the margins of the BC, as shown in Figure 1, the diapirism of floor rocks into the overlying RLS could be widespread across the centre of the BC, assuming that diapirism was generally driven by thermal destabilization of low density rocks of the Transvaal Sequence (Uken and Watkeys, 1997).

An additional factor that could have potentially created non-uniformity across the BC could be attributed to the ~2040 Ma orogenic event corroborated by field, petrographic, and $^{40}Ar/^{39}Ar$ data presented by Alexandre et al. (2006, 2007). The folding, thrusting, and lower greenschist-facies metamorphism of this orogenic event are best observed in the broad area between Pretoria, the village of Magaliesburg, and the Cradle of Humankind (cf. Andreoli, 1988 a, b). Further evidence of this event, tentatively linked to coeval reactivation of the Central Zone in the Limpopo Belt, was also identified in the Malip River – Pilgrim's Rest areas, close to the NE and E margin of the BC, respectively (cf. Alexandre et al., 2006; Harley and Charlesworth, 1994).

3.5 Conclusion

The 1-D shear wave velocity models in this study obtained by jointly inverting high-frequency receiver functions ($f \leq 1.25$ Hz) and Rayleigh wave group velocities (in the period of 2–60 sec) for 16 broadband seismic stations spanning the BC, indicate the following:

1. The crust beneath the centre of the BC is ~45 km thick and could have probably thickened by ~ 5–8 km when compared with the cratonic regions adjacent to the BC.
2. Shear wave velocities of 4.0 km/s or higher are found in a substantial portion of the lower crust (below 30 km depth) beneath the BC. These velocities are indicative of a lower crust that is highly mafic.
3. There could be mafic lithologies in the across the upper crustal structure of the BC with shear wave velocities ≥ 3.7 km/s.

These results favour a "continuous-sheet" as opposed to a "dipping-sheet" model for the BC, in which the mafic layers are continuous at depth beneath the centre of the complex. However, detailed modelling of receiver functions at one locality within the centre of the complex indicates that the mafic layering may be locally disrupted by diapirism and metamorphism. Therefore, the layering of the upper crustal structure in the centre of the BC is more complex than that predicted by both the seismic model in this study and the "continuous-sheet" model. The inhomogeneity and complexity of the upper crust may be the result of thermal diapirism, triggered by the emplacement of the BC at ~2060 Ma, or thermal and tectonic reactivation produced by a ~2040 Ma intraplate event.

References

Alexandre, P., Andreoli, M.A.G., Jamison, A., and Gibson, R.L., 2006. $^{40}Ar/^{39}Ar$ age constraints on low-grade metamorphism and cleavage development in the Transvaal Supergroup (Central Kaapvaal craton, South Africa): implications for the tectonic setting of the Bushveld igneous complex. *South African Journal of Geology*, 109, 393-410.

Alexandre, P., Andreoli, M.A.G., Jamison, A., and Gibson, R.L., 2007. Response to the comment by Reimold *et al.* on $^{40}Ar/^{39}Ar$ age constraints on low-grade metamorphism and cleavage development in the Transvaal Supergroup (central Kaapvaal Craton, South Africa):

implications for the tectonic setting of the Bushveld Igneous Complex (South African Journal of Geology, 109, 393-410), by Alexandre *et al*. (2006). *South African Journal of Geology*, 110, 160 – 162.

Ammon, C.J., Randall, G.E., and Zandt G., 1990. On the nonuniqueness of receiver function inversions, *Journal of Geophysical Research*, 95, 15303 – 15318. doi:10.1029/JB095Ib10p15303.

Ammon, C.J., 2001. Notes on seismic surface-wave processing, Part 1, Group velocity estimation. Saint Louis University, version 3.9.0. http://eqseis.geosc.psu.edu/~cammon.

Andreoli, M.A.G., 1988a. The discovery of a hidden and strange African orogeny: the Transvaalide Fold Belt. *Tectonic Division, Geol. Soc. S. Africa, Abstracts Vol. 4th Annual Conference, Silverton, 25 February 1988,* 1-2

Andreoli, M.A.G., 1988b. Evidence for thrust tectonics in the Transvaal Sequence based on geophysical profiles . *Ext. Abstracts Geocongress '88, Geol Soc. S. Afr., Durban, South Africa,* 3-6.

Biesheuvel, K., 1970. An interpretation of a gravimetric survey in the area west of Pilanesburg in the western Transvaal. Geological Society of South Africa, *Special Publications*, 1, 266 – 282.

Carlson, R.W., Grove, T.L., De Wit, M. J., and Gurney, J.J., 1996. Program to study crust and mantle of the Archean Craton in southern Africa. *Eos Trans. AGU* ,77 (29), 273 – 277. doi:10.1029/96EO00194.

Cassidy, J. F., 1992. Numerical experiments in broad-band receiver function analysis. *Bulletin of the Seismological Society of America*, 82, 1453– 1474.

Cawthorn, R.G., Cooper, G.R.J., and Webb, S.J., 1998. Connectivity between the western and eastern limbs of the Bushveld Complex. *South African Journal of Geology*, 101, 291 – 298.

Cawthorn, R.G., and Webb, S.J., 2001. Connectivity between the western and eastern limbs of the Bushveld Complex, *Tectonophysics*, 300, 195 – 2009.

Cawthorn, R.G., Eales, H.V., Walraven, F., Uken, R., and Watkeys, M.K., 2006. The Bushveld Complex, In: Johnson, M. R., Anhaeusser, C.R., Thomas, R.J., (Eds.) *The Geology of South Africa*, Geological Society of South Africa, Johannesburg/ Council for Geoscience, Pretoria, 261 – 281.

Christensen, N. I., and Mooney, W.D., 1995. Seismic velocity structure and composition of the continental crust: A global view. *Journal of Geophysical Research*, 100, 9761 – 9788.

Christensen, N.I., 1996. Poisson's ratio and crustal seismology. *Journal of Geophysical Research*, 101, 3139 – 3156.

Christensen, N.I., and Stanley, D., 2003. Seismic velocities and densities. In: Lee, W.H.K., Kanamori, H., Jennings, P.C., Kisslinger, C., (Eds.) *International Handbook of Earthquake and Engineering*, 81B, 1587 – 1594.

Claerbout, J.F., 1992. Earth Soundings Analysis: Processing Versus Inversion, Blackwell Scientific Publications, Boston, MA, 304 pages.

Cousins, C.A., 1959. The structure of the mafic portion of the Bushveld Igneous Complex, *Transactions of the Geological Society of South Africa*, 62, 179 – 189.

Du Plessis, A., and Kleywegt, R.J., 1987. A dipping sheet model for the mafic lobes of the Bushveld Complex. *South African Journal of Geology*, 90, 1 – 6.

Du Toit, A.L., 1954. The Geology of South Africa. Oliver and Boyd, Edinburgh, U.K., 539pp.

Dziewonski, A., Bloch, S., and Landisman, L., 1969. A technique for the analysis of transient seismic signals. *Bulletin of the Seismological Society of America*, 59, 427 – 444.

Dziewonski, A.M., and Anderson, D.L., 1981. Preliminary reference Earth model. *Physics of the Earth Planetary Interiors*, 25, S.297 – 356.

Eglington, B.M., and Armstrong, R.A., 2004. The Kaapvaal Craton and adjacent orogens, southern Africa: a geochronological database and overview of the geological development of the Craton. *South African Journal of Geology*, 107, 13 – 32.

Gurrola, H., and Minster, J.B., 1998. Thickness estimates of the uppermantle transition zone from bootstrapped velocity spectrum stacks of receiver functions. *Geophysical Journal International*, 133, 31 – 43, doi:10.1046/j.1365-246X.1998.1331470.x.

Hall, A.L., 1932. The Bushveld Igneous Complex of the central Transvaal. South African Geological Survey Memoir 28, Pretoria, 560 pp.

Harley, M. and Charlesworth, E.G., 1994. Structural development and controls to epigenetic, mesothermal gold mineralization in the Sabie-Pilgrim's Rest goldfield, eastern Transvaal, South Africa. *Exploration and Mining Geology*, 3, 231-246.

Hatton, C.J., and Schweitzer, J.K., 1995. Evidence for synchronous extrusive and intrusive Bushveld magmatism. *Journal of African Earth Sciences*, 21, 579 – 594.

Jorissen, 1904, On the occurrence of the Dolomite and Chert Series in the Rustenburg district. *Transvaal Geological Society of South Africa*, 7, 30 – 38.

Julià, J., Ammon, C.J., Hermann, R.B., and Correig, A.M., 2000. Joint inversion of receiver functions and surface-wave dispersion observations. *Geophysical Journal International*, 143, 99 – 112.

Julià, J., Ammon, C.J., aàànd Hermann, R.B., 2003. Lithospheric structure of the Arabian Shield from the joint inversion of receiver functions and surface-wave group velocities. *Tectonophysics*, 371, 1 – 21.

Julià, J., Ammon, C.J., and Nyblade, A.A., 2005. Evidence for mafic lower crust in Tanzania, East Africa from joint inversion of receiver functions and Rayleigh wave dispersion velocities. *Geophysical Journal International*, 162, 555 – 569.

Keilis-Borok, V. I., 1989. *Seismic surface waves in a laterally inhomogeneous earth*, Kluwer Academic Publishers, Dordrecht.

Kennett, B.L.N., 1983. *Seismic wave propagation in stratified media*, Cambridge University Press, Cambridge.

Kgaswane, E.M., Nyblade, A.A., Julià, J., Dirks, P.H.G.M., Durrheim, R.J., and Pasyanos, M.E., 2009. Shear wave velocity structure of the lower crust in southern Africa: Evidence for compositional heterogeneity within Archaean and Proterozoic terrains. *Journal of Geophysical Research*, 114, B12304. doi:10.1029/2008JB006217.

Levshin, A., Ratnikova, L., and Berger, J., 1992. Peculiarities of surface-wave propagation across central Asia. *Bulletin of the Seismological Society of America*, 82, 2464 – 2493.

Ligorría, J. P., and Ammon, C.J., 1999. Iterative deconvolution and receiver function estimation. *Bulletin of the Seismological Society of America*, 89, 1359 – 1400.

Mellor, E.T., 1906. The geology of the central portion of the Middelburg district. *Annual Report of the Geological Survey of Transvaal*, 55 – 71.

Meyer, R., and De Beer, J.H., 1987. Structure of the Bushveld Complex from resistivity measurements. *Nature*, 325, 610 – 612.

Molengraaff, G.A.F., 1901. Geologie de la Republique S. Africaine. *Bulletin of the Geological Society of France*, 1, 13 – 92.

Molengraaff, G.A.F., 1902. Vice President's address. *Transvaal Geological Society of South Africa*, 5, 69 – 75.

Molyneux, T.G., and Klinkert, P.S., 1978. A structural interpretation of part of the eastern mafic lobe of the Bushveld Complex and its surrounds. *Transactions of the Geological Society of South Africa*, 81, 359 – 368.

Nair, S.K., Gao, S.S., Kelly, H.L., Silver, P.G., 2006. Southern African crustal evolution and composition: Constraints from receiver function studies. *Journal of Geophysical Research*, 111, B02304. doi:10.1029/2005JB003802.

Nguuri, T.K., Gore, J., James, D.E., Webb, S. J., Wright, C., Zengeni, T.G., Gwavava, O., Snoke, J.A., and the Kaapvaal Seismic Group, 2001. Crustal structure beneath southern Africa and its implications for the formation and evolution of the Kaapvaal and Zimbabwe Cratons. *Geophysical Research Letters*, 28, 2501 – 2504.

Owens, T.J., Zandt, G., and Taylor, S.R., 1984. Seismic evidence for an ancient rift beneath the Cumberland Plateau, Tennessee: a detailed analysis of broadband teleseismic P waveforms. *Journal of Geophysical Research*, 89, 7783 – 7795.

Paige, C.C., and Saunders, M.A., 1982. LSQR: An algorithm for sparse linear equations and sparse least squares. *ACM Trans. Math. Software*, 8 (1), 43 – 71, doi:10.1145/355984.355989.

Pasyanos, M.E., and Nyblade, A.A., 2007. A top to bottom lithospheric study of Africa and Arabia. *Tectonophysics*, 444 (1 – 4), 27 – 44.

Ritter, J.R.R., Shapiro, S.A., and Schechinger, B., 1998. Scattering parameters of the lithosphere below the Massif Central, France, from teleseismic wavefield records. *Geophysical Journal International*, 134, 187 – 198.

Ritter, J.R.R., and Rothert, E., 2000. Variations of the lithospheric seismic scattering strength below the Massif Central, France and the Frankonian Jura, SE Germany. *Tectonophysics*, 328, 297–305.

Smith, W.H.F., and Wessel, P., 1990. Gridding with continuous curvature splines in tension. *Geophysics*, 55 (3), 293 – 305, doi:10.1190/1.1442837.

South African Committee for Stratigraphy, 1980, Stratigraphy of South Africa. Part 1 (Kent, L.E., Comp.), Lithostratigraphy of the Republic of South Africa, South West Africa/Namibia, and the Republics of Bophuthatswana, Transkei and Venda, *Handbook of Geological Survey of South Africa*, 8, 690 pp.

Uken, R., and Watkeys, M.K., 1997. Diapirism initiated by the Bushveld Complex, South Africa. *Geology*, 25, 723 – 726.

Van der Merwe, M.J., 1976. The layered sequence of the Potgietersrus limb of the Bushveld Complex. *Economic Geology*, 71, 1337 – 1351.

Walraven, F., and Darracott, B.W., 1976. Quantitative interpretation of a gravity profile across the western Bushveld Complex. *Transactions of the Geological Society of South Africa*, 79, 22 – 26.

Walraven, F., 1987. Geochronological and isotopic studies of Bushveld Complex rocks from the Fairfield borehole at Moloto, northeast of Pretoria. *South African Journal of Geology*, 90, 352 – 360.

Walraven, F., 1997. Geochronology of the Rooiberg Group, Transvaal Supergroup, South Africa. Economic Geology Research Unit, University of the Witwatersrand, Johannesburg, South Africa, *Information Circular*, 316, 21pp.

Webb, S.J., Cawthorn, R.G., Nguuri, T.K., and James, D.E., 2004. Gravity modelling of Bushveld Complex connectivity supported by Southern African Seismic Experiment results. *South African Journal of Geology,* 107, 207 – 218.

Webb, S.J., Ashwal, L.D., and Cawthorn, R.G., 2010. Continuity between eastern and western Bushveld Complex, South Africa, confirmed by xenoliths from kimberlite. *Contributions to Mineralogy and Petrology*, 162, 101 – 107, doi:10.1007/s00410-010-0586-z.

Wielandt, E., 1993. Propagation and structural interpretation of non-plane waves. *Geophysical Journal International*, 113, 45 – 53.

Yang, Y., Li, A., and Ritzwoller, M.H., 2008. Crustal and uppermost mantle structure in southern Africa revealed from ambient noise and teleseismic tomography. *Geophysical Journal International*, 174, 235 – 248, doi:10.1111/j.1365-246X.2008.03779x.

Chapter 4

Shear wave velocity constraints on the source of the Beattie Magnetic Anomaly

Abstract

The variability of the crustal structure beneath the Beattie Magnetic Anomaly (BMA) is investigated by jointly inverting high-frequency teleseismic receiver functions and 10–105 sec Rayleigh wave group velocities for three broadband seismic stations located in the Namaqua-Natal Belt (NNB). The 1-D shear wave velocity models obtained from the joint inversions show upper and middle crustal layering around the northern branch of the BMA to have average velocities ≥ 3.5 km/s at depths of ~5–20 km. These estimates place a constraint on the source of the BMA. The 1-D Vs models further show that high velocity layers (≥ 4.0 km/s) occupy a significant portion of the lower crust and that the crust is on average thicker than 40 km. These results from the 1-D Vs models are consistent with the findings made by previous studies.

The Vs models for the three stations along the northern axis of the BMA show velocities approaching 4.0 km/s around depths of 10 km. This implies that the BMA body (or its crustal host) becomes mafic in composition around those depths. However, the velocities fluctuate below 10 km depth (i.e., low-to-high or high-low-high), suggesting that the 10 km depth marks either the base of the BMA body (or its crustal host) or a change in its composition. Estimates of physical properties (i.e., Vp, Vs, Poisson's ratio, density, and resistivity) favour massive sulphide ore bodies and/or mineralized granulite-facies mid-crustal rocks and/or mineralized Proterozoic anorthosites as plausible models of the BMA source. However, the plausibility of

the massive sulphide model critically depends either on the level of concentration of sulphide minerals within the ore bodies or the degree of metasomatism (on the ore bodies) that could have occurred during the final stages of the NNB evolution. The magnetic mineralization in the anorthosites and/or granulites could either be in the form of iron sulphides (pyrite) and/or iron and titanium oxides such as magnetite, ilmenite, hematite, or crystallographic combinations of hematite and ilmenite.

4.1 Introduction

The Beattie Magnetic Anomaly (BMA) and the Southern Cape Conductive Belt (SCCB) (Figures 4.1, 4.2 and 4.3) are coincident, ~1000-km long geophysical anomalies in the Namaqua-Natal Belt (NNB) and Cape Fold Belt (CFB) of South Africa (e.g., De Beer et al., 1982; Corner, 1989; Weckmann et al., 2007a,b). The BMA straddles both the Namaqua and Natal sectors of the NNB, lies along the axis of the SCCB, and bifurcates into a northern and southern branch towards its westward extension. The NNB is also host to a number of other prominent magnetic anomalies such as the Williston and Mbashe anomalies (e.g., Thomas et al., 1992) (see Figure 4.2b) which are parallel but shorter than the BMA. The crustal source of these magnetic anomalies and the SCCB is still a matter of ongoing investigation. In the last decade a substantial amount of work has been done by the Inkaba yeAfrica research initiative to advance the understanding of the BMA source (de Wit and Horsfield, 2006).

The BMA was first discovered by Beattie (1909). Since then many geophysical models of the crustal source have been proposed: a suture zone consisting of serpentinised mafic and ultramafic rocks in the deeper parts of the crust (e.g. Burke, 1977; De Beer et al., 1982; Pitts et al., 1992; Hälbich, 1993; Harvey et al., 2001); magnetite enrichment of the NNB granite-gneiss lithologies through low-angle thrust faults (Corner, 1989); graphite enriched crustal-scale shear zones (Weckmann et al., 2007a,b); high velocity bodies at crustal depths (Stankiewicz et al., 2007, 2008); granulite-facies mid-crustal rocks within the NNB (Quesnel et al., 2009); massive to disseminated, deformed and metamorphosed stratiform magnetite-sulphide ore bodies flanked by smaller stratiform ore bodies (Lindeque and de Wit, 2009; Lindeque et al., 2011); mineralized fault and joint planes in the granite-gneiss basement of the Bushmanland Terrane in the NNB (Loots, 2012).

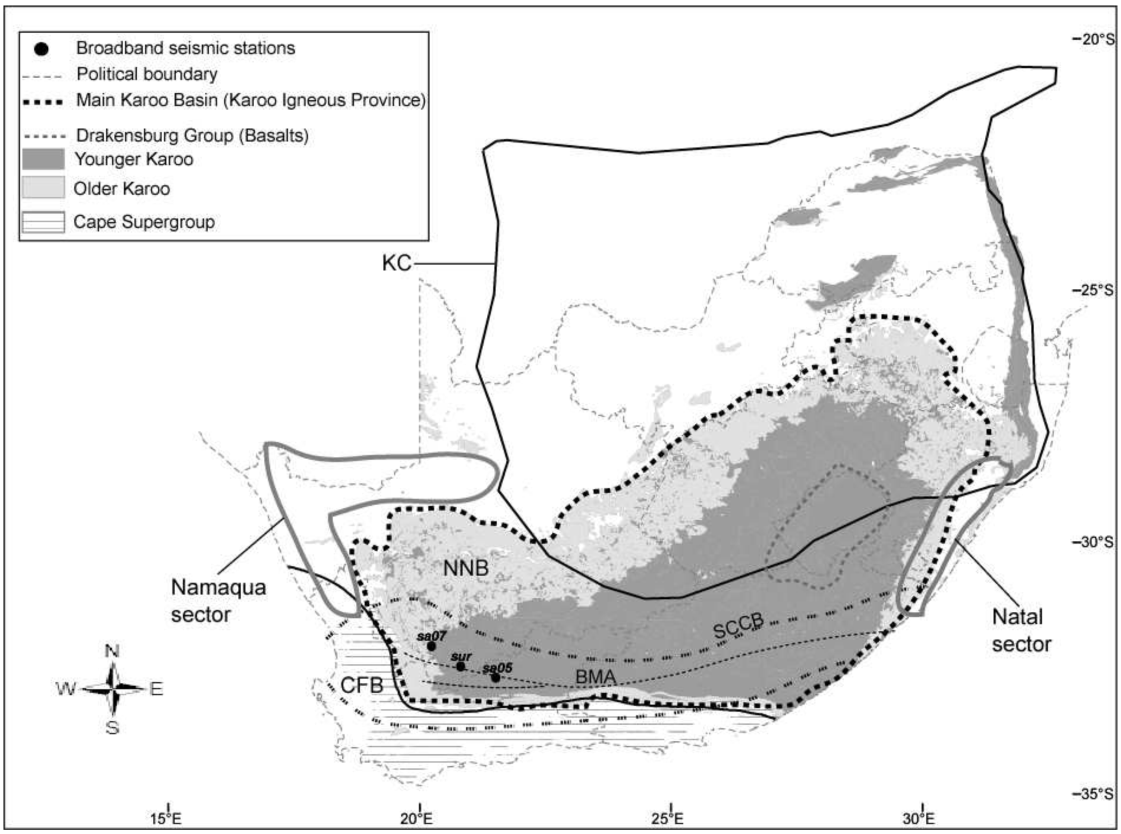

Figure 4.1 Map showing features of the main Karoo Basin (Karoo Igneous Province) with respect to the tectonic regimes delineated by the dark solid lines: KC – Kaapvaal Craton, NNB – Namaqua-Natal Belt, and CFB – Cape Fold Belt. The outline of the Karoo Igneous Province is based on Duncan and Marsh (2006). The approximate positions of the BMA and SCCB are also shown. The map has been reproduced from the 1:1 000 000 geology map of South Africa. The solid gray polygons approximately show outlines of the exposed rocks of the NNB in the Namaqua and Natal sectors.

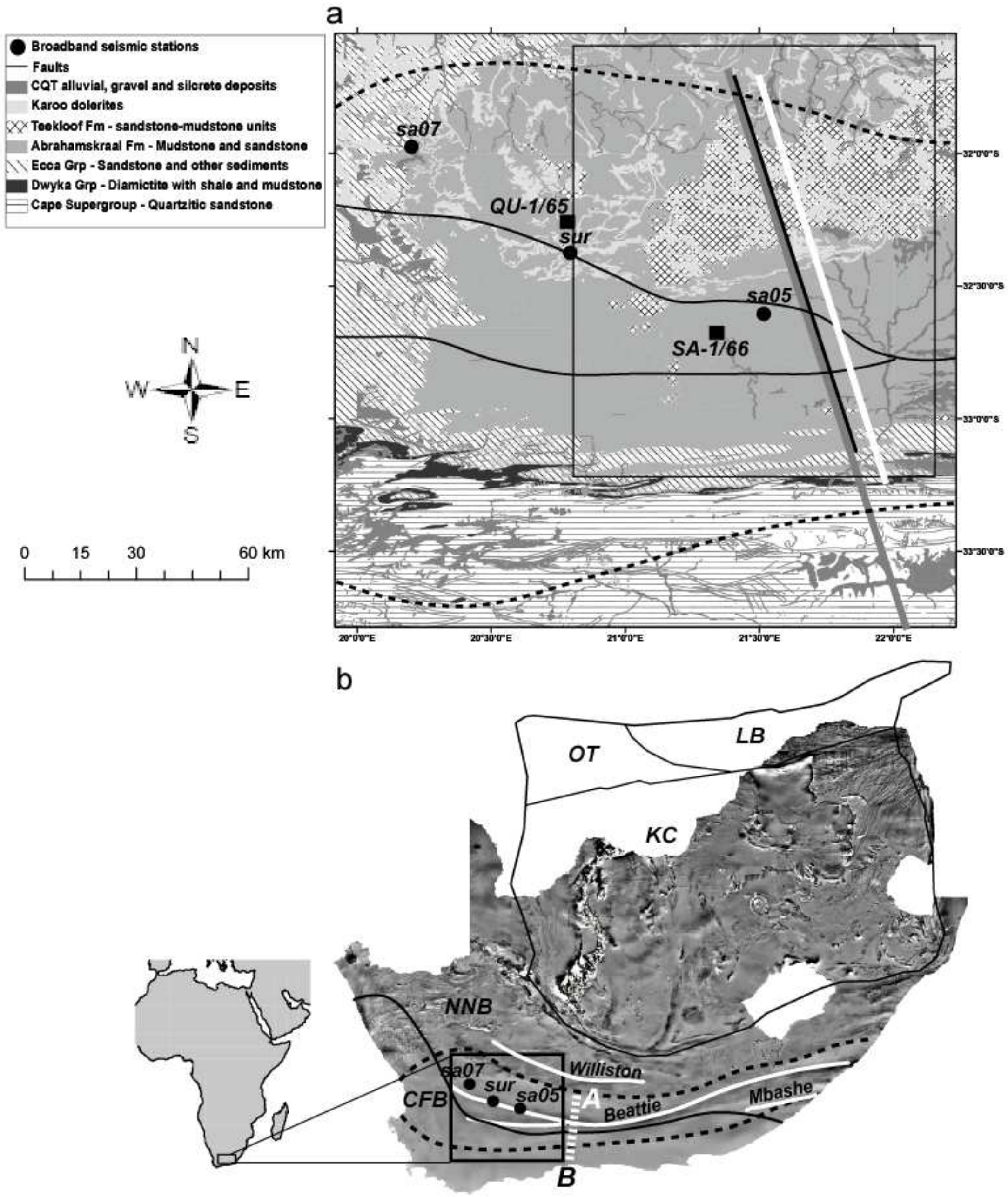

Figure 4.2 **(a).** Map showing simplified geology around the three stations in the NNB (map has been modified from the 1:250 000 geology map of South Africa). Superimposed on the map are the BMA maximum axes (solid curves) and the SCCB (dashed curves). The locations of the BMA and SCCB follow that of other studies (e.g. Lindeque et al., 2007). The solid black, gray and white lines roughly mark the study profiles by Weckmann et al. (2007a), Stankiewicz et al. (2007, 2008) and Lindeque et al. (2007, 2011), respectively. The solid black rectangle approximately encloses the study area of Quesnel et al. (2009). The solid squares represent boreholes. CQT – Cenozoic, Quarternary and Tertiary; Grp – Group; Fm – Formation **(b).** Total free air aeromagnetic field map of South Africa [reproduced from the 1:1,000,000 (CGS, 2000)] showing an overview of the study area (enclosed in black solid square). The SCCB is shown as dashed black curves and the solid white curves show approximately the location of some of the magnetic anomalies within the NNB (the BMA being the longest). Superimposed on the regional aeromagnetic map are major tectonic terrains. The dashed white line between the points A and B marks the reflection seismic line by Loots (2012). The location of this study is marked by the dark solid square and the dark solid lines delineates the tectonic regimes: OT – Okwa Terrain, LB – Limpopo Belt, KC – Kaapvaal Craton, NNB – Namaqua-Natal Belt, and CFB – Cape Fold Belt.

In this study, high-frequency (f ≤ 1.25 Hz) teleseismic receiver functions are jointly inverted with Rayleigh wave group velocities in the period of 10–60 sec for three broadband seismic stations located along the northern branch of the BMA. The purpose of this study is to use the 1-D shear wave velocity models from the joint inversions to place shear wave velocity constraints on the source of the BMA and to evaluate the geophysical models described above. In the next sections of this study, the background geology and past studies of the BMA are described, followed by a description of the data, methodology, and results and a discussion on the possible sources of the BMA.

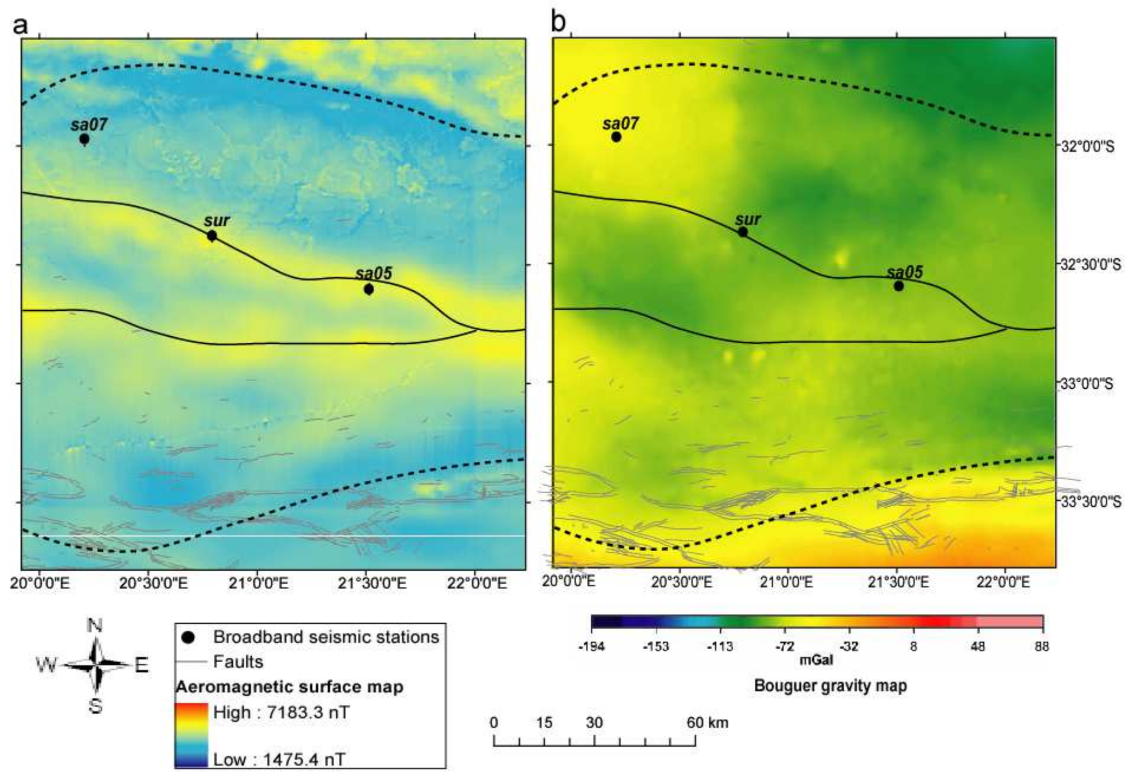

Figure 4.3 **(a).** Aeromagnetic (unfiltered) and **(b).** Bouguer gravity anomaly maps representing the geophysical versions of the geological structure shown in Figure 4.2a. The aeromagnetic and gravity maps have been reproduced from CGS (2000) and Venter et al. (1999), respectively. The BMA axes are shown as black solid lines.

4.2 Background

4.2.1 The geology around the BMA

The main Karoo Basin is well preserved above parts of the NNB and also covers parts of the Kaapvaal Craton (KC) (Figure 4.1). The Mesozoic rocks of the Karoo Basin (e.g. Dwyka, Ecca, Beaufort Groups) make up the upper sedimentary layer covering much of the NNB and overlies the Cape Supergroup (e.g. Johnson et al., 2006; Lindeque et al., 2011, Loots, 2012). Figure 4.2a shows a close-up view of the surface geology (in Figure 4.1) around the three broadband seismic stations used in this study. The Beaufort Group consists of sedimentary formations such as the Abrahamskraal and Teekloof Formations (Figure 4.2a). The Karoo sediments are intruded by the mid-Jurassic Karoo dolerites. The Cape Supergroup (500 – 330 Ma) crops out at the southern rim of the NNB and consists of clastic sediments and quartzites (e.g. Thamm and Johnson, 2006). The Cape Supergroup, together with the overlying Dwyka and Beaufort Groups at the southern rim of the NNB, were deformed in an orogenic event related to the formation of the Cape Fold Belt (CFB) about 250 Ma ago (e.g. Hälbich 1993; Newton et al., 2006). According to seismic reflection studies (e.g. Lindeque et al., 2011, Loots, 2012), the rocks of the NNB (e.g. Bushmanland Terrane, Margate Terrane), which crop out on the westernmost (Namaqua sector) and easternmost (Natal sector) parts of the NNB (see Figure 4.1) most likely continue beneath the younger cover rocks and constitute the Proterozoic mid-crustal fabric below the Cape Supergroup.

4.2.2 Geophysical models

A number of geophysical models from previous studies provide a range of interpretations for the crustal source of the BMA. A summary of the results and interpretations of the BMA source from past studies is provided in Table 4.1.

Table 4.1 Overview of geophysical and seismic results of the BMA from some of the past and recent studies

Results	**Burke, 1977; De Beer et al., 1982; Pitts et al., 1992; Hälbich et al., 1993; Harvey et al., 2001**	**Corner, 1989**	**Weckmann et al., 2007a,b**	**Stankiewicz et al., 2007, 2008**	**Quesnel et al., 2009**	**Lindeque and de Wit, 2009; Lindeque et al., 2007, 2011**	**Loots, 2012**
Vp and Vs (km/s)				6.6–7.0 (Vp) 3.8–4.0 (Vs)			
Depth extent of BMA (km)	8–18 and possibly reaching lower crustal depths of 30 km	Mid-crustal depths	5–10 and possibly reaching lower crustal depths of 30 km	8–15	10–20	7–15	5–10
Width of the BMA from north to south (km)	20–50		~100–150	~ 20–70	80	≥ 15	> 10
Magnetic field anomaly (nT)	200–300		200–300		200–300		
Resistivity (Ωm)			≤ 2 (conductive anomalies)				
Density contrast (g/cm^3)	0.2	-	-	-	-	-	-
Rock type and/or mineralization associated with the BMA	Serpentinized ultramafics	Magnetite enriched granite-gneiss rocks	Graphite enriched shear zones	-	Granulite-facies mid-crustal rocks	Stratabound massive sulphide-magnetite deposits	Mineralized faults and joints in the granite-gneiss basement

An integrated database of geophysical investigations up to 1993, led some studies to conclude that the BMA source are several south-dipping mafic-ultramafic slabs of ophiolites (oceanic crust) with 15 to 20% serpentinization (e.g. De Beer et al. 1982; Hälbich, 1993, Pitts et al. 1992). These slabs were estimated to be at a depth of 30 km and to be 20–50 km wide. They were further interpreted to be representative of a tectonic boundary between the NNB terrains and the younger Pan-African belt to the south. The results of the receiver function modelling by Harvey et al. (2001) suggested intracrustal discontinuities at depths of approximately 8 and 18 km. Harvey et al. (2001) interpreted these discontinuities to be the upper and lower bounds of the BMA and interpreted the BMA source to be a ~10 km thick block of Mesoproterozoic mafic-ultramafic rocks.

Corner (1989) interpreted magnetic data and suggested that the BMA source is magnetite mineralization at mid-crustal depths within the granite-gneiss basement of the NNB and he further postulated that the BMA was connected to the Grenville-age magnetic anomalies in the western Dronning Maud Land in Antarctica prior to the break-up of Gondwana. Based on conductivity studies, Weckmann et al. (2007a,b) rejected both the obducted ophiolite model proposed by Pitts et al. (1992) and the magnetite enriched granite-gneiss model proposed by Corner (1989), and instead proposed that the BMA results from graphite-enriched shear zones spread across the NNB. Conductivity studies by Weckmann et al. (2007a,b) infer the BMA source to be coincident with conductivity anomalies at depths of ~5–10 km, which extend to mid-to-lower crustal depths. The magnetic modelling component by Weckmann et al. (2007b) suggests the BMA source to be 100–150 km wide, but this contradicts the narrow sized (1–2 km) conductivity anomalies required by the conductivity modelling.

The seismic refraction model by Stankiewicz et al. (2007, 2008) reveals a high-velocity body at depths of ~7–15 km with P-wave velocities of ~6.5–7.0 km/s. Stankiewicz et al. (2007, 2008) correlate the high velocity body with a high resistivity zone flanked by two magnetic bodies on the model produced by Weckmann et al. (2007b). This combination of features is required to produce the magnetic response of the BMA at its maxima between 200–300 nT.

Quesnel et al. (2009) confirmed that the 200–300 nT BMA could be produced by a double-prism with a combined width of 80 km and 10–20 km deep. Comparison of the Quesnel et al. (2009) double-prism magnetic model and the refraction tomographic model of Stankiewicz et al. (2007, 2008) suggests that the northern prism coincides with high P-wave velocities (6.5–7.0 km/s) and the southern prism partially coincides with low P-wave velocities (~5.5–6.5 km/s).

Seismic reflection studies (Lindeque and de Wit, 2009; Lindeque et al., 2007, 2011) infer the BMA source to be a zone of strongly reflective anomalies at depths of ~7–15 km with a total width around 15–19 km. The model by Lindeque et al. (2007, 2011) contradicts the serpentinized ophiolitic model as the reflectivity patterns suggest the BMA source is confined to the NNB mid-crust and does not show a deeper extension below the mid-crustal region of the NNB. Lindeque et al. (2011) interprets the BMA source to be interspersed within the NNB mid-crustal layer and attributes it to massive to disseminated, deformed/metamorphosed stratiform sulphide-magnetite ore bodies. Another seismic reflection study by Loots (2012) infers the BMA source to be at depths of ~5–10 km, which is consistent with Lindeque et al. (2007, 2011). The model by Loots (2012) attributes the BMA source to be part of the NNB mid-crustal layer and due to mineralized faults and joints within the granite-gneiss basement.

4.2.3 The magnetic and gravity anomaly around the BMA

The regional field magnetic anomaly in Figure 4.3a was acquired at an elevation of 100 m with a magnetic gridding interval of 250 m (CGS, 2000). It is diurnally-corrected and a constant taken off. The rocks comprising the continental crust frequently contain magnetic minerals that give rise to induced and magnetic anomalies (e.g. Hunt et al., 1995; McEnroe et al., 2009b). It is assumed that the magnetic field in Figure 4.3a has a component of natural remanent magnetization (*NRM*) that is greater than induced magnetization (χH_e) because crustal magnetic anomalies similar to the BMA are usually produced by igneous and metamorphic complexes and show greater remanent magnetization largely due to the prevalence of solid solutions of iron oxides such as magnetite, ilmenite, and hematite (e.g. Brown and McEnroe, 2008; McEnroe et al., 2009a, b). In such cases, the Koenigsberger ratio (i.e., Q_n) is greater than 0.5. This ratio is a dimensionless parameter defined as:

$$Q_n = {}^{NRM}\!/_{\chi H_e} \qquad (4\text{-}1)$$

where the index *n* is the nth layer of the Earth, χ is the magnetic susceptibility and H_e is the local geomagnetic or Earth's magnetic field. The relatively high Bouguer gravity anomaly signature enveloping the area around station SA07 (between -72 and -32 mGal) is in contrast to the relatively low Bouguer gravity anomaly signature (between -113 and -72 mGal) enveloping the areas around SUR and SA05 (i.e., around the BMA axes) (see Figure 4.3b) and these differences in gravity anomaly generally suggest compositional differences at depth. The Bouguer gravity anomaly around the BMA axis (i.e., around SUR and SA05) is consistent with that estimated by previous studies of Hälbich et al. (1993) who reported the Bouguer gravity to be between -100 and -90 mGal across the BMA. Preliminary Bouguer gravity models by Scheiber-Enslin et al. (2012) shows a Bouguer gravity anomaly within the range of -110 to -70 mGal across the BMA.

4.3 Data processing and methodology

4.3.1 Data

Seismograms recorded by three stations located along the northern branch of the BMA axis were used for this study (Figure 4.2a). A total of 37 teleseismic earthquakes recorded by the

Southern African Seismic Experiment (SASE) network, taken from the original database by Kgaswane et al. (2009), were used to compute high-frequency ($f \leq 1.25$ Hz) receiver functions. The list of teleseismic earthquakes recorded by the three stations are included in Appendix A.

4.3.2 Receiver functions

Receiver functions were computed using the iterative time-domain deconvolution method of Ligorría and Ammon (1999). For each teleseismic event, receiver functions were computed at a frequency band of $f \leq 1.25$ Hz (Gaussian bandwidth of 2.5 s) with a maximum number of 200 iterations. The receiver functions were then binned in ray-parameter groups from 0.04 to 0.049 s/km, 0.05 to 0.059 s/km, and 0.06 to 0.079 s/km for each station.

The purpose of grouping the receiver functions according to ray-parameter bins is to account for the phase move out due to varying incidence angles (Cassidy, 1992; Gurrola and Minster, 1998). The receiver functions were then stacked in bins according to ray-parameter and backazimuth. In this study, high-frequency ($f \leq 1.25$ Hz) receiver functions at different backazimuths for each station were used in the joint inversion procedure in order to image small-scale velocity variations in the upper crust. This approach is identical to Kgaswane et al. (2012) for the study of the Bushveld Complex (see section 3.2.2 and attached paper). Subsequently, both low- and high-frequency receiver functions were included in the joint inversion procedure to verify the reliability of Moho depths estimated using only high-frequency receiver functions. Figure 4.4 shows examples of receiver functions for two stations, illustrating the quality of the data.

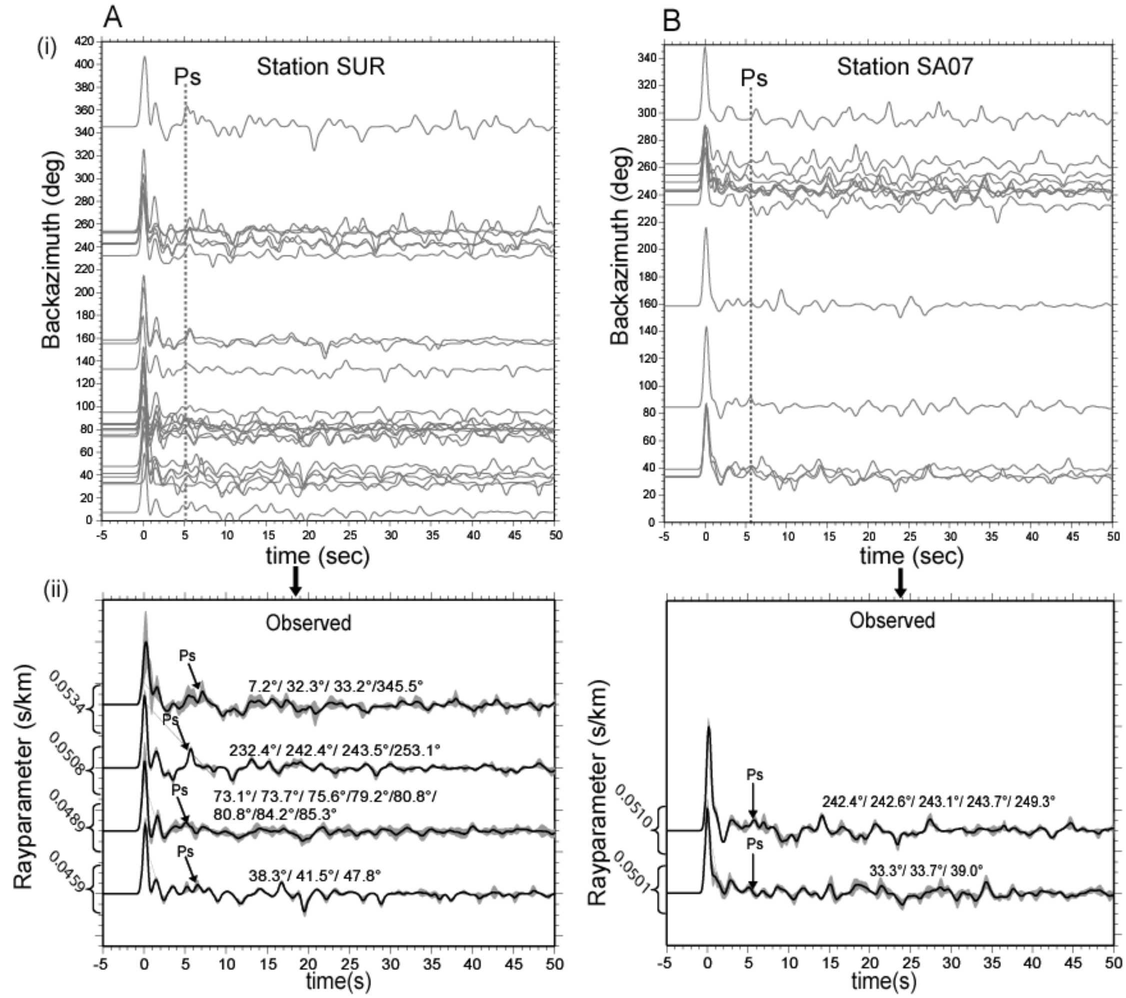

Figure 4.4 Receiver functions at stations SUR and SA07 (columns A and B, respectively). **(i).** Individual receiver functions for each station. The dashed gray lines show the theoretical arrival time of the Moho converted phase (Ps). The theoretical arrival times were computed using the joint inversion code assuming the PREM model and an average crustal thickness of ~42 km. **(ii).** Stacked receiver functions grouped according to ray parameter bins and backazimuth. The gray shading around the observed receiver functions shows 1σ error bounds.

4.3.3 Joint inversion method

The joint inversion approach assumes that the data sets being inverted sample the same part of the Earth structure (Julià et al., 2000). Its advantage lies in providing a model that is consistent with both data sets, benefiting from the ability of the receiver function method to detect relatively abrupt changes in seismic velocity at sub-horizontal boundaries, and the ability of the Rayleigh waves to measure variations in the average seismic velocity with depth (Julià et al., 2000, 2003).

In this study, the joint inversion algorithm has been used to simultaneously invert high-frequency receiver functions and Rayleigh wave group velocities for periods of 10–105 sec to obtain 1-D Vs models for the three stations straddling the BMA. The joint inversion algorithm used in this study is based on the method developed by Julià et al. (2000, 2003) and a detailed description of this method is already provided in section 2.4.2.2 and in two of the attached papers. Rayleigh wave group velocity curves used in this study were taken from recently available Rayleigh wave group velocity tomographic model for the southern and central African region (Raveloson et al., 2012). For each inversion, the influence factor was set to 0.5. A smoothness parameter of 0.1 was used for stations SA05 and SA07, while a smoothness parameter of 0.2 was used for station SUR.

An influence factor of 0.5 equalizes the contribution of the combined misfit from each dataset, and using the smallest possible smoothness parameter results in rougher velocity profiles but with higher resolution. Figure 4.5 shows trade-off curves of (a) waveform misfit versus model roughness and (b) waveform misfit versus model smoothness (i.e. 1/model roughness) for the three stations.

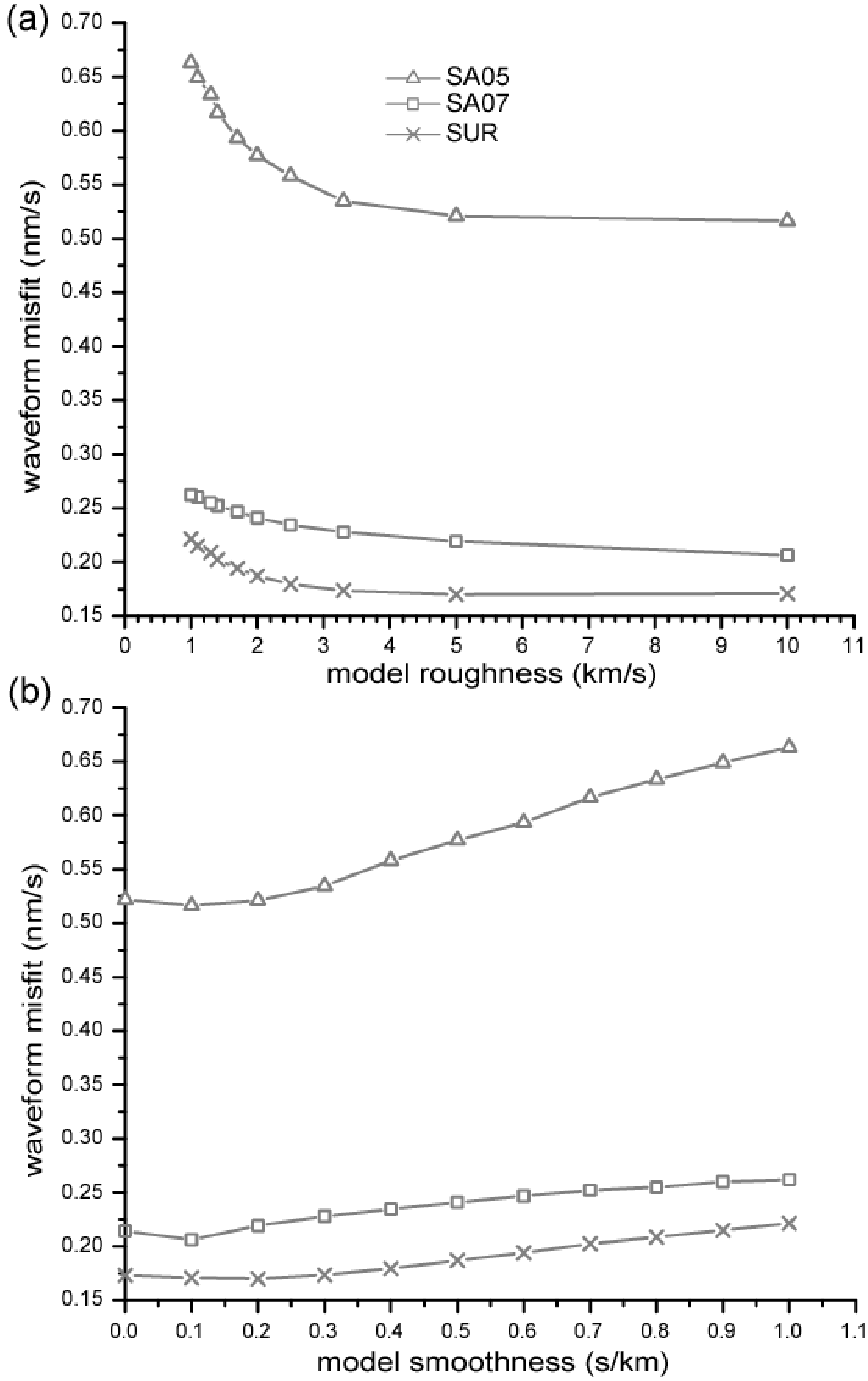

Figure 4.5 Plots of waveform misfit as a function of model roughness and model smoothness (**a** and **b**, respectively) for stations SA05, SA07, and SUR. A single high-frequency receiver function stack in each station has been used for the plots.

Figure 4.5b clearly shows that the chosen smoothness parameters (as indicated above) for the three stations correspond to small waveform misfits and therefore their use in constraining the observations is justified. The starting model used for the inversions is the PREM model (Dziewonski and Anderson, 1981), which was modified for continental structure above 60.5 km depth and further modified for the upper crust above 10 km depth (see Figure 4.6).

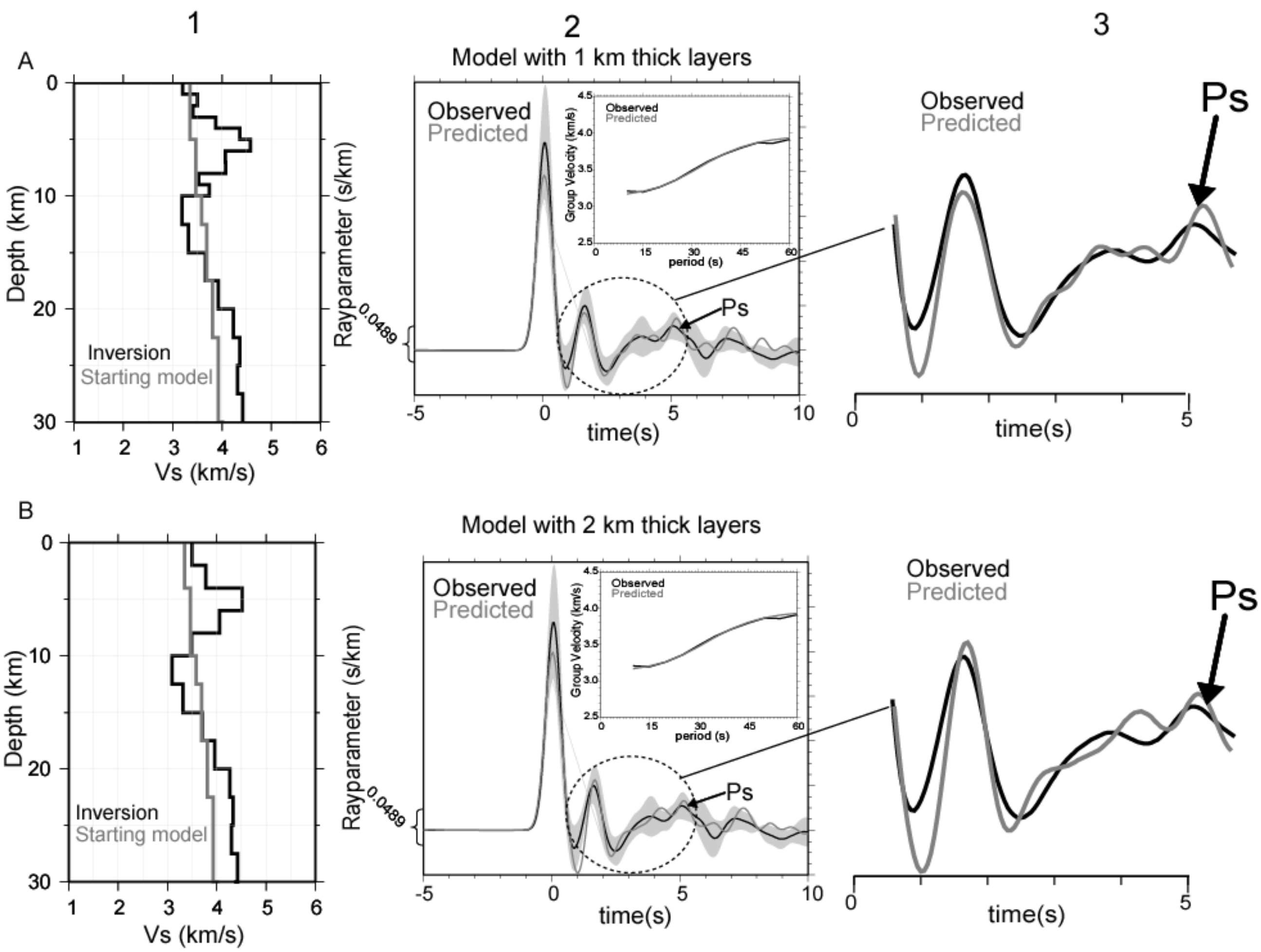

Figure 4.6 Diagram for station SUR illustrating the improved fit to the receiver functions by using 1 km thick layers (column 1 in row A) in the top 10 km of the model versus 2 km thick layers (column 2 in row B). The Ps conversion from the Moho is denoted as “Ps”, and the light gray shading around the observed receiver function shows 1σ error bounds. Column 1 shows the starting model and the inversion results, column 2 shows the fitting of the observed and predicted receiver functions and inset diagrams are the group velocity vs. period curves, and column 3 shows the magnification of the fits in the 0–5 sec domain enclosed by the dashed circles in column 2.

This choice reflects the decrease of resolution with depth in the joint inversion models. The model parameterization consisted of 1-km thick layers to a depth of 10 km, 2.5-km thick layers between depths of 10 to 47.5 km, 5-km thick layers between 47.5 and 242.5 km depth, and 17 to 40-km thick layers below 242.5 km depth. The resolution of the layer thicknesses (Figure 4.6) used in the upper 10 km of the starting model can be demonstrated by comparing two models, one with 1 km thick layers (Figure 4.6a) and the other with 2 km thick layers (Figure 4.6b). Apart from the layer thicknesses, the starting models were identical. The same velocities and densities in each layer were used in both models.

The results in Figure 4.6a shows that the model with 1 km thick layers produces a better fit to the observed receiver functions within the 2–5 sec window (dashed circles). There is little difference in the fit of the group velocity dispersion curves (inset diagrams) in column 2 of Figure 4.6. Therefore, the starting model as used for the joint inversions is appropriate. However, it should be noted that the Vs models for the upper 10 km of the crust are not as well resolved as those obtained for the Bushveld Complex (see Chapter 3) by Kgaswane et al. (2012), simply because there are no group velocity observations at periods shorter than 10 sec (corresponding to depths shallower than approximately 10 km). Therefore it can be assumed in this case that the constraints on the velocity structure in the upper 10 km crust are mostly due to the receiver functions.

The choice of 1 km thick layers in the upper 10 km crust is further justified by interpretations of geology (e.g. Johnson et al., 2006) and the reflection seismic profiles (e.g. Lindeque et al., 2007, 2011; Loots, 2012) which indicate that the major layers of the Karoo Supergroup (e.g. Ecca, Beaufort) have thicknesses ≥ 1 km in the vicinity of the three seismic stations used in this study. The Dwyka Group at the base of the Karoo Supergroup is less than 1 km thick, and therefore cannot be resolved in this study. The Cape Supergroup has composite layering with a total thickness of ±1.5 km in the vicinity of the three stations and gets progressively thicker southward towards the CFB.

The uncertainties in the 1-D Vs models can be determined by following an approach proposed by Julià et al. (2005), whereby inversions are repeated, each time varying the weighting parameters, constraints, and Poisson's ratio. By repeating the inversions for many combinations of model parameters and data, we obtain uncertainties of 0.1–0.2 km/s for the velocities in each layer, which translates into uncertainties of ~2–3 km in the depth of intracrustal boundaries, and uncertainties of no more than 5 km in Moho depth.

4.4 Results

The joint inversion results were generated using Rayleigh wave group velocity curves in the period range of 10–105 sec. The 10–60 sec region of the group velocity dispersions are most relevant for the crust and therefore the results shown in Figures 4.7a and b have only displayed the group velocity dispersions up to 60 sec.

4.4.1 Upper crust

Figures 4.7a and b show the full joint inversion results for the three stations in the NNB (SA07, SUR, SA05). Figure 4.7a shows joint inversion results involving only high-frequency receiver functions at discrete backazimuths whereas Figure 4.7b shows joint inversion results involving combined low- and high-frequency receiver functions. The purpose of using only high-frequency receiver functions (as indicated in Figure 4.7a) is to constrain small-scale velocity variations and to observe the magnitude of these velocity variations with varying azimuth. Table 4.2 provides a summary of the shear wave velocities and other crustal parameters for the three stations. The symbols a, b, c, and d in rows (i) of Figures 4.7a denote average backazimuths for the different backazimuth bins indicated above the receiver functions in row (ii) of both figures. The average backazimuths for each of the stations are also indicated in Table 4.2.

Overall, the results in Table 4.2 indicate average Vs of 2.9–3.6 km/s in the depth interval of 1–5 km beneath the three stations, with the Vs profiles for both SUR and SA05 indicating faster velocities at certain backazimuths. In contrast, at depths of 5–10 km the Vs profiles for all three stations tend to show average velocities ≥ 3.5 km/s. The depth of 5 km was selected because it more or less represents a mid-point within the upper crust and it is also the approximate base of the supracrustal sediments. Therefore, it was selected to see if there is a contrast in the average Vs between layers in the 1–5 km depth range and those in the 5–10 km depth range for each of the three stations. At all three stations high velocity layering (≥ 3.5 km/s) starts around 5 km depth and velocities in the range 3.5–4.0 km/s continue between depths of ~10–20 km (see Figure 4.7a). However, as already indicated in section 4.3.3, there could be an uncertainty of ±2 km associated with the depths as indicated above. The upper crustal variability (shown in both Figure 4.7 and Table 4.2) is further examined in detail in section 4.5.

4.4.2 Lower crust

All three stations show a predominantly high-velocity lower crust (Vs ≥ 4.0 km/s) below 20 km depth (see Figure 4.7a and Table 4.2). The high velocity layers (≥ 4.0 km/s) occupy a substantial part of the lower crust, with thicknesses well over 10 km. The crustal thickness beneath each station was determined by picking the Moho at the depth where Vs exceeds 4.3 km/s (e.g. Christensen and Mooney, 1995; Christensen, 1996; Kgaswane et al., 2009). Vs profiles for a few backazimuths at stations SUR and SA05 show two Moho depths where there is an increase in shear wave velocity above 4.3 km/s, with a region of velocity less than 4.3 km/s in between. This high-low-high velocity structure for these few stations is indicated in Figure 4.7a by showing the first increase in velocity above 4.3 km/s with a dotted line and the second increase with a solid line. Stations or backazimuths with two Moho depths have been excluded from the interpretation of crustal thickness.

To test whether the use of high-frequency receiver functions produced a reasonable estimate of the crustal thicknesses (shown in second column of Tables 4.3 and Figure 4.7a), shear wave velocity models were estimated for the same stations with both the low- and high-frequency receiver functions included in the joint inversion (see Figure 4.7b). The results of these estimates are shown in the third column of Table 4.3. Low-frequency receiver functions have longer wavelengths and therefore their inclusion in the inversion allows for a better estimate of the average background velocity of the underlying structure (e.g. Julià, 2007). The Moho estimates for stations SA05 and SUR show that there is a difference (> 3 km) between those of Kgaswane et al. (2009) and the rest (see Table 4.3). The reason for this disparity, which is significant for SA05 (> 10 km), is primarily due to the fact that the Rayleigh wave group velocity dispersions used by Kgaswane et al. (2009) were not as well resolved as the ones used in this study.

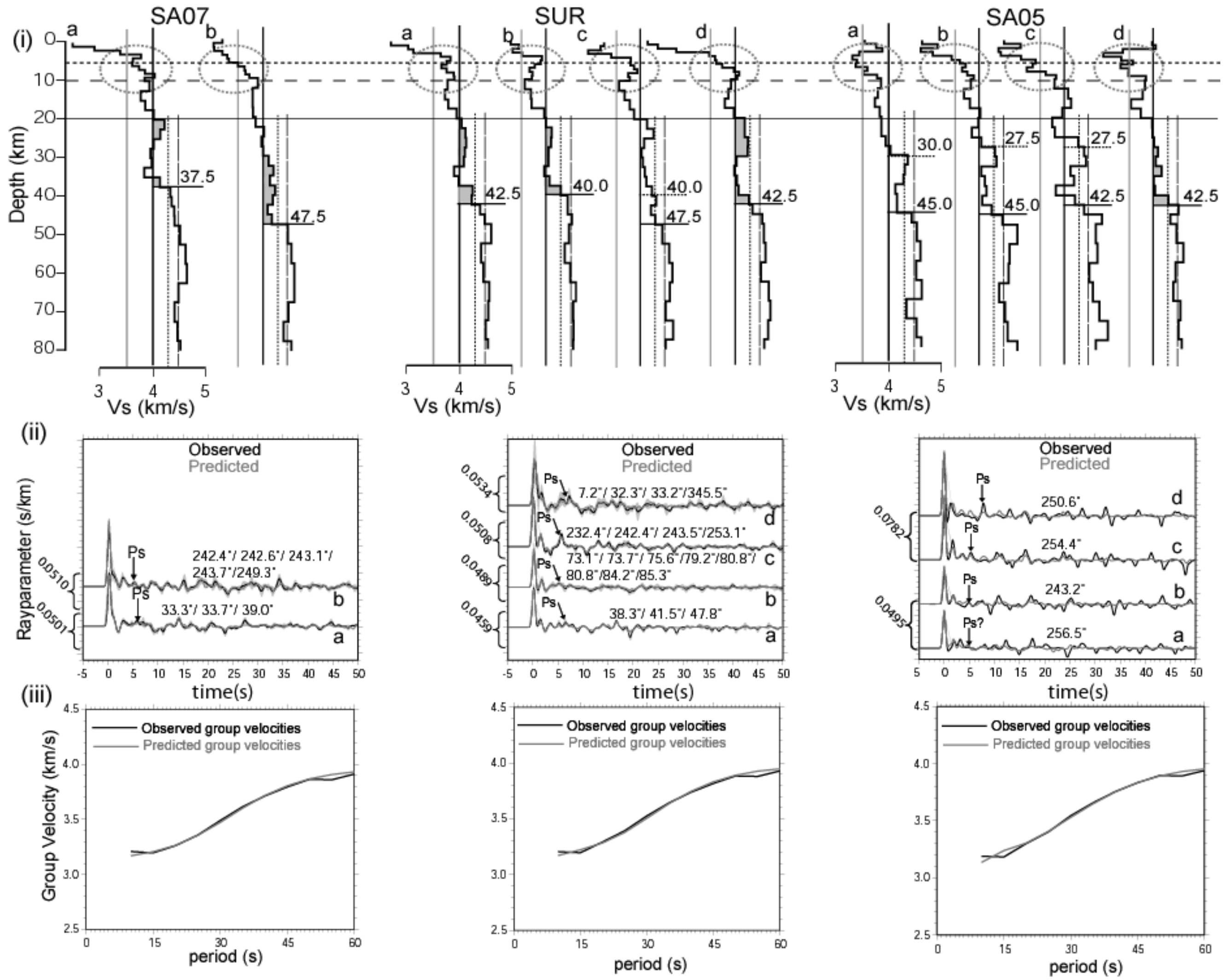

Figure 4.7a Joint inversion results involving only high-frequency receiver functions at discrete backazimuths for each of the three stations used in the study. **(i).** Shear wave velocity profiles obtained from the joint inversion. The dotted, dashed and solid horizontal lines across the three stations mark 5, 10 and 20 km depths, respectively. Lower crustal depths with Vs ≥ 4.0 km/s are shaded and vertical reference lines at 3.5 km/s (gray solid), 4.0 km/s (solid), 4.3 km/s (dotted), and 4.5 km/s (dashed) are shown in each profile. Stations without shading show two Moho depths and indicate two increases above 4.3 km/s on the Vs profiles. **(ii).** Observed (black curves) and predicted (light-gray curves) high-frequency receiver functions with 1σ error bounds shown with gray shading around the observed receiver functions. The backazimuths of the receiver functions within each stack are shown on top. **(iii).** Observed (black curves) and predicted (gray curves) group velocities.

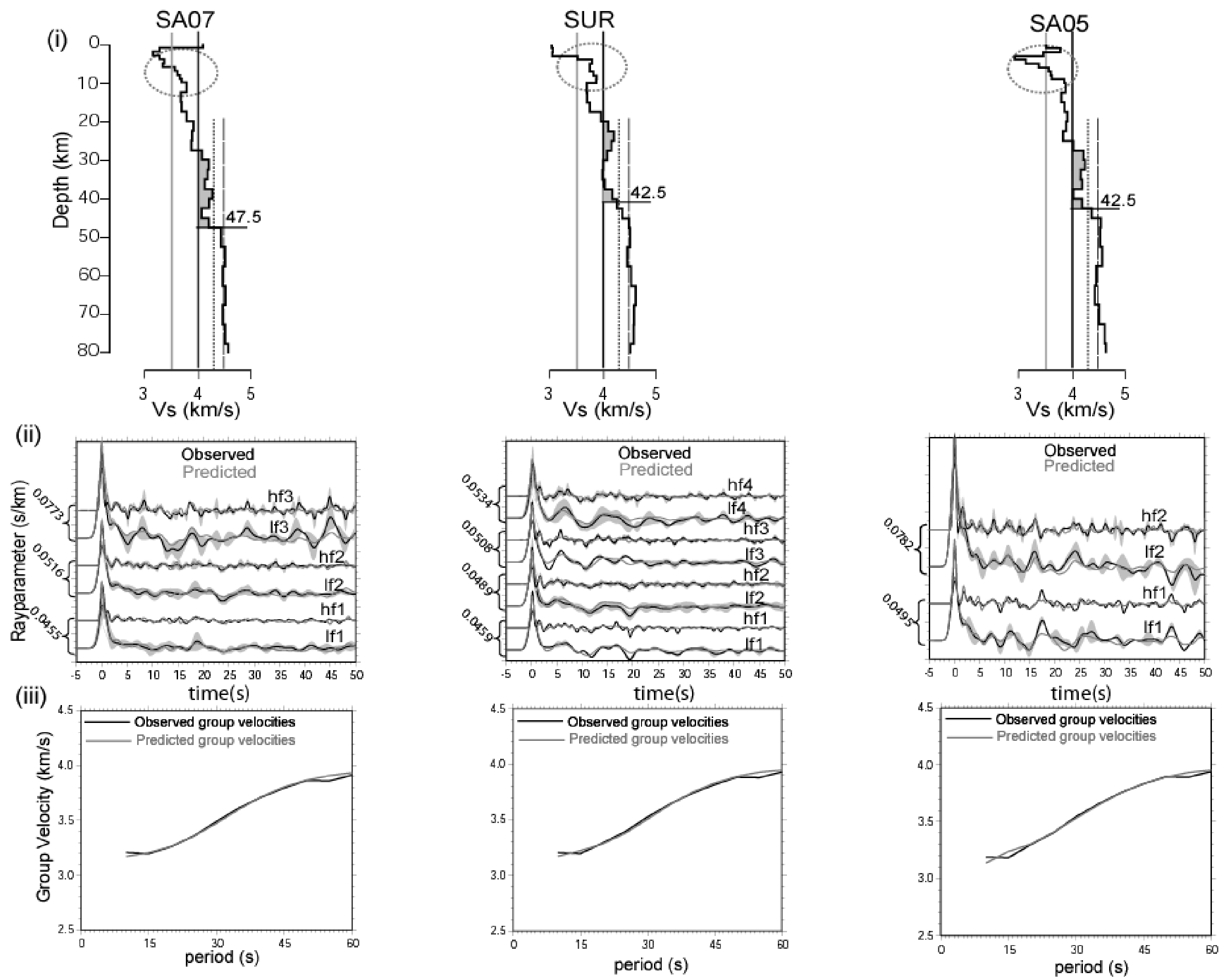

Figure 4.7b Joint inversion results involving both low- and high-frequency receiver functions at an average backazimuth for each of the three stations in Figure 4.6a. The symbols lf1,…,lfn and hf1,…,hfn shown in **(ii)** denote low- and high-frequency receiver functions stacked according to ray-parameter, respectively.

Table 4.2 Summary of crustal parameters shown in Figures 4.7a

Station	Back-azimuth (deg)	Vs (1 – 5 km depth) ± Std. deviation (km/s)	Vs (5 – 10 km depth) ± Std. deviation (km/s)	Vs (10 – 20 km depth) ± Std. deviation (km/s)	Vs below 20 km depth ± Std. deviation (km/s)	Crustal thickness (km)	Thickness of layers with Vs ≥ 4.0 km/s (km)	Average Vs below 20 km depth ± Std. deviation (km/s)	Average Vs below 30 km depth ± Std. deviation (km/s)	Average Crustal thickness (km)	Average thickness of layers in the lower crust with Vs ≥ 4.0 km/s (km)
SA07	35.3°	3.1 ± 0.6	3.8 ± 0.2	3.6 ± 0.2	4.0 ± 0.1	37.5	18	4.1 ± 0.1	4.1 ± 0.2	42.5	21
	244.2°	3.2 ± 0.1	3.7 ± 0.2	3.5 ± 0.1	4.1 ± 0.1	47.5	23				
SUR	42.5°	3.2 ± 0.5	3.8 ± 0.1	3.6 ± 0.2	4.1 ± 0.1	42.5	25	4.1 ± 0.1	4.1 ± 0.1	41.7	24
	79.1°	3.5 ± 0.2	3.7 ± 0.1	3.5 ± 0.2	4.1 ± 0.1	40.0	23				
	242.9°	3.3 ± 0.3	3.8 ± 0.1	3.5 ± 0.2	–	40.0(47.5)	–				
	21.8°	3.0 ± 0.6	3.9 ± 0.2	3.7 ± 0.2	4.1 ± 0.1	42.5	25				
SA05	256.5°	3.6 ± 0.2	3.6 ± 0.2	3.8 ± 0.0	–	30.0(45.0)	–	4.1 ± 0.1	4.1 ± 0.1	42.5	23
	243.2°	3.1 ± 0.2	3.7 ± 0.1	3.9 ± 0.1	–	27.5(45.0)	–				
	254.4°	2.9 ± 0.2	3.5 ± 0.2	4.0 ± 0.1	–	27.5(42.5)	–				
	250.6°	3.5 ± 0.4	3.6 ± 0.2	3.7 ± 0.1	4.1 ± 0.1	42.5	23				

N.B. *Instances with two values in the crustal thickness column indicate two increases above 4.3 km/s on the Vs profiles..*

Table 4.3 Comparison of crustal thicknesses with other studies

Station	Average crustal thickness from this study using only high-frequency RF's (km)	Crustal thicknesses from low- and high-frequency RF's (km)	Harvey et al. (2001) (km)	Nguuri et al. (2001, 2004) (km)	Nair et al. (2006) (km)	Kgaswane et al. (2009) (km)
SA07	42.5	47.5	41 – 46	42.8	46.2	–
SUR	43.1	42.5	42 – 46	38.8	49.2	35.5
SA05	42.5	42.5	40 – 45	40.1	44.1	25.5

N.B. *RF's denote receiver functions*

Otherwise, for the rest of the Moho estimates, Table 4.3 shows that there are minor or insignificant Moho differences (< 5 km) between this study and those of other studies by Harvey et al. (2001), Nguuri et al. (2001), and Nair et al. (2006). Furthermore, Table 4.3 shows that there are insignificant differences in Moho estimates obtained by using only high-frequency receiver functions and using both low- and high-frequency receiver functions in the joint inversion procedure. The shear wave velocities for the uppermost mantle region i.e., Moho–60 km depth (Figures 4.7a and b), are between 4.5 – 4.7 km/s and this is consistent with the findings indicated in Chapter 2 and findings from a recent study (Adams and Nyblade, 2011).

4.5 Discussion and interpretation

The main findings of this study are:

- **a)** high Vs crustal layers between 3.5–4.0 km/s in the 5–10 km depth range at all backazimuths across all the three stations along the northern axis of the BMA (Table 4.2 and Figure 4.7a),
- **b)** crustal layers with Vs fluctuating between 3.5 and 4.0 km/s (i.e., low-to-high or high-low-high) within depths of ~10–20 km (Figure 4.7a), and
- **c)** high velocity layers (≥ 4.0 km/s) beneath the stations occupying a substantial portion of the lower crust (below 20–30 km depths) and a crust with an average thickness greater than 40 km (Table 4.2 and Figure 4.7a).

The high velocity zones within 5–10 km depths appear quite prominently beneath SUR and SA05 and are indicative of anomalous crust and the presence of mafic lithologies. A typical upper crust in normal tectonic settings will show velocities of ~3.5 km/s at similar depths and therefore the high-velocity zones beneath the three stations could be delineating a BMA source body. The velocities tend to approach 4.0 km/s around depths of 10 km for all three stations and this could mean that the BMA body (or its crustal host) becomes more mafic in composition at depths around 10 km. The velocities tend to show some fluctuation (i.e., low-to-high or high-low-high) below 10 km depth and therefore, this depth could be the base of the BMA body (or its crustal host) or marks a compositional transition. The BMA body (or its crustal host) might continue in another compositional form between depths of 10–20 km. The crust beneath the three stations is on average thicker than 40 km, and, similar to the Bushveld Complex, it is possible that the presence of mafic bodies (including the BMA) in the upper and middle crustal parts of the NNB are isostatically compensated by a thick crust. Perhaps this is more so around SA07 than the other two stations.

The receiver functions for each of the stations SA07, SUR, and SA05 (shown in Figures 4.8i–iii) are likely sampling different lithologies (i.e., alluvial deposits, Karoo sediments, and dolerites) depending on azimuth and depth. The Ps conversion points at A, B, C, and D in each of the maps in Figure 4.8 were computed from averages of the backazimuths shown in Figure 4.7a(ii). The Vs profiles for SA07 at backazimuths (a) and (b) (Figure 4.7a) correspond to the conversion points at A and B respectively in Figure 4.8(i), and similarly for the other two stations. The Ps conversions are shown at 5 and 10 km depths in Figure 4.9.

Figure 4.9 is a close-up view (within 9 x 9 km^2 grids) of the magnetic field anomaly shown in Figure 4.3. The magnetic field in Figure 4.9 is unfiltered but has been IGRF (International Geomagnetic Reference Field) corrected for the 1975 magnetic epoch (IAGA, 1975). The spatial correlation between the amplitude of the magnetic field and magnetization is complex and depends on a number of factors or parameters. However, it can be noted from Figure 4.9

that the varying magnetization signatures around each of the three stations are most probably reflecting the presence and the geometrical orientation of the BMA body at crustal depth beneath each of the three stations.

The Ps conversion points (at 5 and 10 km depths) around SUR and SA05 appear to sample a higher intensity of the magnetization (i.e., remanence) whereas the Ps conversion points around SA07 are sampling moderate intensity of magnetization (Figure 4.9). Figure 4.9 shows the Ps conversion points around SUR at backazimuths (b) and (c) sample a region of higher intensity magnetization, and this may imply that the BMA body is shallower south of SUR and deeper north of it.

The geometry of the BMA body at depth is not clear around SA05 since the Ps conversions around this station tend to sample the same intensity of magnetization and are concentrated southwest of the station. The BMA body is probably shallower south of SA07 than north of it. In a more rigorous sense, the depth of the BMA source or sources from the observed magnetic field (Figure 4.9), can be obtained by separating the regional (associated with deep-lying magnetic sources) and residual (associated with shallow magnetic sources) field. The separation can be achieved using several methods (e.g. analytic signal, upward continuation differencing, matched filtering techniques, and wavelet transforms). Matched bandpass filtering techniques (e.g. Spector and Grant, 1970; Syberg, 1972; Phillips, 2001; Sheriff, 2010) have been mostly applied due to their versatility in handling a number of geological models or situations.

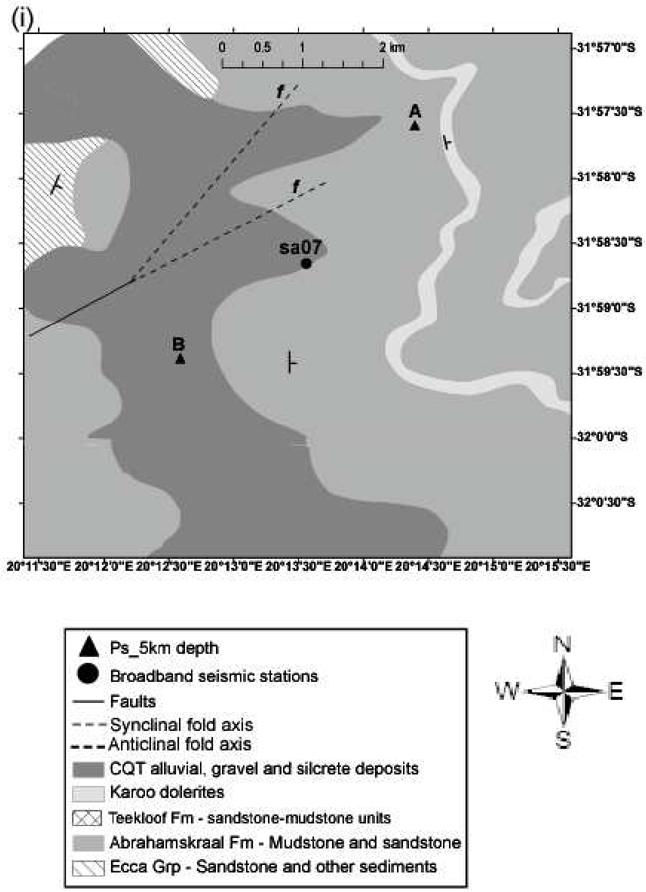

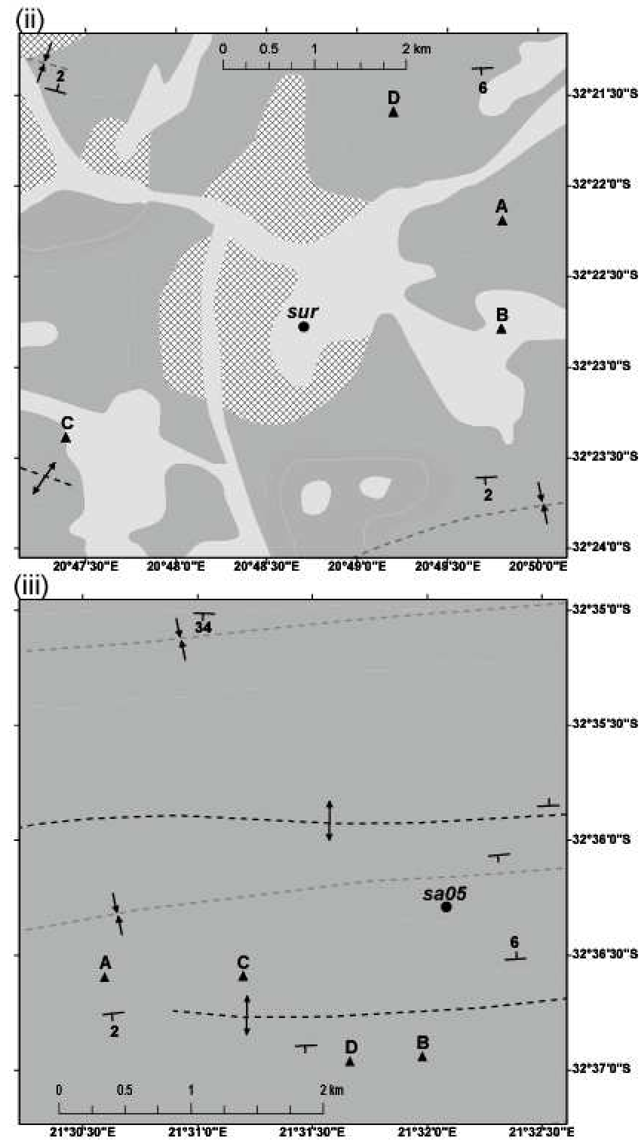

Figure 4.8 Maps (i – iii), each showing a close-up view of the local surface geology around the three broadband stations SA07, SUR, and SA05 and the average Ps conversion points at 5 km depth at different backazimuths (A, B, C, and D). The maps have been modified from the 1:250,000 geology map of South Africa.

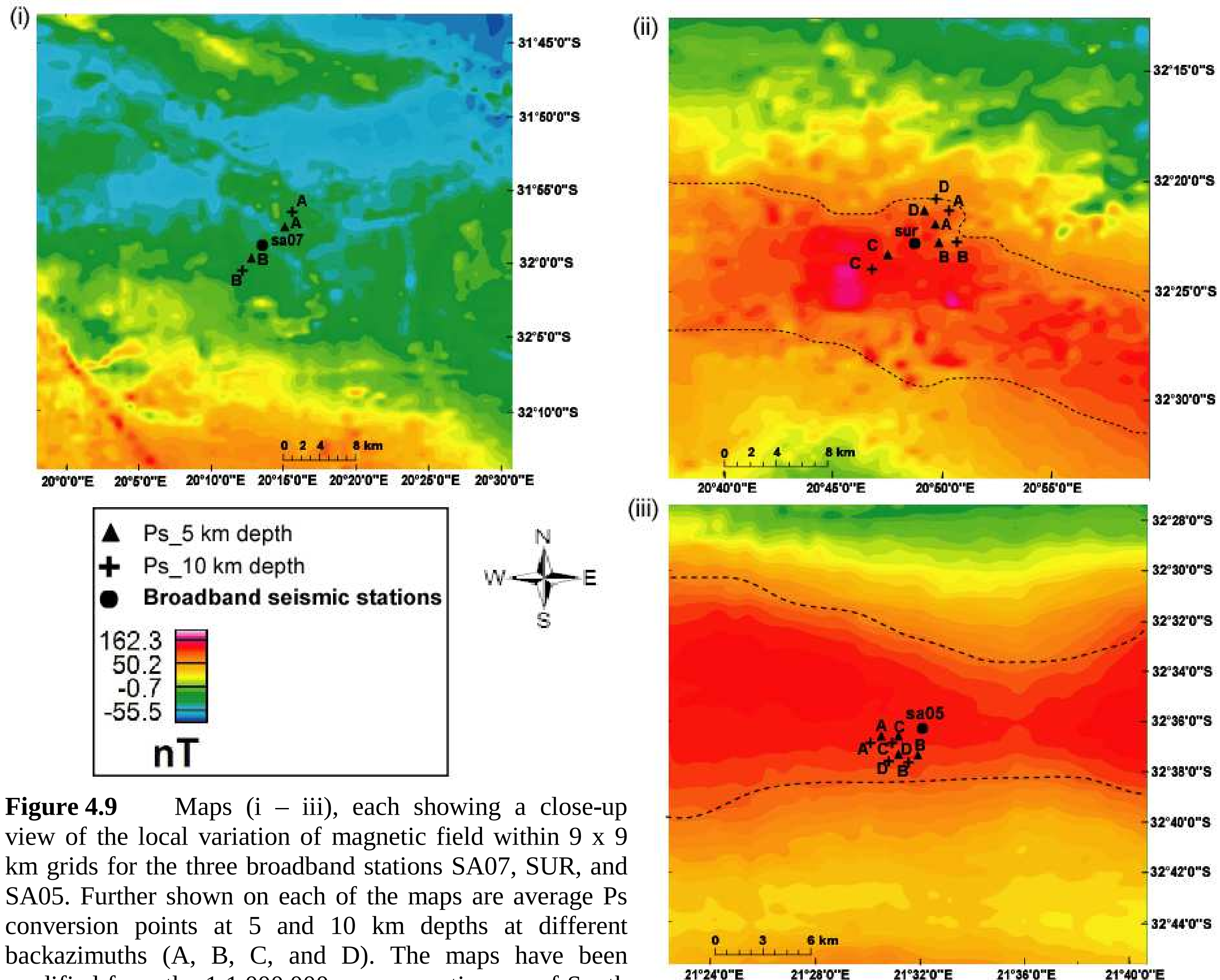

Figure 4.9 Maps (i – iii), each showing a close-up view of the local variation of magnetic field within 9 x 9 km grids for the three broadband stations SA07, SUR, and SA05. Further shown on each of the maps are average Ps conversion points at 5 and 10 km depths at different backazimuths (A, B, C, and D). The maps have been modified from the 1:1,000,000 aeromagnetic map of South Africa. The dashed lines around SA05 and SUR encloses the BMA maxima. See text for further explanation.

Prior to bandpass filtering, the regional trend associated with the geomagnetic field needs to be removed from the observed field. In addition, the observed field has to be decorrugated (i.e., removal of short wavelength features causing corrugations) and reduced to the magnetic pole. Matched bandpass filtering involves fitting a radially averaged logarithmic power spectrum of the observed magnetic field (vertical axis) versus wavenumber (horizontal axis) with power spectra corresponding to regional and residual magnetic anomalies (equivalent source layers) at different depths (e.g. Sheriff, 2010). The filter i.e., *F(k)* required to separate the effect of shallow anomalies from the deep ones could be in the form:

$$F(k) = 1 \Big/ \left(1 + \left(c_2 / c_1\right) exp\left(\left(d_1 - d_2\right)k\right)\right) \qquad (4\text{-}2)$$

where k is the wavenumber; c_1 and c_2 are scaling constants of the amplitude spectrum related to shallow and deep-seated anomalies, respectively; and d_1 and d_2 are apparent depths of the shallow and deep-seated anomalies, respectively. The separation of the regional and residual field is achieved by multiplying the Fourier spectrum of the observed magnetic field with the filter shown in equation (4-2) and the product is inversely Fourier transformed to attain the separation of the two fields (e.g. Sheriff, 2010).

The findings and observations indicated above are used to evaluate the merits of the geophysical models of the BMA. The Vs findings are firstly used to estimate the elastic parameters using seismic and geological constraints.

4.5.1 Estimation of elastic parameters using seismic and geological constraints

As already pointed out in the introduction (section 4.1), there are numerous and varied interpretations as to the crustal source of the BMA. Apart from the fact that different methodologies have been used to study the BMA, an obvious difference in the results between this study and most of the studies indicated in section 4.1 is that the latitudinal extent of the BMA could not be constrained and as such, the BMA width could not be estimated in this study. The other difference is in the orientations of the study profiles (see Figure 4.1).

Although the orientations of the profiles by the other studies are different from the nearly east-west oriented profile that this study is focusing on, the structural trends across and along the BMA axes are similar or should be similar. Figure 4.10 shows a comparison of the joint inversion results from this study and the results from some of the recent studies. The joint inversion results are, in this case, combined high-frequency receiver functions (i.e., stacks of each ray parameter bin) and Rayleigh wave group velocities (10–60 sec period) (column A in Figure 4.10) and density as a function of depth (column B in Figure 4.10) for the three stations. Column C (in Figure 4.10) shows seismic and geophysical results from other studies.

The modelling results by Stankiewicz et al. (2008) shows a high-velocity body (between 50 and 100 km distance) within depths of ~7–15 km and it coincides with the northern prism modelled by Quesnel et al. (2009). This body has P-wave velocities of ~6.5–7.0 km/s (i.e., Vs ~ 3.8–4.0 km/s). These velocities are consistent with the Vs estimates in this study (Table 4.2, Figure 4.7a and column A in Figure 4.10) which indicate a high-velocity layering of 3.5–3.9 km/s at depths of ~5–10 km and ~10–20 km beneath the three stations.

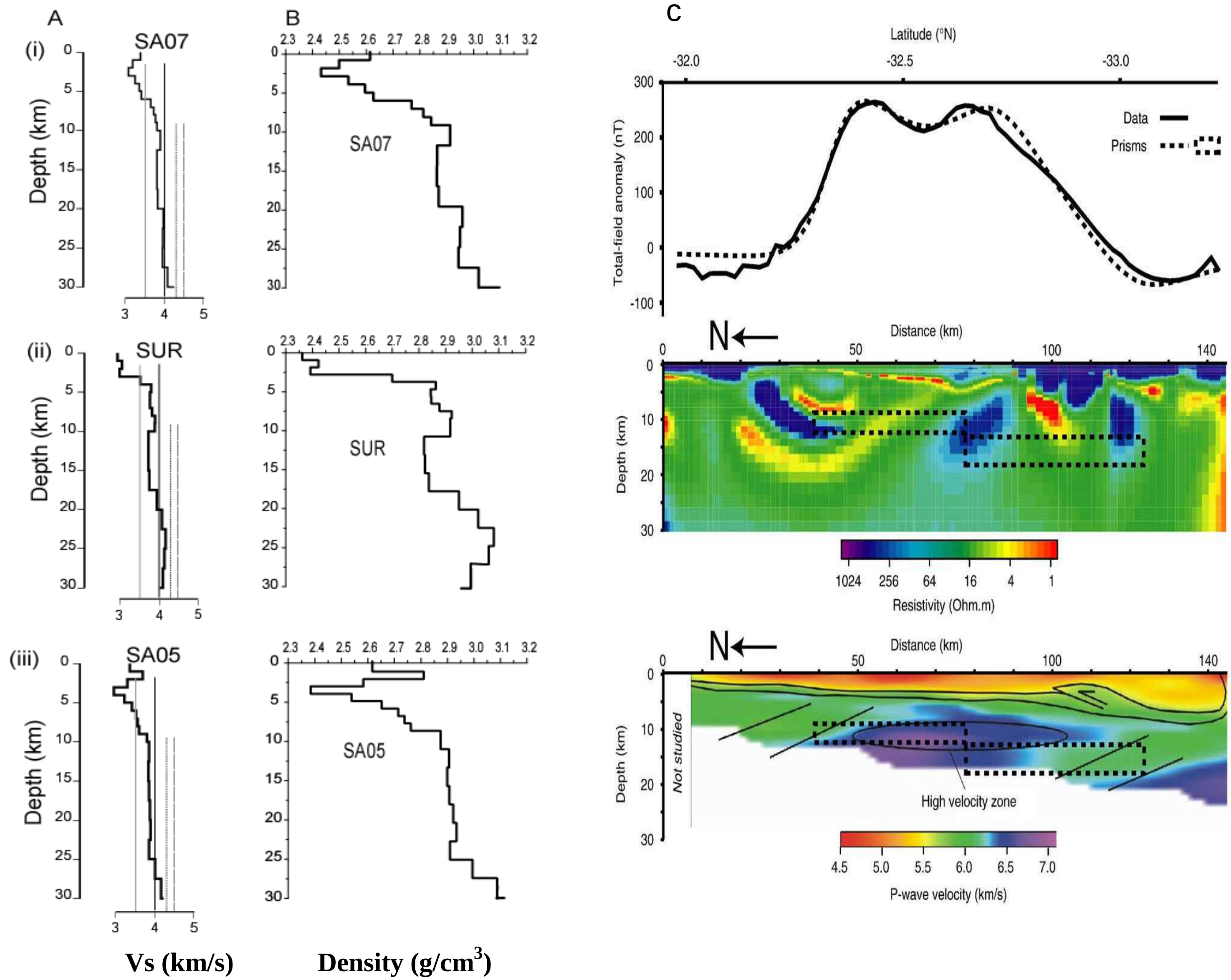

Figure 4.10 **A.** Joint inversion results for stations (i). SA07, (ii). SUR, and (iii). SA05. The vertical reference lines have already been explained in Figure 4.7a. **B.** Density estimates as a function of depth obtained from the joint inversions associated with the velocity models shown in column A. **C.** Seismic and geophysical modelling results from other studies. The upper panel shows modelling by Quesnel et al. (2009) with the magnetic field anomaly from the double-prism model (dashed black rectangles superimposed on the lower panels) matching the observed anomaly. The central panel is the conductivity model from Weckmann et al. (2007a) and the lower panel is the seismic refraction tomography image from Stankiewicz et al. (2007, 2008). The diagram on the right has been reproduced from Quesnel et al. (2009).

Considering that there is consistency in the velocity estimates of the crustal layering around the BMA between this study and Stankiewicz et al. (2008), the Vp estimates from Stankiewicz et al. (lower panel of column C in Figure 4.10) are therefore used as a constraint in determining the rock types within the upper and middle crustal structure around the BMA. In achieving this, the Vp estimates and together with the joint inversion results (Vs and density) from this study, have been used to determine elastic parameters (i.e., Vp/Vs, Poisson's ratio). The Vp estimates from Stankiewicz et al. (2008) have been used because they are much better resolved than the Vp estimates from the joint inversion results.

Table 4.4 shows estimates of elastic parameters (i.e., Vp/Vs, Poisson's ratio, and density) together with resistivity estimates from Weckmann et al. (2007a,b) beneath stations SUR and SA05 following the comparisons made in Figure 4.10. Further shown in Table 4.4 are estimates for SA07 included as a benchmark for areas that spatially coincide with moderate to low intensity of magnetization associated with the BMA (see Figure 4.9). The Vp–depth estimates for the crustal portion between distances of 50 and 100 km (as indicated in the bottom panel of column C of Figure 4.10) were used for the elastic estimates for SUR and SA05 since these stations are located above or near the BMA. Furthermore, the interpretation by Stankiewicz et al. (2008) (as suggested in Figure 4.10) shows the subsurface location of the BMA body to be at those distances. The Vp–depth estimates for the portion of the crust between distances of 0 and 50 km (as indicated in the bottom panel of column C in Figure 4.10) could be assumed to be representative of an area similar to that beneath SA07 since this station is located ±20 km north of the BMA axis. The resultant estimates shown in Table 4.4 assume that the structural trends across and along the BMA axes (at least within the Namaqua sector of the NNB) are similar given that the study profile by Stankiewicz et al. (2007, 2008) is different from the nearly east-west oriented profile adopted in this study (see Figure 4.2a).

Table 4.4 Physical parameters beneath stations SUR, SA05 and SA07

Depth (km)	**Vp/Vs beneath SUR**	**Vp/Vs beneath SA05**	**Vp/Vs beneath SA07**	**Poisson's ratio beneath SUR**	**Poisson's ratio beneath SA05**	**Poisson's ratio beneath SA07**	**Density (g/cm^3) beneath SUR**	**Density (g/cm^3) beneath SA05**	**Density (g/cm^3) beneath SA07**	**Resistivity (Ω.m)**
0 – 2.5	1.65	1.43	1.43	0.21	0.02	0.02	2.36	2.62	2.61	4 – 16
2.5 – 5.0	1.59	1.68	1.88	0.17	0.20	0.30	2.60	2.50	2.47	≤ 2
5.0 – 7.5	1.65	1.86	1.82	0.21	0.30	0.29	2.87	2.63	2.59	4 – 16
7.5 – 10.0	1.69	1.78	1.73	0.23	0.27	0.25	2.90	2.80	2.77	4 – 16
10.0 – 12.5	1.84	1.83	1.70	0.29	0.29	0.23	2.88	2.89	2.84	≥ 16
12.5 – 15.0	1.88	1.82	1.66	0.30	0.28	0.21	2.83	2.91	2.91	~ 16
15.0 – 17.5	1.81	1.76	1.69	0.28	0.26	0.23	2.84	2.90	2.86	≥ 16
17.5 – 20.0	1.80	1.75	1.72	0.28	0.26	0.25	2.85	2.91	2.87	≥ 16
20.0 – 22.5	1.76	1.74	1.78	0.26	0.25	0.27	2.90	2.92	2.96	≥ 16

N.B. *The resistivity values on the last column are from Weckmann et al. (2007a,b) and they have been picked between distances of 60–70 km (central panel in column C of Figure 4.10) which coincide with the high velocity body occurring between 7 and 15 km depth on Stankiewicz et al. (2008) model (lower panel in column C of Figure 4.10).*

Figure 4.11 shows conceptual models (in column A) illustrating the lithostratigraphy beneath SA07, SUR and SA05 using the elastic parameters indicated in Table 4.4. Table 4.5 shows the names and velocities of the lithologies in column A of Figure 4.11. The lithostratigraphic models (shown in Figure 4.11) have been compiled by correlating the estimates of elastic parameters (shown in Table 4.4) with results from laboratory or petrophysical studies (e.g. Christensen, 1996; Christensen and Stanley, 2003).

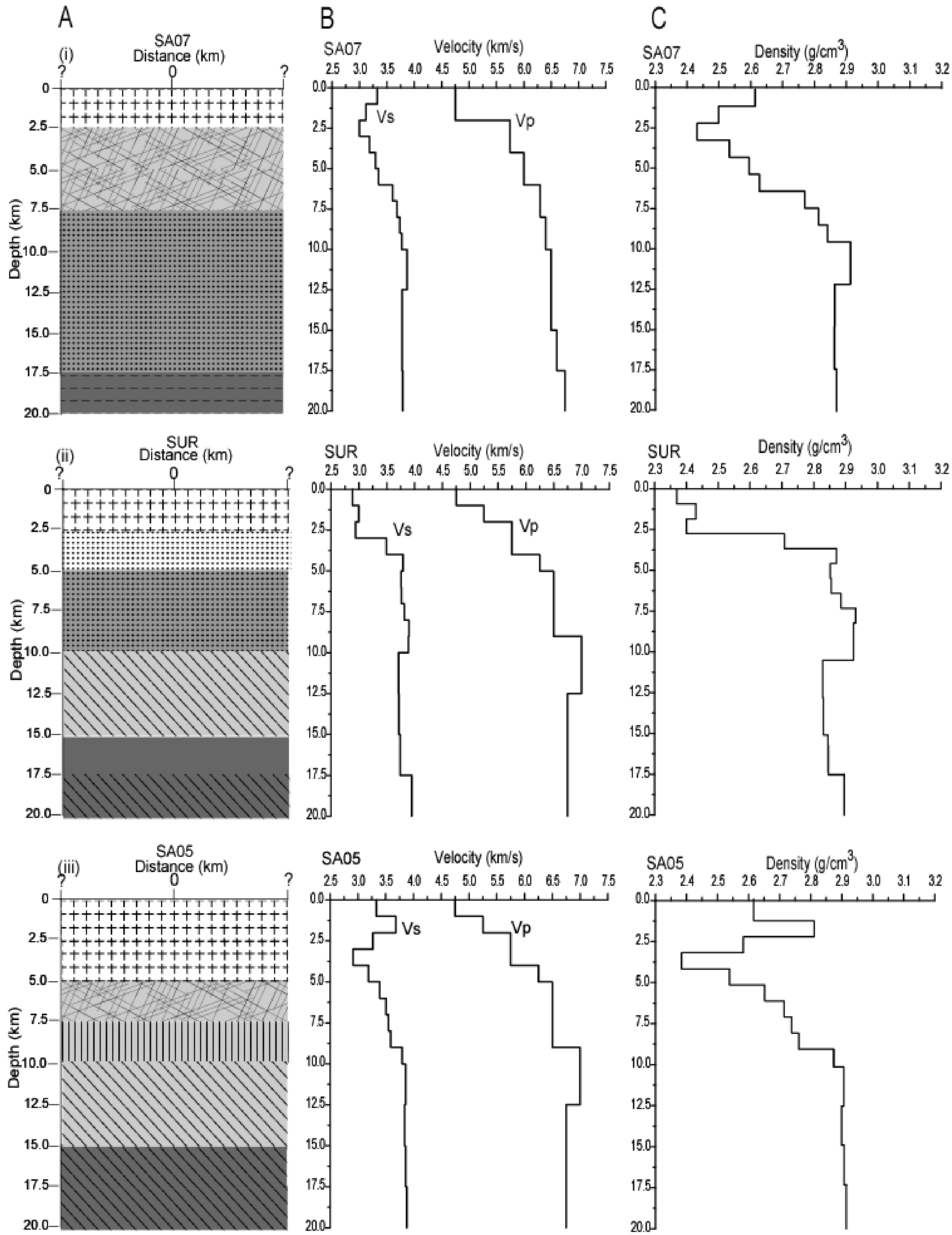

Figure 4.11 **A.** Conceptual models illustrating probable lithostratigraphy beneath the three stations, **(i).** SA07, **(ii).** SUR and **(iii).** SA05. **B.** Velocity, and **C.** Density models (shown up to 20 km depth). The velocity and density models shown in columns B and C have been used to compile the lithostratigraphy down to 20 km depth beneath the three stations in column A. The legend is shown in Table 4.5.

Table 4.5 Names of lithologies shown in column A of Figure 4.12. The Vs ranges associated with each of the lithologies are also indicated.

Sediments (Karoo Supergroup) + Quartzites (Cape Supergroup) (Vs~ 2.8 - 3.4 km/s)	
Slate and/or schist and/or phyllite? (NNB crust) (Vs~ 3.2 - 3.3 km/s)	
Granite (NNB crust) (Vs~ 3.3 - 3.5 km/s)	
Granite gneiss and/or biotite gneiss and/or Greenschist facies basalt (NNB crust) (Vs~ 3.5 - 3.9 km/s)	
Amphibolite (NNB crust) (Vs~ 3.7 - 3.9 km/s)	
Felsic granulite (NNB crust) (Vs ~ 3.6 - 3.7 km/s)	Possible source of the BMA
Anorthosite or Anorthositic granulite (NNB crust) (Vs~ 3.7 - 3.8 km/s)	Possible source of the BMA
Mafic granulite (NNB crust) (Vs~ 3.8 - 3.9 km/s)	Possible source of the BMA
Mafic granulite? + ultramafic rocks (NNB crust) (Vs > 3.9 km/s)	

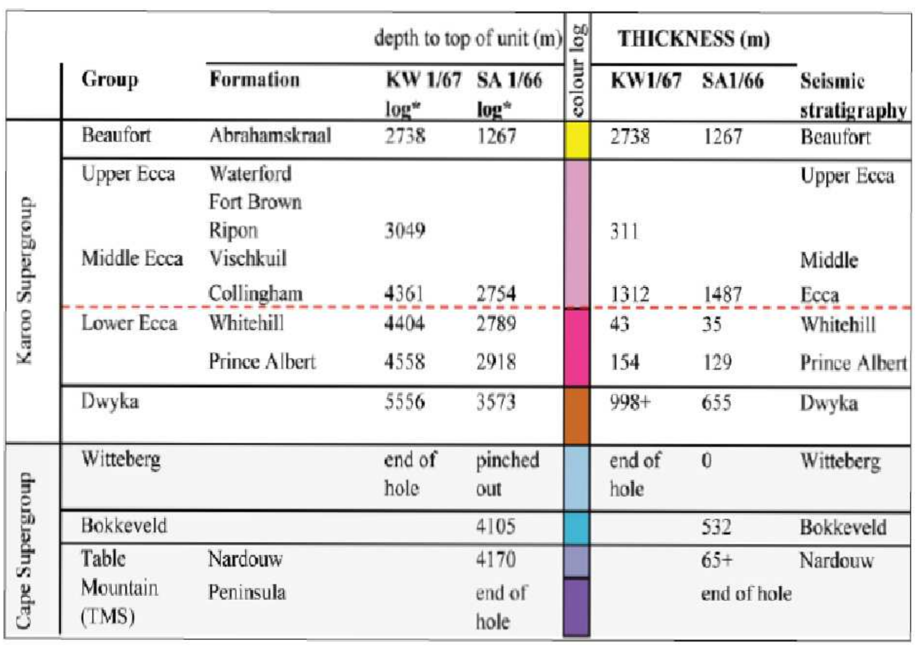

	Group	Formation	depth to top of unit (m) KW 1/67 log*	SA 1/66 log*	colour log	THICKNESS (m) KW1/67	SA1/66	Seismic stratigraphy
Karoo Supergroup	Beaufort	Abrahamskraal	2738	1267		2738	1267	Beaufort
	Upper Ecca	Waterford						Upper Ecca
		Fort Brown						
		Ripon	3049			311		
	Middle Ecca	Vischkuil						Middle
		Collingham	4361	2754		1312	1487	Ecca
	Lower Ecca	Whitehill	4404	2789		43	35	Whitehill
		Prince Albert	4558	2918		154	129	Prince Albert
	Dwyka		5556	3573		998+	655	Dwyka
Cape Supergroup	Witteberg		end of hole	pinched out		end of hole	0	Witteberg
	Bokkeveld			4105			532	Bokkeveld
	Table Mountain (TMS)	Nardouw		4170			65+	Nardouw
		Peninsula		end of hole			end of hole	

Figure 4.12 A table showing simplified vertical stratigraphy at two boreholes including SA 1/66. The high velocity layering at 3–5 km depth southwest of SA05 is probably associated with the rock formations in the Lower Ecca Group around and below the red dashed horizontal line. This diagram has been reproduced from Lindeque et al. (2011).

The reason of using the multiparameters (shown in Table 4.4) to identify lithologies is that, for example diorite and felsic granulite have the same Vp and Vs but different density (i.e., according to Christensen and Stanley, 2003). It is therefore important other constraints are used to assist with the identification. Columns B and C in Figure 4.11 show the velocities and densities, respectively. As already indicated above, the Vp–depth curves in Figure 4.11 come from geophysical models in column C of Figure 4.10 whereas the Vs–depth and density curves are from the joint inversion results of this study. Geological constraints (using borehole data in Figure 4.12 and Table 4.6) have been placed on the lithostratigraphic models (column A) in Figure 4.11. According to seismic reflection studies and Figure 4.12, the upper 5 km of the crust beneath SA05 is representative of the total layer thickness which includes the overlying Karoo Supergroup and the underlying Cape Supergroup.

Table 4.6 Isotopic data for lithologies in four boreholes (reproduced from Eglington and Armstrong, 2003)

Rb–Sr and Sm–Nd isotopic data for basement samples from four boreholes which penetrate Phanerozoic cover in southern Africa

	Borehole				
	QU 1/65		KA 1/66	KC 1/70	WE 1/66
	Depth (m)				
	2493	2993	2579	6005	3735
Lithology	Megacrystic granite	Biotite granodioritic gneiss	Dark grey microporphyry	Granitoid gneiss	Biotite gneiss
Rb	223.8	42.44	16.72	52.67	542.9
Sr	160.6	657.6	34.45	46.78	9.64
$^{87}Rb/^{86}Sr$	4.057	0.1869	1.409	3.268	193.9
$^{87}Rb/^{86}Sr$	0.772224 ± 14	0.708909 ± 14	0.741676 ± 13	0.739391 ± 20	2.651 ± 9
1 sigma errors (%)	0.8, 0.02	0.8, 0.01	0.8, 0.01	0.8, 0.02	0.8, 0.05
Sm	14.90	3.611	1.357	0.7174	2.646
Nd	73.20	19.94	6.372	3.030	10.36
$^{147}Sm^{144}Nd$	0.1231	0.1095	0.1287	0.1431	0.1544
$^{143}Nd^{144}Nd$	0.512327 ± 10	0.511447 ± 10	0.511687 ± 8	0.512267 ± 12	0.512143 ± 13
1 sigma errors (%)	0.6, 0.006	0.6, 0.006	0.6, 0.006	0.6, 0.006	0.6, 0.006
ε_{Nd} (T)	+3.8	−10.5	−8.6	0.0	−3.6
T (Ma)	1053	1150	1150	1150	1134
$^{Nd}T_{DM}$ (Ma)	1199 ± 116	2326 ± 87	2427 ± 96	1662 ± 130	2307 ± 126

Rb, Sr determined following standard dissolution and extraction on cation columns. NIST 987 = 0.71028 ± 19. 1 sigma analytical errors given in percent and refer to $^{87}Rb/^{86}Sr$ and $^{87}Sr/^{86}Sr$, respectively.
Sm, Nd determined following microwave autoclave dissolution and extraction with standard cation and HDEHP on teflon ion exchange techniques. Johnson Matthey standard = 0.511783 ± 2, equivalent to a value of 0.511820 for La Jolla standard. BCR-1 Sm = 6.58, Nd = 28.7, $^{143}Nd/^{144}Nd$ = 0.51264±2.1 sigma analytical errors given in percent and refer to $^{147}Sm/^{144}Nd$ and $^{143}Nd/^{144}Nd$, respectively.
$^{Nd}T_{DM}$ determined using the GEODATE for Windows software (Eglington and Harmer, 1999) and based on the depleted mantle model of DePaolo et al. (1991). Errors are 95% confidence.
ε_{Nd} are based on values of 0.1967 and 0.51264 for $^{147}Sm/^{144}Nd$ and $^{143}Nd/^{144}Nd$, respectively, in CHUR.

The borehole (QU 1/65 in Table 4.6) is ±9 km north of station SUR (see Figure 4.2a) and shows a layer of megacrystic granite at depths of ~2.5 km. This could mean that the composite layer thickness of the Karoo and Cape Supergroups will most likely be less than 5 km beneath SUR since this station is located further north of SA05. The same situation could also be applicable to SA07 since it is located further north of SUR. The implications of the lithostratigraphic models shown in column A of Figure 4.11 are discussed in section 4.5.2 and also used to assess the merits of the existing geophysical models of the BMA.

4.5.2 Source of the BMA – evaluation of the geophysical models

The generally accepted model is that the BMA source is a sutured zone of serpentinised mafic-ultramafic rocks in the deeper parts of the crust (e.g. Burke, 1977; De Beer et al., 1982; Corner, 1989; Pitts et al., 1992; Hälbich, 1993; Harvey et al., 2001). However, the geophysical evidence shown by recent studies (e.g. Lindeque et al., 2007, 2011; Weckmann et al., 2007a,b; Quesnel et al., 2009) has put this model in doubt.

The serpentinized ophiolitic model (e.g. Pitts et al., 1992) postulates that the BMA source is at 30 km depth and this contradicts the findings in this study, which places the BMA body at depths of ~5–10 km with shear wave velocities of 3.5–3.9 km/s and a possible extension of this anomaly to depths of ~10–20 km. The question then becomes, could serpentinized ophiolites be in the upper and middle crustal parts of the NNB and not at 30 km depth as proposed by the ophiolitic wedge model (e.g. Pitts et al., 1992)?

Serpentinized ophiolites (serpentinites) will, in general, show a decrease in density and seismic velocities, but tend to show anomalously high Vp/Vs (~2.05) and a high Poisson's ratio

(~0.34) (e.g. Christensen, 1996; Watanabe et al., 2007). These values are not supported by the estimates shown in Table 4.4. However, this is dependent on the type of serpentinized rock. High-T type (antigorite enriched) serpentinites could have Vp/Vs and Poisson's ratio of 1.8 and 0.28, respectively (e.g. Watanabe, 2007). These estimates are somewhat consistent with the estimates at depth of ~10–15 km (see Table 4.4). It is therefore possible for High-T type serpentinites to predominate mid-crustal depths beneath SUR and SA05, but this is on condition that they are electrically conductive and have an abundance of magnetite spanning a large area.

Electrical conductivity measurements on serpentinite show this rock to be electrically conductive only in active regimes with presence of fluids (e.g. subduction zones) and to be a poor conductor in fossil regimes without fluids (e.g, Airo and Loukola-Ruskeeniemi, 2004). The NNB can be assumed to be a fossilized regime with minor natural seismicity occurring. Therefore, the presence of High-T serpentinites in the NNB mid-crust might not be significant or their existence in the crust is downright questionable and also contradicts the findings by Weckmann et al. (2007a,b) (see central panel of column C in Figure 4.10 that shows the presence of conductive anomalies in the NNB crust within distance of 50–100 km). The presence of serpentinized ophiolites in the NNB mid-crust is therefore not a favourable model of the BMA source.

The models of magnetite-enriched granite gneiss basement by Corner (1989), graphite-enriched shear zones by Weckmann et al. (2007a,b), and mineralized faults and joints in the granite gneiss basement by Loots (2012) represent other possibilities for the BMA source. Granite gneiss rocks are either located at shallow crustal depths (~3–5 km) or likely to be part of undifferentiated metamorphosed rocks as shown in Figure 4.11 and therefore might not fully account for the shear wave velocity signatures of ≥ 3.5 km/s at ~5–10 and ~10–20 km depths as found in this study. Therefore, the models by Corner (1989) and Loots (2012) may not fully account for the source of the BMA. The presence of graphite-enriched sheared rock structures can only mean that these structures are felsic in composition since graphite occurs as a subordinate mineral component in most terrestrial mafic and ultramafic rocks but is otherwise significant in kimberlites and alkali basalts (e.g. Rubin, 1997), which are normally found at mantle depths. Graphite-enriched sheared rock structures may not explain the mafic or intermediate-felsic signatures (Vs ~3.5–3.9 km/s) at upper and middle crustal depths found in this study. Therefore, the graphite-enriched shear zones proposed by Weckmann et al. (2007a,b) is not a favoured model.

The suggestion of granulite-facies mid-crustal rocks by Quesnel et al. (2009) presents a strong possibility in accounting for the BMA source. The estimates in Table 4.4 (and also reflected in Figure 4.11) support the presence of granulites at upper crustal depths (5–10 km) and mid-crustal depths (10–20 km) beneath SA05 and SUR. The model by Quesnel et al. (2009) is consistent with the findings in this study and it is therefore a plausible model for the BMA source. Some of the mid-Proterozoic granulites have been shown to be possible bearers of hematite-ilmenite mineralization (exsolved hematite-ilmenite microstructures) which has recently been found to be the source of large remanence-dominated crustal magnetism similar to the BMA (e.g. McEnroe et al., 2001 and references therein). It is possible that the presence of granulite-facies rocks at mid-crustal depths (as suggested in Figure 4.11) could give rise to the BMA via this type of mineralization indicated above.

The model by Lindeque et al. (2011) suggests the presence of massive sulphide ore bodies to be the BMA source and further suggest these ore bodies to be coinciding with the conductivity anomalies found by Weckmann et al. (2007a,b). The presence of pyrite (iron sulphide) mineralization at shallow crustal depths across the BMA axis has been suggested by conductivity studies (Branch et al., 2007; Weckmann et al., 2007a,b) and it is quite possible that this mineralization contributes to the strong reflectivity anomalies (ore bodies) found by Lindeque et al. (2011) between depths of ~7–15 km. Remanent magnetism in continental layered intrusions could be due to pyrite, pyrrhotite, and/or other mineral combinations such as members of the hematite-ilmenite solid solution (e.g. Pucher and Wonik, 1998; McEnroe et al., 2001).

Massive sulphide ore bodies are normally hosted by sediments and volcanic rocks but might also occur in igneous intrusives such as anorthosites and norites (e.g. Hulbert, 1987). Iron sulphide minerals such as pyrite and pyrrhotite normally found within sulphide deposits are often highly dense with typical densities of 4–5 g/cm^3 and their presence in crustal rocks can produce a Bouguer gravity high (typically between 0–30 mGal) (e.g. Morgan, 2012 and references therein). This gravity high is greater than the Bouguer gravity anomaly (i.e., -113 to -72 mGal) associated with the BMA (Figure 4.3b). The depths of the reflectivity anomalies (associated with the massive sulphide ore bodies) as suggested by the model of Lindeque et al. (2011) are consistent with the depths of crustal layers at ~5–10 and ~10–20 km depths found in this study. However, the presence of massive sulphide ore bodies can in theory produce a gravity high (as indicated above) and this is in contradiction with the magnitude of the gravity anomaly associated with the BMA (Figure 4.3b).

Therefore, massive sulphide ore bodies (in their pure compositional form) are not a favourable model for the BMA source. Their plausibility in accounting for the BMA source hinges on either of the two possible requirements: (1) Depending on the parental magma that originally emplaced these ore bodies, the content of the iron sulphide minerals within the ore bodies should be moderate or low enough to produce a gravity anomaly similar to the one associated with the BMA or (2) The model by Lindeque et al. (2012) suggested metasomatic overprinting on the sulphide ore bodies. It is critical that the degree of metasomatism that could have occurred during the final stages of the NNB evolution (Cornell et al., 2006) should have been sufficient to lower the density of the sulphide mineralization within the ore bodies whilst concurrently preserving their magnetization (i.e., the magnetic high associated with the BMA).

Another plausible model is that of Proterozoic anorthosites (massif anorthosites) formed by coalesced plagioclase plutons at shallow crustal depths (e.g. Ashwal, 1993). Anorthosites, charnockites, and a variety of other igneous intrusives are usually in coexistence in many Proterozoic tectonic settings and due to polybaric fractionation, mafic/ultramafic cumulates will normally underlie these intrusive igneous complexes in magma chambers or settle at the base of the crust (e.g. Ashwal, 1993; Markl et al., 1998; Bédard, 2001). This model of Proterozoic anorthosites is likely to be the type of setting defining much of the Namaqua sector of the NNB (i.e., suboutcropping Bushmanland and Areachap Terranes) at crustal depths. Massif anorthosite complexes (probably with origins from a basaltic or mafic parental magma) are usually emplaced into high-grade metamorphic rocks at high temperature conditions (~1000–1200°C) (e.g. Westphal et al., 2003).

Several studies have estimated emplacement depths of ~10–15 km and ~6–14 km for anorthosites (Royse and Park, 2000 and references therein). These emplacement depths are supported by the lithostratigraphic models beneath SUR and SA05 (Figure 4.11) which indicate layers of anorthositic rocks at 10–15 km depths. Although the models in Figure 4.11 indicate the presence of these rocks at 10–15 km depths, their presence at shallower crustal depths at certain localities along the BMA axes is quite possible. Anorthosites are less dense than mafic/ultramafic rocks and this might explain the differences in the Bouguer gravity anomalies in Figure 4.3b where a relatively low gravity anomaly signature (i.e., -113 to -72 mGal) envelops SUR and SA05 and in contrast to a relatively high gravity anomaly (i.e., -72 to -32 mGal) engulfing SA07. The gravity anomaly around SA07 could be in response to mafic rocks which could possibly be lying beneath this station (e.g. greenschist facies basalts, amphibolites) (see Figure 4.11).

High-grade metamorphism (granulite-facies metamorphism) associated with the emplacement of anorthosites could enable ilmenite and hematite minerals within the anorthosites to be miscible and a complete solid solution of the two minerals is possible at temperatures around or above 950°C. As the temperature lowers, the solid solution of ilmenites and hematites form exsolved hematite-ilmenite microstrucutres (hemo-ilmenite) and these microstructures have been shown to be predominant in Proterozoic anorthosites (and also granulite-facies rocks as noted above). These microstructures have recently been associated with the so-called lamellar magnetism (e.g. Brown and McEnroe, 2008; McEnroe et al., 2009b and references therein). Lamellar magnetism is thermally stable and resistant to demagnetization and it is therefore capable of retaining the natural remanence of rocks over long geological periods. This makes it an ideal candidate and possibly a common source for generating large remanence-dominated magnetic anomalies similar to the BMA. In addition, hematite-ilmenite solid solutions display semiconducting properties with varying temperature and composition (e.g. Ishikawa, 1958). The low to moderate resistivity (shown in Table 4.4 and between distances of 50–100 km in central panel of column C in Figure 4.10) at depths (~ 5–20 km) coincident with the BMA body, tend to corroborate this semiconducting property.

The possibilities raised above are partly or entirely applicable to the Namaqua sector (i.e., suboutcropping Bushmanland, Kaaien and Areachap Terranes). The iron mineralization giving rise to the BMA in the Natal sector could be found in the sub-outcropping Oribi Gorge charnockite-rapakivi granite plutons of the Margate Terrane (Cornell et al., 2006). These plutons were emplaced around 1050 Ma in amphibolite to granulite-facies metamorphic conditions. This contrasts with the anorthosites which were emplaced around 1030–1010 Ma in the Bushmanland Terrane and circa 1086 Ma in the Areachap Terrane (Cornell et al., 2006 and references therein) in high-grade metamorphic conditions.

The contiguity of the postulated anorthosite belt in the Namaqua sector and the equally suboutcropping granite plutons in the Natal sector is probably somewhere in the middle of the NNB and is kinematically defined by a convergent collisional margin of the palaeo–Areachap and –Tugela Ocean basins which were subsequently subducted. The contiguity of these rocks in the different sectors facilitated the east-west continuity of the surface expression of the BMA signature as seen in Figure 4.2b. An alternative of the BMA model in the Natal sector is that the charnockite-granite plutons could be underlain by anorthosites based on observations that indicate the co-existence of anorthosites, charnockites and rapakavi granites in most Proterozoic tectonic settings. Therefore, the underlying anorthosites in the Natal sector could have the same or similar iron mineralization (that gives rise to the BMA) as their counterparts in the Namaqua sector.

4.6 Conclusion

The crustal structure across the BMA has been investigated by jointly inverting high-frequency receiver functions and Rayleigh wave group velocities for periods of 10–60 sec. The 1-D shear wave velocity models obtained from the joint inversions show upper crustal layering around the northern axis of the BMA to have average velocities ≥ 3.5 km/s at depths of ~5–10 km and 10–20 km. These estimates place a constraint on the BMA source (or its crustal host) that is likely to be located at depths of ~5–20 km. However, crustal regions that are within ±20 km of the BMA axis suggest the presence of mineralized Proterozoic high-grade metamorphic rocks and/or igneous intrusions whereas regions elsewhere in the NNB suggest the presence of mafic rocks that are compositionally variable from those in the vicinity of the BMA.

The Vs models for the three stations located along the northern branch of the BMA show velocities approaching 4.0 km/s around depths of 10 km and this could mean that the BMA body (or its crustal host) becomes mafic in composition around those depths. The fluctuating velocities (i.e., low-to-high or high-low-high) below 10 km depth could mean that this depth is either the base of the BMA body (or its crustal host) or marks its compositional transition. The BMA body (or its crustal host) might continue in another compositional form below 10 km depth. If the BMA body continues below 10 km depth, then the BMA is a compositional anomaly independent of rock type and is highly dependent on the crystallization history of the rocks hosting it and the accompanying metamorphic conditions driving the crystallization. The 1-D Vs models further show a high velocity rock (≥ 4.0 km/s) beneath the stations occupying a substantial portion of the lower crust (below 20–30 km depths) and also a crust that is thick (≥ 37 km). The high velocity rock beneath 20–30 km depths implies that the BMA has a common mafic and/or ultramafic source originating from the deeper parts of the crust or uppermost mantle. The results from the 1-D Vs models are consistent with the findings made by past studies of the BMA.

Estimates of physical properties (i.e., Vp, Vs, Poisson's ratio, density, and resistivity) favour massive sulphide ore bodies and granulite-facies mid-crustal rocks as models of the BMA source. However, massive sulphide ore bodies (in theory) show gravity anomaly trends that are higher than the gravity anomaly trends associated with the BMA. Therefore, the plausibility of the massive sulphide model hinges on either of the two possible requirements: (1) the presence of sulphide mineralization (associated with the parental magma) within the ore bodies should be moderate or low enough to produce a gravity anomaly consistent with that associated with the BMA, or (2) the degree of metasomatism that could have occurred during the final stages of the NNB evolution should have been adequate to lower the density of the sulphide mineralization within the ore bodies while at the same time preserving their magnetic properties (i.e., high magnetic signature associated with the BMA).

Another plausible model emerging from the estimates of physical properties is that the BMA source could be hosted within Proterozoic anorthositic layered intrusions which could be giving rise to the BMA via iron bearing mineralization. This iron bearing mineralization could be in the form of iron sulphides (pyrite) or iron and titanium oxides such as magnetite, ilmenite, hematite, etc. Ilmenites and hematites can exist as exsolved hematite-ilmenite intergrowths at lower temperatures and this can potentially give rise to remanence-dominated crustal anomalies similar to the BMA.

References

Adams, A., and Nyblade, A., 2011. Shear wave velocity structure of the southern African upper mantle with implications for the uplift of southern Africa. *Geophysical Journal International*, 186, 808 – 824.

Airo, M., Loukola-Ruskeeniemi, K., 2004. Characterization of sulfide deposits by airborne magnetic and gamma-ray responses in eastern Finland. *Ore Geol. Rev*., 24, 67–84.

Ashwal, L. D., 1993. *Anorthosites*. Berlin: Springer-Verlag.

Beattie, J., 1909. Report of the Magnetic Survey of South Africa. Cambridge University Press, New York.

Bédard, J., 2001. Parental magmas of the Nain Plutonic Suite anorthosites and mafic cumulates: a trace element modelling approach. *Contributions to Mineralogy and Petrology*, 141, issue 6, 747 – 771.

Blakely, R.J., 1995. *Potential Theory in Gravity and Magnetic Apllications*. Cambridge University Press.

Branch, T., Ritter, O., Weckmann, U., Sachsenhofer, R.F. and Schilling, F., 2007. The Whitehill Formation – a high conductivity marker horizon in the Karoo Basin. *South African Journal of Geology*, 110, 465–476.

Brown, L. L., and McEnroe, S.A., 2008. Magnetic properties of anorthosites: A forgotten source for planetary magnetic anomalies? *Geophysical Research Letters*, 35, L02305, doi:10.1029/2007GL032522.

Burke, K., Dewey, J.F., and Kidd, W.S.F., 1977. World distribution of sutures – the sites of former oceans. *Tectonophysics*, 40, 69 – 99.

Cassidy, J. F., 1992. Numerical experiments in broad-band receiver function analysis. *Bulletin of the Seismological Society of America*, 82, 1453– 1474.

CGS, 2000. Regional Aeromagnetic data, 1:1 000 000 Total Magnetic Intensity Map of the Republic of South Africa. Compiled by: Stettler, E.H., Fourie, C.J.S., Cole, P. Council for Geoscience CGS, Pretoria, South Africa.

Christensen, N. I., and Mooney, W.D., 1995. Seismic velocity structure and composition of the continental crust: A global view. *Journal of Geophysical Research*, 100, 9761 – 9788.

Christensen, N.I., 1996. Poisson's ratio and crustal seismology. *Journal of Geophysical Research*, 101, 3139 – 3156.

Christensen, N.I., and Stanley, D., 2003. Seismic velocities and densities. *In*: W.H..K Lee, H. Kanamori, P.C. Jennings, C. Kisslinger (Editors) *International Handbook of Earthquake and Engineering*, 81B, 1587 – 1594.

Cornell, D.H., Thomas, R.J., Moen, H.F.G., Reid, D.L., Moore, J.M., and Gibson, R.L., 2006. The Namaqua-Natal Province, in: M. R. Johnson, C. R. Anhaeusser, R. J. Thomas (Editors), *The Geology of South Africa*, Geological Society of South Africa, Johannesburg/ Council for Geoscience, Pretoria, 325 – 379.

Corner, B., 1989. The Beattie anomaly and its significance for crustal evolution within the Gondwana framework, paper presented at First Technical Meeting. *South African Geophysical Association*, Johannesburg.

De Beer, J., van Zijl, J., and Gough, D., 1982. The Southern Cape Conductive Belt (South Africa): Its composition, origin and tectonic significance. *Tectonophysics*, 83, 205 – 225.

De Wit, M.J. and Horsfield, B., 2006. Inkaba ye Africa Project Surveys Sector of Earth from Core to Space. EOS, *American Geophysical Union*, 87, 113–117.

Duncan, A.R., and Marsh, J.S., 2006. The Karoo Igneous Province, in: M. R. Johnson, C. R. Anhaeusser, R. J. Thomas (Editors), *The Geology of South Africa*, Geological Society of South Africa, Johannesburg/ Council for Geoscience, Pretoria, 501–520.

Dziewonski, A.M., and Anderson, D.L., 1981. Preliminary reference Earth model. *Physics of the Earth Planetary Interiors*, 25, S.297 – 356.

Eglington, B.M., and Armstrong, R.A., 2003. Geochronological and isotopic constraints on the Mesoproterozoic Namaqua-Natal Belt: evidence from deep borehole intersection in South Africa. *Precambrian Research*, 125, 179–189.

Eglington, B.M., 2006. Evolution of the Namaqua-Natal Belt, southern Africa – a geochronological and isotope geochemical review. *Journal of African Earth Sciences*, 46, 93–111.

Green, R.W.E., and Durrheim, R.J., 1990. A seismic refraction investigation of the Namaqualand Metamorphic Complex, South Africa. *Journal of Geophysical Research*, 95, No. B12, 19927– 19932.

Gurrola, H., Minster, J.B., 1998. Thickness estimates of the uppermantle transition zone from bootstrapped velocity spectrum stacks of receiver functions. *Geophysical Journal International*, 133, 31 – 43, doi:10.1046/j.1365-246X.1998.1331470.x.

Hälbich, I.W., et al., 1993. Cape Fold Belt –Agulhas Bank Transect across Gondwana suture, southern Africa. *Global Geoscience Transect*, 9, 18 pp., AGU, Washington, D. C.

Harvey, J.D., de Wit, M.J., Stankiewicz, J., and Doucouré, C.M., 2001. Structural variations of the crust in the Southwestern Cape, deduced from seismic receiver functions. *South African Journal of Geology*, 104, 231 – 242.

Hulbert, L., 1987. Investigation of mafic and ultramafic rocks, and platinum group element mineralization in northern Saskatchewan: preliminary findings; in *Summary of Investigations 1987*, Saskatchewan Geological Survey; Saskatchewan Energy and Mines, Miscellaneous Report 87–4.

Hunt, C.P., Moskowitz, B.M., and Banerjee, S.K., 1995. Magnetic properties of rocks and minerals. *In*: *Rock Physics and Phase Relations* – a handbook of physical constants, AGU reference shelf, 3, 189 – 204.

IAGA Division 1., 1975. Study group on geomagnetic reference field, international magnetic reference field 1975. *Journal of Geomagnetism and Geoelctricity*, 27, 437 – 439.

Ishikawa, Y., 1958. Electrical properties of $FeTiO_3$-Fe_2O_3 solid solution series. *Journal of the Physical Society of Japan*, 13, 37 – 42.

Johnson, M.R., Van Vuuren, C.J., Visser, J.N.J., Cole, D.I., Wickens, H.de V., Christie, A.D.M., Roberts, D.L., and Brandl, G., 2006. Sedimentary rocks of the Karoo Supergroup. *In*: M. R. Johnson, C. R. Anhaeusser, R. J. Thomas (Editors) *The Geology of South Africa*, Geological Society of South Africa, Johannesburg/ Council for Geoscience, Pretoria, 461–499.

Julià, J., Ammon, C.J., Hermann, R.B., Correig, A.M., 2000. Joint inversion of receiver functions and surface-wave dispersion observations. *Geophysical Journal International*, 143, 99 – 112.

Julià, J., Ammon, C.J., Hermann, R.B., 2003. Lithospheric structure of the Arabian Shield from the joint inversion of receiver functions and surface-wave group velocities. *Tectonophysics*, 371, 1 – 21.

Julià, J., Ammon,C.J., and Nyblade, A.A., 2005. Evidence for mafic lower crust in Tanzania, East Africa from joint inversion of receiver functions and Rayleigh wave dispersion velocities. *Geophysical Journal International*, 162, 555 – 569.

Julià, J., 2007. Constraining velocity and density contrasts across the crust-mantle boundary with receiver function amplitudes. *Geophysical Journal International*, 171, 286 – 301.

Kgaswane, E.M., Nyblade, A.A., Julià, J., Dirks, P.H.G.M., Durrheim, R.J., Pasyanos, M.E., 2009. Shear wave velocity structure of the lower crust in southern Africa: Evidence for compositional heterogeneity within Archaean and Proterozoic terrains. *Journal of Geophysical Research*, 114, B12304. doi:10.1029/2008JB006217.

Kgaswane, E.M., Nyblade, A.A., Durrheim, R.J., Julià, J., Dirks, P.H.G.M., and Webb, S.J., 2012. Shear wave velocity structure of the Bushveld Complex, South Africa. *Tectonophysics*, 554–557, 83–104, doi:10.1016/j.tecto.2012.06.003.

Ligorría, J. P., Ammon, C.J., 1999. Iterative deconvolution and receiver function estimation. *Bulletin of the Seismological Society of America*, 89, 1359 – 1400.

Lindeque, A.S., Ryberg, T., Stankiewicz, J., Weber, M.H., and de Wit, M.J., 2007. Deep crustal seismic reflection experiment across the Southern Karoo Basin, South Africa. *South African Journal of Geology*, 110, 419 – 438.

Lindeque, A.S., and de Wit, M.J., 2009. Revealing the Beattie Magnetic Anomaly and the anatomy of the crust of southernmost Africa: Geophysics and deep subsurface where the Cape Fold Belt and Karoo Basin meet, in: 11th SAGA Biennial Technical Meeting and Exhibition, 490 – 499.

Lindeque, A., de Wit, M.J., Ryberg, T., Weber, M., and Chevalier, L., 2011. Deep crustal profile across the southern Karoo Basin and Beattie Magnetic Anomaly, South Africa: an integrated interpretation with tectonic implications. *South African Journal of Geology*, 114, no. 3 – 4, 265 – 292. doi:10/2113/gssajg.114.3-4.265

Loots, L., 2012. Investigation of the crust in the southern Karoo using the seismic reflection technique. MSc (*in preparation*), University of the Witwatersrand, Johannesburg, South Africa.

Markl, G., Frost, B.R., and Bucher, K., 1998. The origin of anorthosites and related rocks from the Lofoten Islands, Northern Norway: I. Field relations and estimation of intrinsic variables. *Journal of Petrology*, 39, 8, 1425 – 1452.

McEnroe, S.A., Harrison, R.J., Robinson, P., Golla, U., and Jercinovic, M.J., 2001. Effect of fine-scale microstructures in titanohematite on the acquisition and stability of natural remanent in granulite facies metamorphic rocks, southwest Sweden: Implications of crustal magnetism. *Journal of Geophysical Research*, 106, B12, 30523 – 30546.

McEnroe, S.A., Brown, L.L., and Robinson, P., 2009a. Remanent and induced magnetic anomalies over a layered intrusion: Effects from crystal fractionation and magma recharge. *Tectonophysics*, 478, 119 – 134.

McEnroe, S.A., Fabian, K., Robinson, P., Gaina, C., and Brown, L.L., 2009b. Crustal magnetism, lamellar magnetism and rocks that remember. *Elements*, 5, 241 – 246. doi: 10.2113/gselements.5.4.241

Morgan, L.A., 2012. Geophysical characteristics of volcangenic massive sulphide deposits in volcanogenic massive sulphide occurrence model: *U.S. Geological Survey Scientific Investigations Report 2010 – 5070*, Chapter 7, 16p.

Nair, S.K., Gao, S.S., Kelly, H.L. and Silver, P.G., 2006. Southern African crustal evolution and composition: Constraints from receiver function studies. *Journal of Geophysical Research*, 111, B02304, doi:10.1029/2005JB003802.

Newton, A.R., Shone, R.W., and Booth, P.W.K., 2006. The Cape Fold Belt, *In*: M. R. Johnson, C. R. Anhaeusser, R. J. Thomas (Editors) *The Geology of South Africa*, Geological Society of South Africa, Johannesburg/ Council for Geoscience, Pretoria, 521 – 530.

Nguuri, T.K., Gore, J., James, D.E., Webb, S. J., Wright, C., Zengeni, T.G., Gwavava, O., Snoke, J.A., and Kaapvaal Seismic Group, 2001. Crustal structure beneath southern africa and its implications for the formation and evolution of the Kaapvaal and Zimbabwe Cratons.

Geophysical Research Letters, 28 (13), 2501 – 2504.

Nguuri, T.K., 2004. *Crustal structure of the Kaapvaal Craton and surrounding mobile belts: analysis of teleseismic P waveforms and surface wave inversions*, Ph.D. dissertation, University of the Witwatersrand (unpublished).

Pasyanos, M.E., Nyblade, A.A., 2007. A top to bottom lithospheric study of Africa and Arabia. *Tectonophysics*, 444 (1 – 4), 27 – 44.

Pitts, B., Mahler, M., de Beer, J., Gough, D., 1992. Interpretation of magnetic, gravity and magnetotelluric data across the Cape Fold Belt and Karoo Basin, in *Inversion Tectonics of the Cape Fold Belt, Karoo and Cretaceous Basins of Southern Africa*, edited by M. de Wit and I. Ransome, pp. 27 – 32, A.A. Balkema, Brookfield, Vt.

Phillips, J.D., 2001. Designing matched bandpass and azimuthal filters for the separation of potential-field anomalies by source region and source type. *15th ASEG Geophysical Conference and Exhibition*, Expanded Abstracts.

Pucher, R, and Wonik, T., A different interpretation of the MAGSAT anomalies of central Europe. *J. Phys. Chem. Earth*, 23, 981 – 985.

Quesnel, Y., Weckmann, U., Ritter, O., Stankiewicz, J., Lesur, V., Mandea, M., Langlais, B., Sotin, C., Galdéano, A., 2009. Simple models for the Beattie Magnetic Anomaly in South Africa. *Tectonophysics*, 478, 111 – 118.

Raveloson, A., Nyblade, A., Fishwick, S., Mangongolo, A., and Master, S., 2012. The upper mantle seismic velocity structure of central Africa and the architecture of Precambrian lithosphere beneath the Congo Basin, in: *Geology and Resource Potential of the Congo Basin*, edited by M. de Wit, F. Guillocheau, M. Fernandez-Alonso, M. de Wit, Springer-Verlag, submitted.

Royse, K., Park, R., 2000. Emplacement of the Nain anorthosite: diapiric versus conduit ascent. *Canadian Journal of Earth Sciences*, 37, issue 8, pp. 1195–1207, doi: 10.1139/cjes-37-8-1195.

Rubin, A.E., 1997. Igneous graphite in enstatite chondrites. *Mineralogical Magazine*, 61, 699 – 703.

Scheiber-Enslin, S.E., Ebbing, J., Eberle, D.G., and Webb, S.J., 2012. Geophysical 3D modelling of the Karoo Basin. *LASI V Workshop* – “The physical geology of subvlocanic systems: laccoliths, sills and dykes”. Port Elizabeth.

Sheriff, S.D., 2010. Matched filter separation of magnetic anomalies caused by scattered surface debris at archaeological sites. *Near Surface Geophysics*, 8, 145 – 150.

Spector, A., and Grant, F., 1970. Statiscal models for interpreting aeromagnetic data. *Geophysics*, 35, 293 – 302.

Stankiewicz, J., Ryberg, T., Schulze, A., Lindeque, A., Weber, M., de Wit, M., 2007. Initial results from wide-angle seismic refraction lines in the Southern Cape. *South African Journal of Geology*, 110, 407 – 418.

Stankiewicz, J., Parsiegla, N., Ryberg, T., Gohl, K., Weckmann, U., Trumbull, R., Weber, M., 2008. Crustal structure of the southern margin of the African continent: Results from geophysical experiments. *Journal of Geophysical Research*, 113, B10313, doi:10.1029/2008JB005612.

Syberg, F.J.R., 1972. A Fourier method for the regional-residual problem of potential fields. *Geophysical Prospecting*, 20, 47 – 75.

Thamm, A. G., and Johnson, M. R., 2006. The Cape Supergroup, in *The Geology of South Africa*, edited by M. R. Johnson, C. R. Anhaeusser, and R. J. Thomas, pp. 443– 460, Geol. Soc. of S. Afr., Johannesburg, South Africa.

Thomas, R.J., Eglington, B.M., Evans, M.J., and Kerr, A., 1992. The petrology of the Proterozoic Equeefa Suite, southern Natal, South Africa. *South African Journal of Geology*, 95, 116–130.

Venter, C.P., du Plessis, J.G., Stettler, R.H., Potgieter, T.D., Kleywegt, R.J., Hattingh, E., Fourie, C.J.S., Wolmarans, L.G., Cloete, A.J., Maré, L.P., 1999. Gravity. *South African Geophysical Atlas*, Council for Geoscience, South Africa, 1 – 77.

Watanabe, T., Kasami, H., and Ohshima, S., 2007. Compressional and shear wave velocities of serpentinized peridotites up to 200 MPa. *Earth Planets Space*, 59, 233 – 244.

Weckmann, U., Ritter, O., Jung, A., Branch, T., de Wit, M., 2007a. Magnetotelluric measurements across the Beattie magnetic anomaly and the Southern Cape Conductive Belt, South Africa. *Journal of Geophysical Research*, 112, doi:10.1029/2005JB003975.

Weckmann, U., Jung, A., Branch, T., Ritter, O., 2007b. Comparison of electrical conductivity structures and 2D magnetic modelling along two profiles crossing the Beattie Magnetic Anomaly, South Africa. *South African Journal of Geology*, 110, 449 – 464.

Westphal, M., Schumacher, J.C., and Boschert, S., 2003. High-temperature metamorphism and the role of magmatic heat sources at the Rogaland Anorthosite Complex in Southern Norway. *Journal of Petrology*, 44, 6, 1145 – 1162.

Chapter 5

Conclusions and recommendations

5.1 Chapter 2 – Structure of the lower crust of southern Africa

5.1.1 Summary

The compositional variability of the lower crust is investigated using the joint inversion of P-wave teleseismic receiver functions and Rayleigh wave group velocities for 89 broadband seismic stations distributed across southern Africa. The resulting 1-D shear wave velocity signatures of the lower crust of the Precambrian shield of southern Africa can be classified into two groups:

1. Most parts in the Kimberley terrain [western part of the Kaapvaal Craton (KC)] including the western part of the Tokwe terrain [Zimbabwe Craton (ZC)] show a Vs ≤ 4.0 km/s suggesting an intermediate-to-felsic lower crust and further associated with this is a crust that is thinner than 37 km.
2. The remainder of the Archaean and Proterozoic terrains in southern Africa show a Vs ~ 4.0 km/s indicating a lower crust that is mafic in most parts of the KC and more mafic (Vs > 4.0 km/s) in certain parts of the Bushveld Complex and the surrounding mobile belts and further associated with this is a crust that is thicker than 37 km.

The Sn velocities in the uppermost mantle region (i.e., from Moho to 60 km depth) are in the range of 4.5–4.7 km/s and this suggests that there are minor compositional differences in the uppermost mantle regions of the different tectonic terrains across southern Africa. An intermediate-to-felsic lower crust could be due to rifting associated with the tectonomagmatic effect of the Ventersdorp event (~2.7 Ga) in the case of the Kimberley terrain, whereas 3.1–

2.95 Ga rift sequences could have been responsible for the attenuation of the mafic layering in the lower crust of the western part of the Tokwe terrain. The mafic lower crust in regions such as the BC may be attributed to magmatic underplating, whereas the Namaqua-Natal Belt (NNB), Central Zone [Limpopo Belt (LB)], and Kheis Province are consistent with typical ‘‘suture’’ thickened crust found in Precambrian tectonic settings globally. The crustal thicknesses found in this study are consistent with past studies. Crustal xenoliths are more frequent in regions with a mafic lower crust than those with an intermediate-to-felsic lower crust.

5.1.2 Recommendations for future studies

1. A potential disadvantage with the use of the joint inversion technique is that it is assumed that the receiver functions and surface wave dispersions sample the same Earth structure. This may not always be the case. Some kind of a quality control, perhaps in the form of a ray-tracing algorithm, will be required to ensure that the two data sets are indeed sampling the same structure.

2. Another potential problem is that the propagation path or structure beneath the seismic station or receiver site can be complex. This could destabilize the inversion algorithm resulting in poorly constrained velocity models. This problem could be resolved by using a 2nd or 3rd degree polynomial equation in an optimization procedure to identify the local structural terms or parameters. Alternatively, structural parameters (σ, a, L and c) of a random or heterogeneous medium can be deduced using the following approach suggested by Ritter et al. (1998) i.e.,

$$ln\left(\left\langle \varepsilon^2 \right\rangle + 1\right) = \frac{8\pi^2\sigma^2 aL}{c^2} f^2 = \gamma f^2 \qquad (5\text{-}1)$$

where ε is a dimensionless parameter defining the measure of wavefield fluctuations, c is the seismic velocity, σ^2 and a are the variance of the velocity fluctuations and correlation length of the heterogeneities, respectively, of either an exponential or Gaussian correlation function used to model the random medium, L is the length of the ray path in the heterogeneous medium and f is the frequency of the ray propagation. For a number of teleseismic or regional recordings, the co-efficient γ in equa. (5-1) above can be determined by calculating a least-squares fit of $ln\left(\left\langle \varepsilon^2 \right\rangle + 1\right)$ in the frequency domain. By using different velocity contrasts σ (in percentages) for the fluctuations in a heterogeneous medium, the correlation lengths (a) can be calculated for L/c^2 (in equa. 5-1) in the upper, lower crustal and the lithospheric regions. Whilst the parameter, L, can be assumed to be the layer thicknesses of each of the upper, lower crustal and lithospheric regions, the seismic velocity, c, can either be determined from $k = \frac{2\pi f}{c}$, where k is the wavenumber (in km^{-1}) or as the reciprocal of the ray-parameter (in s/km).

Therefore, the receiver functions and surface wave dispersions (recorded by a station located in a complex geological region) can each be perturbed with the variance of velocity fluctuations (σ^2) and correlation lengths (a) and jointly inverted for each of the perturbations. The final Vs model can be obtained as an average of the ensemble of joint inversions resulting from each of the perturbations. This approach, together with the implementation of the so-called *virtual stations* (e.g. Curtis et al., 2009) could be used to improve the resolution especially where local geology is complex and the observing network is widely-spaced or sparse. All this, can easily extend the joint inversion technique to 3-D applications.

5.2 Chapter 3 – Shear wave velocity structure of the Bushveld Complex, South Africa

5.2.1 Summary

Fine-scale details of the structure of the crust within the Bushveld Complex (BC) has been investigated by jointly inverting high-frequency teleseismic receiver functions ($f \leq 1.25$ Hz) and Rayleigh wave group velocities (in the period range of 2–60 sec) for 16 broadband seismic stations positioned across the BC. The resulting 1-D shear wave velocity models are better constrained in the upper crust than those used by Kgaswane et al. (2009) because group velocities in the period range of 2–15 sec were obtained by tomography in this study. The Rayleigh group velocities in the period range of 20–60 sec were taken from the revised Pasyanos and Nyblade (2007) model. The 1-D shear wave velocity models obtained in this study for each of the seismic stations show the following:

1. A crust that is ~45 km thick beneath the centre of the BC. The crust in this region could have thickened by ~5–8 km owing to isostatic adjustment following the intrusion of the BC.
2. A substantial portion of the lower crust (below 30 km depth) has shear wave velocities that are ≥ 4.0 km/s. This is indicative of a highly mafic lower crust beneath the BC.
3. Shear wave velocities in some upper crustal layers may be as high as 3.7–3.8 km/s, consistent with the presence of mafic lithologies.
4. The Sn velocities in the uppermost mantle region (i.e., from Moho to 60 km depth) are in the range of 4.5–4.7 km/s and therefore the petrological structure of the uppermost mantle region below the BC does not deviate significantly from what is beneath the rest of the Archaean crust (see Chapter 2).

These results favour a "continuous-sheet" model for the BC in which the mafic layers that crop out in the western and eastern limbs are continuous at depth beneath the centre of the complex. However, detailed modelling of receiver functions at one station within the centre of the complex indicates that the mafic layering may be locally disrupted due to thermally-driven diapirism associated with the emplacement of the BC itself and/or tectonic reactivation due to the ~2040 Ma intraplate orogeny.

5.2.2 Recommendations for future studies

1. The 3-D Vs models obtained in this study using Rayleigh wave group velocity tomography lack resolution. One way of improving resolution will be to supplement the existing surface wave measurements with ambient noise measurements in the period range of 2–15 sec and apply the tomographic method as indicated in this study.
2. Alternatively, the 3-D Vs models can be obtained by jointly inverting teleseismic or regional or local receiver functions (i.e., depending which gives better constraint at depth for part of the Earth structure that is of focus or interest to the investigation) and ambient noise measurements using the joint inversion procedure (Julià et al., 2000, 2003). However, this might require that an additional temporary seismic network is deployed across the BC to compensate for the wide spacing (~100 km) of the 16 broadband seismic stations used in this study. The use of receiver functions derived from local or regional earthquakes has recently become a strong possibility and has already been applied in certain areas (e.g. Calkins et al., 2006; Barros and Assumpção, 2011).

5.3 Chapter 4 – Shear wave velocity constraints on the source of the Beattie Magnetic Anomaly, South Africa

5.3.1 Summary

The crustal structure across the Beattie Magnetic Anomaly (BMA) has been investigated by jointly inverting high-frequency teleseismic receiver functions and Rayleigh wave group velocity dispersions. Past geophysical studies constrain the BMA source to be at depths of ~5–20 km and exhibit the following characters: a resistivity of ~2–16 Ωm, P-wave velocities of ~6.6–7.0 km/s, and a magnetization of 6 Am^{-1}. The 1-D shear wave velocity models obtained from the joint inversions show the following:

1. High Vs crustal layers between 3.5–4.0 km/s in the 5–10 km depth range at all backazimuths across all the three stations along the northern branch of the BMA. However, crustal regions that are within ±15 km of the BMA axis suggest the presence of mineralized Proterozoic high-grade metamorphic rocks and/or igneous intrusions whereas regions elsewhere in the NNB suggest the presence of mafic rocks that are compositionally variable from those in the vicinity of the BMA.
2. Crustal layers with Vs fluctuating between 3.5 and 4.0 km/s (i.e., low-to-high or high-low-high) within depths of ~10–20 km, and
3. High velocity layers (≥ 4.0 km/s) beneath the stations occupying a significant portion of the lower crust (below 20–30 km depths) and a crust with an average thickness greater than 40 km. It is possible that the thick crust could be isostatically compensating for the presence of mafic bodies (including the crustal host of the BMA) in the upper crustal parts of the NNB. A similar geodynamic scenario has been deduced for the BC.

4. The Sn velocities in the uppermost mantle region (i.e., from Moho to 60 km depth) are in the range of 4.5–4.7 km/s and therefore the petrological structure of the uppermost mantle region below the NNB does not show significant differences from what is beneath the rest of the southern African crust (see Chapter 2).

The findings indicated above are consistent with the findings made by past geophysical studies of the BMA. The Vs models for three localities along the northern branch of the BMA show a mafic composition around 10 km depths and this could mean that the BMA body (or its crustal host) occurs around those depths. The fluctuating velocities (i.e., low-to-high or high-low-high) below 10 km depth could mean that this depth is either the base of the BMA body (or its crustal host) or marks its compositional change. The BMA body (or its crustal host) might continue in another compositional form below 10 km depth.

Physical properties (i.e., Vp, Vs, Poisson's ratio, density and resistivity) of the crustal source of the BMA favour massive sulphide ore bodies or granulite-facies mid-crustal rocks as models of the BMA source. However, the plausibility of the massive sulphide model depends either on the presence of sulphide mineralization within the ore bodies or the metasomatic effect on the sulphide ore bodies. A proposed model from this study is that of the BMA source being a belt of coalesced anorthosites formed during the Proterozoic by Andean-type subduction tectonics. Anorthosites are less dense than mafic rocks and are more likely to produce a Bouguer gravity response consistent with the one around the BMA. The magnetic mineralization in the anorthosites and/or granulites could either be in the form of iron sulphides (pyrite) and/or iron and titanium oxides such as magnetite, ilmenite, hematite, or exsolved lamellae of hematite and ilmenite.

5.3.2 Recommendations for future studies

1. A detailed analysis of the BMA with high resolution seismics is still required and for this, 3-D Vs models of the anomaly can be obtained using the same or similar approaches indicated in 5.2.2.
2. Alternatively, since the BMA is a magnetic entity, a better constraint on the anomaly can be obtained by jointly inverting magnetics and gravity (e.g. Zeyen and Pous, 1993). From this joint inversion, the following parameters can be obtained i.e., upper and lower depth bounds, susceptibility, magnetization (remanent and/or induced) and density of the subsurface body. However, the main disadvantage arising from this method is that the magnetic and gravimetric anomalies are assumed to originate from the same rock source. In certain instances, highly magnetic rock sources might not give measurable gravimetric responses or the gravimetric responses could be due to other conditions in the host rock. In other cases, high-density anomalies might not have magnetic mineralization and as such give non-measurable magnetic responses. In both situations, standard magnetic or gravity fields (just a little above zero) will have to be assumed for the non-measurable parameter and more weight could be given to the measurable parameter in the joint inversion for the purposes of stabilizing the inversion procedure.
3. A couple of other methods such as the joint inversion of seismic and gravity data (e.g. Tiberi et al., 2003) can also be attempted to model the BMA.

5.4 Implications of the research findings with regard to lithospheric heterogeneity, crustal genesis and evolution of southern Africa

5.4.1 Studies prior to SASE

One of the main objectives of this research was to obtain new insights into the evolution of the crust and uppermost mantle of southern Africa. In 1994 paper entitled *"Evolution of the Precambrian Lithosphere: seismological and geochemical constraints"* was published in the Journal of Geophysical Research (Durrheim and Mooney, 1994). The authors attempted a global synthesis of seismic investigations of the Precambrian lithosphere. At that time it was widely believed that the thickness of the continental crust was proportional to its age, with the exception of young orogens. The worldwide review of seismic structure contradicted this belief and falsified these models, at least for the Archaean. Durrheim and Mooney (1994) found that Proterozoic crust had a thickness of 40–55 km and a substantial high P-wave velocity (>7 km/s) layer at its base, while Archaean crust was only 27–40 km thick (except at the sites of younger rifts and collisional boundaries) and lacks the high-velocity basal layer.

Durrheim and Mooney (1994) presented a model to explain the secular change in crust-forming processes, which they largely ascribed to a decrease in mantle temperature leading to a change in the chemistry of the magmas produced in the mantle and the resultant lithospheric keel (see Figure 5.1). However, the model was based on quite limited data. For example, only a handful of refraction seismic profiles had been surveyed in southern Africa. Witwatersrand mine tremors had been the energy source for several refraction surveys that investigated the KC, while explosions were used for profiles that probed the Namaqualand and Damara Mobile Belts, the Rehoboth Province and the Agulhas Bank.

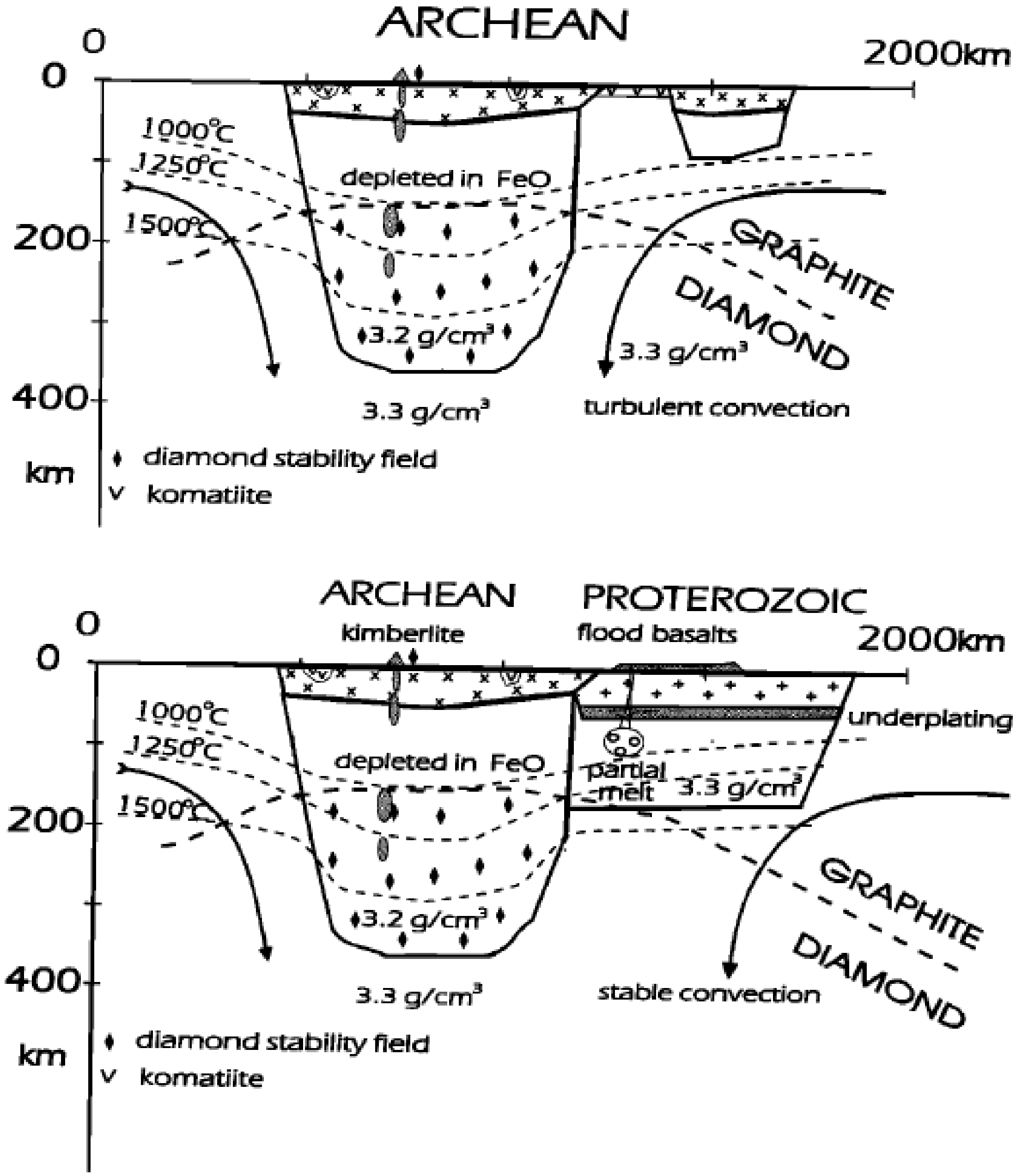

Figure 5.1 A model showing the different elements that drive Archaean and Proterozoic lithospheric evolution. The pluses indicate Archaean crust whereas the crosses indicate Proterozoic crust. Komatiitic volcanism and stiff lithospheric mantle roots were produced at mantle temperatures almost double present-day temperatures during the Archaean. The stiff lithospheric mantle roots were approximately 150 km thick, were devolatized of FeO and other lithophile elements. These conditions were favourable to the creation of an Archaean crust. In contrast, the Proterozoic crust lacked the sublithospheric mantle root architecture similar to that below the Archaean crust. As a result, Proterozoic crust developed on a convective mantle that controlled magmatic intrusions into the overlying crust. Magmatic underplating arising from the intrusions produced a high-velocity basal layer in the crust and also thickened the crust. The geothermal and diamond stability field data indicated in the diagrams are from Jones (1998) and Kennedy and Kennedy (1976). The diagrams were reproduced from Durrheim and Mooney (1994).

The Kaapvaal Seismic Experiment (1997-1999) provided an opportunity to investigate the southern African lithosphere in far more detail. In April 1997, the same month as the SASE deployment, the *International Symposium of Plumes, Plates and Mineralisation* (PPM'97) was held at Pretoria University. A workshop entitled "*The Geophysical Framework of the Kaapvaal Craton"* was held to review geophysical research conducted in the preceding decade, to identify key unsolved problems, and to formulate hypotheses to be tested by the Kaapvaal Project. Papers addressing the theme were published in a Special Issue of the *South African Geophysical Review* (Durrheim and Webb, 1998). The work carried out for this thesis has addressed some of these issues.

5.4.2 Studies based on SASE data

The SASE data acquired at more than 80 stations stretching from Cape Town to Zimbabwe were used to image the seismic velocity structure of the lithosphere using a wide range of analysis techniques. For instance, Nguuri et al. (2001) computed P-wave receiver functions and both Nguuri (2004) and Yang et al. (2008) inverted surface waves, while I jointly inverted the P-wave receiver functions and surface waves (Kgaswane et al., 2009). The work confirmed the broad features of the Durrheim and Mooney model, *viz.* a thin Archaean crust (~36–37 km) with a low basal velocity ($V_s \leq 3.9$ km/s) in the western part of the KC and the ZC, and a thick Proterozoic crust ($\geq$ 39 km) with a high basal velocity ($V_s > 4.0$ km/s). However, this study and a number of other studies based on the SASE data showed that the Durrheim and Mooney model is rather simplistic. Significant new observations relevant to models of lithospheric evolution include:

- The seismic velocity structure of the Archaean crust (Kaapvaal and Zimbabwe cratons and Limpopo Belts) was found to vary considerably, with some regions having a high

Vs layer in the lower crust. For example, a relatively thick Archean crust (~39 km) with a high basal velocity (Vs ~ 4.0 km/s) was found to be present in the eastern part of the KC. The regions within the KC lacking a high Vs layer generally coincided with the extent of the Ventersdorp Supergroup, suggesting a genetic link.

- In the Proterozoic crust, considerable variation was found in Vs and the depth of the Moho.
- Little variation was found in Vs in the uppermost mantle (Moho to 70 km) of southern Africa. Sn was in the range 4.5-4.7 km/s.
- Silver et al. (2001, 2004) showed that the seismic anisotropy correlated with fossil tectonic fabrics rather than with present-day plate tectonic motions. Several domains (coincident with the lower crustal Vs variations found in this study) were recognised within the Archaean cratons.
- This study also provided new constraints on the structure and evolution of two first-order features of the South African crust, the Bushveld Complex and the Beattie Magnetic Anomaly.

5.4.3 Structural evolution of the Archaean cratonic regions

5.4.3.1 The eastern parts of the KC and ZC

Geochronological studies of the KC (e.g. Poujol et al., 2003) point to the early stages of craton formation to have occurred in the eastern part of the KC where the oldest rocks (granite-greenstone sequences) in the Swaziland terrain amalgamated to form a proto-cratonic block. The anomalously high temperatures and devolatization during the Archaean were favourable to the creation of stiff and adiabatic subcratonic mantle roots (e.g. Pollack, 1986). Probably towards the inception of the Mesoarchaean period, the eastern cratonic protolith already had a lithospheric mantle root with high viscosity and could effectively divert heat from the surrounding mantle either to its margins or beneath the juvenile adjacent cratonic fragments that were being accreted to its margins. This would imply that during these early stages of cratonization, the old eastern cratonic block already had a much more developed mantle root compared to the other adjacent blocks accreting onto it.

Seismological studies show the lithospheric mantle root beneath the KC to be ~150–200 km thick. The thicknesses of these lithospheric mantle roots were probably attained prior to the formation of diamonds which have been dated at 3.2–3.4 Ga (Durrheim and Mooney, 1994 and references therein). However, it is not clear whether the thickening of these sublithospheric roots formed synchronously or asynchronously beneath the cratonic subdomains that were being accreted. It is reasonable to make a deduction that these mantle roots were acquired asynchronously based on the present-day geological differences seen within the cratonic platforms. Each of these cratonic units were affected differently throughout geological time by tectonic events and as such exhibit different geological characters in their crustal architectures. The exposure of the accretionary margins and the accreting cratonic subdomains to heat derived from events such as mantle plume activity over a period of million years during the Archaean would imply that areas of mechanical lithospheric weakness either within the cratonic subdomains or accretionary margins of the cratons were exploited by magmatic intrusions from the mantle during and subsequent to cratonization.

The evolution of early Archaean crust (~3.5 Ga) in the eastern part of the KC involved komatiitic intrusions along the axes of mid-ocean ridges, resulting in the formation of oceanic crust (McCarthy and Rubidge, 2006 and references therein). The subduction of oceanic crust formed magmas enriched with granodiorites and basalts. The extruding magma occurred in an island arc-type of setting and these island arcs could not be subducted due to their buoyancy. Lateral accretion of these island arcs in processes similar to modern day plate tectonics resulted in the formation of a felsic upper crust characterized by the presence of potassium-rich granites, greenstones and trondhjemite-tonalite-granodiorite (TTG) gneiss terrains and also a lower crust that has a primitive mafic composition and most probably enriched with magnesium. These granite and TTG gneiss terrains are predominantly exposed in the eastern part of the KC and both the eastern and central parts of the ZC (see Figure 1.2). The TTG terrains predominantly form part of the felsic upper crust in the eastern Pilbara Craton (Western Australia) suggesting similar geochronology and mechanisms of formation as with the eastern part of the KC (e.g. Zegers and van Keken, 2001).

Figure 5.2 is a model by Silver et al. (2004, 2006) based on SKS studies of mantle anisotropy, which provides a detailed summary of a sequence of the magmatic events in both the KC and ZC and the stress interactions that facilitated their genesis. The high velocities ($V_s \geq 4.0$ km/s) in the lowermost crust and the fairly thick crust (~39 km) in the eastern part of the KC (see Swaziland and Pietersburg terrains in Table 2.1) coincide with an isotropic mantle pattern (see Figures 1.3 and 5.2), which implies that the eastern shield of the KC has been stable since 2.9 Ga. This stability is evidenced by the presence of granite and gneiss terrains which have remained intact since their formation during Archaean times. This is in contrast to the western part of the KC which has been extensively deformed by the Ventersdorp tectonomagmatic event (~2.7 Ga) and has a comparatively thinner crust (~36–37 km) with a low basal velocity ($V_s \leq 3.9$ km/s) (see Table 2.1 and Figure 2.7 in Chapter 2). The high viscosity of early Archaean lithosphere in the eastern part of the KC was probably due to the high MgO content than Fe content and therefore was resistant to deformation or subduction (e.g., Pollack, 1986; de Wit et al., 1992 and references therein).

This could imply that late Archaean craton development (mainly in the western parts of the KC and ZC) was characterized by depleted amounts of MgO and gradually cooling temperatures. Due to these changing conditions, the Archaean crust, especially in the western parts of the KC and ZC, was probably more susceptible to magmatic intrusions and deformation. These variations in both MgO and the thermal regime during the Archaean could have been partially or entirely responsible for differences in the crustal evolution of the eastern and western parts of both the KC and ZC. These differences are reflected in the low and high Vs in the lowermost crust of the western and eastern parts of both cratons, respectively (see Figure 2.7). Furthermore, the eastern part of the KC shows a crust that is thicker than that in the western part of the KC. These variations within the Archaean cratons were not taken into account in the model of Durrheim and Mooney (1994).

5.4.3.2 The western and central part of the KC and ZC

The strong mantle anisotropic pattern (shown in Figures 1.3 and 5.2) in the western part of the KC (i.e., the Kimberley region) is spatially coincident with the low velocity ($Vs < 4.0$ km/s) layering in the lowermost crust and a thin Archaean crust seen in that part of the KC (see Table 2.1 and Figure 2.7 in Chapter 2). These coincidences are replicated in the western part of the Tokwe terrain in the ZC.

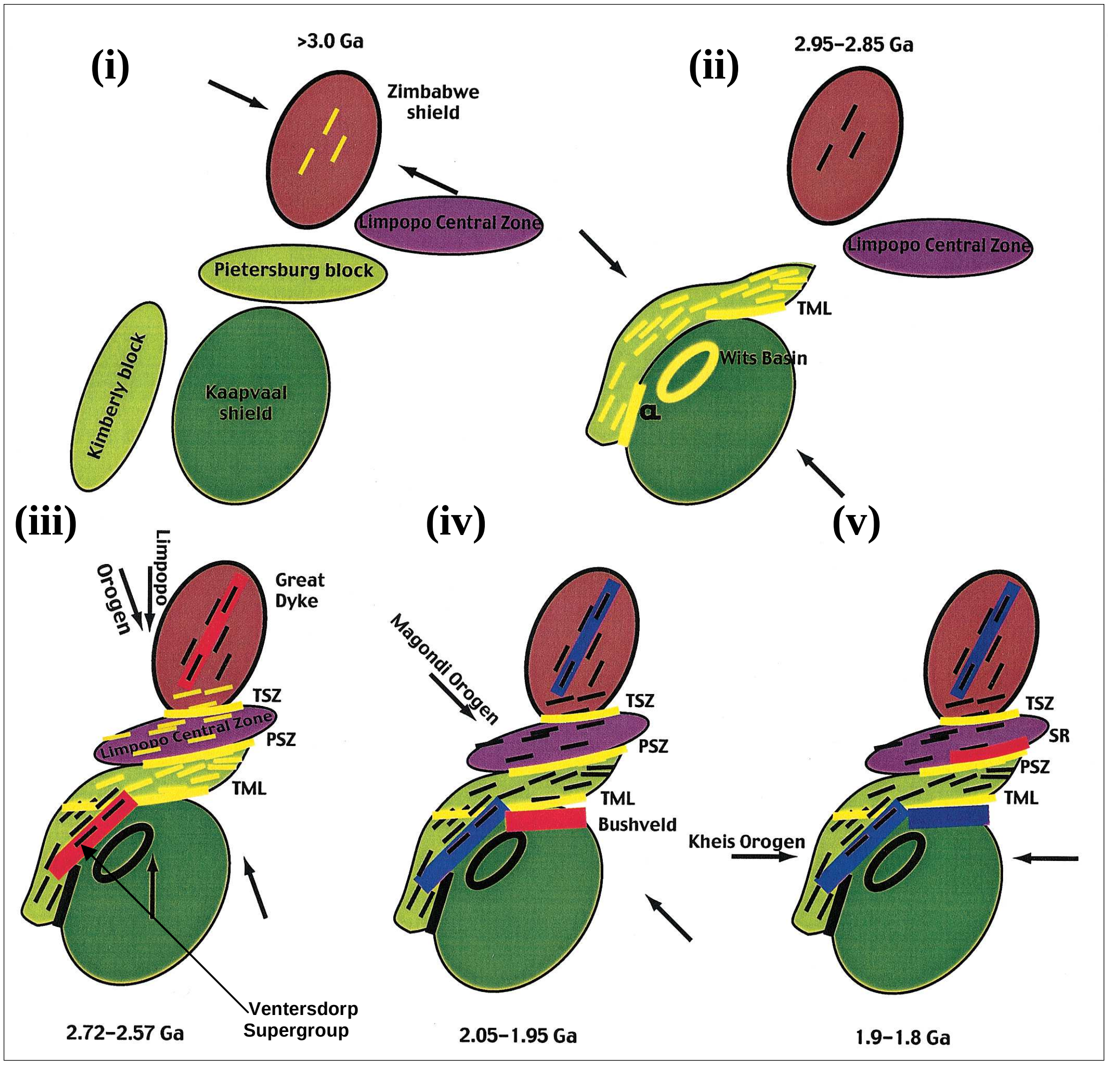

Figure 5.2 Model of crustal evolution spanning a period of 3.0 – 1.8 Ga. The model is based on anisotropic studies of the mantle in southern Africa. The arrows show direction of compressional stress induced either by the orogens or collision of continental fragments. The short lines indicate orientation of the mantle fabric which is either being formed (in yellow) or fossilized (black). The red (blue) bars indicate magmatic activity that **is occurring** (**has occurred**). The yellow (black) ellipses indicate orientation of the mantle fabric that **is being formed** (**has fossilized**). **(i).** Northeast-southwest trending mantle fabric in ZC and the isotropic structure in the eastern part of the KC were formed ca. > 2.9 Ga. **(ii).** Around 2.9 Ga, collisional assembly of terrains occurred along the northern and western rims of the KC and accompanying this, was the formation of the northeast-southwest to east-west trending arc of lithospheric mantle fabric. **(iii).** Development of eastwest to northeast-southwest trending mantle fabric, continued during and within the 2.7 Ga orogenic event of the Limpopo Belt and its marginal zones within the KC and ZC. Around this time, the Great Dyke in ZC was emplaced and the Ventersdorp Supergroup in the KC was deposited. **(iv).** The Bushveld magmatic event was produced through the collisional rift created by the Magondi Orogen and the Limpopo Belt. The east-west oriented intrusion of the Bushveld magma was controlled by pre-existing mantle fabric. **(v).** The compression of the Kheis Orogen into the KC, created the collisional Soutpansberg Rift (SR). This diagram was reproduced from Silver et al. (2004).

These crustal features in the western part of both cratons could be the consequence of alternating periods of tectonic extension and compression exploiting a mechanically weak lithospheric structure within the KC. These tectonic stress interactions resulted in a “simple tectonic style” of deformation in certain situations and were responsible for creating conditions favourable for the generation of a series of Mesoarchaean basins in the central and eastern parts of the KC i.e., Dominion (~3.1–3.0 Ga), Pongola (~2.9 – 2.7 Ga) and the Witwatersrand (~3.0–2.8 Ga). A “simple tectonic style” of deformation is defined as a stress regime where neither extensional nor compressional stresses dominate (see Clendenin et al., 1988).

The mixed Vs and anisotropic signatures seen in the Witwatersrand terrain (see Figures 1.3 and 2.7) could mean that the simple mechanism of tectonic deformation was more predominant in the Witwatersrand Basin than the Dominion and Pongola basins. The predominance of this mechanism in the Witwatersrand Basin is further corroborated by the following:

1. Current geochronological data indicate regionalized strike-slip motion (transpression) during the deposition of the Central Rand Group (upper layer of the Witwatersrand Basin) and regionalized transtension during the deposition of the West Rand Group (lower layer of the Witwatersrand Basin) (McCarthy, 2006 and references therein). These regional stresses where significant during Witwatersrand age (much later than the Dominion formation period) around the period when the KC and ZC were converging and finally amalgamating (see McCarthy, 2006 and references therein).
2. Both the Pongola and Witwatersrand basins were formed during more or less the same period. However, the Witwatersrand Basin is spatially located more at the centre of the KC (in the Witwatersrand terrain) than the Pongola Basin (located in the Swaziland

terrain) (see Figures 1.1 and 1.2). As such the formation of the Wiwatersrand Basin was more influenced by the regional stresses (indicated above) than the Pongola Basin and was further influenced by a host of other regional deformational episodes: (i) the thrusting from the north associated with the emplacement of the BC, (ii) east-west, dextral strike slip faulting, and (iii) northwesterly directed thrusting associated with the formation of the NNB.

Extensional tectonics together with a simple style of tectonic deformation (in certain cases), was responsible for triggering conditions that led to the formation of igneous, volcano-sedimentary and metasedimentary supracrustal basins scattered in the western, northern and central parts of the KC (see Figure 1.2) i.e., Ventersdorp (~2.7 Ga), Transvaal (~2.6–2.2 Ga), Olifantshoek (~2.0–1.8 Ga), the BC (~2.06 Ga), Waterberg (~2.0–1.7 Ga), Soutpansberg (~2.0–1.7 Ga), Karoo (~280–180 Ma) (e.g. Eglington and Armstrong, 2004; Johnson et al., 2006a). The low Vs signatures in the western part of the KC (including a part of the Kheis Province and the Witwatersrand terrain; see Figure 2.7) are spatially coincident with the occurrence of the Ventersdorp rocks, of which the underlying lower crust could have been delaminated by the Ventersdorp volcanism. The Karoo Basin is perhaps an exception because it is not geographically confined to the cratonic regions. The sedimentary component of the Karoo Basin evolved out of subglacial and marine depositions in depressions and downwarped zones (Johnson et al., 2006b and references therein), whereas the volcanic component was primarily due to rifting associated with Gondwana fragmentation (e.g. Duncan and Marsh, 2006 and references therein). Similar interpretations could be made for the ZC where the western cratonic subdomain of the Tokwe terrain was disrupted by rift sequences (3.1–2.95 Ga) and at a later stage, stress interactions upon pre-existing lithospheric weakness generated a north-south lying tectonic structure (i.e., the Great Dyke) emplaced by a major tectonothermal event circa 2.58 Ga across the central part of the ZC (Jelsma and Dirks, 2002).

5.4.3.3 The Limpopo Belt

The crustal features (i.e., crustal thickening and high-velocity basal layer in the crust) (see Table 2.1, Figures 2.4 and 2.7) of the Limpopo Belt (LB) tend to be quite significant in the Central Zone and can also be seen in similar polymetamorphic sutured terrains in other parts of the globe e.g. Superior Province (Gibb et al., 1983), Yilgarn Craton (Drummond, 1988), the Tanzania Craton (Nyblade and Pollack, 1992). The LB evolved out of a series of orogenic events that occurred sometime around the Neoarchaean to Palaeoproterozoic period. Collisional orogenesis in the form of crustal thickening-related collision (convergence of the KC and ZC), deformation, folding, high-grade metamorphism, magmatism, uplift, and exhumation was primarily responsible for the formation of a number of shear zones (e.g. Palala Shear Zone, see Figures 1.1 and 1.2), and the present-day crustal structure of the LB (e.g. Kramers et al., 2006 and references therein). The collisional orogenesis of the LB was pivotal in the amalgamation of the KC and ZC circa 2.6 Ga.

The crustal features of the LB are, in some ways, similar to those seen beneath the BC. It should however be noted that there are differences both in terms of genesis and structure between the two tectonic terrains. The BC is more of a layered igneous intrusion that could have possibly been initiated by mechanism such as mantle plume magmatism (e.g. Hatton, 1995; McCarthy and Rubidge, 2006 and references therein) whereas the LB is more of a tectonometamorphic structure that evolved from orogenic processes at several geological periods and therefore had a protracted and complex structural history than the BC. The most significant differences between the LB and BC are:

(1) The LB is about 5 km thicker than the BC. Moreover, the crustal thickening effect in the BC tends to be concentrated around areas where there have been significant isostatic adjustments that resulted in Moho depressions due to magma intrusion. Station SA47 in Figure 3.11 is an example of such an area. In contrast, crustal thickening in the LB (especially in the Central Zone) seems to have been ubiquitous (see Table 2.1, Figures 2.4 and 3.11);

(2) the mafic layer (Vs > 4.0 km/s) in the lower crust seems to be thicker in the Central Zone of the LB.

These structural differences between the two terrains suggest that crustal thickening in the LB (especially in the Central Zone) was a combined effect of thrusting (continental collision) and magmatic underplating.

5.4.3.4 The Bushveld Complex

The original Archaean crustal structure in the BC (in the northern part of the KC) and the western part of the KC (Kimberley region) was disrupted by the Bushveld (~2.06 Ga) and the Ventersdorp (~2.7 Ga) magmatic events, respectively. Therefore, it could be expected that the crust in both regions will display the same or similar structural crustal features. However, structural differences between these two crustal regions may be attributed to two factors that could have determined the way in which the Archaean crust around the BC and in the western part of the KC was to be modified:

1. Parental magma of the events had different compositions. The Ventersdorp event was probably dominated by an intermediate and felsic type of magma, while Bushveld

event was more of a mafic type (e.g. van der Westhuizen et al., 2006 and the references therein; Cawthorn et al., 2006 and the references therein). Hence, the BC event produced a layered complex of mafic rocks in the crust whereas the Ventersdorp event produced irregular successions of volcanic (mafic and felsic) and sedimentary formations in the crust.

2. Significant amounts of mantle melts relating to the Ventersdorp event intruded the crust all the way to the surface, whilst some of the magma melts of the Bushveld were impeded by pre-existing crustal rocks of the Transvaal Supergroup (~2.6–2.2 Ga) (e.g. Hatton, 1995). In essence, this means magmatic underplating could occur beneath the BC and could not occur in the western part of the KC. The magmatic underplating beneath the BC produced a high-Vs basal layer in the crust and also thickened the crust as confirmed by the results in Table 3.1 and Figure 3.11 (Chapter 3).

5.4.4 Structural evolution of the Proterozoic and Phanerozoic regions

5.4.4.1 Proterozoic terrains

Overall, Archaean cratonic terrains have been supported by a thick and deformation-resistant lithospheric mantle root (although asynchronously formed as noted in 5.4.3.1). Seismological studies have noted this thick mantle root to be lacking beneath Proterozoic terrains (e.g. James et al., 2001; Fouch et al., 2004). Towards the inception of the Proterozoic period, the Earth cooled and mantle temperatures became lower than during early Archaean and this resulted in the alteration of magma composition from komatiites to basalts (e.g. Durrheim and Mooney, 1994 and references therein). More heat was being diverted to the mantle beneath young peripheral units accreting onto the cratonic regions.

As a result, the mantle beneath Proterozoic terrains was continuously fertilized by partial melting and triggered magmatism in the overlying young crustal subdomains. Magma intruded the crust either through rift structures or crustal-scale shear zones created by extensional or thrust tectonics. The intruding magma eventually caused large structural deformation in the overlying crust. Crustal growth in southern Africa during the Proterozoic was characterized by the formation of the NNB (~1.2–1.0 Ga), Kheis Province (~2.0–1.7 Ga), and the LB (~3.5–2.0 Ga) on the southern, western and northern margins of the KC, respectively (see Figures 1.1 and 1.2). The Okwa-Magondi Belt (~2.0–1.8 Ga) accreted on the western margin of the ZC. The growth of Proterozoic crust on a fertile mantle, as suggested by the model of Durrheim and Mooney (1994), means mantle melts were rich in FeO and other volatiles during the Proterozoic period and therefore magmatic influxes into the overlying crust were enriched with FeO and other iron oxide compounds.

Crustal extension and rifting, repeated magmatism, repeated continental-arc collisions, subduction, intense deformation and high-grade metamorphism are some of the occurrences that were fundamental in generating a Proterozoic crust which among other things is characterized by high heat flow ($\geq$ 40 mW/m^2) (e.g. Nyblade and Pollack, 1993a,b; Jones, 1998), a high-velocity (Vs $\geq$ 4.0 km/s) basal layer in the crust and crustal thickening. With the exception of high heat flow, the results for the Proterozoic terrains indicated in Tables 2.1 and 4.2 and further shown in Figures 2.4 and 4.7 are a confirmation of the Proterozoic crust-forming process indicated above. These crustal features are typical of other Proterozoic settings globally. An additional aspect of the tectonometamorphic evolution was the formation of crustal remanent magnetic anomalies which exist as mineral assemblages predominantly within the metamorphic (e.g. granulites) and igneous (e.g. anorthosite) rocks of Proterozoic terrains. In situations like this, remanent magnetization is usually dominant and greater than induced magnetization. These crustal remanent magnetic anomalies, similar to the BMA (see sections 4.1, 4.2 and 4.5 of Chapter 4), are located at upper to mid-crustal depths, and span tens or hundreds of kilometres across Proterozoic terrains. The complex generation of these crustal remanent magnetic anomalies in Proterozoic terrains is quite a distinctive and a unique character characterizing Proterozoic crust (e.g. McEnroe et al., 2009).

5.4.4.2 Phanerozoic region - the Cape Fold Belt

The Cape Supergroup and other Precambrian-Cambrian rocks accreted on the southern margin of the NNB and were later deformed during the Cape Orogeny (~278–230 Ma) by thrust-type tectonics to form the Phanerozoic Cape Fold Belt (CFB) (e.g. Newton et al., 2006). The formation of the CFB on the southern margin of the NNB augmented the size of the southern African shield. In this study I have imporved the velocity-depth models for the CFB based on better resolved Rayleigh wave group velocity tomography (Raveloson et al., 2012). An example is shown in Figure 5.3. Station SA02 is, according to Figure 2.1, located in the middle of the CFB. The average crustal thickness estimate at this station (showed by the gray curve on the far right on row i) is around 37.5 km and is similar to estimates of 36.0 and 38.5 km obtained by Nguuri et al. (2001) and Nair et al. (2006), respectively. The crustal thickness estimate is further consistent with the global average crustal thickness of Palaeozoic orogens (in non-European continents), which, according to Rudnick and Fountain (1995), is 37.43 ± 3.95 km. Figure 5.3 further shows that the CFB has a thick (±17 km) mafic layer in the lower crust.

Current models on the formation of the CFB suggest the following (Newton et al., 2006 and references therein):

1. The CFB is a typical basin that has underwent inversion tectonics (i.e. from subsidence to uplift). However, much is still unknown about the deep structure of the fold belt.
2. In the absence of direct evidence of the proximity of a subduction zone or the lack of typical features indicative of subduction, there is a possibility that a pre-existing crustal shear zone, dipping shallowly to the south, formed a major thrust fault above which an imbricate zone formed. Most probably, much of thrusting and folding occurred above this shear zone.
3. North-verging folding and thrusting initiated thin-skinned deformation (perhaps together with sporadic thick-skinned deformation) in the upper crust, including the cover rocks of the Karoo Basin.

Within the context of current postulates (as indicated above) it is quite possible that the presence of a substantial mafic layer in the lower crust (as shown in Figure 5.3), originated from mafic melts that were underplated as a result of continental collision. Probably this collision was northward and involved the sutured Palaeozoic orogen (initial crustal fragment of the CFB) thrusting onto the southern margin of the NNB.

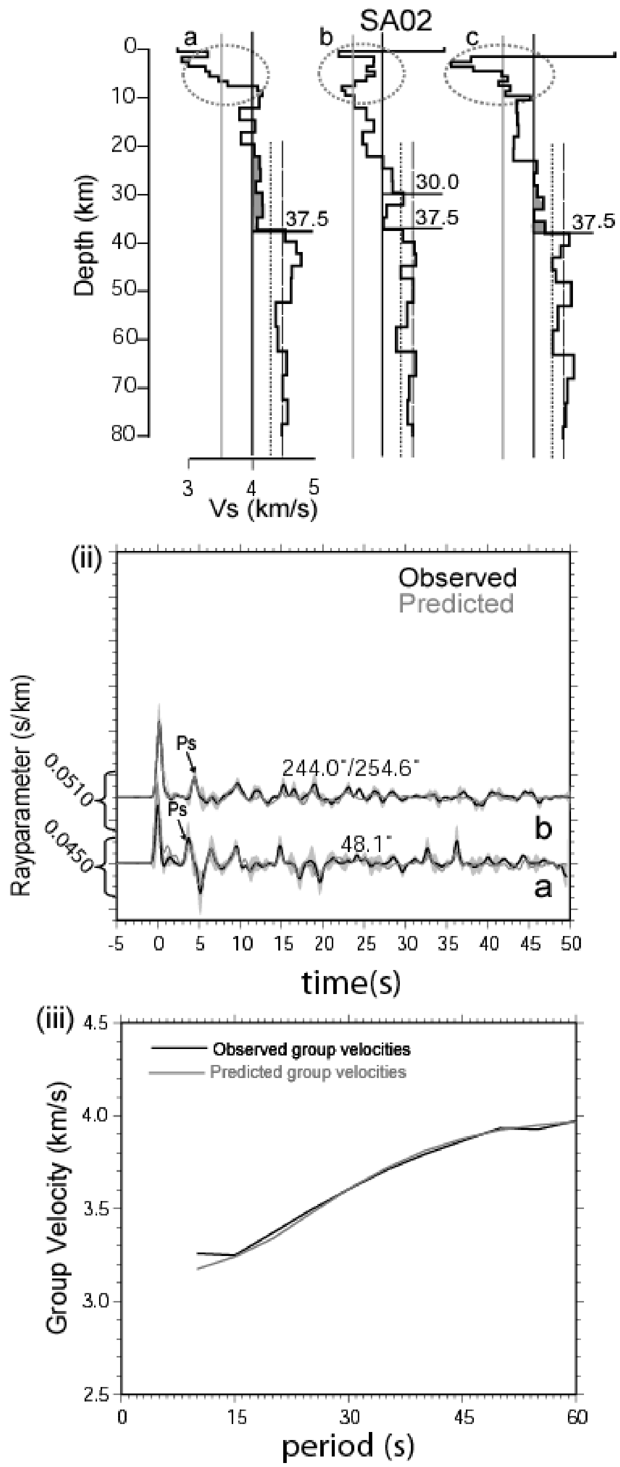

Figure 5.3 Joint inversion results for station SA02 in the CFB. (i). Shear wave velocity profiles obtained from the joint inversion for each of the receiver function stacks at backazimuths (a) and (b) indicated on top of the receiver function stacks in (ii). The Vs profile at (c) on the far right is representative of the combined inversion of the stacks at backazimuths (a) and (b). Lower crustal depths with Vs ≥ 4.0 km/s are shaded and reference lines at 4.0 km/s (solid), 4.3 km/s (dotted), and 4.5 km/s (dashed) are shown in each profile. The Vs profile without shading show two Moho depths and indicate two increases above 4.3 km/s on the Vs profiles. (ii). Observed (black curves) and predicted (light-gray curves) high-frequency receiver functions with 1σ error bounds shown with gray shading around the observed receiver functions. The position of the Moho conversion phase (Ps) is shown. (iii). Observed (black curves) and predicted (gray curves) group velocities.

References

Adam, J.M.-C., and Lebedev, S., 2012. Azimuthal anisotropy beneath southern Africa from very broad-band surface-wave dispersion measurements. *Geophysical Journal International*, 191, 155 – 174.

Barros, L.V., and Assumpção, M., 2011. Basement depths in the Parecis Basin (Amazon) with receiver functions from small local earthquakes in the Porto dos Gaúchos seismic zone. *Journal of South American Earth Sciences*, 32, 142 – 151, doi:10.1016/j.jsames.2011.04.002.

Calkins, J.A., Zandt, G., Gilbert, H.J., and Beck, S.L., 2006. Crustal images from San Juan, Argentina, obtained using high frequency local event receiver functions. *Geophysical Research Letters*, 33, L07309, doi:10.1029/2005GL025516.

Cawthorn, R.G., Eales, H.V., Walraven, F., Uken, R.and Watkeys, M.K., 2006. The Bushveld Complex, *In*: M. R. Johnson, C. R. Anhaeusser, R. J. Thomas (Editors), *The Geology of South Africa*, Geological Society of South Africa, Johannesburg/ Council for Geoscience, Pretoria, 261 – 281.

Clendenin, C.W., Charlesworth, E.G., and Maske, S., 1988. Tectonic style and mechanism of early Proterozoic successor basin development, southern Africa. *Tectonophysics*, 156, 275 – 291.

Curtis, A., Nicolson, H., Halliday, D., Trampert, J., and Baptie, B., 2009. Virtual seismometers in the subsurface of the Earth from seismic interferometry. *Nature Geoscience*, 1 – 5, doi:10.1038/NGEO615.

De Wit, M.J., Roering, C., Hart, R.J., Armstrong, R.A., Ronde, C.E.J., Green, R.W.E., Tredoux, M., Peberdy, E., Hart, R.A., 1992. Formation of an Archaean continent. *Nature*, 357, 553 – 562.

Drummond, B.J., 1988. A review of crust/upper mantle structure in the Precambrian areas of Australia and implications for Precambrian crustal evolution. *Precambrian Research*, 40/41, 101 – 116.

Durrheim, R.J., and Mooney, W.D., 1994. Evolution of the Precambrian lithosphere: constraints from seismological and petrochemical constraints. *Journal of Geophysical Research*, 99, B8, 15359 – 15374.

Durrheim, R.J., and Webb, S.J., (Eds) 1998. *South African Geophysical Review*, Vol. 2, Special issue: Geophysical Framework of the Kaapvaal Craton, ISSN 1021-4461.

Eglington, B.M., and Armstrong, R.A., 2004. The Kaapvaal Craton and adjacent orogens, southern Africa: a geochronological database and overview of the geological development of the craton. *South African Journal of Geology*, 107, 13 – 32.

Fouch, M.J., James, D.E., VanDecar, J.C., van der Lee, S., and the Kaapvaal Seismic Group, 2004. Mantle seismic structure beneath the Kaapvaal and Zimbabwe Cratons. South *African Journal of Geology*, 107, 33 – 44.

Gibb, R. A., Thomas, M.D., Lapointe, P., and Mukhopadhay, M., 1983.Geophysics of proposed Proterozoic sutures in Canada.*Precambrian Research*, 19, 349 – 384.

Hatton, C.J., 1995. Mantle plume origin for the Bushveld and Ventersdorp magmatic provinces. *Journal of African Earth Sciences*, 21, 4, 571 – 577.

James, D.E., Fouch, M.J., VanDecar, J.C., van der Lee, S., and Kaapvaal Seismic Group, 2001. Tectospheric structure beneath southern Africa. *Geophysical Research Letters*, 28, 13, 2485 – 2488.

Jelsma, H. A. and Dirks, P.H.G.M., 2002.Neoarchaean tectonic evolution of the Zimbabwe Craton. In C.M.R. Fowler, C.J. Ebinger and C.J. Hawkesworth (Editors), *The Early Earth:*

Physical, Chemical and Biological Development. Geological Society of London, Special Publications, 199, 183 – 211.

Johnson, M.R., Anhaeusser, C.R., and Thomas, R.J., 2006a. *The Geology of South Africa*. Geological Society of South Africa, Johannesburg/ Council for Geoscience, Pretoria, 691 pp.

Johnson, M.R., Van Vuuren, C.J., Visser, J.N.J., Cole, D.I., Wickens, H.de V., Christie, A.D.M., Roberts, D.L., and Brandl, G., 2006b. Sedimentary rocks of the Karoo Supergroup. *In*: M. R. Johnson, C. R. Anhaeusser, R. J. Thomas (Editors), *The Geology of South Africa*, Geological Society of South Africa, Johannesburg/ Council for Geoscience, Pretoria, 461 – 499

Jones, M.Q.W., 1988. Heat flow in the Witwatersrand basin and environs and its significance for the South African Shield geotherm and lithosphere thickness. *Journal of Geophysical Research*, 93, 3243 – 3260.

Jones, M.Q.W., 1998. A review of heat flow in southern Africa and the thermal structure of the lithosphere. *Southern African Geophysical Review*, 2, 115 – 122.

Julià, J., Ammon, C.J., Hermann, R.B., Correig, A.M., 2000. Joint inversion of receiver functions and surface-wave dispersion observations. *Geophysical Journal International*, 143, 99 – 112.

Julià, J., Ammon, C.J., Hermann, R.B., 2003. Lithospheric structure of the Arabian Shield from the joint inversion of receiver functions and surface-wave group velocities. *Tectonophysics*, 371, 1 – 21.

Kennedy, C.S., and Kennedy, G.C., 1976. The equilibrium boundary between graphite and diamond. *Journal of Geophysical Research*, 81, 2467 – 2470.

Kgaswane, E.M., Nyblade, A.A., Julià, J., Dirks, P.H.G.M., Durrheim, R.J., and Pasyanos, M.E., 2009. Shear wave velocity structure of the lower crust in southern Africa: Evidence for compositional heterogeneity within Archaean and Proterozoic terrains. *Journal of Geophysical Research*, 114, B12304, doi:10.1029/2008JB006217.

Kramers, J.D., McCourt, S., and van Reenen, D.D., 2006. The Limpopo Belt, *In*: M. R. Johnson, C. R. Anhaeusser, R. J. Thomas (Editors) *The Geology of South Africa*, Geological Society of South Africa, Johannesburg/ Council for Geoscience, Pretoria, 209 – 236.

Lindeque, A., de Wit, M.J., Ryberg, T., Weber, M., and Chevalier, L., 2011. Deep crustal profile across the southern Karoo Basin and Beattie Magnetic Anomaly, South Africa: an integrated interpretation with tectonic implications. *South African Journal of Geology*, 114, no. 3 – 4, 265 – 292. doi:10/2113/gssajg.114.3-4.265

McCarthy, T.S., 2006. The Witwatersrand Supergroup, *In*: *The Geology of South Africa* edited by M. R. Johnson, C. R. Anhaeusser, R. J. Thomas, pp. 155–186, *Geological Society of South Africa*, Johannesburg and the Council for Geoscience, Pretoria, South Africa.

McCarthy, T.S., and Rubidge, B., 2006. *The story of Earth & Life: A southern African perspective on a 4.6-Billion-Year Journey*. Cape Town, Struik Publishers, 333 pp.

McEnroe, S.A., Fabian, K., Robinson, P., Gaina, C., and Brown, L.L., 2009. Crustal magnetism, lamellar magnetism and rocks that remember. *Elements*, 5, 241 – 246. doi: 10.2113/gselements.5.4.241

Newton, A.R., Shone, R.W., and Booth, P.W.K., 2006. The Cape Fold Belt, *In*: M. R. Johnson, C. R. Anhaeusser, R. J. Thomas (Editors) *The Geology of South Africa*, Geological Society of South Africa, Johannesburg/ Council for Geoscience, Pretoria, 521 – 530.

Nair, S.K., Gao, S.S., Kelly, H.L. and Silver, P.G., 2006. Southern African crustal evolution and composition: Constraints from receiver function studies. *Journal of Geophysical Research*, 111, B02304, doi:10.1029/2005JB003802.

Nguuri, T.K., Gore, J., James, D.E., Webb, S. J., Wright, C., Zengeni, T.G., Gwavava, O., Snoke, J.A., and Kaapvaal Seismic Group, 2001. Crustal structure beneath southern africa and its implications for the formation and evolution of the Kaapvaal and Zimbabwe Cratons. *Geophysical Research Letters, 28*, 13, 2501 – 2504.

Nguuri, T., 2004. Crustal structure of the Kaapvaal Craton and SURrounding mobile belts: analysis of teleseismic P waveforms and Surface wave inversions, Ph.D. thesis (unpublished), University of the Witwatersrand.

Nyblade, A.A., and Pollack, H.N., 1992. A gravity model for the lithosphere in western Kenya and northeastern Tanzania.*Tectonophysics*, 212, 257 – 267.

Nyblade, A.A., and Pollack, H.N., 1993a. Can differences in heat flow between east and southern Africa be easily interpreted?: Implications for understanding regional variability in continental heat flow. *Tectonophysics*, 219, 257 – 272.

Nyblade, A.A., and Pollack, H.N., 1993b. A global analysis of heat flow from Precambrian terrains: Implications for the thermal structure of Archaean and Proterozoic lithosphere. *Journal of Geophysical Research*, 98, B7, 12207 – 12218.

Pasyanos, M.E., and Nyblade, A.A., 2007. A top to bottom lithospheric study of Africa and Arabia, *Tectonophysics*, 444, no. 1 – 4, 27 – 44.

Pollack, H.N., 1986. Cratonization and thermal evolution of the mantle. *Earth and Planetary Science Letters*, 80, 175 – 182.

Poujol, M., Robb, L.J., Anhaeusser, C.R., and Gericke, B., 2003. A review of the geochronological constraints on the evolution of the Kaapvaal Craton, South Africa. *Precambrian Research*, 127, 181 – 213.

Raveloson, A., Nyblade, A., Fishwick, S., Mangongolo, A., and Master, S., 2012. The upper mantle seismic velocity structure of central Africa and the architecture of Precambrian lithosphere beneath the Congo Basin, in: *Geology and Resource Potential of the Congo Basin*, edited by M. de Wit, F. Guillocheau, M. Fernandez-Alonso, M. de Wit, Springer-Verlag, submitted.

Ritter, J.R.R., Shapiro, S.A., and Schechinger, B., 1998. Scattering parameters of the lithosphere below the Massif Central, France, from teleseismic wavefield records. *Geophysical Journal International*, 134, 187 – 198.

Silver, P.G., Gao, S.S., Liu, K.H. and K.S. Group, 2001. Mantle deformation beneath southern Africa. *Geophysical Research Letters*, 28, 2493 – 2496.

Silver, P.G., Fouch, M.J., Gao, S.S., Schmitz, M., and Kaapvaal Seismic Group, 2004. Seismic anisotropy, mantle fabric, and the magmatic evolution of Precambrian southern Africa. *South African Journal of Geology*, 107, 45 – 58.

Silver, P.G., Behn, M.D., Kelly, K., Schmitz, M., and Savage, B., 2006. Understanding cratonic flood basalts. *Earth and Planetary Science Letters*, 245, 190 – 201.

Tiberi, C., Diament, M., Déverchère, J., Petit-Mariani, C., Mikhailov, V., Tikhotsky, S., and Achauer, U., 2003. Deep structure of the Baikal rift zone revealed by joint inversion of gravity and seismology. *Journal of Geophysical Research*, 108, B3, 2133, doi: 10.1029/2002JB001880.

Van der Westhuizen, W.A., de Bruiyn, H., and Meintjes, P.G., 2006. The Ventersdorp Supergroup, *In*: M. R. Johnson, C. R. Anhaeusser, R. J. Thomas (Editors) *The Geology of South Africa*, Geological Society of South Africa, Johannesburg/ Council for Geoscience, Pretoria, 187 – 208.

Yang, Y., Li, A., and Ritzwoller, M.H., 2008. Crustal and uppermost mantle structure in southern Africa revealed from ambient noise and teleseismic tomography. *Geophysical Journal International*, 174, 235 – 248, doi:10.1111/j.1365-246X.2008.03779x.

Zegers, T.E., and van Keken, P.E., 2001. Middle Archaean continent formation by crustal delamination. *Geology*, 29, 12, 1083 – 1086.

Zeyen, H., and Pous, J., 1993. 3-D joint inversion of magnetic and gravimetric data with *a priori* information. *Geophysical Journal International*, 112, 244 – 256.

Appendix A
List of teleseismic events used to compute receiver functions

Event number	Event date (d-m-y)	Origin time (hr:min:sec.0)	Latitude (deg)	Longitude (deg)	Depth (km)	Magn-itude (Mw)	Station list
1	14-03-1994	04:30:07.7	-1.40	-24.12	10	6.9	lbtb
2	09-06-1994	00:33:16.2	-13.84	-67.55	631	8.2	lbtb
3	30-07-1995	05:11:23.5	-23.36	-70.31	47	8.1	lbtb
4	18-02-1996	23:49:28.1	-1.27	-14.27	10	6.6	lbtb
5	02-06-1996	02:52:09.5	10.80	-42.25	10	7.0	lbtb
6	12-11-1996	16:59:44.0	-14.99	-75.68	33	7.7	lbtb
7	23-01-1997	02:15:22.9	-22.00	-65.72	276	7.1	lbtb
8	25-04-1997	09:11:34.6	-48.34	-10.04	10	5.8	sa11, sa16, sa17, sa22, sa29, sa50, sa59, sa62, sa73, sa74, sa75, sa76, sa77, sa79, sa80
9	10-05-1997	07:57:29.7	33.83	59.81	10	7.2	sa07, sa13, sa18, sa22, sa23, sa24, sa25, sa29, sa31, sa32, sa37, sa38, sa39, sa40, sa45, sa46, sa47, sa50, sa51, sa52, sa55, sa56, sa57, sa64, sa65, sa66, sa67, sa68, sa70, sa71, sa73, sa74, sa76, sa77, sa79, sa80, sa81
10	13-05-1997	14:13:45.7	36.41	70.95	196	6.4	sa07,sa11, sa17, sa18, sa22, sa23, sa24, sa25, sa29, sa30, sa32, sa37, sa38, sa39, sa40, sa45, sa46, sa47, sa50, sa51, sa52, sa55, sa56, sa57, sa59, sa60, sa62, sa63, sa64, sa65, sa66, sa67, sa68, sa70, sa71, sa74, sa76, sa77, sa78, sa80, sa81
11	06-07-1997	09:54:00.7	-30.06	-71.87	19	6.8	sa07, sa16, sa22, sa25, sa31, sa37, sa39, sa40, sa45, sa47, sa50, sa51, sa55, sa57, sa60, sa62, sa64, sa66, sa67, sa68, sa70, sa71, sa73, sa77, sa78, sa79, sa80, sa81
12	09-07-1997	19:24:13.1	10.60	-63.49	19	7.0	sa13, sa22, sa24
13	13-10-1997	13:39:37.4	36.38	22.07	24	6.5	sa22, sa29, sa37
14	15-10-1997	01:03:33.4	-30.93	-71.22	58	7.1	sa07, sa08, lbtb, sa11, sa16, sa18, sa22, sa25, sa29, sa30, sa31, sa32, sa37, sa38, sa39, sa45, sa47, sa55, sa57, sa59,

							sa60, sa61, sa62, sa63, sa64, sa65, sa66, sa67, sa68, sa70, sa71, sa72, sa73, sa74, sa75, sa76, sa77, sa78, sa79, sa80, sa81, sur
15	28-10-1997	06:15:17.3	-4.37	-76.68	112	7.2	sa07, lbtb, sa16, sa18, sa22, sa23, sa29, sa32, sa37, sa38, sa39, sa45, sa60, sa62, sa65
16	08-11-1997	10:02:52.6	35.07	87.33	33	7.5	lbtb, sa13, sa16, sa17, sa18, sa23, sa24, sa25, sa29, sa31, sa32, sa37, sa39, sa40, sa45, sa46, sa47, sa51, sa55, sa56, sa57, sa59, sa60, sa61, sa62, sa63, sa65, sa67, sa73, sa74, sa76, sa77, sa78, sa79, sa80, sa81
17	25-11-1997	12:14:33.6	1.24	122.54	24	7.0	sa13, sa16, sa17, sa18, sa23, sa24, sa25, sa30, sa31, sa32, sa38, sa39, sa40, sa45, sa47, sa50, sa51, sa55, sa57, sa59, sa61, sa64, sa65, sa68, sa71, sa72, sa73, sa74, sa75, sa76, sa77, sa78, sa79, sa80
18	28-11-1997	22:53:41.5	-13.74	-68.79	586	6.7	sa67
19	27-12-1997	20:11:01.3	-55.78	-4.22	10	6.2	sa16, sa18, sa38, sa50, sa55, sa63
20	12-01-1998	10:14:07.6	-30.99	-71.41	35	6.6	sa07, lbtb, sa11, sa13, sa16, sa169, sa23, sa25, sa29, sa32, sa38, sa47, sa55, sa59, sa61, sa62, sa63, sa64, sa65, sa68, sa70, sa71, sa72, sa74, sa76, sa78, sa80
21	30-01-1998	12:16:08.6	-23.91	-70.21	42	7.1	sa07, lbtb, sa11, sa16, sa169, sa17, sa18, sa25, sa29, sa32, sa37, sa38, sa40, sa46, sa47, sa51, sa55, sa56, sa59, sa60, sa62, sa64, sa65, sa66, sa67, sa70, sa72, sa75, sa76, sa77, sa78
22	14-03-1998	19:40:27.0	30.15	57.61	9	6.6	sa07, lbtb, sa13, sa16, sa169, sa17, sa23, sa24, sa25, sa29, sa31, sa32, sa37, sa38, sa40, sa45, sa46, sa50, sa55, sa57, sa59, sa60, sa61, sa62,

							sa63, sa65, sa66, sa67, sa68, sa70, sa71, sa72, sa74, sa75, sa77, sa79, sa81, sur
23	25-03-1998	12:17:22.5	-63.61	147.94	10	6.4	sa07, sa08, sa50, sa55, sur
24	25-03-1998	03:12:25.0	-62.88	149.53	10	8.1	lbtb, sa13, sa16, sa169, sa17, sa23, sa24, sa25, sa29, sa31, sa32, sa37, sa38, sa40, sa45, sa50, sa51, sa55, sa56, sa57, sa59, sa60, sa61, sa62, sa63, sa64, sa65, sa66, sa67, sa68, sa70, sa72, sa74, sa75, sa76, sa77, sa78, sa79, sa81, sur
25	01-04-1998	22:42:56.9	-40.32	-74.87	9	6.7	sa07, lbtb, sa16, sa169, sa25, sa29, sa50, sa57, sa72, sa74, sa76, sa77, sa78, sa81, sur
26	01-04-1998	17:56:23.3	-0.54	99.26	55	7.0	sa07, lbtb, sa23, sa24, sa25, sa29, sa31, sa32, sa40, sa45, sa46, sa50, sa51, sa55, sa56, sa72, sa74, sa75, sa76, sa77, sa78, sa79, sa81, sur
27	25-04-1998	06:07:23.4	-35.27	-17.33	10	6.3	sa04, sa05, sa09, sa169, sa19, sa34
28	21-05-1998	05:34:25.5	0.21	119.58	33	6.6	sa15, sa19, sa28, sa34, sa36, sa48
29	22-05-1998	04:48:50.4	-17.73	-65.43	65	6.6	sa05, sa48
30	30-05-1998	06:22:28.9	37.11	70.11	33	6.5	sa47, sa53, sa56
31	18-06-1998	04:17:54.9	-11.57	-13.89	10	6.3	sa04, sa09, sa13, sa15, sa19, sa25, sa26, sa28, sa34, sa35, sa36, sa37, sa42, sa48, sa50
32	24-06-1998	10:44:30.8	-37.30	-17.39	10	6.0	sa05, sa07, sa09, sa13, sa15, sa20, sa28, sa31, sa33, sa34, sa38, sa44, sa48, sa53, sa55, sa81
33	27-06-1998	13:55:52.0	36.88	35.31	33	6.3	sa40
34	03-09-1998	17:37:58.2	-29.45	-71.72	27	6.6	lbtb, sa02, sa04, sa05, sa07, sa09, sa10, sa14, sa19, sa20, sa26, sa27, sa28, sa31, sa33, sa34, sa36, sa42, sa44, sa47, sa48, sa49, sa50, sa56, sa57, sa81, sur
35	08-11-1998	07:25:48.5	-9.14	121.42	33	6.4	sa19, sa20, sa35
36	09-11-1998	05:38:44.2	-6.92	128.95	33	7.0	sa10, sa17, sa18, sa19, sa24, sa27, sa28, sa30, sa31, sa33, sa35, sa37,

							sa40, sa45, sa46, sa47, sa48, sa53, sa56
37	29-11-1998	14:10:31.9	-2.07	124.89	33	7.7	sa04, sa05, sa07, sa09, sa10, sa13, sa14, sa17, sa20, sa24, sa26, sa27, sa30, sa31, sa33, sa34, sa35, sa36, sa38, sa40, sa43, sa44, sa45, sa47, sa48, sa49, sa51, sa53, sa54, sa56, sa57, sa76, sa78
38	24-01-1999	08:00:08.5	-26.46	74.48	10	6.3	sa09, sa10, sa14, sa15, sa169, sa20, sa26, sa34, sa48, sa50, sa53
39	04-03-1999	05:38:26.5	28.34	57.19	33	6.6	bb08, bb14, bb31, sa02, sa04, sa19, sa32, sa34
40	04-03-1999	08:52:01.9	5.40	121.94	33	7.1	lbtb, bb02, bb08, bb14, bb24, bb31, sa10, sa169, sa18, sa19, sa20, sa26, sa30, sa32, sa33, sa34, sa42, sa43, sa44, sa47, sa48, sa49, sa54, sa56, sa57, sa76, sa78
41	28-03-1999	19:05:11.0	30.51	79.40	15	6.6	bb02, bb08, bb14, bb24, sa02, sa04, sa08, sa10, sa14, sa15, sa17, sa19, sa20, sa23, sa24, sa25, sa26, sa31, sa32, sa34, sa36, sa42, sa43, sa44, sa45, sa46, sa48, sa49, sur
42	29-03-1999	06:17:58.4	-4.00	87.28	10	5.8	bb02
43	03-04-1999	06:17:18.3	-16.66	-72.66	87	6.8	bb02, bb08, bb14, bb24, bb31, sa04, sa10, sa14, sa15, sa20, sa23, sa26, sa31, sa43, sa49, sur
44	06-05-1999	23:00:53.1	29.50	51.88	33	6.2	bb08, bb24, bb31
45	17-08-1999	00:01:39.1	40.75	29.86	17	7.6	lbtb, sur
46	18-06-2000	14:44:13.3	-13.80	97.45	10	7.8	lbtb, sur
47	25-10-2000	09:32:23.9	-6.55	105.63	38	6.8	lbtb
48	26-01-2001	03:16:40.5	23.42	70.23	16	7.7	lbtb, sur
49	14-11-2001	09:26:10.0	35.95	90.54	10	7.8	lbtb
50	12-12-2001	14:02:35.0	-42.81	124.69	10	7.1	sur
51	03-03-2002	12:08:19.7	36.50	70.48	226	7.4	lbtb, sur
52	21-05-2003	18:44:20.1	36.96	3.63	12	6.8	sur
53	15-07-2003	20:27:50.2	-2.60	68.38	10	7.6	lbtb
54	23-12-2004	14:59:04.4	-49.31	161.35	10	8.1	lbtb, sur
55	25-07-2004	14:35:18.6	-2.40	104.02	578	7.3	lbtb
56	23-12-2004	14:59:04.4	-49.31	161.35	10	8.1	lbtb
57	26-12-2004	00:58:50.7	3.30	95.98	30	9.0	lbtb, sur
58	01-01-2005	06:25:44.8	5.10	92.30	12	6.6	bosa, lbtb, sur
59	24-01-2005	04:16:48.1	7.37	92.45	30	6.3	bosa
60	16-02-2005	20:27:52.4	-36.32	-16.56	10	6.6	bosa, sur

61	22-02-2005	02:25:22.7	30.74	56.73	14	6.4	bosa, lbtb, sur
62	02-03-2005	10:42:12.2	-6.53	129.93	202	7.1	bosa
63	28-03-2005	16:09:36.5	2.09	97.11	30	8.7	sur
64	10-04-2005	10:29:13.4	-1.62	99.56	30	6.8	bosa, lbtb, sur
65	19-05-2005	01:54:52.8	1.99	97.04	30	6.9	bosa, sur
66	13-06-2005	22:44:33.5	-19.90	-69.13	111	7.9	bosa, sur
67	05-07-2005	01:52:04.8	1.90	97.10	30	6.7	bosa
68	24-07-2005	15:42:06.2	7.92	92.19	10	7.3	bosa, sur
69	26-09-2005	01:55:37.6	-5.68	-76.40	115	7.5	lbtb
70	02-01-2006	06:10:49.2	-60.93	-21.58	10	7.4	lbtb
71	27-01-2006	16:58:53.6	-5.47	128.10	341	7.6	lbtb
72	30-04-2006	19:17:17.2	-27.01	-70.96	26	6.6	slr
73	16-05-2006	15:28:25.9	0.09	97.05	12	6.8	slr
74	16-07-2006	11:42:45.4	-28.66	-72.39	35	6.0	sek
75	17-07-2006	15:45:59.8	-9.45	108.27	10	6.3	sek, slr
76	17-07-2006	08:19:25.0	-9.33	107.26	10	7.7	grm, sek, slr
77	20-08-2006	03:41:47.6	-61.02	-34.37	10	6.9	grm, poga, slr
78	25-08-2006	00:44:43.2	-24.32	-66.89	156	6.4	sek
79	13-11-2006	01:26:34.0	-26.08	-63.29	550	6.8	grm, hvd, mopa, pka
80	20-02-2007	08:04:27.9	-1.06	127.07	31	6.5	hvd, sek
81	03-04-2007	03:35:06.7	36.53	70.67	210	6.2	sek
82	21-07-2007	15:34:47.9	-22.33	-65.81	247	6.2	cvna
83	21-07-2007	13:27:03.7	-7.98	-71.13	633	6.1	cvna
84	08-08-2007	17:04:57.4	-5.92	107.74	282	7.4	grm, swz
85	15-08-2007	23:40:56.8	-13.36	-76.52	30	8.0	cvna, grm, mopa
86	20-08-2007	22:43:02.0	8.51	-40.16	253	6.5	hvd
87	12-09-2007	11:10:24.1	-4.37	101.56	16	7.9	pka, poga, cvna, mopa, grm, upi, sek
88	12-09-2007	23:48:59.8	-2.67	100.80	10	7.9	poga, cvna, mopa, grm, pka, upi, lbtb
89	13-09-2007	03:35:26.2	-2.28	99.59	10	6.5	pka
90	14-09-2007	06:01:34.2	-4.11	101.22	35	6.4	poga, swz, grm
91	24-10-2007	21:02:51.2	-3.91	101.06	30	7.1	mopa, upi, swz, grm
92	14-11-2007	15:40:53.0	-22.99	-69.84	60	7.7	pka, cvna, mopa, upi, sek, swz
93	15-11-2007	15:06:00.6	-22.88	-70.07	35	6.8	pka, poga, cvna, mopa, upi, sek, grm
94	08-02-2008	09:38:14.1	-10.70	-41.88	9	6.8	slr
95	10-02-2008	12:22:02.6	-60.75	-25.51	8	6.5	slr
96	23-02-2008	15:57:24.8	-57.11	-23.60	35	6.8	slr
97	25-02-2008	08:36:35.6	-2.37	100.02	35	7.3	slr
98	28-06-2008	12:54:49.6	10.82	91.76	35	6.3	slr
99	30-06-2008	06:17:43.9	-58.16	-21.89	10	6.7	slr
100	10-08-2009	19:55:39.2	14.01	92.92	33	7.6	slr

Appendix B

The Linearized Joint Inversion Scheme by Julia et al. (2000, 2003)

The joint inversion scheme developed Julia et al. (2000, 2003) inverts both surface wave dispersion observations and body wave receiver functions beneath the surface of each recording station assuming consistency and complementarity. Consistency is the requirement by which the surface wave dispersions and receiver functions sample the same part of the Earth structure. Complementarity is the desired outcome for which there is an improved constraint on the joint inversion results provided by the resolution abilities of the two data sets that are jointly inverted. As a product to the joint inversion procedure, shear wave velocity models are obtained.

In this appendix, the joint inversion of P-wave receiver functions and Rayleigh wave group velocity dispersion observations has been described as applied to determine the shear wave velocity structure of several regions of my research program. To develop the scheme of joint inversion of receiver functions and surface wave measurements, Julia et al. (2000) defined a joint prediction error or minimization for surface wave dispersion measurements and receiver functions as follows:

$$E_{s|r} = \frac{p}{N_s} \sum_{i=1}^{N_s} \left(\frac{r_{s_i} - \sum_{j=1}^{M} D_{s_{ij}} x_j}{\sigma_{s_i}} \right)^2 + \frac{1-p}{N_r} \sum_{i=1}^{N_r} \left(\frac{r_{r_i} - \sum_{j=1}^{M} D_{r_{ij}} x_j}{\sigma_{r_i}} \right)^2 \qquad \text{(B-1)}$$

where differences in physical units and number of data points for the two different data sets has been taken care of by dividing each data set using the number of data points (N_s and N_r) and standard deviations (σ_s and σ_r) of surface wave dispersion measurements and receiver functions, respectively, m is the shear wave velocity model with certain number of layers and fixed thicknesses, D_s and D_r are partial derivative matrices for the surface wave dispersion curve and receiver functions with the indices *ij* indicating the ith row and jth column element of each matrix, and r_s and r_r are the residuals for the surface wave dispersions and receiver functions. The influence factor p (with $q = 1 - p$) controls the relative influence of each data set so that p=0 inverts receiver functions alone while p=1 inverts dispersion measurements alone. The joint inversion scheme has been implemented using parameters from the joint prediction error by the following system of equations (Julia et al., 2003):

$$\begin{bmatrix} \sqrt{\frac{p}{w_s^2}} D_s \\ \sqrt{\frac{q}{w_r^2}} D_r \\ \eta\Delta \\ W \end{bmatrix} \vec{m} = \begin{bmatrix} \sqrt{\frac{p}{w_s^2}} \vec{r}_s \\ \sqrt{\frac{q}{w_r^2}} \vec{r}_r \\ \vec{0} \\ \vec{0} \end{bmatrix} \begin{bmatrix} \sqrt{\frac{p}{w_s^2}} D_s \\ \sqrt{\frac{q}{w_r^2}} D_r \\ 0 \\ 0 \end{bmatrix} \vec{m}_0 + \begin{bmatrix} 0 \\ 0 \\ 0 \\ W \end{bmatrix} \vec{m}_a \tag{B-2}$$

where $\vec{r}_s$ and $\vec{r}_r$ are vector residuals for surface wave observations and receiver functions, respectively, w_s^2 and w_r^2 are weights that equalize the data sets and are obtained from $N_s\sigma_s^2$ and $N_r\sigma_r^2$ for surface wave dispersion measurements and receiver functions, respectively, as indicated in equation (B-1), $\vec{m}$ is a vector of shear wave velocities in fixed-thickness layers overlying a half-space, $\vec{m}_0$ is the initial guess of the shear wave velocities, η is the smoothnes parameter controlling the trade-off between data fits and model smoothness, the matrix Δ constructs a second-order difference model and smoothes out the variations in the resulting Vs models and the matrix W represents a set of constraint weights for the *a priori* shear wave velocities i.e., $\vec{m}_a$.

Appendix C – Joint inversion results

infl - influence parameter smth - smoothing parameter

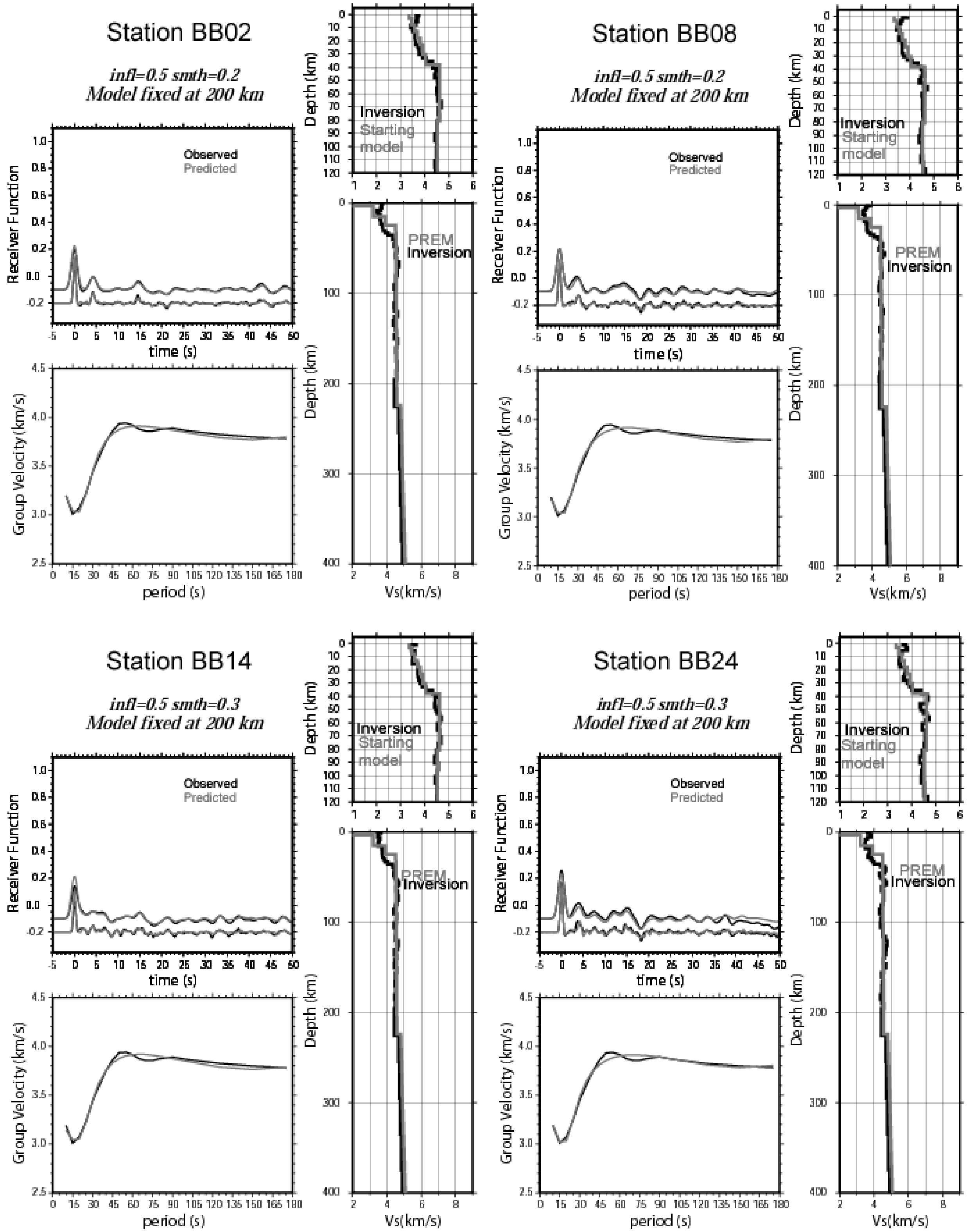

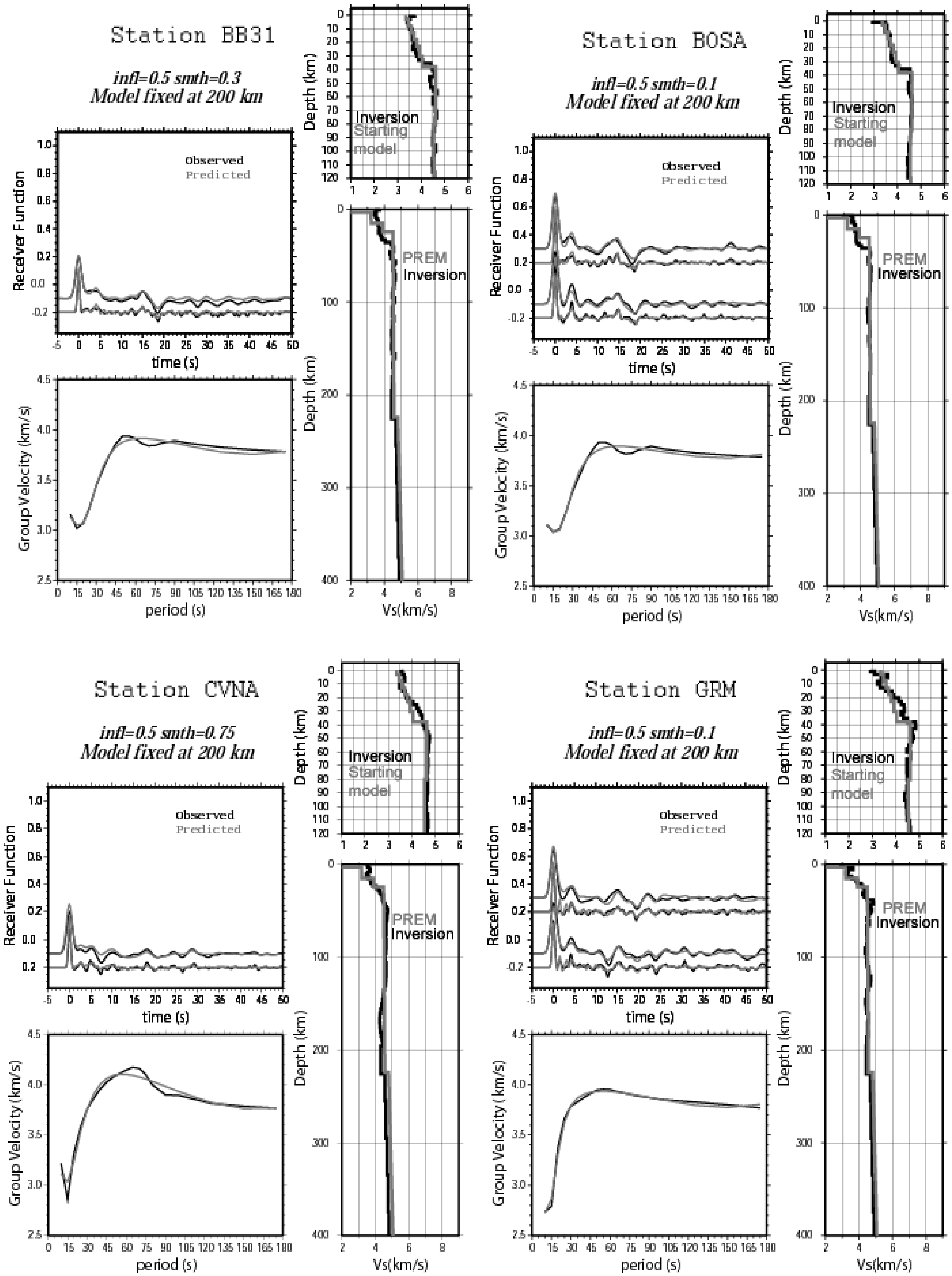
Station BB31
infl=0.5 smth=0.3
Model fixed at 200 km
Observed
Predicted
Receiver Function
time (s)
Group Velocity (km/s)
period (s)
Depth (km)
Inversion
Starting model
PREM
Inversion
Vs(km/s)
Station BOSA
infl=0.5 smth=0.1
Model fixed at 200 km
Station CVNA
infl=0.5 smth=0.75
Model fixed at 200 km
Station GRM
infl=0.5 smth=0.1
Model fixed at 200 km

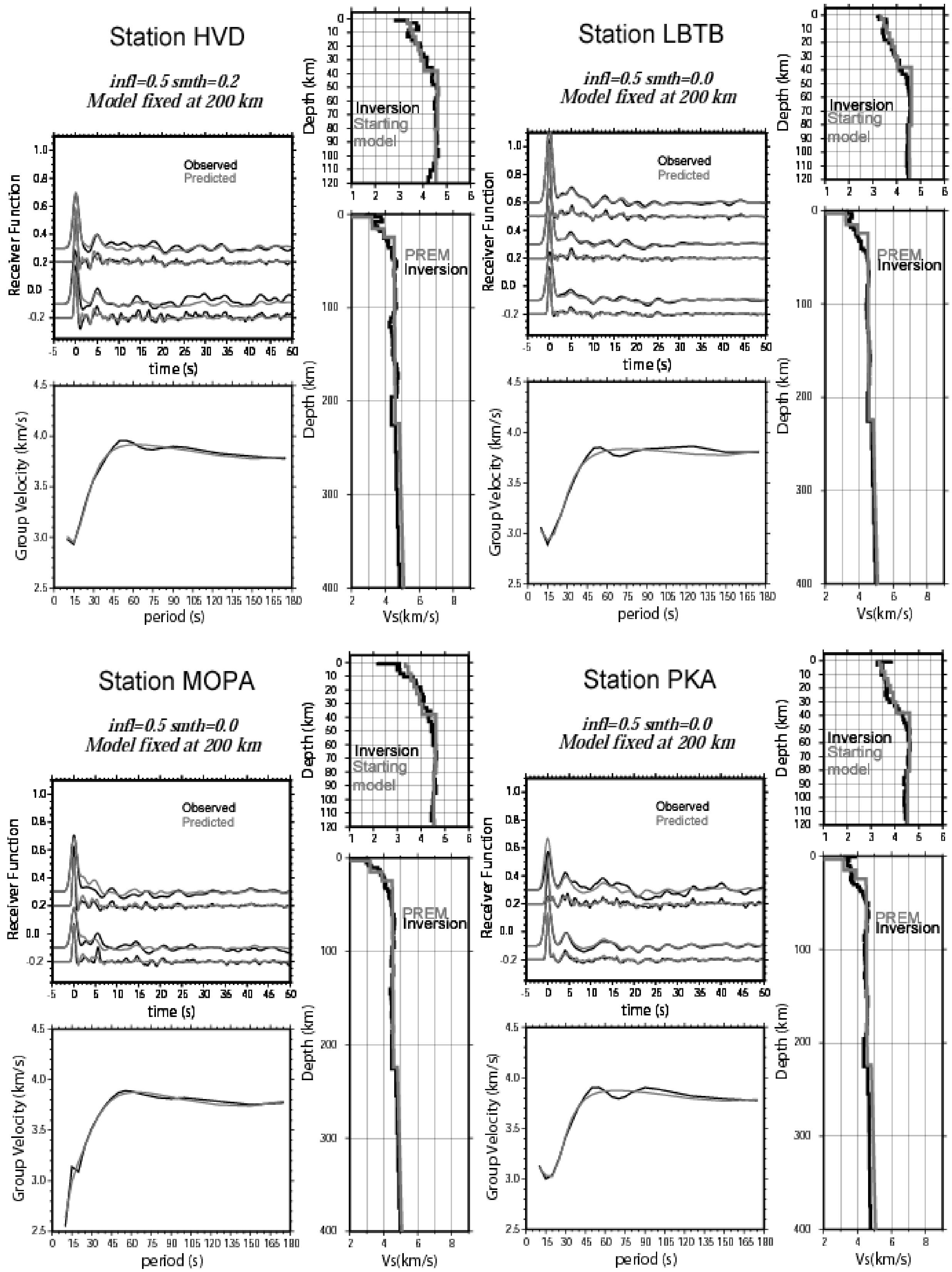

Station HVD
infl=0.5 smth=0.2
Model fixed at 200 km
Station LBTB
infl=0.5 smth=0.0
Model fixed at 200 km
Station MOPA
infl=0.5 smth=0.0
Model fixed at 200 km
Station PKA
infl=0.5 smth=0.0
Model fixed at 200 km
Observed
Predicted
Receiver Function
time (s)
Group Velocity (km/s)
period (s)
Depth (km)
Inversion
Starting model
PREM
Inversion
Vs(km/s)

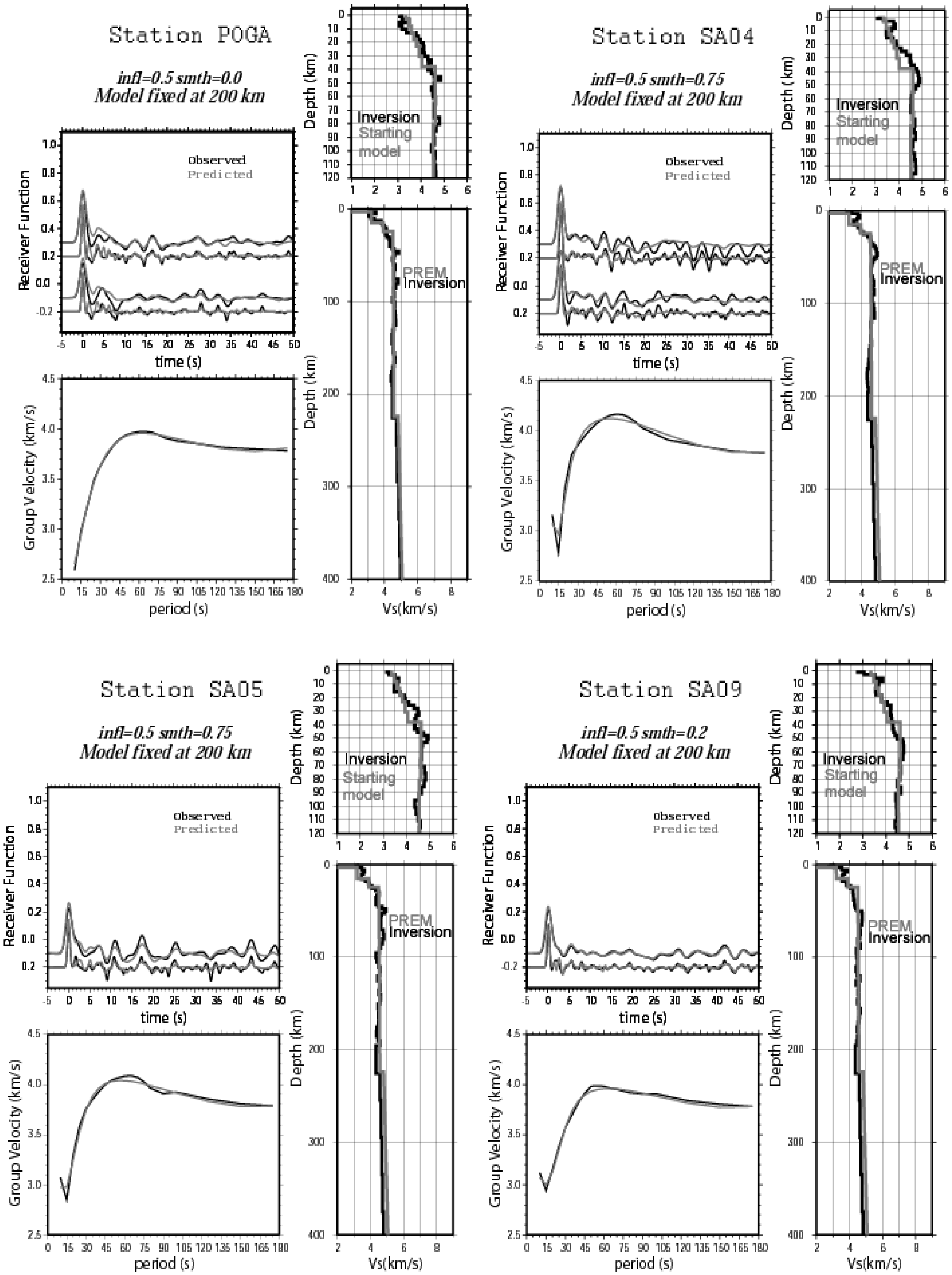
Station POGA
infl=0.5 smth=0.0
Model fixed at 200 km
Observed
Predicted
Receiver Function
time (s)
Group Velocity (km/s)
period (s)
Depth (km)
Inversion
Starting model
PREM
Inversion
Vs(km/s)
Station SA04
infl=0.5 smth=0.75
Model fixed at 200 km
Observed
Predicted
Receiver Function
time (s)
Group Velocity (km/s)
period (s)
Depth (km)
Inversion
Starting model
PREM
Inversion
Vs(km/s)
Station SA05
infl=0.5 smth=0.75
Model fixed at 200 km
Observed
Predicted
Receiver Function
time (s)
Group Velocity (km/s)
period (s)
Depth (km)
Inversion
Starting model
PREM
Inversion
Vs(km/s)
Station SA09
infl=0.5 smth=0.2
Model fixed at 200 km
Observed
Predicted
Receiver Function
time (s)
Group Velocity (km/s)
period (s)
Depth (km)
Inversion
Starting model
PREM
Inversion
Vs(km/s)

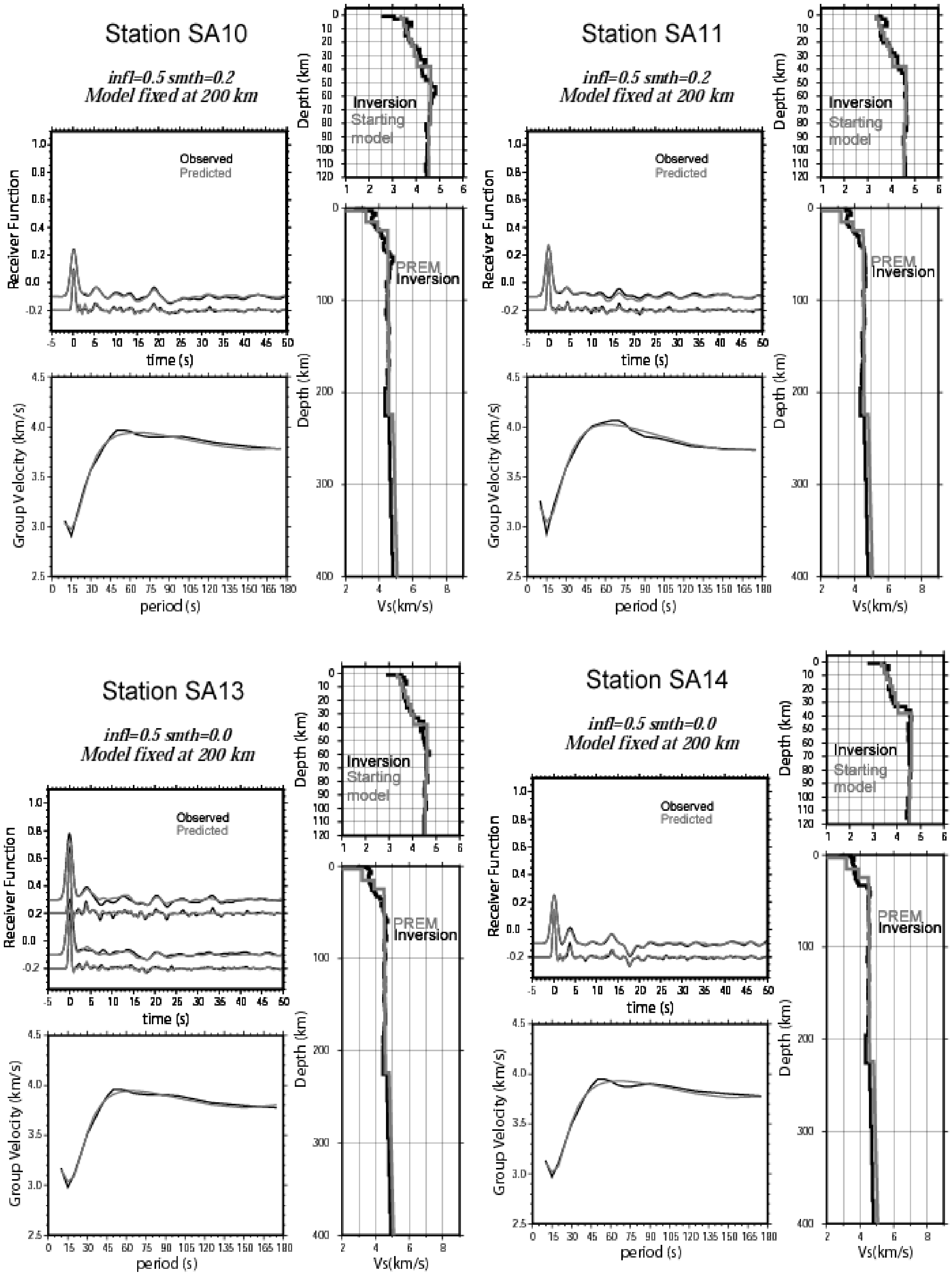

Station SA10
infl=0.5 smth=0.2
Model fixed at 200 km
Observed
Predicted
Receiver Function
time (s)
Group Velocity (km/s)
period (s)
Depth (km)
Inversion
Starting model
PREM
Inversion
Vs(km/s)
Station SA11
infl=0.5 smth=0.2
Model fixed at 200 km
Observed
Predicted
Receiver Function
time (s)
Group Velocity (km/s)
period (s)
Depth (km)
Inversion
Starting model
PREM
Inversion
Vs(km/s)
Station SA13
infl=0.5 smth=0.0
Model fixed at 200 km
Observed
Predicted
Receiver Function
time (s)
Group Velocity (km/s)
period (s)
Depth (km)
Inversion
Starting model
PREM
Inversion
Vs(km/s)
Station SA14
infl=0.5 smth=0.0
Model fixed at 200 km
Observed
Predicted
Receiver Function
time (s)
Group Velocity (km/s)
period (s)
Depth (km)
Inversion
Starting model
PREM
Inversion
Vs(km/s)

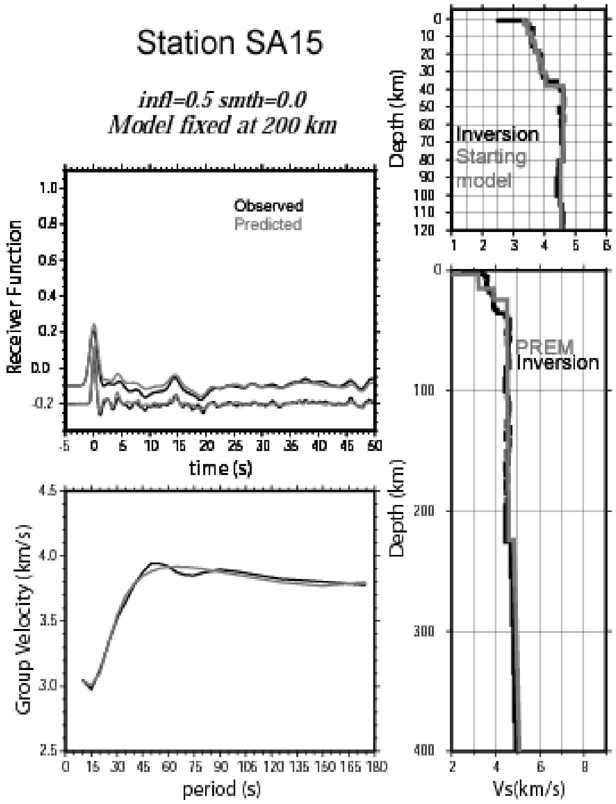
Station SA15
infl=0.5 smth=0.0
Model fixed at 200 km
Observed
Predicted
Receiver Function
time (s)
Group Velocity (km/s)
period (s)
Depth (km)
Inversion
Starting model
PREM
Inversion
Vs(km/s)

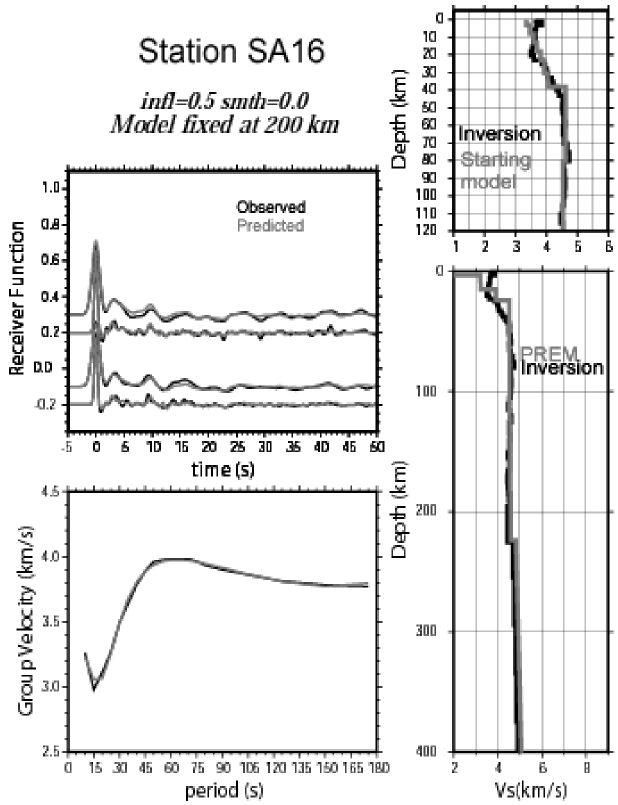
Station SA16
infl=0.5 smth=0.0
Model fixed at 200 km
Observed
Predicted
Receiver Function
time (s)
Group Velocity (km/s)
period (s)
Depth (km)
Inversion
Starting model
PREM
Inversion
Vs(km/s)

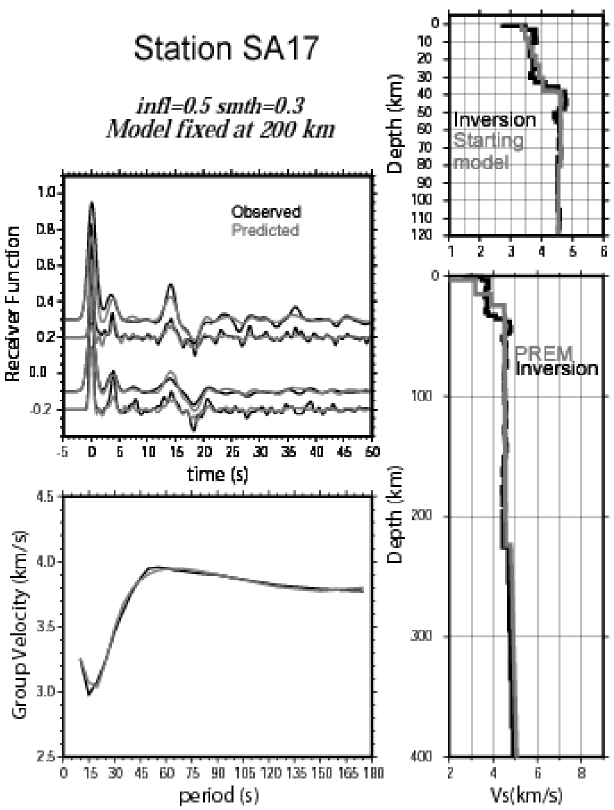
Station SA17
infl=0.5 smth=0.3
Model fixed at 200 km
Observed
Predicted
Receiver Function
time (s)
Group Velocity (km/s)
period (s)
Depth (km)
Inversion
Starting model
PREM
Inversion
Vs(km/s)

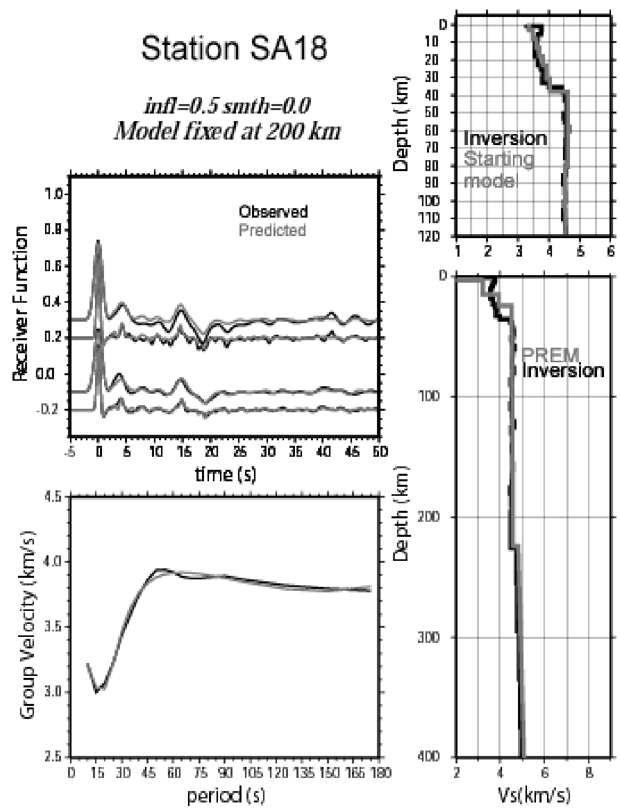
Station SA18
infl=0.5 smth=0.0
Model fixed at 200 km
Observed
Predicted
Receiver Function
time (s)
Group Velocity (km/s)
period (s)
Depth (km)
Inversion
Starting model
PREM
Inversion
Vs(km/s)

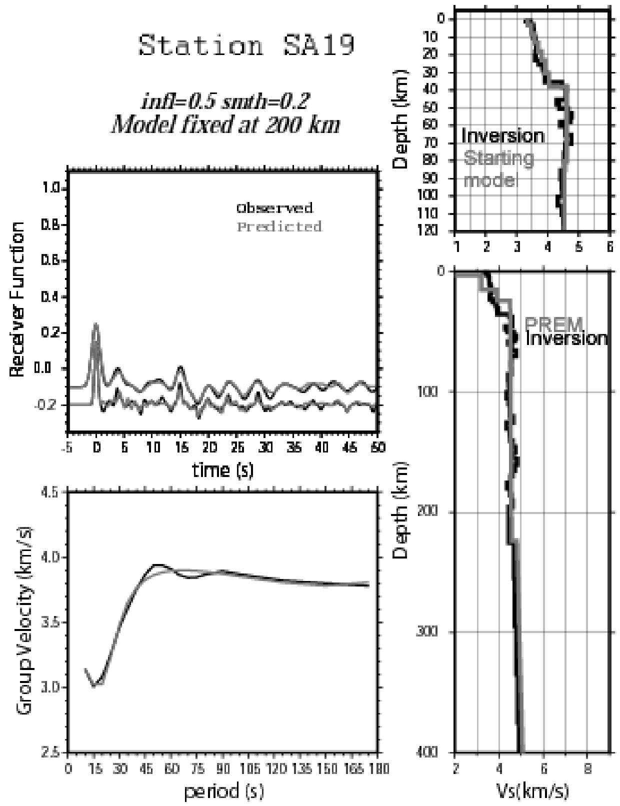
Station SA19
infl=0.5 smth=0.2
Model fixed at 200 km
Observed
Predicted
Receiver Function
time (s)
Group Velocity (km/s)
period (s)
Depth (km)
Inversion
Starting model
PREM
Vs(km/s)

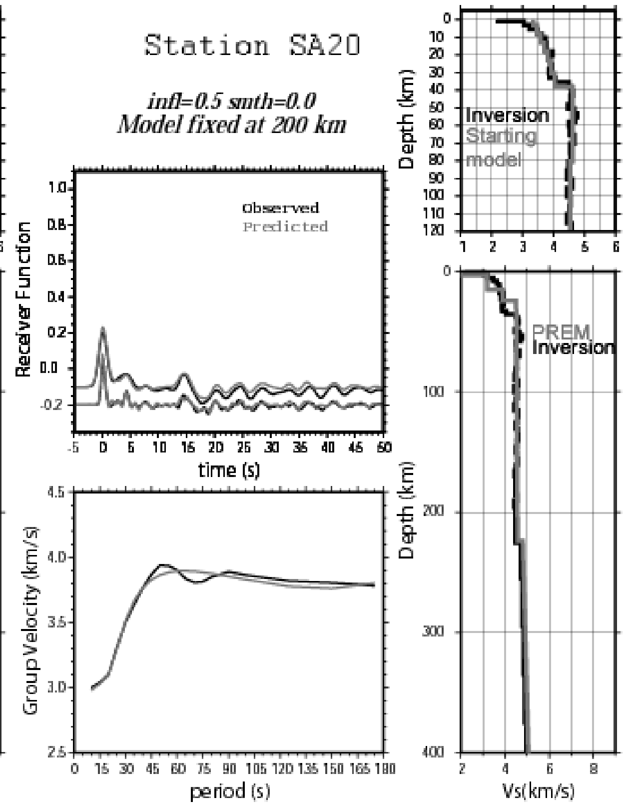
Station SA20
infl=0.5 smth=0.0
Model fixed at 200 km
Observed
Predicted
Receiver Function
time (s)
Group Velocity (km/s)
period (s)
Depth (km)
Inversion
Starting model
PREM
Vs(km/s)

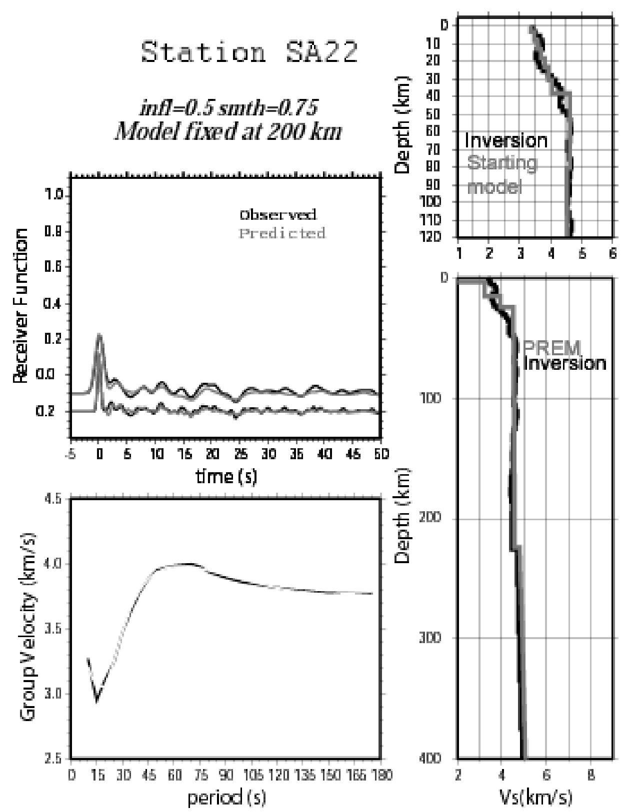
Station SA22
infl=0.5 smth=0.75
Model fixed at 200 km
Observed
Predicted
Receiver Function
time (s)
Group Velocity (km/s)
period (s)
Depth (km)
Inversion
Starting model
PREM
Vs(km/s)

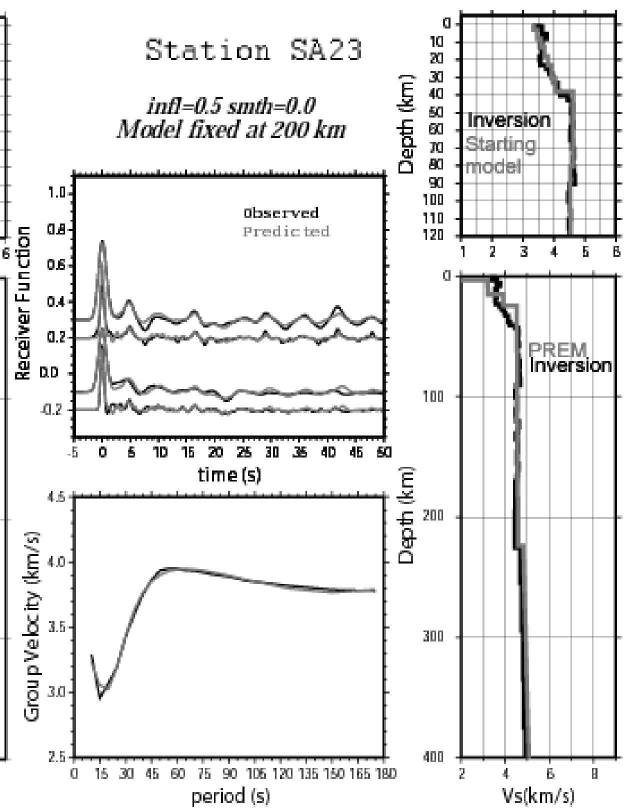
Station SA23
infl=0.5 smth=0.0
Model fixed at 200 km
Observed
Predicted
Receiver Function
time (s)
Group Velocity (km/s)
period (s)
Depth (km)
Inversion
Starting model
PREM
Vs(km/s)

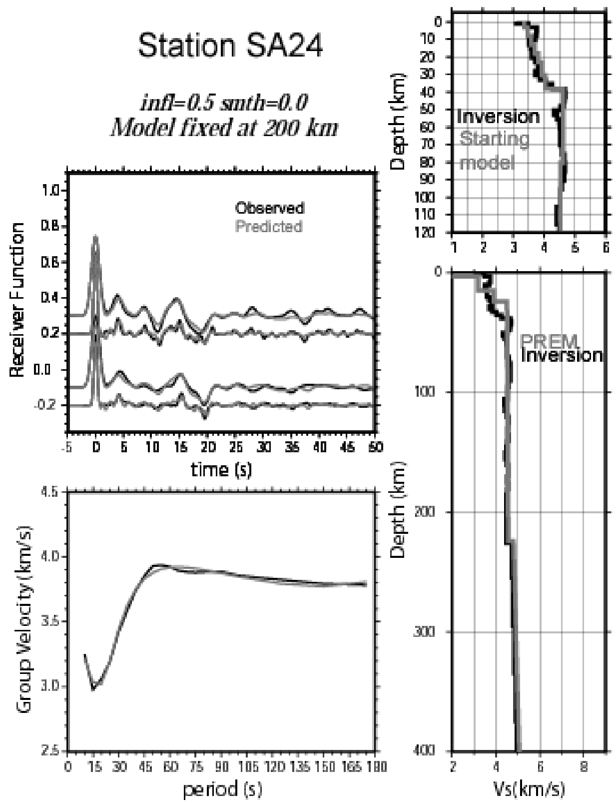
Station SA24
infl=0.5 smth=0.0
Model fixed at 200 km
Observed
Predicted
Receiver Function
time (s)
Group Velocity (km/s)
period (s)
Depth (km)
Inversion
Starting model
PREM
Inversion
Vs(km/s)

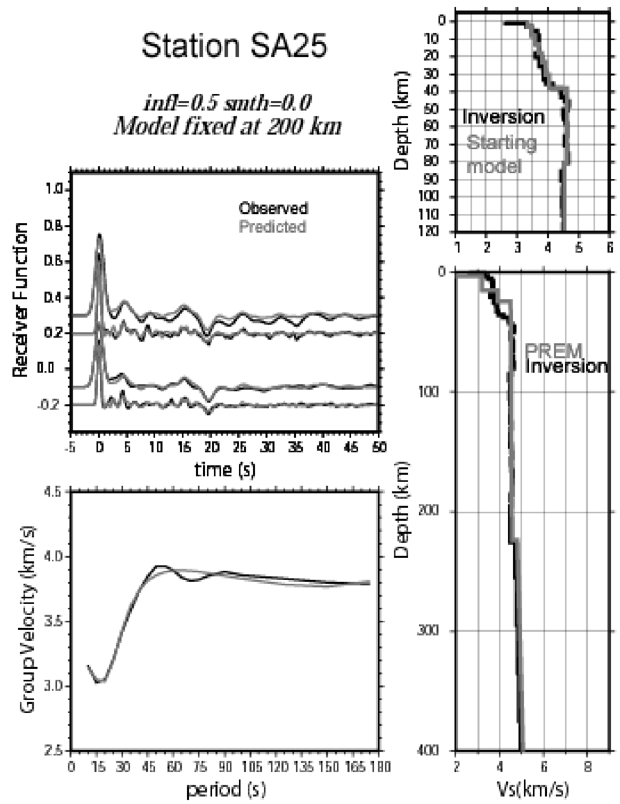
Station SA25
infl=0.5 smth=0.0
Model fixed at 200 km
Observed
Predicted
Receiver Function
time (s)
Group Velocity (km/s)
period (s)
Depth (km)
Inversion
Starting model
PREM
Inversion
Vs(km/s)

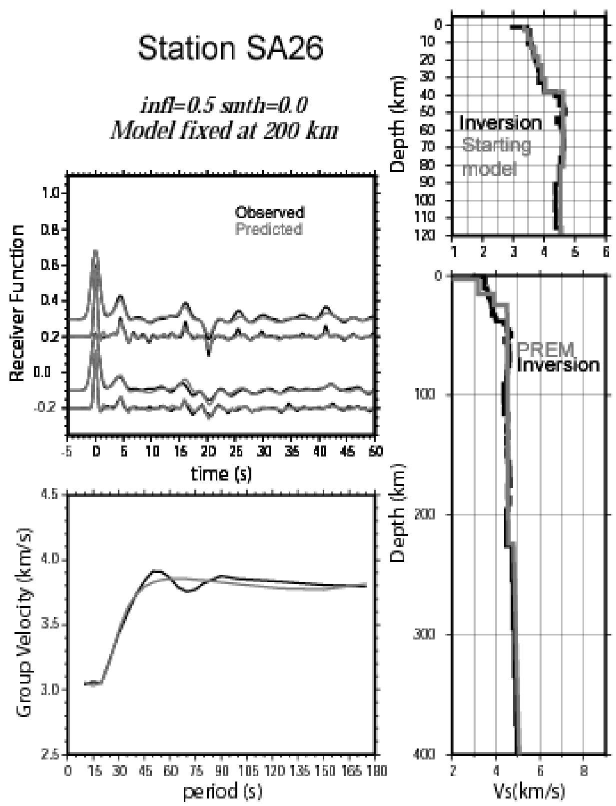
Station SA26
infl=0.5 smth=0.0
Model fixed at 200 km
Observed
Predicted
Receiver Function
time (s)
Group Velocity (km/s)
period (s)
Depth (km)
Inversion
Starting model
PREM
Inversion
Vs(km/s)

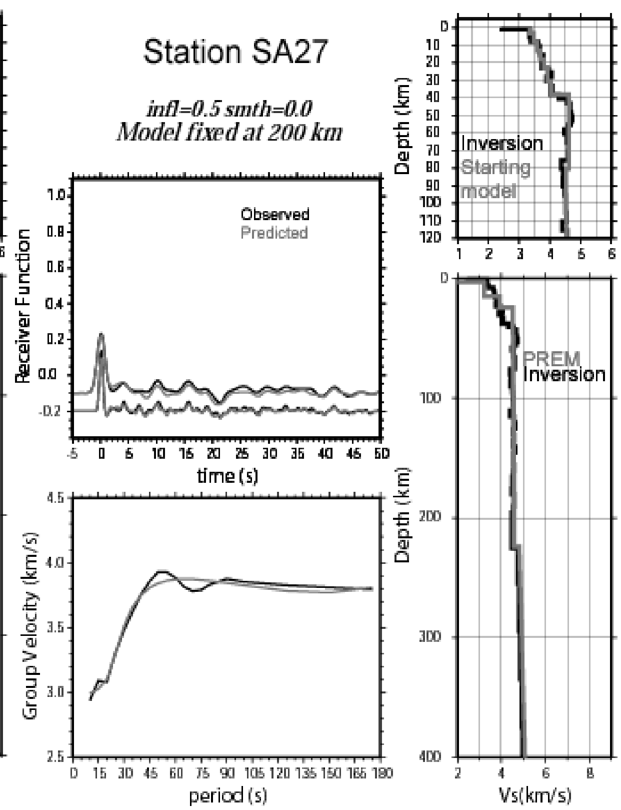
Station SA27
infl=0.5 smth=0.0
Model fixed at 200 km
Observed
Predicted
Receiver Function
time (s)
Group Velocity (km/s)
period (s)
Depth (km)
Inversion
Starting model
PREM
Inversion
Vs(km/s)

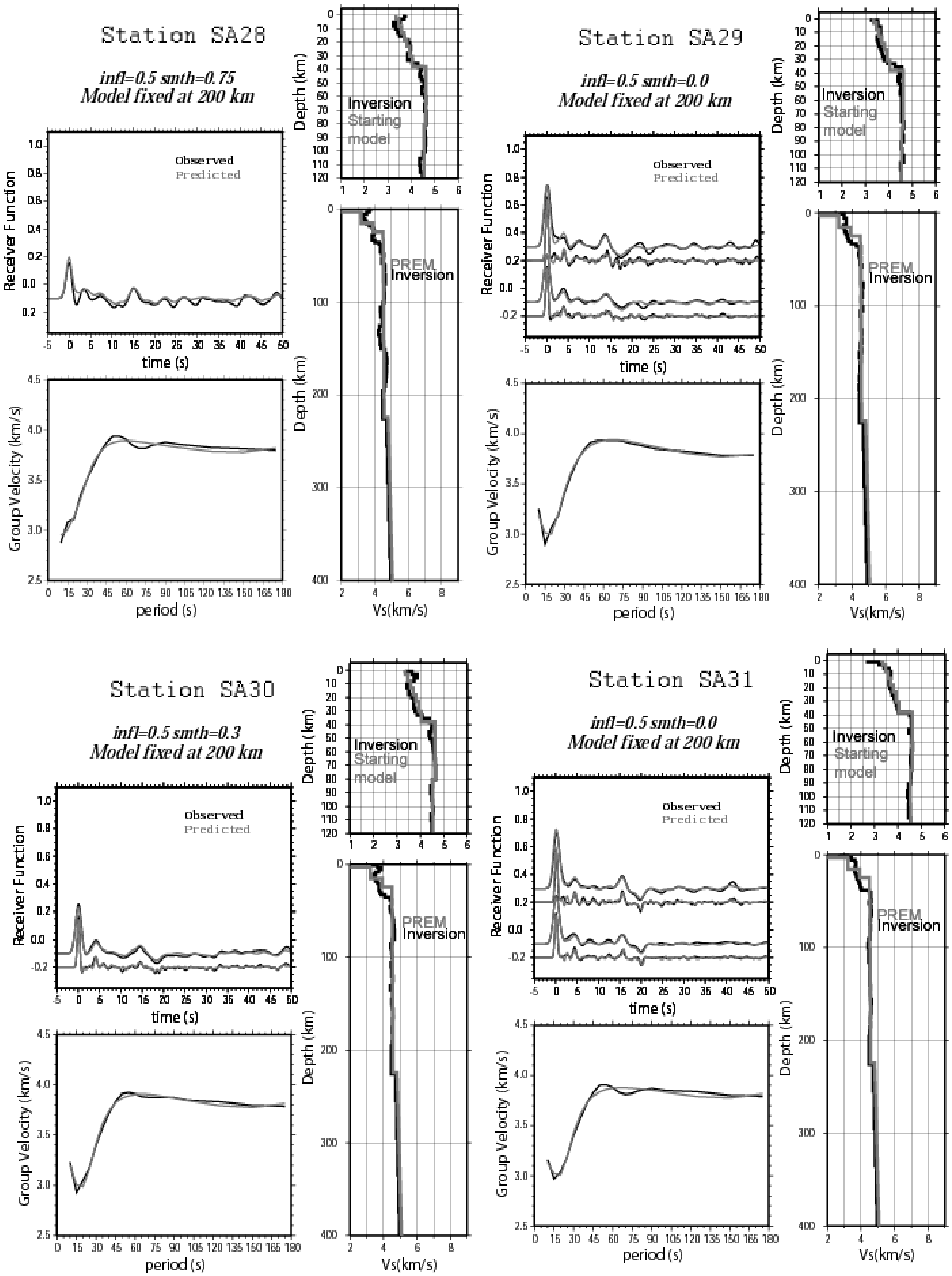

Station SA28
infl=0.5 smth=0.75
Model fixed at 200 km
Observed
Predicted
Receiver Function
time (s)
Group Velocity (km/s)
period (s)
Depth (km)
Inversion
Starting model
PREM
Inversion
Vs(km/s)
Station SA29
infl=0.5 smth=0.0
Model fixed at 200 km
Observed
Predicted
Receiver Function
time (s)
Group Velocity (km/s)
period (s)
Depth (km)
Inversion
Starting model
PREM
Inversion
Vs(km/s)
Station SA30
infl=0.5 smth=0.3
Model fixed at 200 km
Observed
Predicted
Receiver Function
time (s)
Group Velocity (km/s)
period (s)
Depth (km)
Inversion
Starting model
PREM
Inversion
Vs(km/s)
Station SA31
infl=0.5 smth=0.0
Model fixed at 200 km
Observed
Predicted
Receiver Function
time (s)
Group Velocity (km/s)
period (s)
Depth (km)
Inversion
Starting model
PREM
Inversion
Vs(km/s)

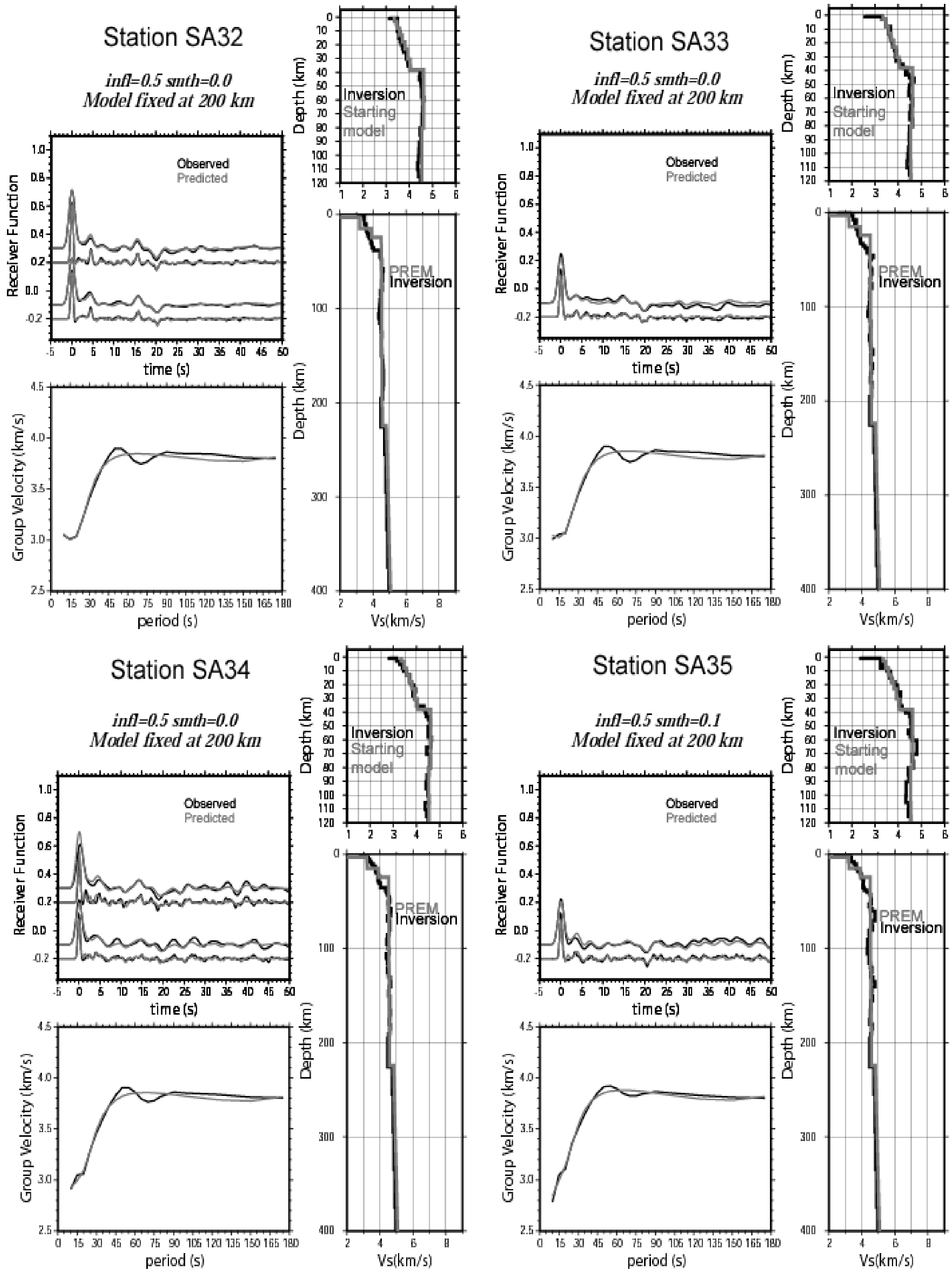

Station SA32
infl=0.5 smth=0.0
Model fixed at 200 km
Observed
Predicted
Receiver Function
time (s)
Group Velocity (km/s)
period (s)
Depth (km)
Inversion
Starting
model
PREM
Inversion
Vs(km/s)
Station SA33
infl=0.5 smth=0.0
Model fixed at 200 km
Observed
Predicted
Receiver Function
time (s)
Group Velocity (km/s)
period (s)
Depth (km)
Inversion
Starting
model
PREM
Inversion
Vs(km/s)
Station SA34
infl=0.5 smth=0.0
Model fixed at 200 km
Observed
Predicted
Receiver Function
time (s)
Group Velocity (km/s)
period (s)
Depth (km)
Inversion
Starting
model
PREM
Inversion
Vs(km/s)
Station SA35
infl=0.5 smth=0.1
Model fixed at 200 km
Observed
Predicted
Receiver Function
time (s)
Group Velocity (km/s)
period (s)
Depth (km)
Inversion
Starting
model
PREM
Inversion
Vs(km/s)

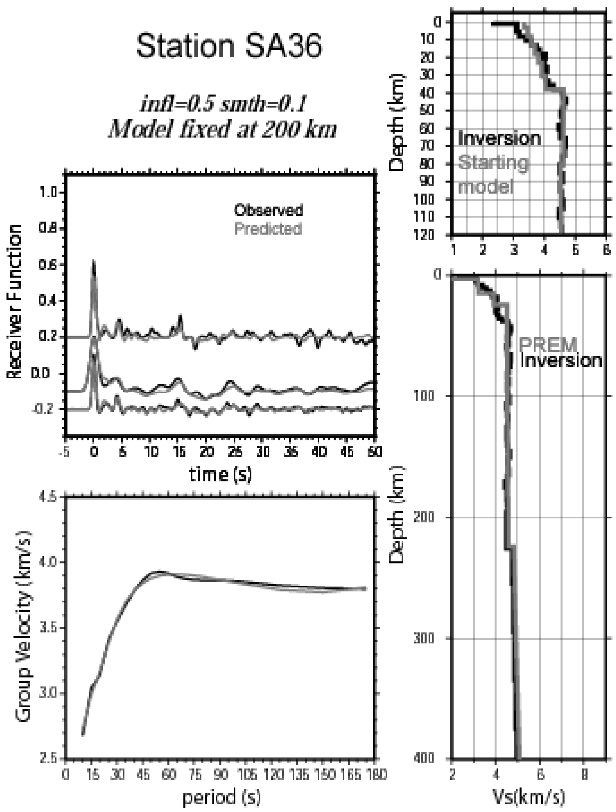
Station SA36
infl=0.5 smth=0.1
Model fixed at 200 km
Observed
Predicted
Receiver Function
time (s)
Group Velocity (km/s)
period (s)
Depth (km)
Inversion
Starting model
PREM
Inversion
Vs(km/s)

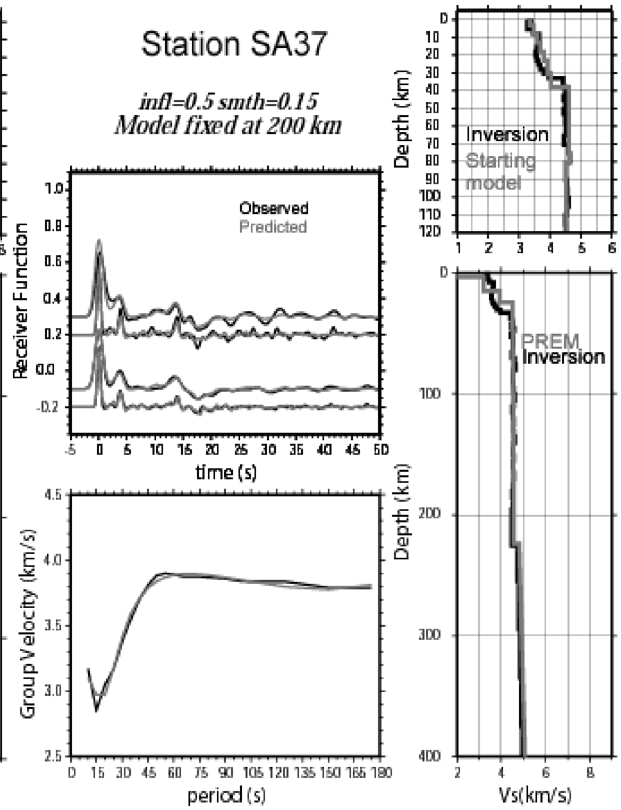
Station SA37
infl=0.5 smth=0.15
Model fixed at 200 km
Observed
Predicted
Receiver Function
time (s)
Group Velocity (km/s)
period (s)
Depth (km)
Inversion
Starting model
PREM
Inversion
Vs(km/s)

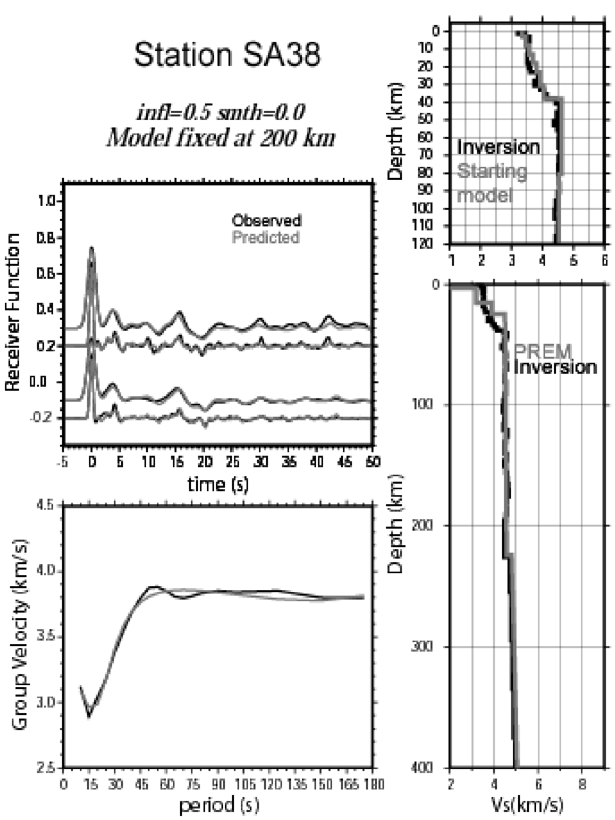
Station SA38
infl=0.5 smth=0.0
Model fixed at 200 km
Observed
Predicted
Receiver Function
time (s)
Group Velocity (km/s)
period (s)
Depth (km)
Inversion
Starting model
PREM
Inversion
Vs(km/s)

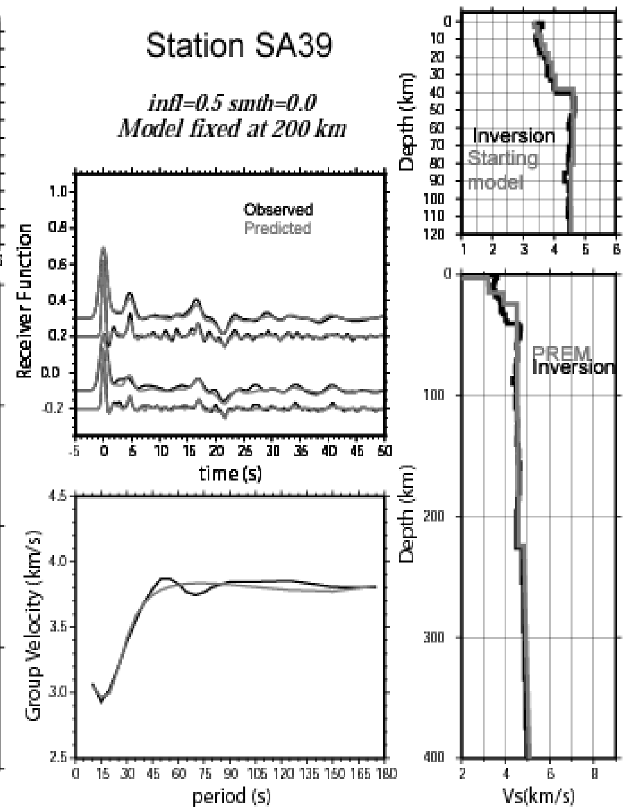
Station SA39
infl=0.5 smth=0.0
Model fixed at 200 km
Observed
Predicted
Receiver Function
time (s)
Group Velocity (km/s)
period (s)
Depth (km)
Inversion
Starting model
PREM
Inversion
Vs(km/s)

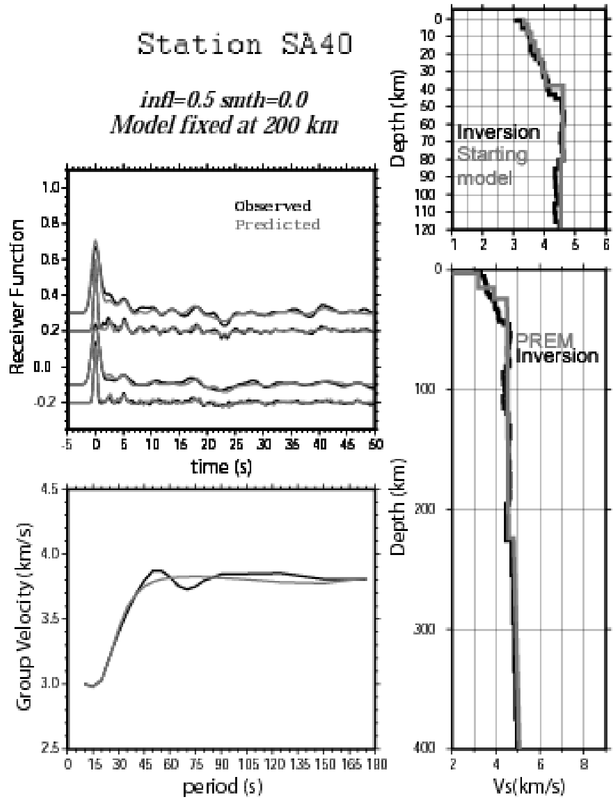
Station SA40
infl=0.5 smth=0.0
Model fixed at 200 km
Observed
Predicted
Receiver Function
time (s)
Group Velocity (km/s)
period (s)
Depth (km)
Inversion
Starting model
PREM
Inversion
Vs(km/s)

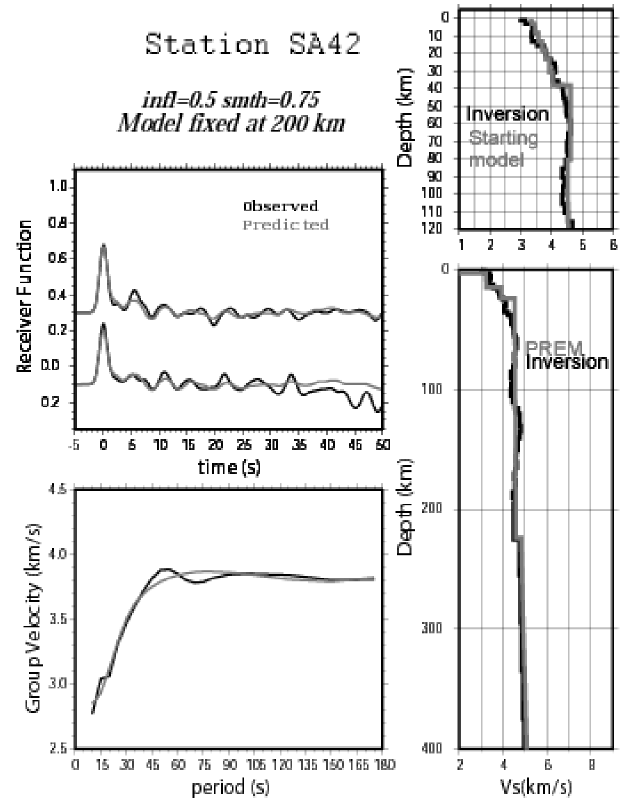
Station SA42
infl=0.5 smth=0.75
Model fixed at 200 km
Observed
Predicted
Receiver Function
time (s)
Group Velocity (km/s)
period (s)
Depth (km)
Inversion
Starting model
PREM
Inversion
Vs(km/s)

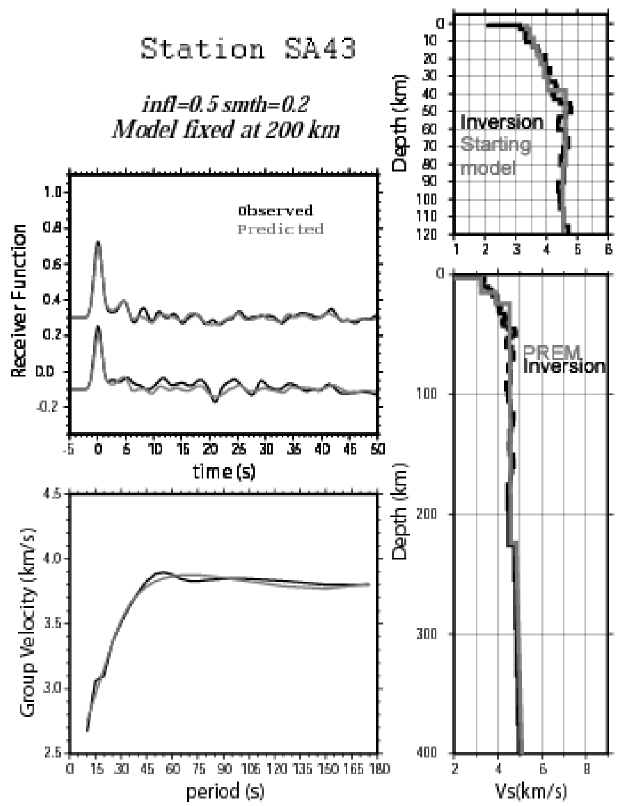
Station SA43
infl=0.5 smth=0.2
Model fixed at 200 km
Observed
Predicted
Receiver Function
time (s)
Group Velocity (km/s)
period (s)
Depth (km)
Inversion
Starting model
PREM
Inversion
Vs(km/s)

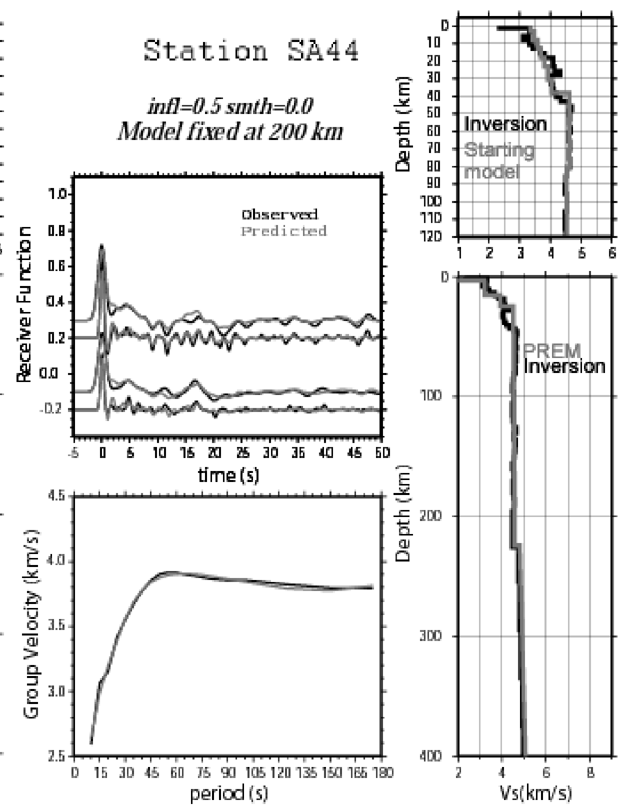
Station SA44
infl=0.5 smth=0.0
Model fixed at 200 km
Observed
Predicted
Receiver Function
time (s)
Group Velocity (km/s)
period (s)
Depth (km)
Inversion
Starting model
PREM
Inversion
Vs(km/s)

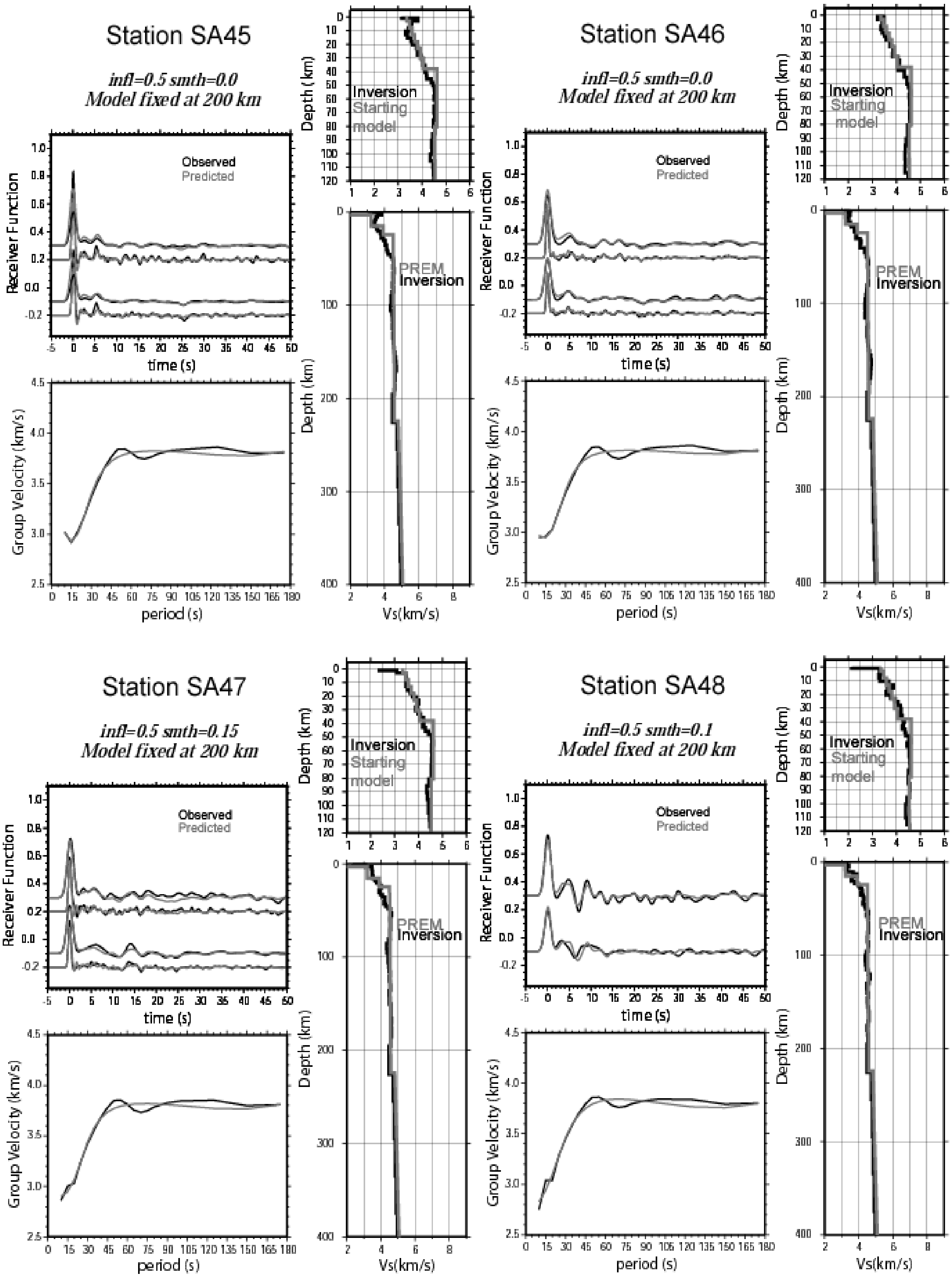
Station SA45
infl=0.5 smth=0.0
Model fixed at 200 km
Observed
Predicted
Receiver Function
time (s)
Group Velocity (km/s)
period (s)
Depth (km)
Inversion
Starting model
PREM
Inversion
Vs(km/s)
Station SA46
infl=0.5 smth=0.0
Model fixed at 200 km
Observed
Predicted
Receiver Function
time (s)
Group Velocity (km/s)
period (s)
Depth (km)
Inversion
Starting model
PREM
Inversion
Vs(km/s)
Station SA47
infl=0.5 smth=0.15
Model fixed at 200 km
Observed
Predicted
Receiver Function
time (s)
Group Velocity (km/s)
period (s)
Depth (km)
Inversion
Starting model
PREM
Inversion
Vs(km/s)
Station SA48
infl=0.5 smth=0.1
Model fixed at 200 km
Observed
Predicted
Receiver Function
time (s)
Group Velocity (km/s)
period (s)
Depth (km)
Inversion
Starting model
PREM
Inversion
Vs(km/s)

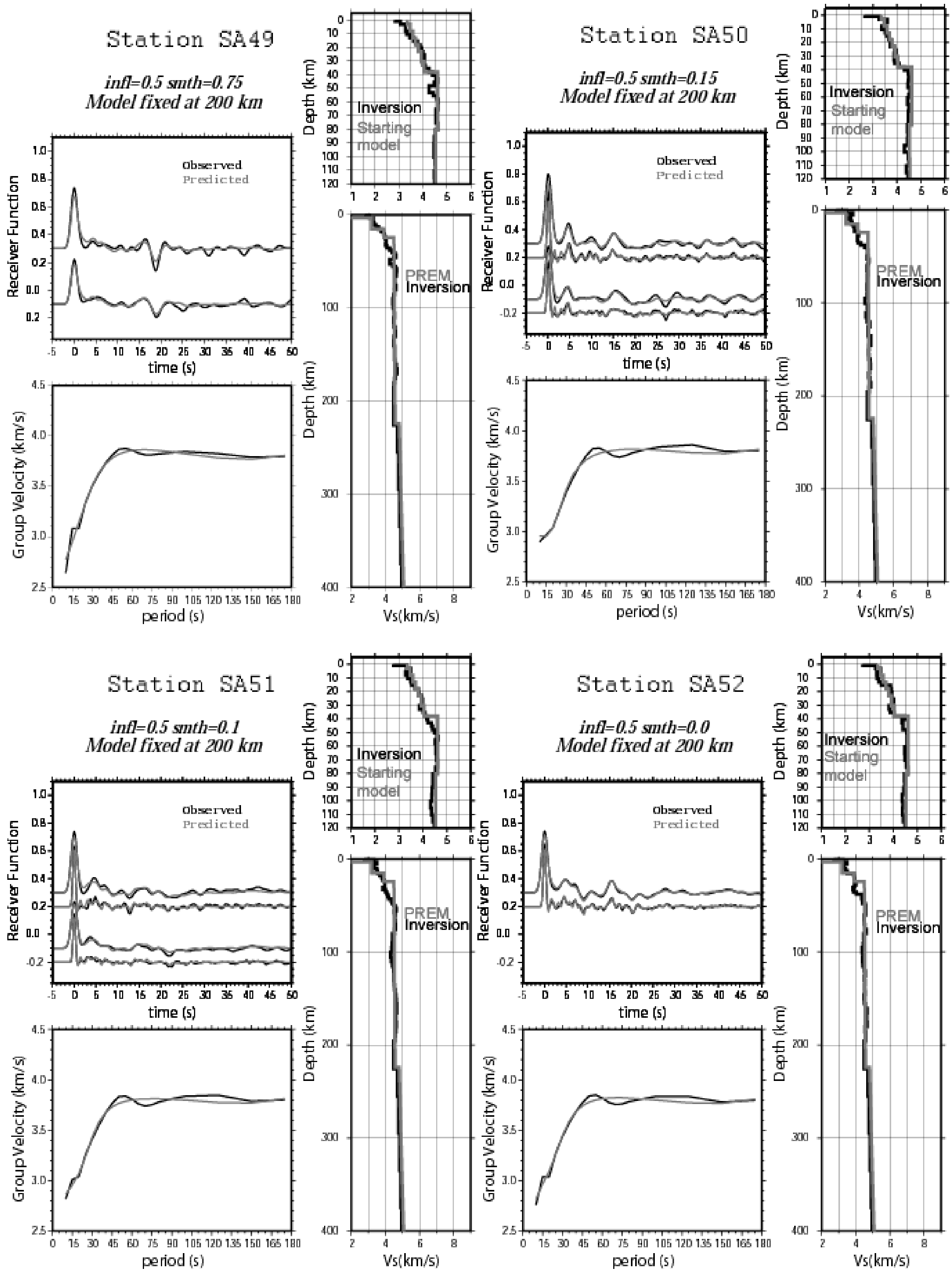
Station SA49
infl=0.5 smth=0.75
Model fixed at 200 km
Observed
Predicted
Receiver Function
time (s)
Group Velocity (km/s)
period (s)
Depth (km)
Inversion
Starting model
PREM
Inversion
Vs(km/s)
Station SA50
infl=0.5 smth=0.15
Model fixed at 200 km
Observed
Predicted
Receiver Function
time (s)
Group Velocity (km/s)
period (s)
Depth (km)
Inversion
Starting model
PREM
Inversion
Vs(km/s)
Station SA51
infl=0.5 smth=0.1
Model fixed at 200 km
Observed
Predicted
Receiver Function
time (s)
Group Velocity (km/s)
period (s)
Depth (km)
Inversion
Starting model
PREM
Inversion
Vs(km/s)
Station SA52
infl=0.5 smth=0.0
Model fixed at 200 km
Observed
Predicted
Receiver Function
time (s)
Group Velocity (km/s)
period (s)
Depth (km)
Inversion
Starting model
PREM
Inversion
Vs(km/s)

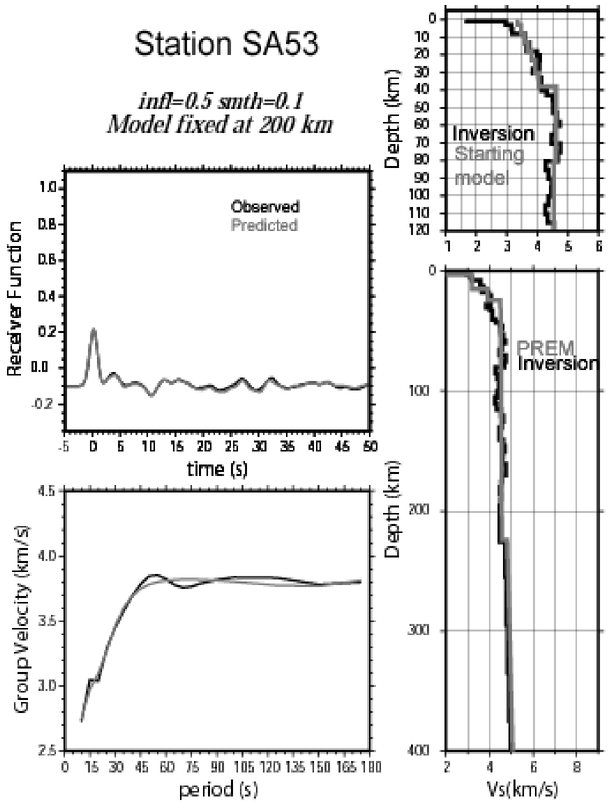
Station SA53
infl=0.5 smth=0.1
Model fixed at 200 km
Observed
Predicted
Receiver Function
time (s)
Group Velocity (km/s)
period (s)
Depth (km)
Inversion
Starting model
PREM
Inversion
Vs(km/s)

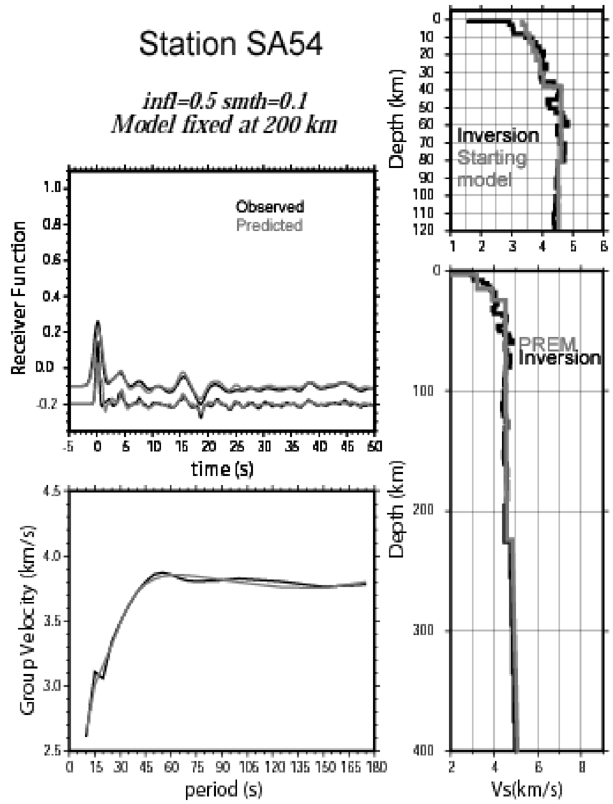
Station SA54
infl=0.5 smth=0.1
Model fixed at 200 km
Observed
Predicted
Receiver Function
time (s)
Group Velocity (km/s)
period (s)
Depth (km)
Inversion
Starting model
PREM
Inversion
Vs(km/s)

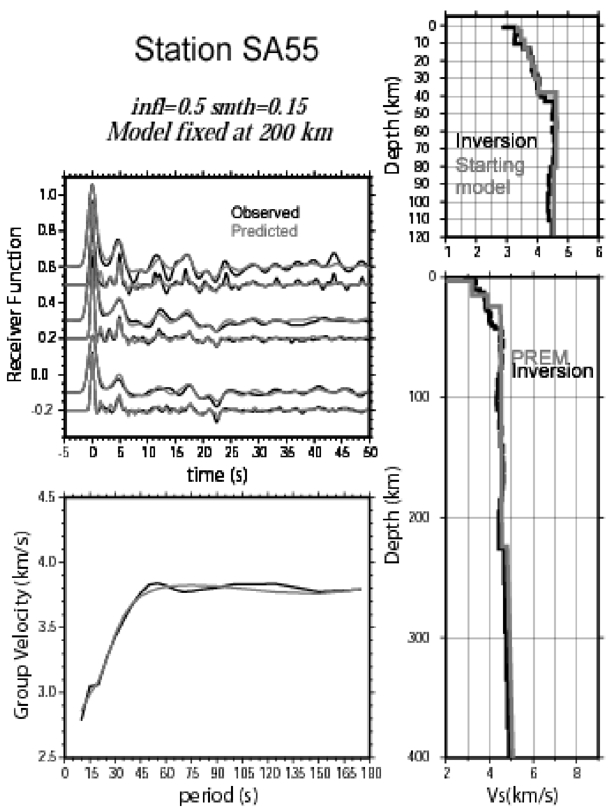
Station SA55
infl=0.5 smth=0.15
Model fixed at 200 km
Observed
Predicted
Receiver Function
time (s)
Group Velocity (km/s)
period (s)
Depth (km)
Inversion
Starting model
PREM
Inversion
Vs(km/s)

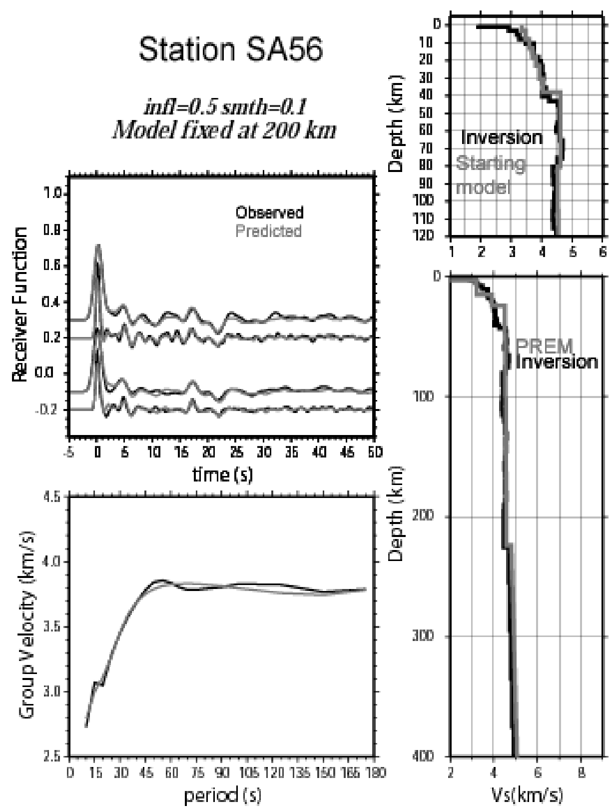
Station SA56
infl=0.5 smth=0.1
Model fixed at 200 km
Observed
Predicted
Receiver Function
time (s)
Group Velocity (km/s)
period (s)
Depth (km)
Inversion
Starting model
PREM
Inversion
Vs(km/s)

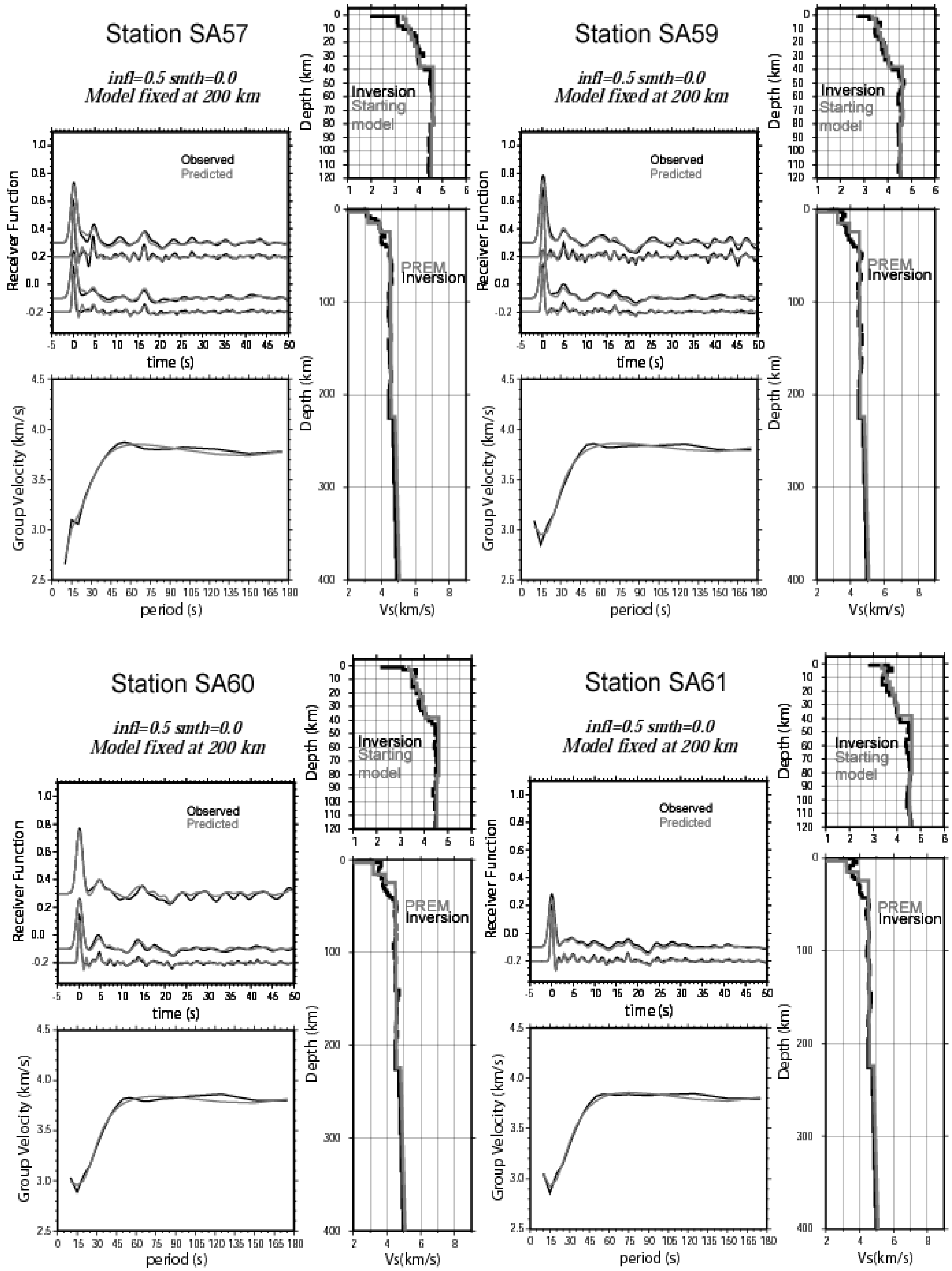
Station SA57
infl=0.5 smth=0.0
Model fixed at 200 km
Observed
Predicted
Receiver Function
time (s)
Group Velocity (km/s)
period (s)
Depth (km)
Inversion
Starting model
PREM
Vs(km/s)
Station SA59
infl=0.5 smth=0.0
Model fixed at 200 km
Station SA60
infl=0.5 smth=0.0
Model fixed at 200 km
Station SA61
infl=0.5 smth=0.0
Model fixed at 200 km

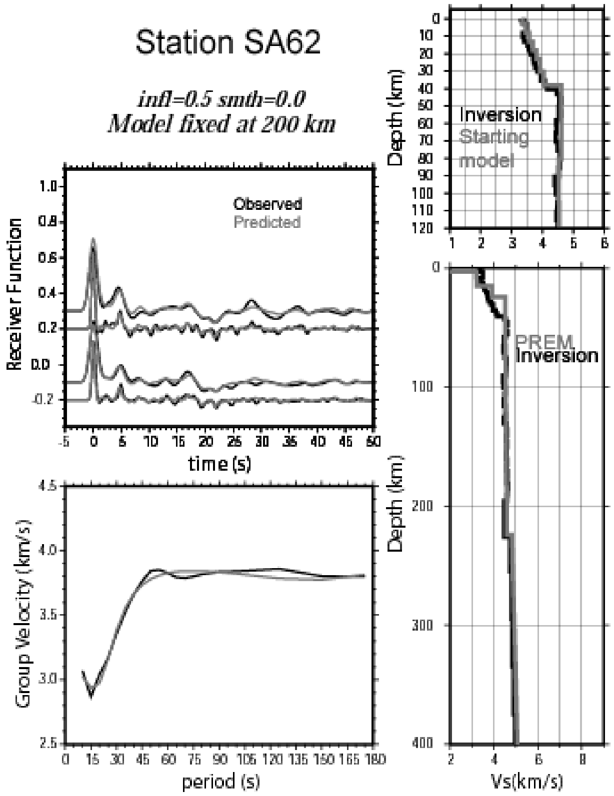
Station SA62
infl=0.5 smth=0.0
Model fixed at 200 km
Observed
Predicted
Receiver Function
time (s)
Group Velocity (km/s)
period (s)
Depth (km)
Inversion
Starting model
PREM
Inversion
Depth (km)
Vs(km/s)

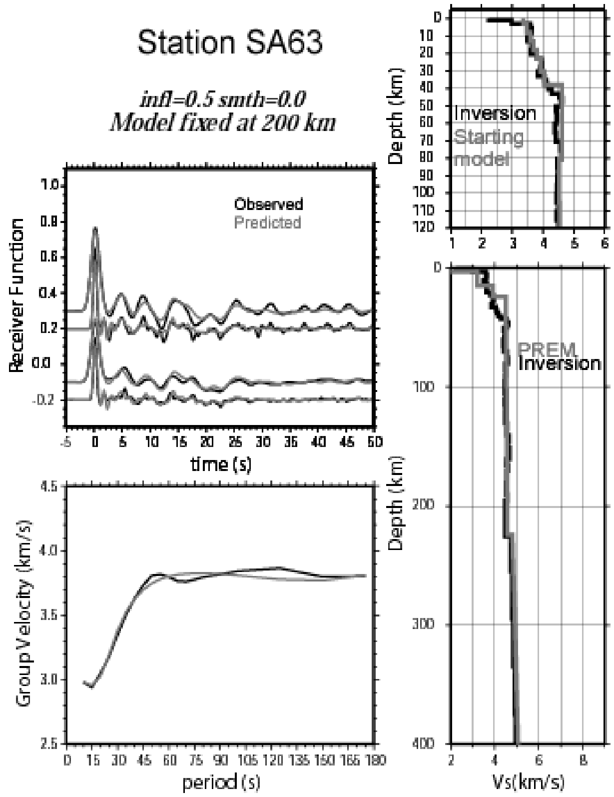
Station SA63
infl=0.5 smth=0.0
Model fixed at 200 km
Observed
Predicted
Receiver Function
time (s)
Group Velocity (km/s)
period (s)
Depth (km)
Inversion
Starting model
PREM
Inversion
Depth (km)
Vs(km/s)

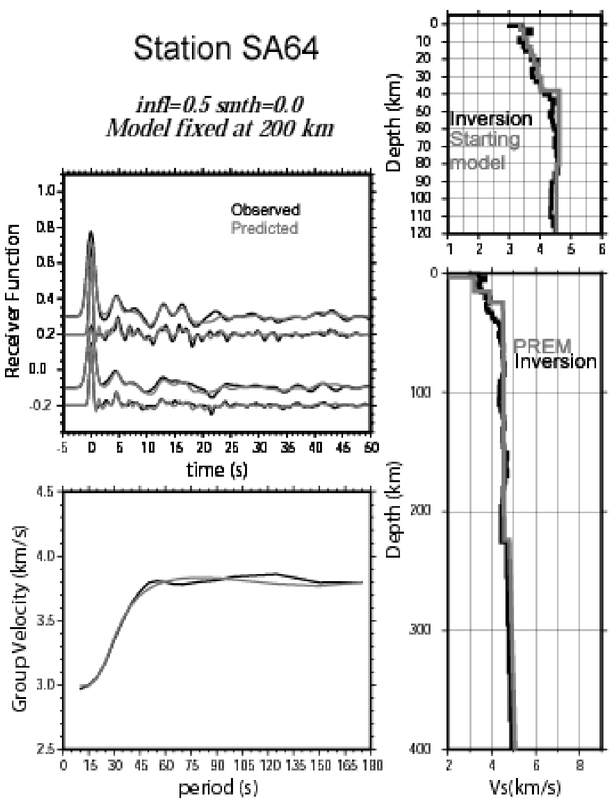
Station SA64
infl=0.5 smth=0.0
Model fixed at 200 km
Observed
Predicted
Receiver Function
time (s)
Group Velocity (km/s)
period (s)
Depth (km)
Inversion
Starting model
PREM
Inversion
Depth (km)
Vs(km/s)

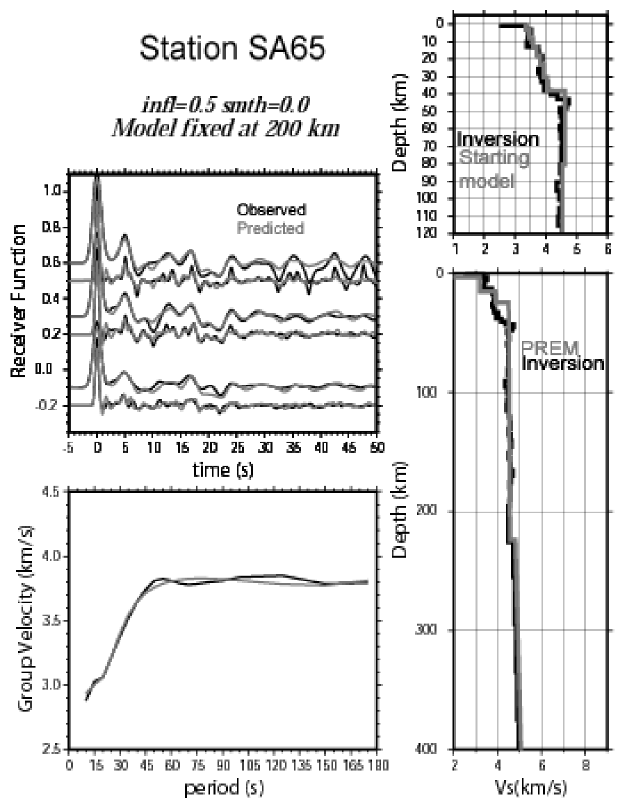
Station SA65
infl=0.5 smth=0.0
Model fixed at 200 km
Observed
Predicted
Receiver Function
time (s)
Group Velocity (km/s)
period (s)
Depth (km)
Inversion
Starting model
PREM
Inversion
Depth (km)
Vs(km/s)

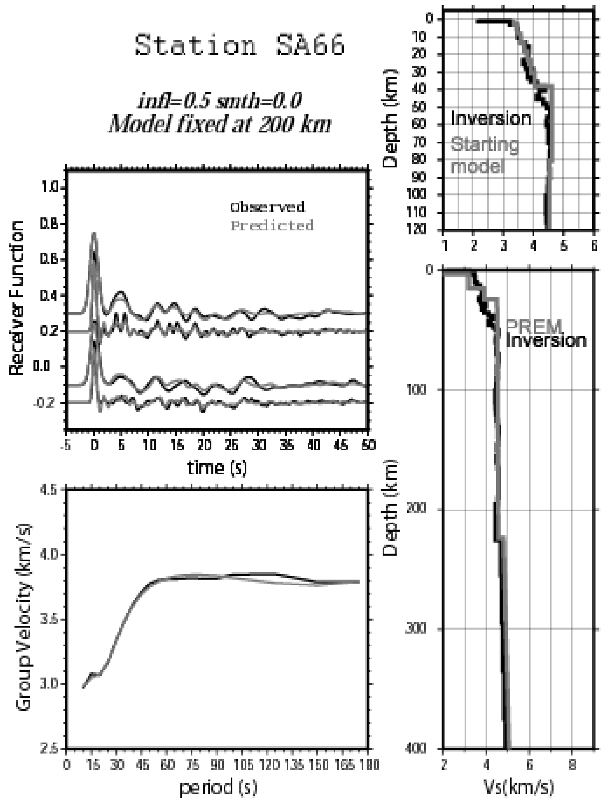
Station SA66
infl=0.5 smth=0.0
Model fixed at 200 km
Observed
Predicted
Receiver Function
time (s)
Group Velocity (km/s)
period (s)
Depth (km)
Inversion
Starting model
PREM
Inversion
Vs(km/s)

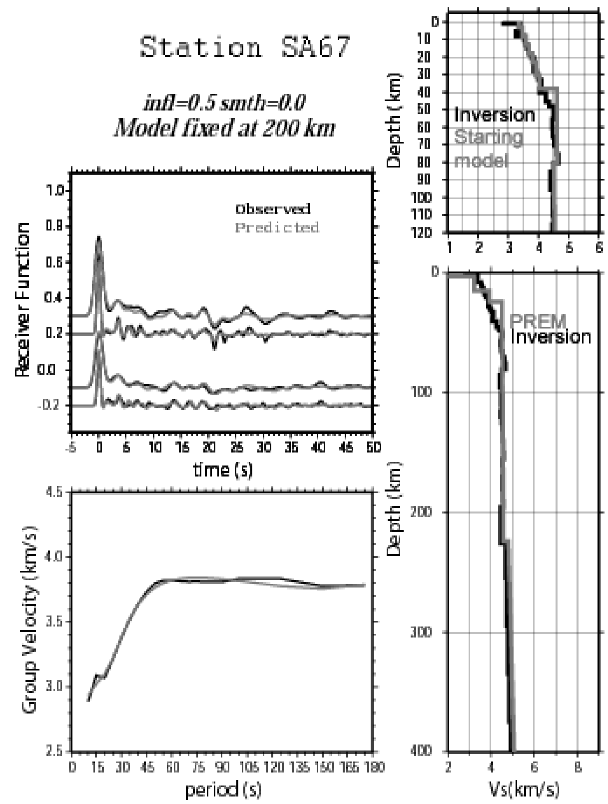
Station SA67
infl=0.5 smth=0.0
Model fixed at 200 km
Observed
Predicted
Receiver Function
time (s)
Group Velocity (km/s)
period (s)
Depth (km)
Inversion
Starting model
PREM
Inversion
Vs(km/s)

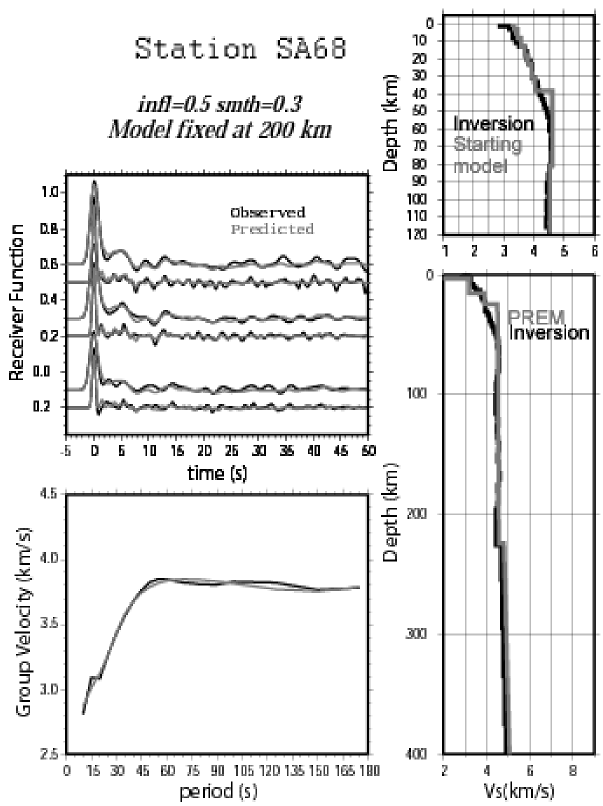
Station SA68
infl=0.5 smth=0.3
Model fixed at 200 km
Observed
Predicted
Receiver Function
time (s)
Group Velocity (km/s)
period (s)
Depth (km)
Inversion
Starting model
PREM
Inversion
Vs(km/s)

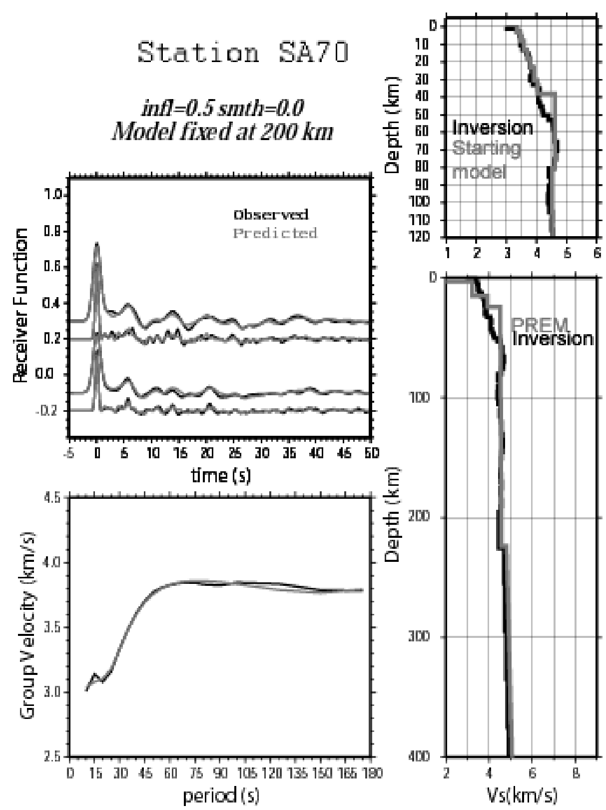
Station SA70
infl=0.5 smth=0.0
Model fixed at 200 km
Observed
Predicted
Receiver Function
time (s)
Group Velocity (km/s)
period (s)
Depth (km)
Inversion
Starting model
PREM
Inversion
Vs(km/s)

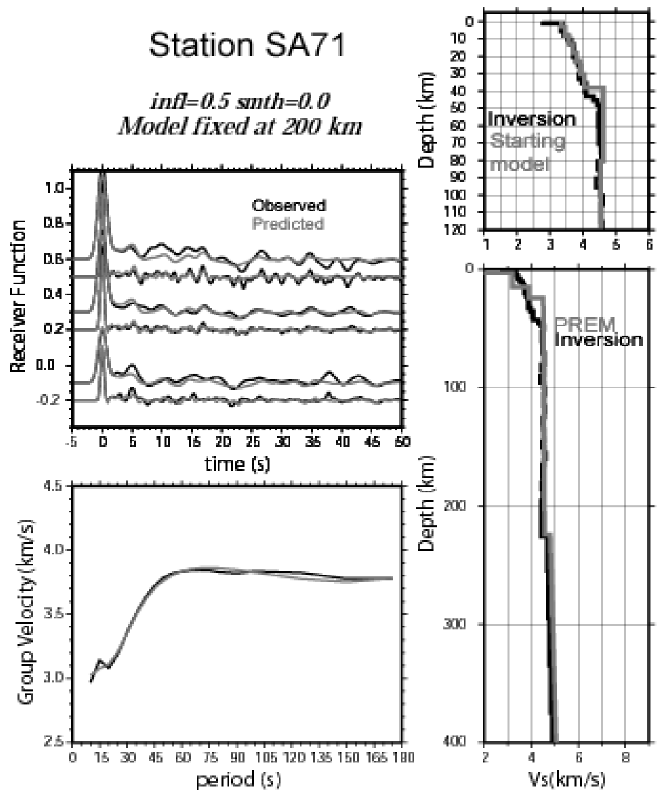
Station SA71
infl=0.5 smth=0.0
Model fixed at 200 km
Observed
Predicted
Receiver Function
time (s)
Group Velocity (km/s)
period (s)
Depth (km)
Inversion
Starting
model
PREM
Inversion
Vs(km/s)

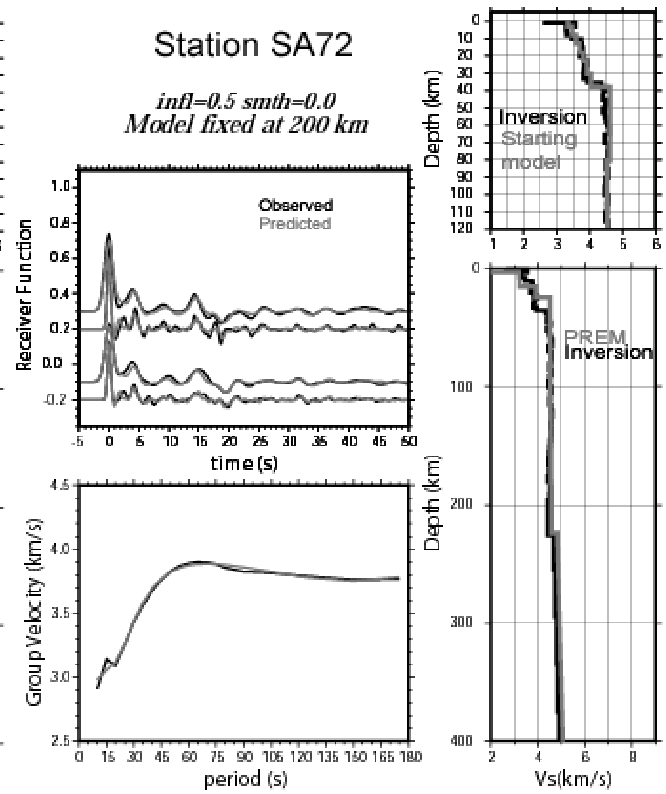
Station SA72
infl=0.5 smth=0.0
Model fixed at 200 km
Observed
Predicted
Receiver Function
time (s)
Group Velocity (km/s)
period (s)
Depth (km)
Inversion
Starting
model
PREM
Inversion
Vs(km/s)

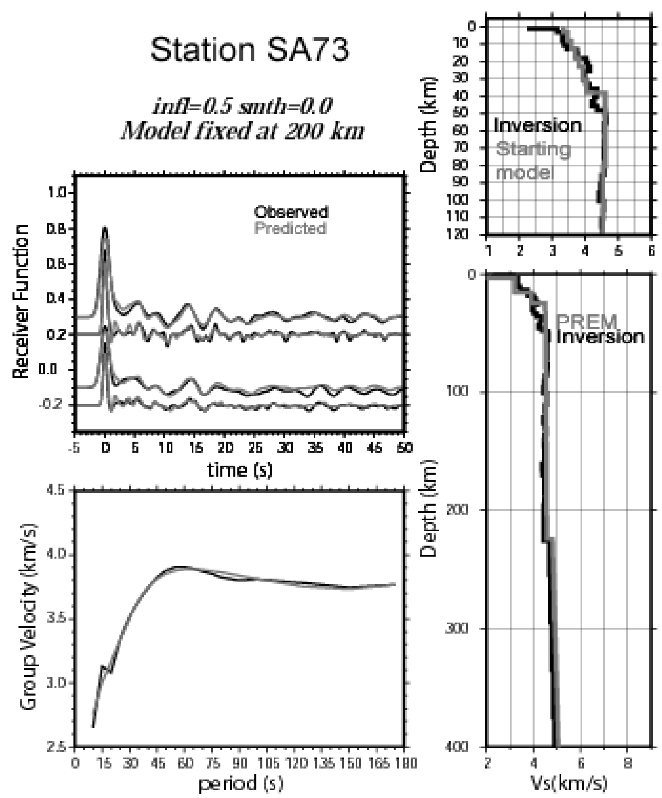
Station SA73
infl=0.5 smth=0.0
Model fixed at 200 km
Observed
Predicted
Receiver Function
time (s)
Group Velocity (km/s)
period (s)
Depth (km)
Inversion
Starting
model
PREM
Inversion
Vs(km/s)

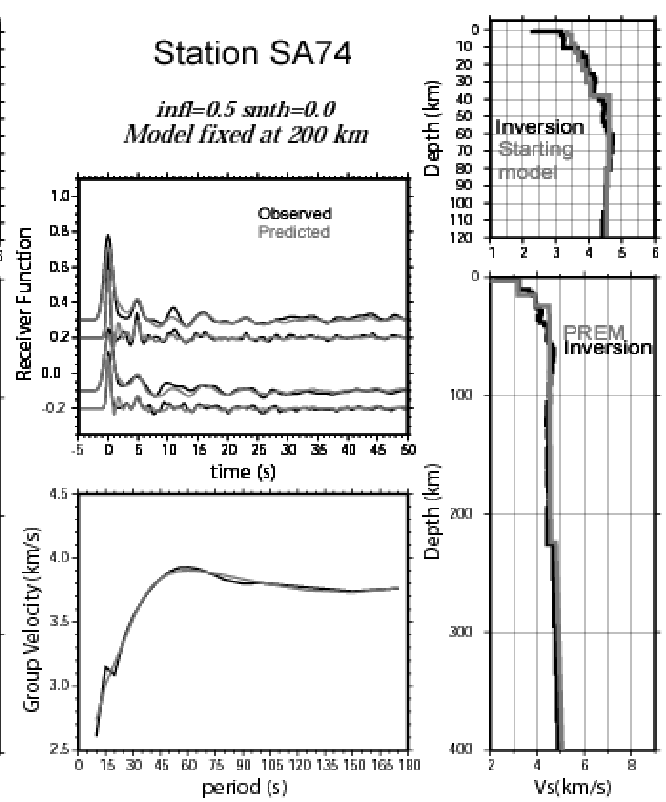
Station SA74
infl=0.5 smth=0.0
Model fixed at 200 km
Observed
Predicted
Receiver Function
time (s)
Group Velocity (km/s)
period (s)
Depth (km)
Inversion
Starting
model
PREM
Inversion
Vs(km/s)

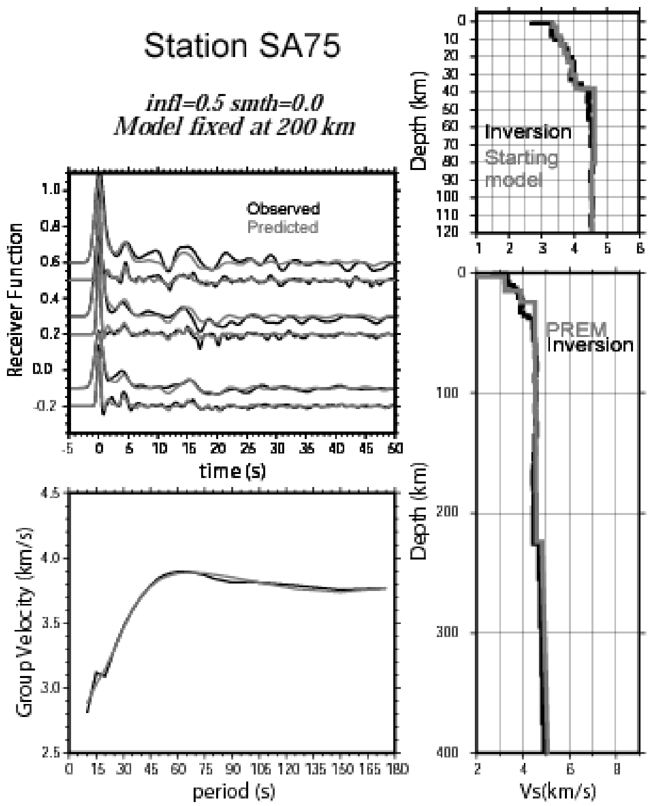
Station SA75
infl=0.5 smth=0.0
Model fixed at 200 km
Observed
Predicted
Receiver Function
time (s)
Group Velocity (km/s)
period (s)
Depth (km)
Inversion
Starting model
PREM
Vs(km/s)

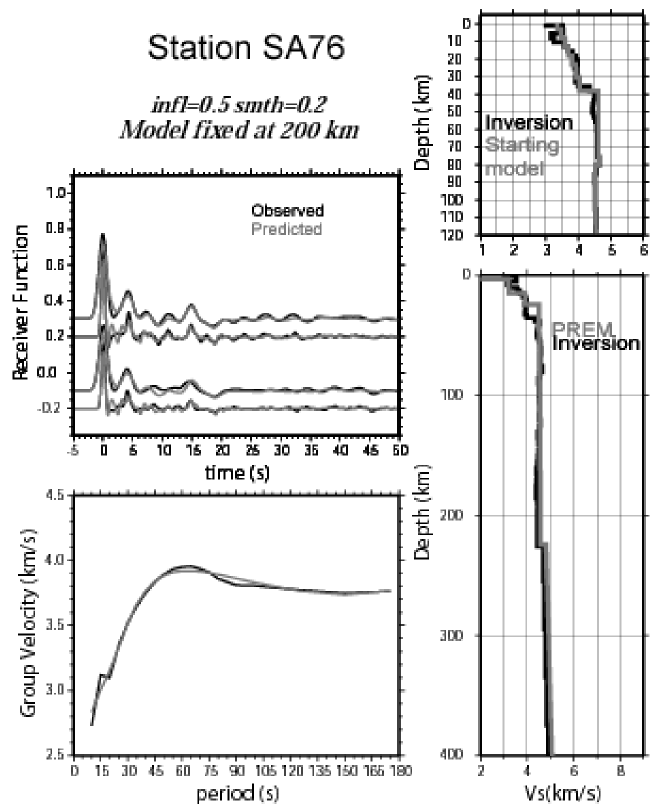
Station SA76
infl=0.5 smth=0.2
Model fixed at 200 km
Observed
Predicted
Receiver Function
time (s)
Group Velocity (km/s)
period (s)
Depth (km)
Inversion
Starting model
PREM
Vs(km/s)

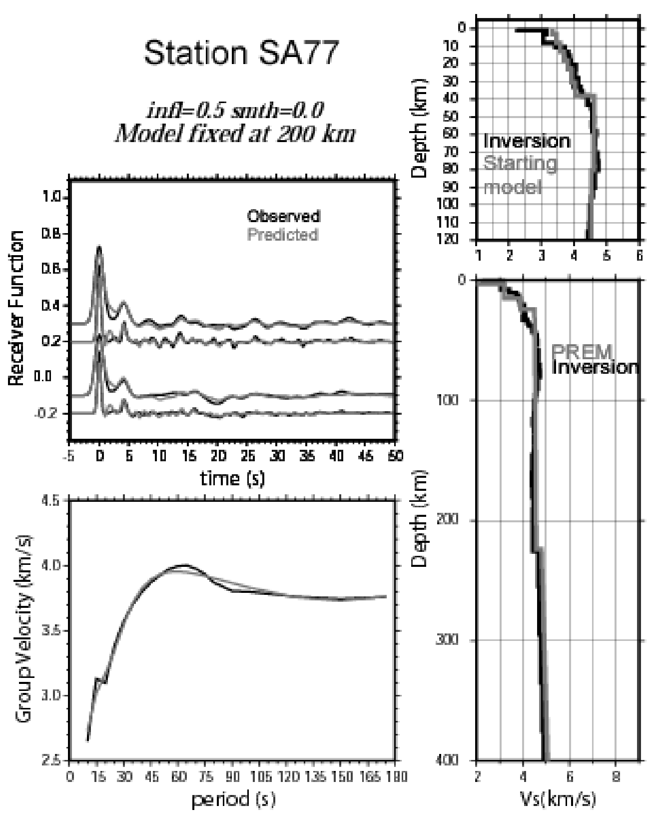
Station SA77
infl=0.5 smth=0.0
Model fixed at 200 km
Observed
Predicted
Receiver Function
time (s)
Group Velocity (km/s)
period (s)
Depth (km)
Inversion
Starting model
PREM
Vs(km/s)

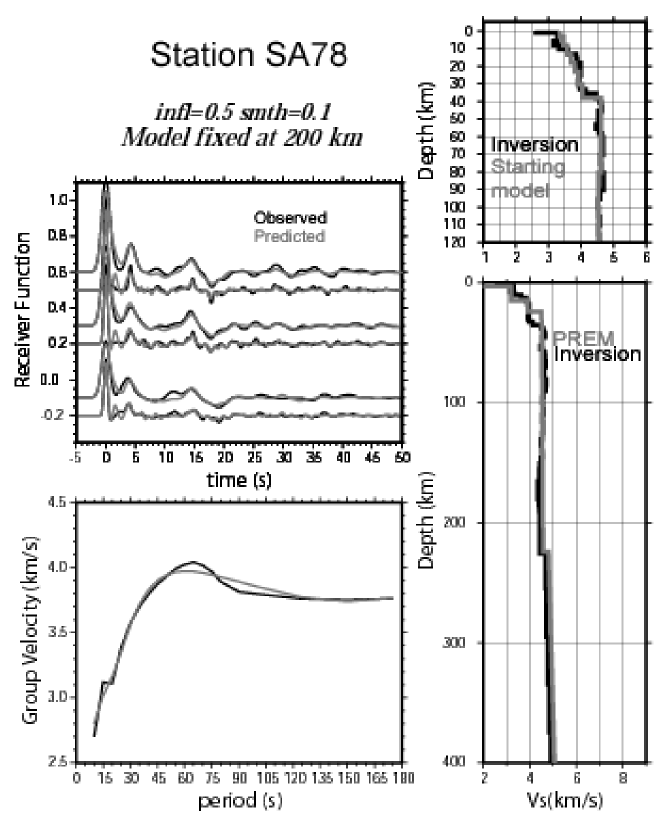
Station SA78
infl=0.5 smth=0.1
Model fixed at 200 km
Observed
Predicted
Receiver Function
time (s)
Group Velocity (km/s)
period (s)
Depth (km)
Inversion
Starting model
PREM
Vs(km/s)

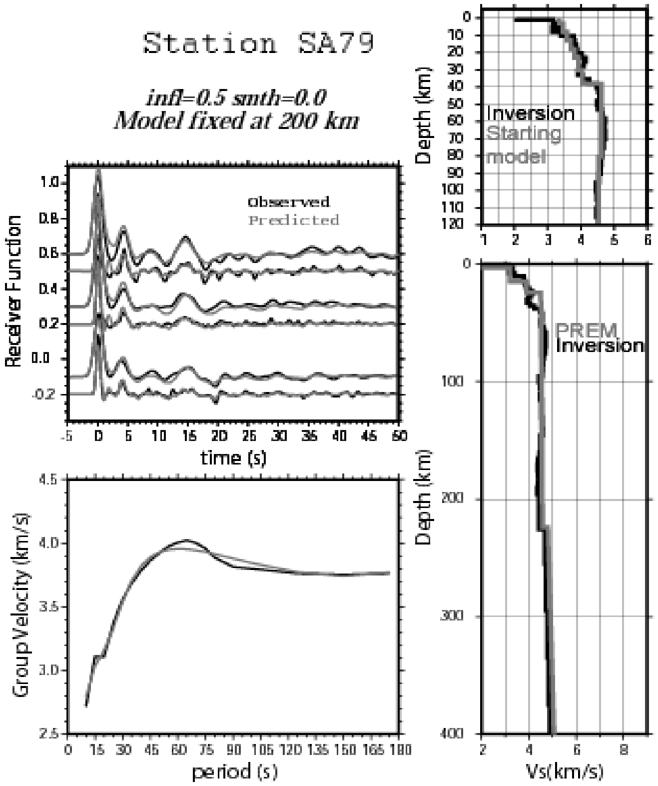

Station SA79
infl=0.5 smth=0.0
Model fixed at 200 km
Observed
Predicted
Receiver Function
time (s)
Group Velocity (km/s)
period (s)
Depth (km)
Inversion
Starting
model
PREM
Inversion
Vs(km/s)

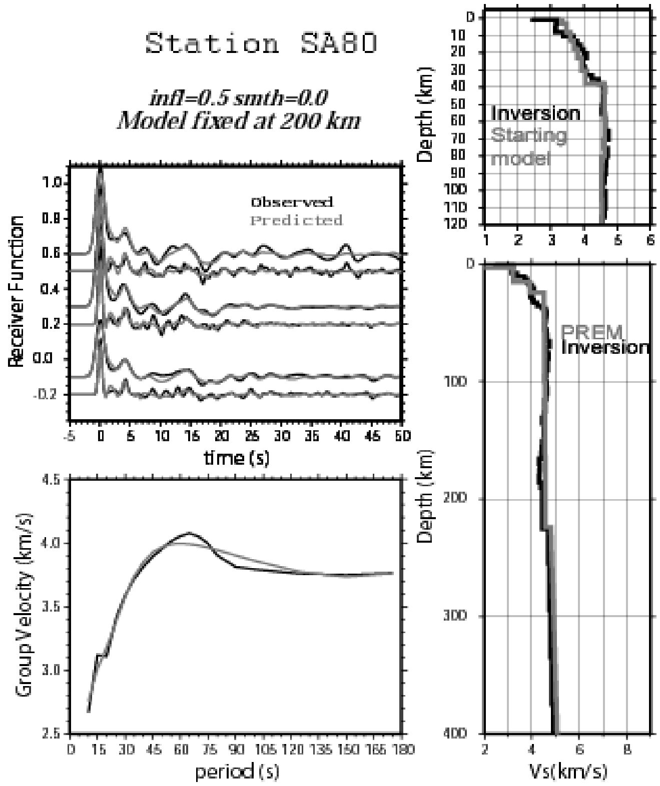

Station SA80
infl=0.5 smth=0.0
Model fixed at 200 km
Observed
Predicted
Receiver Function
time (s)
Group Velocity (km/s)
period (s)
Depth (km)
Inversion
Starting
model
PREM
Inversion
Vs(km/s)

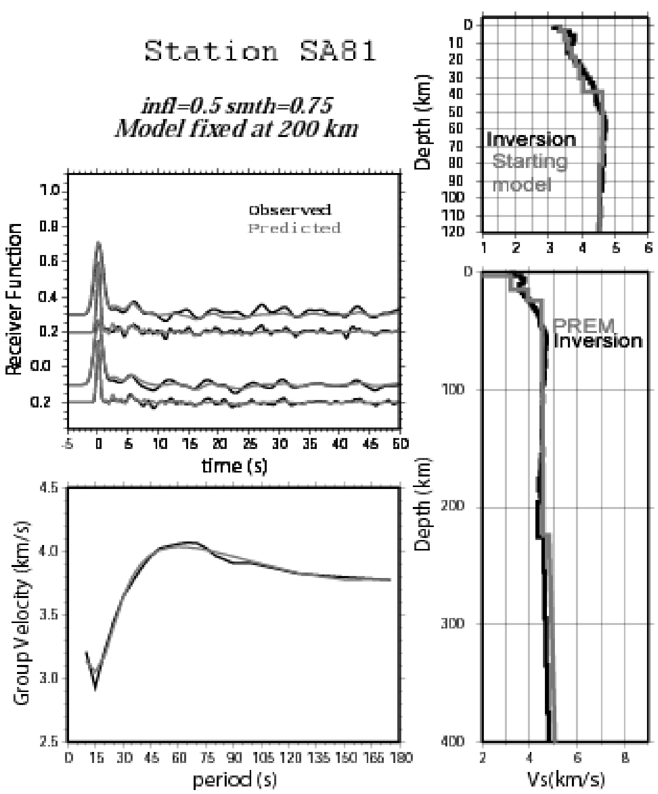

Station SA81
infl=0.5 smth=0.75
Model fixed at 200 km
Observed
Predicted
Receiver Function
time (s)
Group Velocity (km/s)
period (s)
Depth (km)
Inversion
Starting
model
PREM
Inversion
Vs(km/s)

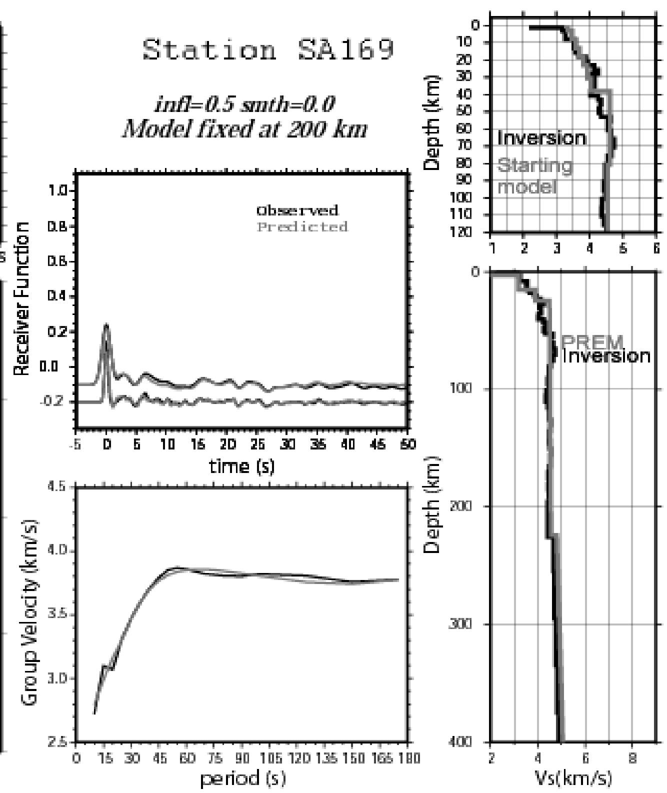

Station SA169
infl=0.5 smth=0.0
Model fixed at 200 km
Observed
Predicted
Receiver Function
time (s)
Group Velocity (km/s)
period (s)
Depth (km)
Inversion
Starting
model
PREM
Inversion
Vs(km/s)

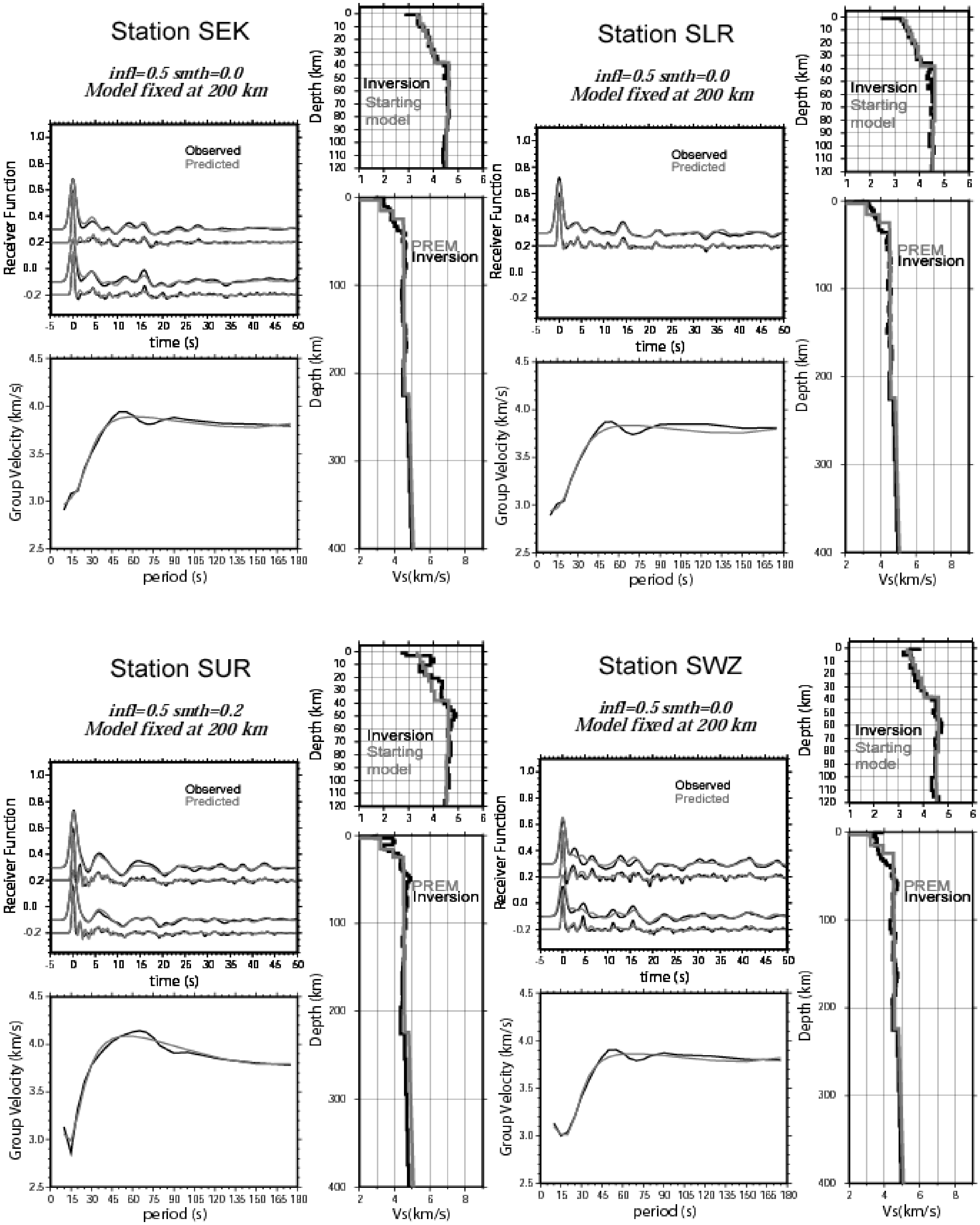

Station SEK
infl=0.5 smth=0.0
Model fixed at 200 km
Observed
Predicted
Receiver Function
time (s)
Group Velocity (km/s)
period (s)
Depth (km)
Inversion
Starting model
PREM
Inversion
Vs(km/s)
Station SLR
infl=0.5 smth=0.0
Model fixed at 200 km
Observed
Predicted
Receiver Function
time (s)
Group Velocity (km/s)
period (s)
Depth (km)
Inversion
Starting model
PREM
Inversion
Vs(km/s)
Station SUR
infl=0.5 smth=0.2
Model fixed at 200 km
Observed
Predicted
Receiver Function
time (s)
Group Velocity (km/s)
period (s)
Depth (km)
Inversion
Starting model
PREM
Inversion
Vs(km/s)
Station SWZ
infl=0.5 smth=0.0
Model fixed at 200 km
Observed
Predicted
Receiver Function
time (s)
Group Velocity (km/s)
period (s)
Depth (km)
Inversion
Starting model
PREM
Inversion
Vs(km/s)

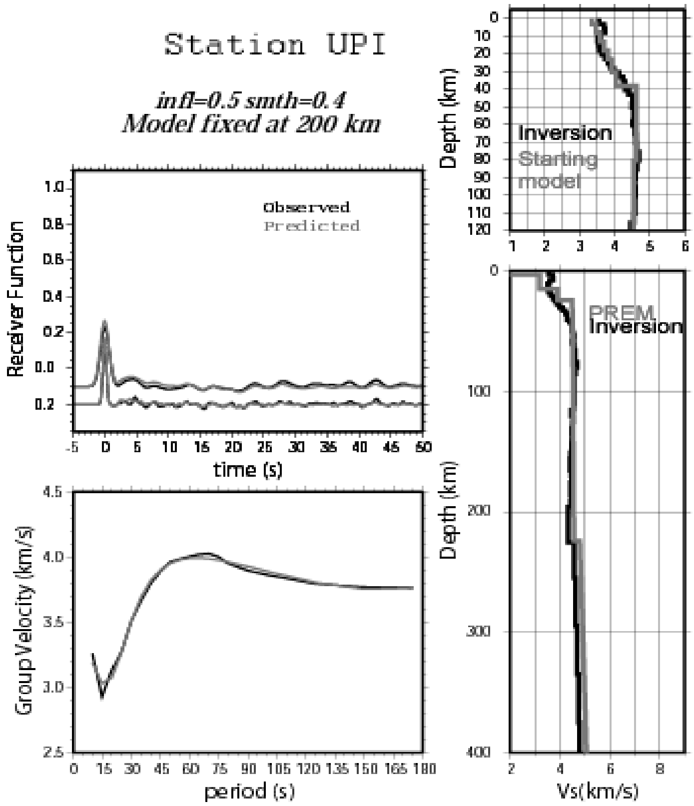

Station UPI
infl=0.5 smth=0.4
Model fixed at 200 km
Observed
Predicted
Receiver Function
time (s)
Group Velocity (km/s)
period (s)
Depth (km)
Inversion
Starting model
PREM
Inversion
Depth (km)
Vs(km/s)

Appendix D

List of mining-related and regional earthquakes used for the measurement of Rayleigh wave group velocities

Event number	Event date (d-m-y)	Origin time (hh:mm:ss.0)	Latitude (deg)	Longitude (deg)	Depth (km)	Magnitude (ML)	Number of stations per event for which measurements were obtained
1	18-04-1997	13:05:20.3	-25.9690	29.4010	0.1	4.4	2
2	23-04-1997	10:13:39.2	-24.4980	28.2750	0.2	4.4	10
3	23-04-1997	11:23:13.0	-23.9300	24.1920	15	4.8	1
4	05-05-1997	23:58:43.3	-25.3300	28.2430	0.3	3.7	4
5	13-05-1997	01:01:55.9	-26.3750	27.4900	0.1	3.0	17
6	13-05-1997	01:50:03.6	-25.6310	27.3510	5.6	4.8	1
7	13-05-1997	08:15:25.0	-26.1320	29.6200	0.1	4.6	4
8	13-05-1997	11:37:49.4	-26.0960	29.6170	0.1	4.3	2
9	14-05-1997	06:31:06.9	-23.8160	25.5890	0.1	4.0	8
10	14-05-1997	08:07:37.3	-23.1870	28.7840	0.6	4.5	4
11	14-05-1997	13:02:45.6	-24.9250	31.7150	0.6	4.6	3
12	14-05-1997	14:11:32.9	-25.4820	29.7810	0.3	4.5	3
13	15-05-1997	05:54:49.7	-25.4930	28.7770	1.4	4.5	2
14	15-05-1997	10:20:32.0	-26.1560	29.5070	0.1	4.6	5
15	15-05-1997	10:46:41.9	-26.2610	29.1720	0.0	4.3	5
16	15-05-1997	15:00:46.9	-26.1170	29.6970	0.0	4.9	5
17	16-05-1997	03:49:04.4	-25.7670	26.6820	0.7	3.6	9
18	16-05-1997	10:01:34.6	-24.0380	28.9640	0.7	4.3	8
19	16-05-1997	12:21:50.7	-24.2420	28.8690	0.2	4.3	6
20	17-05-1997	10:18:23.0	-26.3950	27.4820	0.8	2.8	18
21	17-05-1997	21:31:15.1	-24.6170	27.4380	0.0	3.2	6
22	20-05-1997	09:39:23.0	-26.5750	31.8370	0.0	4.9	9
23	20-05-1997	13:00:21.7	-25.9270	29.4250	6.8	4.0	9
24	21-05-1997	10:49:38.2	-25.2830	27.5750	0.0	4.1	5
25	21-05-1997	11:41:34.8	-23.6970	27.5310	5.7	3.3	5
27	22-05-1997	08:00:56.7	-24.7930	26.7680	8.7	3.4	10
28	22-05-1997	09:12:41.6	-24.0410	31.2510	0.1	4.4	12
29	23-05-1997	16:13:52.0	-26.9003	26.7710	2.0	3.6	13
30	24-05-1997	10:03:38.7	-22.4310	29.3260	2.0	3.7	2
31	24-05-1997	15:02:31.0	-22.2100	29.9170	8.3	3.6	7
32	25-05-1997	23:58:39.5	-22.2470	27.9160	6.5	7.9	10
33	26-05-1997	10:32:43.4	-23.9970	28.8770	0.9	3.1	8
34	26-05-1997	13:50:01.4	-24.6090	27.3530	0.0	3.5	4
35	27-05-1997	08:56:53.9	-25.5280	28.7440	3.4	4.3	11
36	27-05-1997	11:45:39.6	-25.9730	29.5510	0.0	4.8	9
37	27-05-1997	16:02:13.7	-26.1280	29.6690	0.0	5.1	9
38	28-05-1997	11:44:04.1	-23.6670	27.4910	0.0	3.1	5
39	28-05-1997	12:13:06.8	-22.4200	29.2770	6.2	3.0	3
40	30-05-1997	18:34:29.4	-26.3800	27.4000	2.0	3.1	12
41	31-05-1997	12:01:50.3	-25.2930	28.7560	0.0	4.3	1

42	02-06-1997	11:11:46.8	-23.6810	27.5290	0.1	4.2	2
43	02-06-1997	13:14:48.1	-25.9190	29.4650	0.0	4.6	9
44	04-06-1997	11:05:43.9	-24.5170	24.6950	4.5	3.3	5
45	04-06-1997	11:42:59.8	-23.7290	27.5490	0.0	2.7	8
46	04-06-1997	14:32:20.6	-25.2570	27.6220	0.0	3.4	2
47	05-06-1997	13:32:44.0	-24.5980	27.3340	0.0	3.5	6
48	05-06-1997	15:37:54.8	-26.1990	25.2200	0.0	4.2	1
49	06-06-1997	08:46:45.3	-23.9650	31.0450	0.0	3.8	14
50	07-06-1997	08:56:46.3	-24.5750	27.3480	0.0	3.6	4
51	07-06-1997	10:23:26.8	-25.9810	29.3880	0.0	3.4	10
52	07-06-1997	11:19:15.1	-25.9830	29.3520	0.0	4.2	2
53	08-06-1997	19:56:29.9	-26.4330	27.3920	1.6	2.8	13
54	10-06-1997	15:23:54.5	-25.5340	28.7720	0.1	3.5	5
55	11-06-1997	05:15:37.5	-22.4440	29.3280	4.9	3.0	8
56	11-06-1997	11:39:15.7	-23.7100	27.5210	0.1	2.8	14
57	11-06-1997	11:51:20.0	-19.5210	30.1030	11.7	4.5	1
58	11-06-1997	12:07:03.0	-24.5620	24.7470	0.0	3.8	1
59	11-06-1997	13:56:23.6	-24.7180	27.3900	0.0	3.3	1
60	12-06-1997	12:40:10.1	-25.9910	29.3460	0.0	4.7	3
61	29-06-1997	12:17:14.7	-26.4400	27.3500	2.0	3.4	10
62	29-06-1997	15:24:02.6	-26.3800	27.4600	2.0	3.5	7
63	09-07-1997	14:03:12.1	-26.4300	27.4400	2.0	3.6	6
64	16-07-1997	08:10:18.5	-26.4400	27.5300	2.0	3.4	1
65	18-07-1997	15:10:22.5	-26.4300	27.4400	2.0	3.2	14
66	19-07-1997	19:06:05.2	-26.3471	27.6293	2.0	3.3	4
67	26-07-1997	03:22:44.2	-26.3444	27.6275	2.0	3.5	15
68	29-07-1997	11:25:06.0	-27.9577	26.7022	2.0	4.0	5
69	01-08-1997	02:17:24.2	-27.9492	26.6992	2.0	4.1	3
70	11-08-1997	16:30:20.4	-28.0098	26.7584	2.0	3.7	3
71	18-08-1997	04:46:13.6	-26.4196	27.6003	2.0	3.4	22
72	07-09-1997	08:45:39.8	-26.4530	27.3464	2.0	3.0	19
73	13-09-1997	22:43:36.1	-26.8877	26.7816	2.0	4.0	12
74	17-09-1997	01:53:23.0	-26.3408	27.6322	2.0	3.2	15
75	17-09-1997	11:58:18.3	-26.4374	27.3873	2.0	3.7	20
76	05-10-1997	19:01:58.4	-26.3700	27.3100	2.0	3.6	9
77	20-10-1997	19:20:42.2	-26.4326	27.4200	2.0	3.8	20
78	02-11-1997	06:27:09.4	-26.3600	27.5100	2.0	3.4	12
79	20-11-1997	00:31:48.4	-26.3500	27.4600	2.0	3.4	14
80	17-12-1997	14:30:51.3	-26.4200	27.6030	2.0	3.0	16
81	21-12-1997	10:35:55.5	-26.4012	27.4670	2.0	3.4	14
82	06-01-1998	21:22:38.8	-26.4610	27.3221	2.0	3.0	12
83	11-02-1998	21:18:52.7	-26.4051	27.6073	2.0	3.3	11
84	22-04-1998	12:44:32.3	-26.3894	27.4288	2.0	3.2	9
85	26-04-1998	00:50:25.1	-26.3748	27.5041	2.0	3.9	13
86	14-05-1998	10:36:43.3	-28.0590	26.8025	2.0	3.1	3
87	16-05-1998	16:26:47.8	-28.0404	26.8115	2.0	3.1	2
88	30-05-1998	16:34:01.6	-26.4325	27.4130	2.0	3.0	20
89	17-06-1998	12:50:24.3	-26.3959	27.4880	2.0	2.9	17
90	19-06-1998	15:52:07.4	-26.4200	27.4100	2.0	3.3	16
91	22-06-1998	14:22:26.7	-26.4368	27.4208	2.0	3.1	15
92	22-06-1998	14:47:56.5	-26.3823	27.4830	2.0	3.2	20
93	27-06-1998	04:35:56.5	-26.3800	27.4800	2.0	3.1	17
94	09-07-1998	22:55:24.8	-26.3700	27.5900	2.0	3.5	9

95	13-07-1998	07:05:06.7	-27.9500	26.7500	2.0	3.8	14
96	17-07-1998	12:49:25.0	-26.3500	27.5300	2.0	3.2	11
97	18-07-1998	05:16:26.1	-26.4700	27.4800	2.0	3.5	9
98	23-07-1998	05:22:03.3	-26.3982	27.4387	2.0	3.2	11
99	27-07-1998	18:56:52.1	-26.4400	27.4000	2.0	3.6	13
100	01-08-1998	06:33:26.5	-25.8933	28.3949	2.0	3.7	9
101	04-08-1998	11:50:59.5	-26.4774	27.3272	2.0	2.9	6
102	17-08-1998	09:17:40.9	-26.3879	27.4814	2.0	3.5	14
103	04-09-1998	11:35:47.3	-26.3472	27.6304	2.0	3.3	14
104	08-09-1998	16:22:32.4	-26.3875	27.4441	2.0	3.3	15
105	02-10-1998	07:35:29.2	-26.4311	27.3833	2.0	3.7	17
106	02-10-1998	10:17:52.1	-26.3953	27.4703	2.0	3.8	20
107	07-10-1998	04:51:05.9	-26.3916	27.4920	2.0	3.7	18
108	07-10-1998	06:46:51.2	-26.3905	27.4981	2.0	3.5	16
109	08-10-1998	22:44:07.2	-25.2380	27.3401	5.0	3.2	9
110	12-10-1998	14:20:57.0	-24.7500	27.4200	0	4.7	5
111	12-10-1998	16:09:08.9	-22.8830	28.9430	6.5	3.1	5
112	13-10-1998	05:12:07.0	-25.9340	27.0130	3.5	4.4	5
113	13-10-1998	06:05:20.2	-26.4343	27.6024	2.0	3.1	14
114	13-10-1998	08:54:47.3	-25.8300	29.5490	0	4.3	7
115	13-10-1998	09:26:24.5	-27.7000	23.0980	22.0	4.3	3
116	13-10-1998	10:44:37.1	-26.0080	29.4320	0	4.7	4
117	13-10-1998	14:01:43.3	-26.2160	25.2420	1.0	4.6	2
118	13-10-1998	15:52:39.1	-24.4810	30.4740	3.8	4.7	8
119	14-10-1998	00:16:44.8	-28.0700	26.8210	1.1	3.6	2
120	14-10-1998	00:55:18.5	-26.4620	27.4510	3.8	3.7	5
121	14-10-1998	06:36:25.3	-26.4710	27.4800	4.7	4.3	5
122	14-10-1998	10:52:13.1	-28.1010	26.7190	1.0	4.8	2
123	15-10-1998	11:43:15.9	-26.3680	29.2600	0	4.3	8
124	15-10-1998	11:52:25.5	-23.6210	27.4680	0	4.3	1
125	15-10-1998	13:04:48.6	-22.4570	29.3300	19.0	4.0	4
126	15-10-1998	13:52:04.5	-26.4650	27.3660	0.5	5.1	2
127	15-10-1998	17:26:07.1	-26.4730	27.4550	1.0	4.9	4
128	16-10-1998	00:17:16.4	-27.5000	27.3700	0	2.8	2
129	16-10-1998	02:39:05.3	-27.0230	26.8000	0	3.9	2
130	16-10-1998	10:17:59.2	-23.9600	30.7790	3.6	3.4	3
131	17-10-1998	05:03:12.8	-25.0000	30.2440	0	3.3	2
132	17-10-1998	07:27:23.8	-22.4230	29.2970	7.1	4.7	3
133	19-10-1998	09:39:41.8	-27.7010	23.0160	12.0	3.5	7
134	20-10-1998	08:23:24.0	-25.9830	29.5340	0.9	3.9	5
135	20-10-1998	09:59:57.5	-25.9980	29.6690	0	4.3	4
136	20-10-1998	11:46:20.1	-23.6770	27.5200	0	3.2	10
137	20-10-1998	18:31:41.2	-26.3830	27.4290	0.1	3.1	17
138	21-10-1998	06:31:40.9	-25.6570	27.2970	0	3.8	4
139	21-10-1998	14:14:03.5	-26.2070	25.0190	23.9	5.1	4
140	21-10-1998	19:43:10.0	-24.7630	27.2630	0	3.7	2
141	22-10-1998	07:22:21.7	-24.6770	27.3500	0	4.0	11
142	23-10-1998	10:10:36.6	-22.4090	29.3680	3.3	4.0	4
143	23-10-1998	11:10:11.7	-24.5340	27.3280	0	3.2	8
144	27-10-1998	10:34:57.2	-23.9430	30.6400	0	4.8	1
145	27-10-1998	11:43:50.2	-23.6700	27.5940	0	5.6	1
146	28-10-1998	10:00:09.5	-24.0220	28.9040	0	5.4	1
147	28-10-1998	11:41:07.3	-23.6800	27.5090	0	4.4	2

148	29-10-1998	08:17:08.8	-24.2900	27.7810	0	3.3	5
149	29-10-1998	09:21:28.0	-22.3770	29.9920	10.0	2.6	2
150	30-10-1998	13:00:47.8	-24.4710	24.6260	0.1	4.5	7
151	30-10-1998	14:46:30.1	-24.2400	29.3020	0	3.6	3
152	30-10-1998	21:40:25.3	-26.4000	27.4700	2.0	3.4	18
153	01-11-1998	04:57:05.3	-24.8710	27.2960	0	5.0	3
154	01-11-1998	05:15:36.8	-24.7730	27.2900	0	4.7	3
155	02-11-1998	08:04:40.1	-24.8800	27.1480	0	4.3	8
156	02-11-1998	09:58:50.2	-24.6620	27.3810	0	4.2	7
157	02-11-1998	14:08:18.3	-25.1810	27.6200	0	4.2	7
158	03-11-1998	10:21:54.6	-24.0090	28.8040	0	3.9	3
159	03-11-1998	10:54:26.6	-24.6600	27.3630	0	4.7	4
160	03-11-1998	14:59:16.8	-24.1630	29.9090	0	4.3	2
161	04-11-1998	15:36:17.3	-24.7730	27.2990	0	4.5	3
162	05-11-1998	09:08:28.7	-23.8450	30.7040	0	4.0	5
163	06-11-1998	14:44:20.8	-26.0800	27.7800	2.0	2.6	11
164	07-11-1998	07:54:05.5	-24.7730	27.2060	1.1	3.7	3
165	07-11-1998	08:04:55.0	-24.2100	29.2590	0	3.9	1
166	09-11-1998	11:42:05.2	-23.6650	27.5890	2.6	3.3	13
167	10-11-1998	09:09:39.1	-27.7660	23.1890	19.3	4.8	2
168	10-11-1998	13:42:08.8	-25.8880	29.5350	1.6	3.6	10
169	11-11-1998	11:25:36.3	-24.3070	29.2640	0	4.5	7
170	13-11-1998	00:42:07.6	-24.8610	27.2970	0	3.9	7
171	13-11-1998	01:06:19.4	-24.8760	27.2880	0	4.3	2
172	13-11-1998	09:57:04.0	-24.0150	28.8900	0	4.1	11
173	13-11-1998	10:45:39.2	-23.9310	31.1160	9.0	4.1	4
174	14-11-1998	07:18:57.4	-26.9300	26.7500	2.0	3.8	14
175	17-11-1998	10:09:29.0	-24.0120	28.9050	0.6	3.1	5
176	17-11-1998	11:41:59.8	-23.6800	27.5000	1.8	4.6	4
177	17-11-1998	20:17:58.4	-26.8000	26.7600	2.0	4.4	18
178	18-11-1998	16:30:05.7	-26.9460	26.7810	1.2	3.9	14
179	18-11-1998	13:01:32.2	-23.8460	30.6570	6.6	3.6	2
180	18-11-1998	13:30:39.3	-24.9520	30.1580	2.4	4.4	2
181	19-11-1998	14:07:43.5	-26.4780	27.3380	0.9	3.1	16
182	20-11-1998	10:06:06.1	-24.0090	28.9080	1.4	4.2	5
183	24-11-1998	11:37:29.3	-23.6630	27.5960	4.8	4.0	5
184	25-11-1998	11:44:25.2	-23.6630	27.4930	4.7	5.1	10
185	26-11-1998	06:55:07.3	-26.3800	27.4200	2.0	3.0	12
186	26-11-1998	23:52:33.9	-26.9800	26.7600	2.0	3.5	13
187	27-11-1998	10:19:04.4	-22.2990	29.2720	3.3	4.3	2
188	30-11-1998	09:47:22.96	-26.3520	30.1190	0	3.8	2
189	01-12-1998	09:22:49.3	-26.9200	26.8200	2.0	3.6	13
190	01-12-1998	23:01:47.8	-27.7000	30.1600	5.0	3.5	1
191	01-12-1998	18:12:16.3	-28.0400	26.8800	2.0	3.7	11
192	05-12-1998	04:52:44.8	-26.3500	27.5400	2.0	4.3	16
193	05-12-1998	13:11:10.2	-23.3660	30.1910	3.1	4.7	3
194	07-12-1998	16:58:46.9	-26.8600	26.7500	2.0	3.4	12
195	16-12-1998	16:00:02.1	-26.4000	27.4500	2.0	3.9	18
196	23-12-1998	07:39:01.6	-26.4400	27.2800	2.0	3.1	13
197	24-12-1998	14:02:57.6	-26.3900	27.3500	2.0	3.0	13

JOURNAL OF GEOPHYSICAL RESEARCH, VOL. 114, B12304, doi:10.1029/2008JB006217, 2009

Shear wave velocity structure of the lower crust in southern Africa: Evidence for compositional heterogeneity within Archaean and Proterozoic terrains

Eldridge M. Kgaswane,[1,2] Andrew A. Nyblade,[3] Jordi Julià,[3] Paul H. G. M. Dirks,[2,4] Raymond J. Durrheim,[2,5] and Michael E. Pasyanos[6]

Received 18 November 2008; revised 29 June 2009; accepted 19 August 2009; published 15 December 2009.

[1] The nature of the lower crust across the southern African shield has been investigated by jointly inverting receiver functions and Rayleigh wave group velocities for 89 broadband seismic stations located in Botswana, South Africa and Zimbabwe. For large parts of both Archaean and Proterozoic terrains, the velocity models obtained from the inversions show shear wave velocities $\geq$4.0 km/s below $\sim$20–30 km depth, indicating a predominantly mafic lower crust. However, for much of the Kimberley terrain and adjacent parts of the Kheis Province and Witwatersrand terrain in South Africa, as well as for the western part of the Tokwe terrain in Zimbabwe, shear wave velocities of $\leq$3.9 km/s are found below $\sim$20–30 km depth, indicating an intermediate-to-felsic lower crust. The areas of intermediate-to-felsic lower crust in South Africa coincide with regions where Ventersdorp rocks have been preserved, suggesting that the more evolved composition of the lower crust may have resulted from crustal reworking and extension during the Ventersdorp tectonomagmatic event at c. 2.7 Ga.

Citation: Kgaswane, E. M., A. A. Nyblade, J. Julià, P. H. G. M. Dirks, R. J. Durrheim, and M. E. Pasyanos (2009), Shear wave velocity structure of the lower crust in southern Africa: Evidence for compositional heterogeneity within Archaean and Proterozoic terrains, *J. Geophys. Res.*, *114*, B12304, doi:10.1029/2008JB006217.

1. Introduction

[2] Motivated by previous studies suggesting that there may be significant variability in the composition of the lower crust across the southern African shield, here we investigate the nature of both Archaean and Proterozoic lower crust in southern Africa using 1-D shear wave velocity models obtained by jointly inverting receiver functions and Rayleigh wave group velocities. Characterizing the variability in lower crustal composition across southern Africa is important not only for improving our understanding of crustal growth and tectonics in Africa, but also globally. As many studies have shown, the composition of the lower crust remains one of the largest unknowns in the overall structure of the crust, leading to considerable uncertainty in the role of the lower crust in continental dynamics [e.g., *Christensen and Mooney*, 1995; *Rudnick and Fountain*, 1995; *Rudnick and Gao*, 2003].

[3] Much of the evidence for variability in lower crustal composition across southern Africa comes from interpreting seismic data. *Niu and James* [2002], for example, using receiver function analysis, found that the lower crust around the Kimberley region in the western part of the Kaapvaal Craton has an intermediate-to-felsic composition. From this result, they suggested that the lower crust beneath the Kaapvaal Craton could be dominated by intermediate-to-felsic lithologies. Receiver function analyses by *Nguuri* [2004] and *Nair et al.* [2006], however, yielded crustal Vp/Vs ratios as high as 1.78 for parts of the Kaapvaal Craton and surrounding Proterozoic mobile belts, suggesting that in some areas the lower crust may contain a significant proportion of mafic rock. Crustal velocity models developed using seismic reflection and refraction data also suggest significant variability in lower crustal composition [e.g., *Green and Durrheim*, 1990; *Durrheim and Green*, 1992; *de Wit and Tinker*, 2004].

[4] The 1-D shear wave velocity models obtained from jointly inverting receiver functions and Rayleigh wave group velocities span the greater part of the exposed Precambrian shield of southern Africa (Figures 1 and 2) and indicate considerable differences in lower crustal composition within and between a number of terrains. In this paper, following a brief review of the geological framework of southern Africa, we describe the data sets and technique used for the joint inversions, discuss similarities and differences in lower

[1] Council for Geoscience, Pretoria, South Africa.
[2] School of Geosciences, University of the Witwatersrand, Johannesburg, South Africa.
[3] Department of Geosciences, Pennsylvania State University, University Park, Pennsylvania, USA.
[4] School of Earth and Environmental Sciences, James Cook University, Townsville, Queensland, Australia.
[5] Council for Scientific and Industrial Research, Johannesburg, South Africa.
[6] Lawrence Livermore National Laboratory, Livermore, California, USA.

0148-0227/09/2008JB006217$09.00

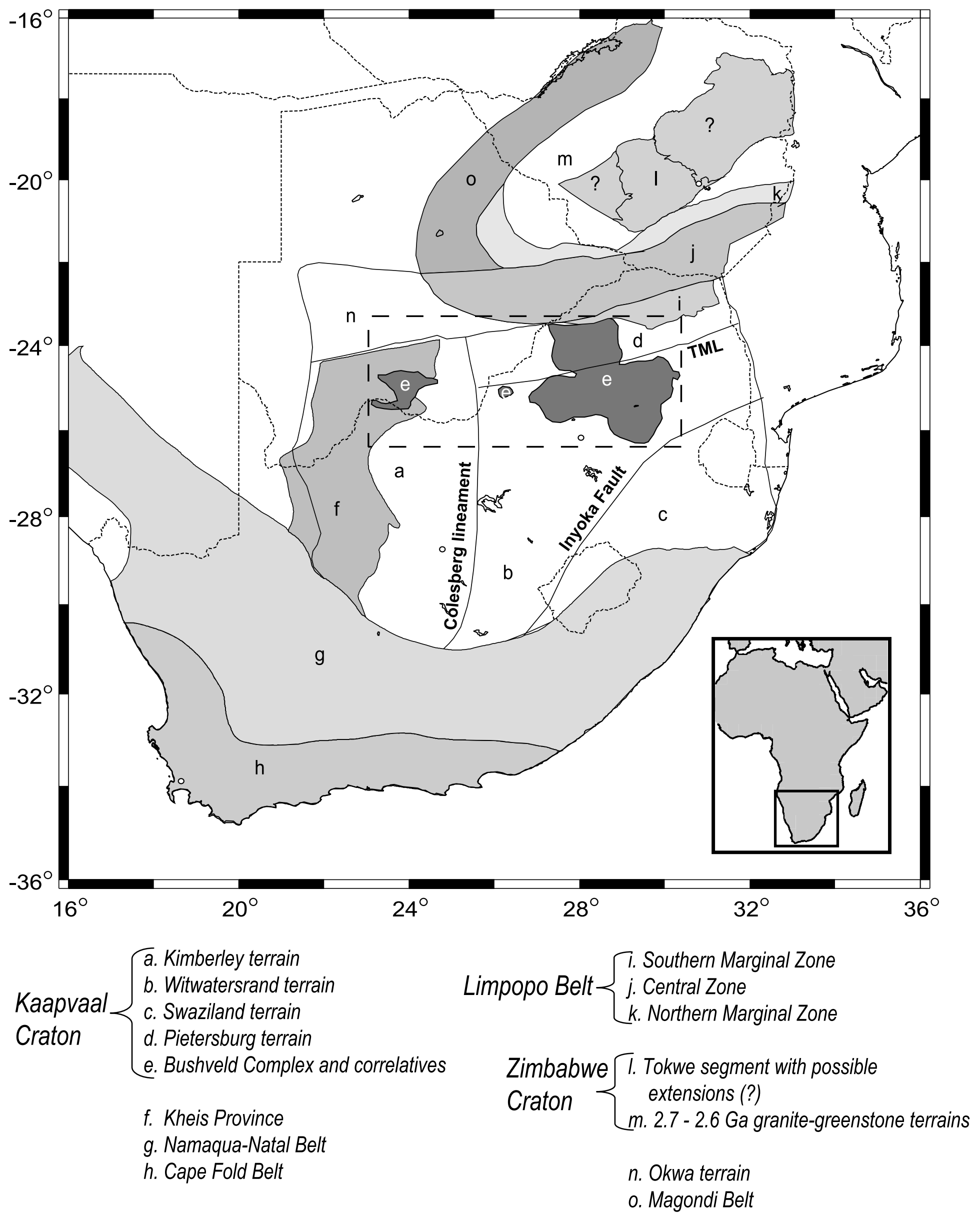

Figure 1. Tectonic map of southern Africa showing major Precambrian terrains. Terrain names and boundaries are taken from *Eglington and Armstrong* [2004] and *Jelsma and Dirks* [2002]. Political boundaries are shown with thin dashed lines. The box shown with bold dashed lines encloses the region affected by the Bushveld Complex. TML, Thabazimbi Murchison Lineament.

crustal composition indicated by the velocity models, and examine possible causes for the lower crustal heterogeneity that we observe vis-à-vis major Precambrian tectonothermal events that affected the region.

2. Tectonic and Geological Framework of Southern Africa

2.1. Overview of Precambrian Structure

[5] The Kalahari Craton, which forms the nucleus of the southern African shield, is comprised of the Archaean Kaapvaal Craton welded to the Archaean Zimbabwe Craton by the Archaean and Palaeoproterozoic Limpopo Belt [*de Wit et al.*, 1992] (Figure 1). The Kalahari Craton is bounded by the Palaeoproterozoic Okwa-Magondi Belt to the northwest, the Mesoproterozoic Namaqua-Natal Belt, including Kheis Province, to the south and southwest, and the Palaeozoic Cape Fold Belt even further to the south (Figure 1). A brief description of these tectonic terrains follows.

2.2. Kaapvaal Craton

[6] The Kaapvaal Craton is an Archaean granite-greenstone terrain that formed between 3.7 and 2.7 Ga [*de Wit et al.*, 1992; *Eglington and Armstrong*, 2004]. Based on the age distribution of supracrustal and intrusive rocks, and the presence of major structural boundaries, the craton has been subdivided into four tectonostratigraphic terrains; the

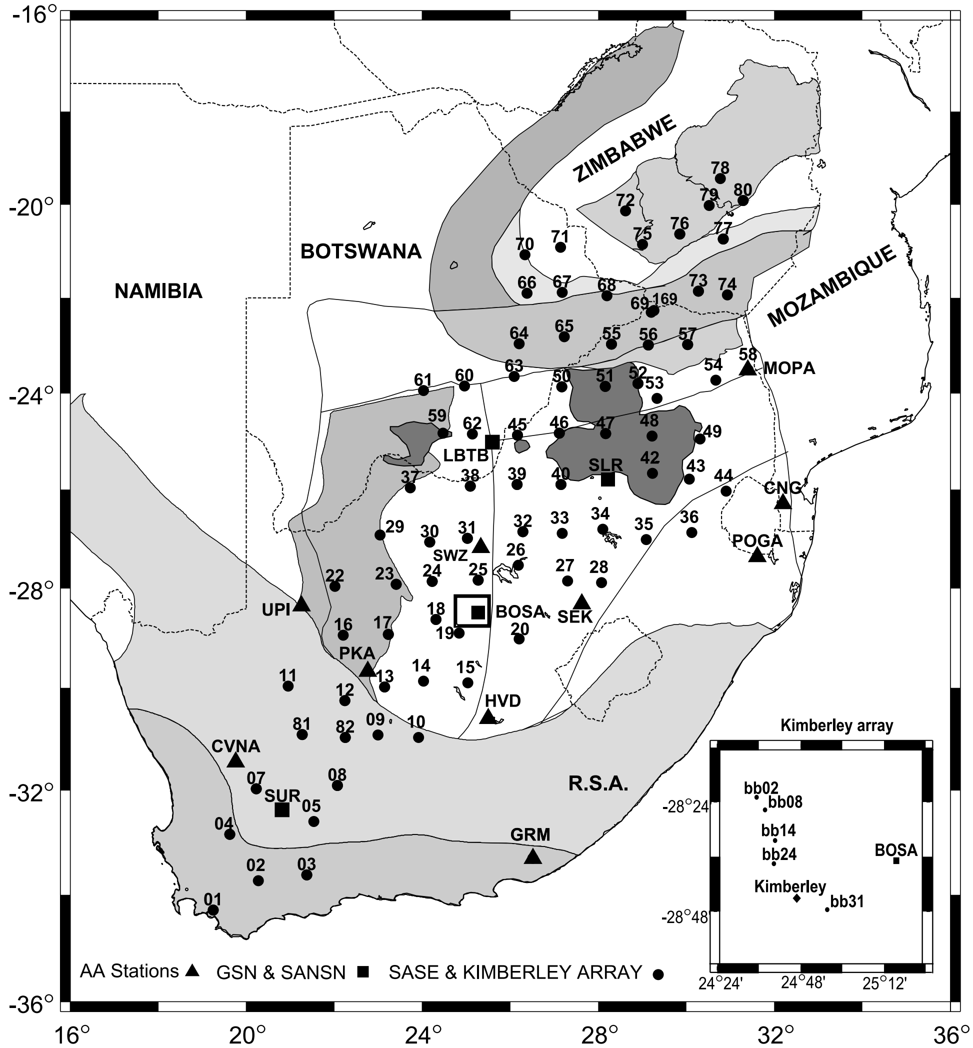

Figure 2. Map showing distribution of broadband seismic stations used in this study in relation to the terrain boundaries shown in Figure 1. The open square in the central part of the Kimberley terrain shows the location of the Kimberley array. The area within the box is enlarged in map in the bottom right corner. AA, AfricaArray network; GSN, Global Seismic Network; SANSN, South Africa National Seismic Network; SASE, Southern African Seismic Experiment.

Kimberley (3.0–2.8 Ga), the Pietersburg (3.0–2.8 Ga), the Witwatersrand and Swaziland terrains (3.6–3.1 Ga) separated by the Thabazimbi-Murchison and Colesburg lineaments and the Inyoka Fault (Figure 1) [*de Wit et al.*, 1992; *Eglington and Armstrong*, 2004]. The Swaziland terrain is the oldest (>3.2 Ga) and the Witwatersrand terrain was accreted to it at ~3.2 Ga. The Pietersburg and Kimberely terrains were joined to the Witwatersrand-Swaziland terrain between 3.0 and 2.8 Ga. Other tectonothermal events that affected the craton are represented by a series of rift-related, intracratonic basins, including the Dominion (3.1 Ga), Witwatersrand (3.0–2.8 Ga), Ventersdorp (2.7 Ga), Transvaal (2.6–2.2 Ga) and Waterberg (2.0–1.8 Ga) basins, and the emplacement of the Bushveld Complex (2.05 Ga) [*Eglington and Armstrong*, 2004; *Johnson et al.*, 2006].

2.3. Zimbabwe Craton

[7] The Zimbabwe Craton consists of granite-greenstone terrains that formed between 3.6 and 2.5 Ga in three stages of crustal formation [e.g., *Dirks and Jelsma*, 2002]. The Tokwe Gneiss terrain in the center of the craton, which formed at 3.6–3.3 Ga, contains mafic fragments that represent the remnants of highly deformed and metamorphosed greenstone belts. A sequence of clastic sediments and greenstones accreted against the western part of the Tokwe Gneiss terrain between 3.2 and 2.8 Ga. The principal period of greenstone formation and accretion occurred between 2.7 and 2.6 Ga, with stabilization of the craton around 2.6 Ga. The Great Dyke was emplaced around 2.58 Ga, marking the last major tectonothermal event to affect the craton [*Jelsma and Dirks*, 2002].

2.4. Limpopo Belt

[8] The Limpopo Belt is a roughly east-west trending zone of high-grade metamorphic rocks that separates the Kaapvaal and Zimbabwe Cratons [e.g., *McCourt and Armstrong*, 1998; *Kramers et al.*, 2006]. The belt has been subdivided into three domains, the Northern Marginal Zone (NMZ), the

Central Zone (CZ) and the Southern Marginal Zone (SMZ), separated by major shear zones [*Kramers et al.*, 2006]. The NMZ and SMZ contain remnants of Archaean granite-greenstone terrains that were modified by a major orogenic event at 2.6–2.5 Ga during which the rocks attained amphibolite to granulite facies metamorphism [e.g., *Berger et al.*, 1995; *Kreissig et al.*, 2000; *Kramers et al.*, 2006]. The CZ (>3.0 and 2.6 and 2.0 Ga) is dominated by granulite facies gneiss with minor metasedimentary and ultramafic intercalations [e.g., *Barton et al.*, 1979; *Kramers et al.*, 2006] affected by orogenic activity at 2.6–2.5 Ga and then again, importantly, at 2.0 Ga, during which the CZ, the NMZ and the SMZ attained their current configuration.

2.5. Bushveld Complex

[9] The Bushveld Complex (BC) (2.05 Ga) is the largest known layered mafic intrusion, extending >350 km in both north-south and east-west directions across the northern Kaapvaal Craton, and reaching a vertical thickness of about 8 km [e.g., *Webb et al.*, 2004] (Figure 1). The intrusion is divided into the Rustenburg Mafic Layered Suite, the Lebowa Granite Suite, the Rashoop Granophyre Suite, and the Rooiberg Group, which consists of rhyolites and basaltic andesites [*South African Committee for Stratigraphy*, 1980; *Hatton and Schweitzer*, 1995; *Cawthorn et al.*, 2006].

2.6. Mesoproterozoic to Palaeozoic Mobile Belts

[10] The Magondi Belt (~2.0–1.8 Ga) to the west and northwest of the Zimbabwe Craton is dominated by passive margin, shelf sediments of the Magondi supergroup thrust eastward onto the craton during the Magondi Orogeny [*McCourt et al.*, 2001]. Magondi Belt rocks have been correlated with deformed mafic and felsic magmatic rocks of the 2.05 Ga Okwa terrain in central Botswana (Figure 1) [*Stowe*, 1989], suggesting the presence of a continuous northeast trending orogenic belt to the west of the Zimbabwe Craton, possibly merging with the CZ of the Limpopo Belt.

[11] The Namaqua-Natal Belt (NNB) to the south and west of the Kaapvaal Craton is comprised of igneous and supracrustal rocks that accreted against the craton during the Namaqua Orogeny (1.2–1.0 Ga). The NNB is exposed to the west (the Namaqua Sector) and southeast (the Natal Sector) of the craton [*Cornell et al.*, 2006], but the central part of the belt is covered by younger sediments of the Karoo Supergroup. The Namaqua Sector is composed of five distinct terrains with ages between 2.0 to 1.3 Ga. These terrains are separated from the Kaapvaal Craton by a passive margin sequence of siliciclastic rocks of the Olifantshoek Supergroup (2.0–1.7 Ga), referred to as the Kheis Province [*Cornell et al.*, 2006]. Accretion of the Namaqua Sector to the craton at 1.0–1.2 Ga coincided with eastward thrusting of Olifantshoek sediments onto the craton [*Moen*, 1999; *Eglington and Armstrong*, 2004], resulting in a thin-skinned fold-and-thrust belt, called the Kheis Belt. The Kheis Belt has been correlated with the Okwa terrain and Magondi Belt to the north [e.g., *Stowe*, 1986], but this correlation is in doubt in light of recent dating summarized by *Cornell et al.* [2006].

[12] The Cape Fold Belt (CFB) is comprised of the siliciclastic passive margin Cape Supergroup (500–330 Ma) [*Thamm and Johnson*, 2006], deformed in a northeast verging fold-and-thrust belt during the Cape Orogeny (~278–245 Ma). The belt is thought to have formed as a result of a subduction zone along the southern margin of the Gondwana supercontinent and also resulted in the formation of the Karoo foreland basin [e.g., *Ransome and de Wit*, 1992; *Newton et al.*, 2006].

3. Seismic Structure of Southern African Crust

[13] Early studies of the crust in the Kaapvaal Craton mainly used seismic recordings of mine tremors associated with gold mining activity in the Witwatersrand basin [e.g., *Gane et al.*, 1949; *Willmore et al.*, 1952; *Gane et al.*, 1956; *Hales and Sacks*, 1959]. *Hales and Sacks* [1959] describe a two-layered crust in the eastern Kaapvaal Craton with a Moho depth of 37 km and a ~24 km thick upper crustal layer with P and S wave velocities of 6.0 and 3.6 km/s, respectively. They also found a lower crustal layer ~13 km thick with P and S wave velocities of 7.0 and 4.0 km/s, respectively. In an early surface wave study, *Bloch et al.* [1969] inverted Rayleigh and Love wave group and phase velocities from regional earthquakes and obtained a Poisson's ratio of 0.28 for the lower crust in the northern Kaapvaal Craton and a crustal thickness in the range of 40–45 km. The first seismic refraction studies in and around the Witwatersrand basin yielded a crustal thickness of 35 km and lower crustal P wave velocities in the range of 6.4 to 6.7 km/s [*Durrheim and Green*, 1992]. A similar study by *Green and Durrheim* [1990] of the NNB obtained a Moho depth of 42 km and lower crustal P wave velocities in the range 6.6 to 6.9 km/s.

[14] More recently, crustal structure in southern Africa has been investigated using data from the Southern African Seismic Experiment (SASE) [*Carlson et al.*, 1996]. A compilation of results from *Harvey et al.* [2001], *Nguuri et al.* [2001], *Stankiewicz et al.* [2002], *Niu and James* [2002], *James et al.* [2003], *Kwadiba et al.* [2003], *Wright et al.* [2003], *Webb et al.* [2004], and *Nair et al.* [2006] show crustal thicknesses of 35–45 km and 34–37 km, respectively, for the Kaapvaal and Zimbabwe cratons. The studies reported Moho depths for the Kheis Province, BC, Limpopo Belt, Okwa/Magondi Belt, NNB and CFB of 40 km, 40–53 km, 37–55 km, 40–45 km, 40–50 km and 26–45 km, respectively.

[15] *Nguuri* [2004] and *Nair et al.* [2006] reported variable Vp/Vs ratios for a number of crustal terrains across southern Africa (Table 1) and interpreted Vp/Vs ratios > 1.76 to be indicative of mafic and ultramafic lithologies in the crust. The differences in the Vp/Vs ratio for some terrains, as well as the number of stations used to compute the average ratios, reflect different selections of geographic regions and data in the two studies. One of the most detailed investigations of crustal structure in the Kaapvaal Craton has been undertaken by *Niu and James* [2002] for a small area in the Kimberley terrain using data from the Kimberley seismic array. *Niu and James* [2002] obtained for the lowermost crust P and S velocities of 6.75 and 3.90 km/s, respectively, and a Poisson's ratio of 0.25, indicating an intermediate-to-felsic composition for the lowermost crust. They also found a sharp (i.e., less than 0.5 km wide) and flat (i.e., topographic relief less than 1 km) Moho. Petrologic studies of the Kimberley area by *Schmitz and Bowring* [2003a, 2003b] show that mafic granulites are absent from

Table 1. Summary of Average Vp/Vs Ratios of the Geological Terrains in Southern Africa

	Kaapvaal Craton		Zimbabwe Craton		Bushveld Complex		Namaqua-Natal Belt		Limpopo Belt		Kheis terrain	
	Vp/Vs	Stations[a]	Vp/Vs	Stations[a]	Vp/Vs	Stations[a]	Vp/Vs	Stations[a]	Vp/Vs	Stations[a]	Vp/Vs	Stations[a]
Nguuri [2004]	1.72 ± 0.05	35	-	-	1.79 ± 0.06	14	1.78 ± 0.05	10	1.84 ± 0.06	12	1.74 ± 0.06	4
Nair et al. [2006]	1.74 ± 0.01	25	1.73 ± 0.01	5	1.78 ± 0.02	5	1.72 ± 0.01	5	1.74 ± 0.01	4	1.73 ± 0.01	4

[a]Number of stations.

lower crustal xenolith suites, consistent with the findings of *Niu and James* [2002].

4. Sources of Data

[16] Broadband seismic data from a total of 101 seismic stations were initially used in this study to compute receiver functions, however, as discussed in section 6, results from only 89 stations are presented and used for interpretation. The stations belong to the SASE network (82 stations), the AfricaArray network (10 stations), the South Africa National Seismic Network (1 station) and the Global Seismic Network (3 stations) (Figure 2). The SASE network was deployed over 2 years (1997–1999) (Figure 2), and data from five stations in the Kimberley array (1999), which was operated as a high resolution extension to the SASE network [*Niu and James*, 2002], were also used. The AfricaArray network began operation in 2006 and consists of permanent seismic stations spread across eastern and southern Africa. More than 1 year of data from the AfricaArray stations in southern Africa were used for this study (Figure 2). A total of 89 teleseismic earthquakes with epicentral distances between 30° and 99° recorded by the stations were selected for computing receiver functions (Figure 3). The earthquakes have moment magnitudes ranging from 5.8 to 9.0.

[17] Rayleigh wave group velocities used in this study for periods of 10 to 90 s were taken from a revised version of the model presented by *Pasyanos and Nyblade* [2007]. In the revised *Pasyanos and Nyblade* [2007] model, group velocity measurements from 39 broadband seismic stations spread across southern Africa were combined with the measurements used for constructing the original *Pasyanos and Nyblade* [2007] model (Figure 4). The group velocity

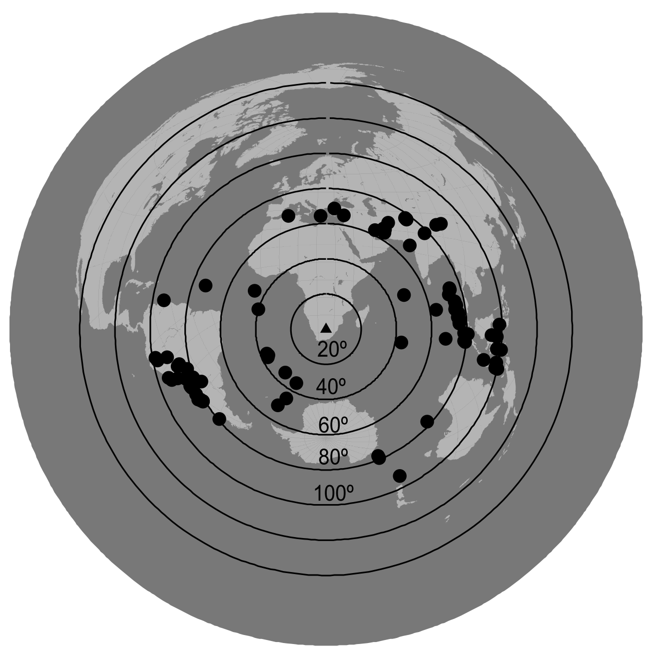

Figure 3. Distribution of teleseismic earthquakes used for this study (small solid circles). The triangle shows the center of the SASE network. Large circles show distance in 20° increments from the center of the network.

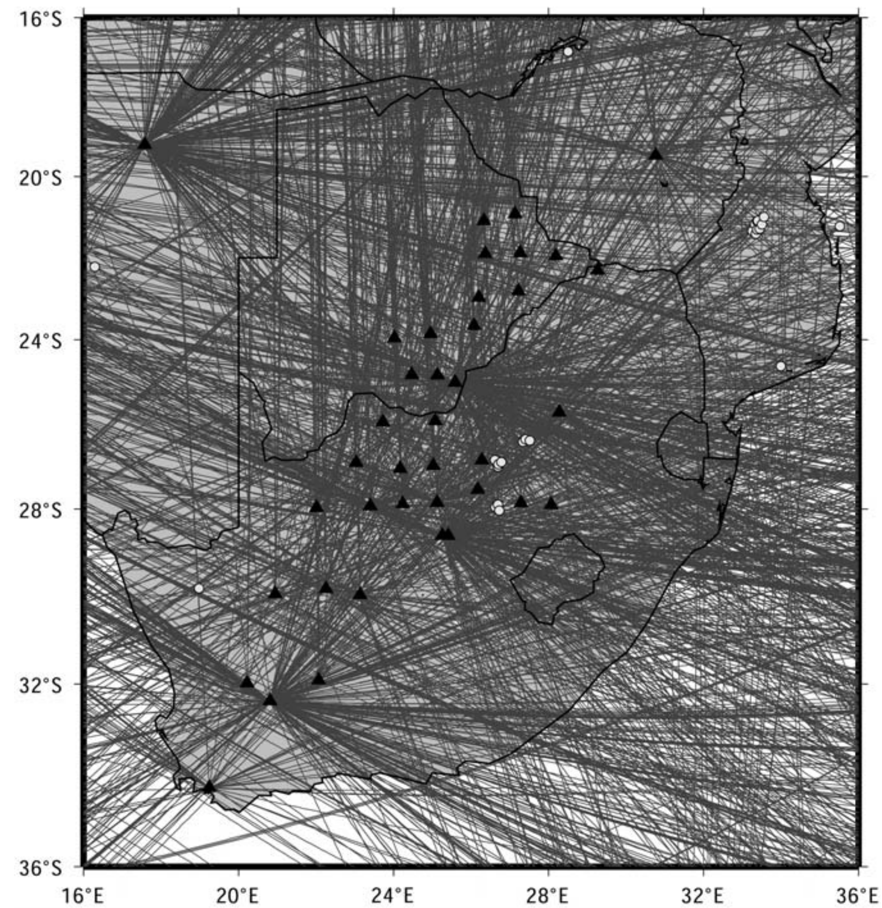

Figure 4. Map showing raypath coverage for 20 s Rayleigh waves used in the revised *Pasyanos and Nyblade* [2007] group velocity model. Station locations are shown with solid triangles, and event locations are shown with white circles. Most of the events are located outside of the area shown in the map.

measurements were made using single station measurements (event to station) and the inversion method used to obtain group velocity maps is based on ray approximation.

[18] For periods of 100 to 175 s, group velocities were taken from the Harvard model [*Larson and Ekström*, 2001]. A single dispersion curve for each station was obtained by first joining the group velocities from 10 to 90 s and 100 to 175 s and then smoothing the composite curve using a 3-point running average. The group velocity measurements from the Harvard model were included in the composite curve so that the 1-D models obtained from the inversions would show mantle structure that is regionally representative of southern Africa.

5. Data Processing and Modeling Methodology

5.1. Receiver Functions

[19] Receiver functions were computed using the iterative deconvolution method of *Ligorría and Ammon* [1999]. The deconvolution procedure equalizes the teleseismic waveforms so that near-source and instrumental effects are removed from the resulting time series [*Langston*, 1979]. Only the radial receiver functions were used in the joint inversion with the Rayleigh wave group velocity curves. The transverse receiver functions are identically zero for isotropic and laterally homogeneous media, and were computed to verify that this is the case for crust and upper mantle structure under each station.

[20] For each station, receiver functions were binned in ray parameter groups from 0.04 to 0.049 s/km, 0.05 to 0.059 s/km and 0.06 to 0.069 s/km. The purpose of grouping the receiver functions according to ray parameter is to properly account for the phase move out due to varying incidence angles [*Cassidy*, 1992; *Gurrola and Minster*, 1998]. Receiver function averages were then computed for each ray parameter bin.

[21] For each teleseismic event, receiver functions were computed at two overlapping frequency bands: a low frequency band of $f \leq 0.5$ Hz (Gaussian bandwidth of 1.0 s), and a high frequency band of $f \leq 1.25$ Hz (Gaussian bandwidth of 2.5 s). The low frequency bandwidth provides a better constraint on longer wavelength features in the subsurface, while the high frequency bandwidth provides a better constraint on shorter wavelength features. The combination of low and high frequency receiver functions help in discriminating sharp versus gradational transitions in the subsurface [*Owens and Zandt*, 1985; *Julià*, 2007].

5.2. Joint Inversion of Receiver Functions and Rayleigh Wave Group Velocities

[22] The joint inversion of receiver functions and surface wave dispersion curves results in 1-D shear wave depth-

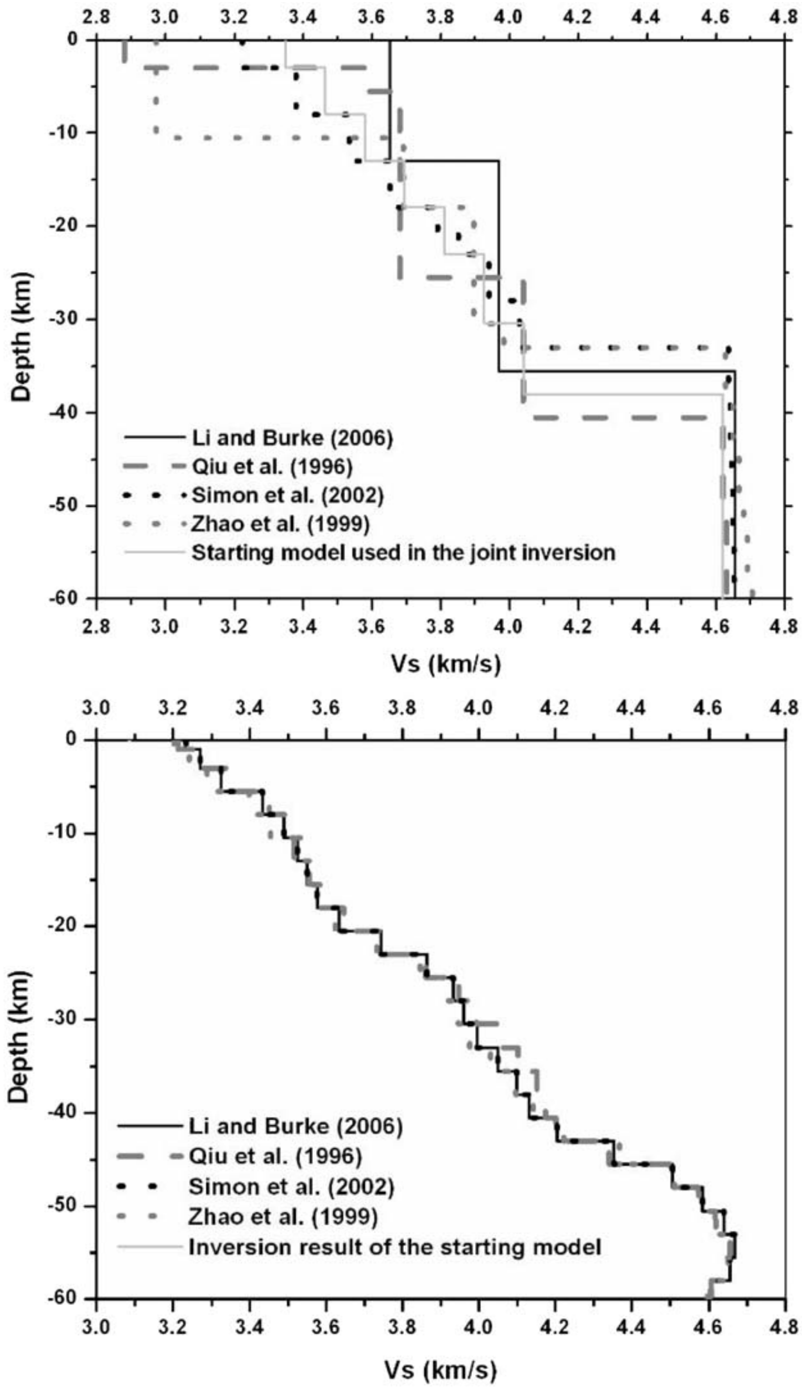

Figure 5. (top) Five different starting models used in the joint inversion algorithm to produce (bottom) velocity models for station SA40. This illustrates that the inversion results are not sensitive to the starting model.

velocity profiles for each recording station [*Julià et al.*, 2000, 2003]. The technique has been widely used to investigate crustal and upper mantle structure in other continental regions, for example, the Arabian shield [*Julià et al.*, 2003], the Tanzania Craton [*Julià et al.*, 2005] and the Ethiopian Plateau [*Dugda et al.*, 2007]. The advantage of jointly inverting receiver functions and surface wave dispersion measurements is that better resolution of the subsurface shear wave velocity structure can be obtained compared to independent inversions of either data set [*Julià et al.*, 2000, 2003].

[23] The joint inversion method makes use of a linearized inversion procedure that minimizes a weighted combination of the L2 norm of the vector residuals corresponding to each data set. The weights consist of a normalization constant that accounts for the different number of data points and different physical units in each data set, as well as an influence parameter that controls the relative influence

of each data set on the inverted model [*Julià et al.*, 2000]. In order to obtain smoothly varying depth-velocity profiles, the objective function also includes a model vector difference norm of the second order differences between adjacent layers [*Ammon et al.*, 1990; *Julià et al.*, 2000].

[24] Influence factors and smoothing parameters were selected for each tectonic domain in order to obtain smooth depth-velocity profiles that match the observations. For most of the stations, a good fit to the data was obtained for an influence factor of 0.5 and a smoothing parameter from zero to 0.2. The smoothing parameter had to be raised as high as 0.3 for some of the stations within the mobile belts, suggesting a greater degree of small-scale heterogeneity.

[25] The model parameterization consisted of 74 layers extending to a depth of 532 km. Layer thicknesses of 1 and 2 km were used for the first and second layer, 2.5 km for layers between 3 and 60.5 km depth, 5 km for layers between 60.5 and 255.5 km depth, and 17 to 40 km for layers below 255.5 km depth. The increase in layer thicknesses with depth corresponds to a decrease in the resolving power of the dispersion velocities with increasing period. The starting model used for the inversions is the PREM model [*Dziewonski and Anderson*, 1981] modified for continental structure above 60.5 km depth (Figure 5). Poisson's ratio in the starting model was set at 0.25 in the crust and mantle to a depth of 86 km, 0.28 between depths of 86–230 km, 0.29 between depths of 230 and 374 km, 0.30 between depths of 374–430 km and 0.29 between depths of 430–532 km. Densities were obtained from P wave velocities using the empirical relationship of *Berteussen* [1977].

5.3. Starting Model Dependence and Trade-Offs

[26] To test the dependence of the inversion results on the starting model, a range of regional models were used as starting models for the inversion [*Qiu et al.*, 1996; *Zhao et al.*, 1999; *Simon et al.*, 2002; *Li and Burke*, 2006]. P wave velocities were computed using the same Vp/Vs ratio as for the starting model. The outcome of this test, illustrated in Figure 5, shows that the inversion results in the 0–60 km depth range are not sensitive to the starting models.

[27] Because long-period group velocities constrain average velocity structure within relatively large depth ranges in the upper mantle, a trade-off exists between shallow and deep structure [e.g., *Julià et al.*, 2005]. To constrain this trade-off, we forward modeled structure below 200 km depth using a trial-and-error process by finding models that best fit the 140–175 s period group velocities. This was done by fixing velocities below 200 km between a range of −5 and +5% of the PREM velocities and then inverting for the velocity structure above 200 km depth. The best fitting model for each station was selected when the predicted group velocities in the 140–175 s range matched the observed group velocities. Figure 6 shows an example for one station with velocities of PREM and −2, −3, −5% PREM below 200 km depth. The best fitting model for this station is −3% PREM. For most of the stations, it was found that a −2% PREM model tends to fit the 140–175 s period group velocities best. However, a −3% PREM model was used for the stations in the Kheis Province, Limpopo Belt, Okwa terrain and Zimbabwe Craton and a −5% PREM model was used for both the NNB and CFB.

5.4. Model Uncertainties

[28] To determine the uncertainties in the model results at crustal depths, we have examined the uncertainty introduced by our selection of model parameters for the inversions as well as by the group velocities taken from the revised *Pasyanos and Nyblade* [2007] model. Following the approach by *Julià et al.* [2005], we estimated the uncertainties in the inversion results from parameter selection by repeating inversions for each station using a range of weighting parameters, constraints and Poisson's ratio. The uncertainties in the shear wave velocities for the crust obtained from this procedure are around 0.1 km/s.

[29] Resolution tests of the revised *Pasyanos and Nyblade* [2007] group velocity model indicate that the spatial resolution at periods most sensitive to crustal structure (∼10–50 s) is 3 to 4 degrees, and thus the revised *Pasyanos and Nyblade* [2007] group velocity model has sufficient resolution to image differences in group velocities between regions that are ∼300 to 400 km wide. To assess the uncertainty in crustal velocities possibly introduced by the group velocity measurements for regions smaller than that, we have taken two dispersion curves from the revised *Pasyanos and Nyblade* [2007] model showing "end-member" high and low group velocities, and have rerun the inversions for many stations using them.

[30] The results are illustrated in Figure 7 for two stations. For station BOSA in the middle of the Kaapvaal Craton, group velocities in the 10–50 s range are lower than for station SA81 in the NNB, and the 1-D inversions for these stations show very different lower crustal structure (Figures 7a and 7c). When the 1D inversion is performed for BOSA using the higher group velocities for SA81, the shear wave velocities increase by 0.1 to 0.2 km/s (Figure 7b). When the 1D inversion is performed for SA81 using the lower group velocities for BOSA, the shear wave velocities decrease by 0.1 to 0.2 km/s. In all four models, the dispersion curves and receiver functions are fit equally well (Figure 7). This exercise indicates that even for regions less than 300 to 400 km wide, at most an uncertainty of 0.1 to 0.2 km/s in shear wave velocity is introduced by using the group velocities from the revised *Pasyanos and Nyblade* [2007] model.

Figure 6. Diagram for station SA55 to illustrate the procedure used for determining structure below 200 km. Shown are different models tested for structure below 200 km depth using velocities from PREM and 2%, 3%, and 5% less than PREM. (a) Observed (black line) and predicted (gray line) group velocity curves. The insets show the fit to the longest period (140–175 s) group velocities for the four different models tested. (b) Observed (black line) and predicted (gray line) receiver functions. (c) The shear wave velocity models obtained from the joint inversion (black line) and the PREM shear wave velocity model (gray line) for reference. The 3% less than PREM model for shear wave velocities below 200 km depth gives the best fit to the longest period group velocities.

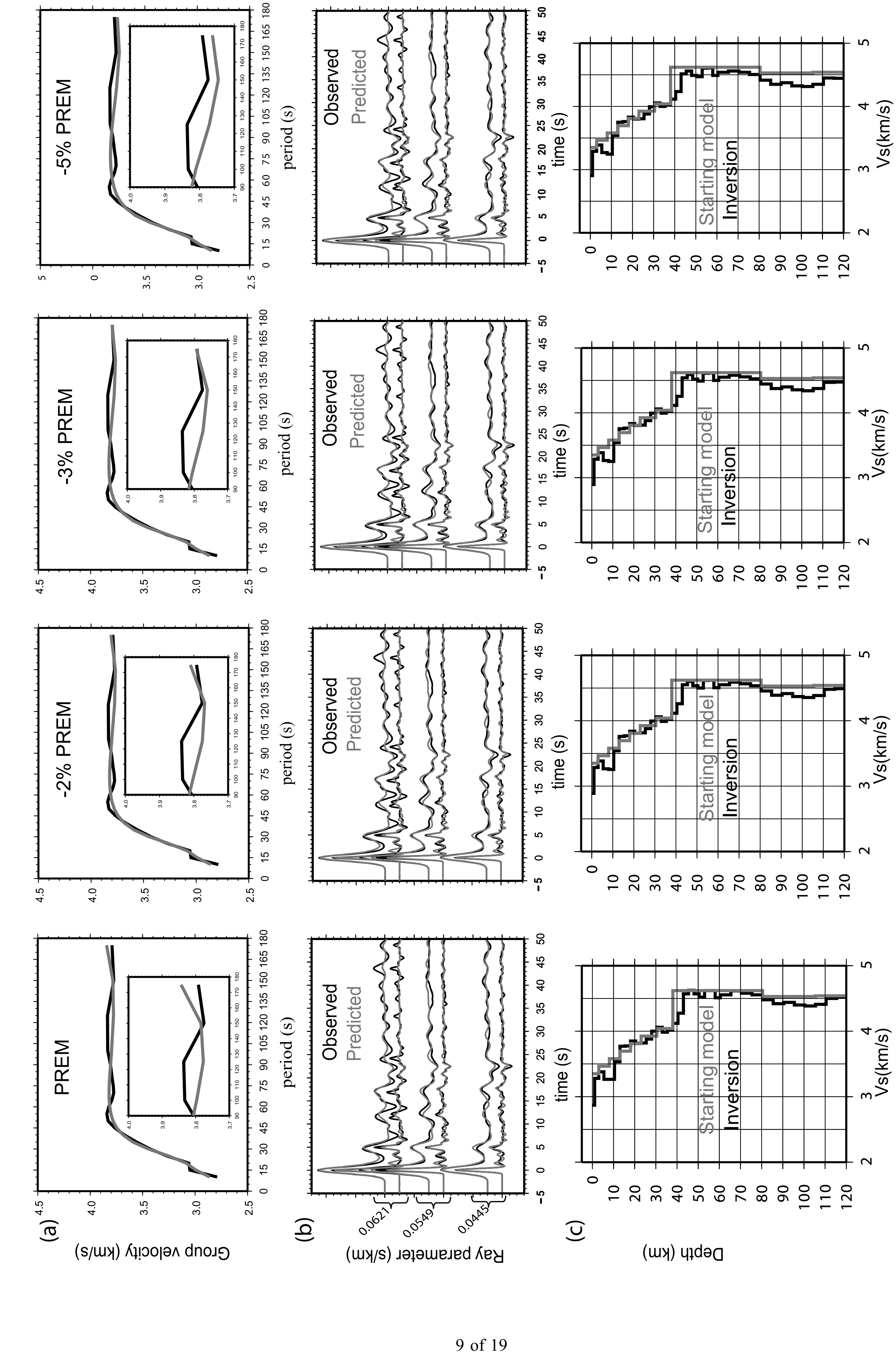
(a)
(b)
(c)
Group velocity (km/s)
Ray parameter (s/km)
Depth (km)
PREM
-2% PREM
-3% PREM
-5% PREM
period (s)
Observed
Predicted
time (s)
0.0621
0.0549
0.0445
Starting model
Inversion
Vs(km/s)

Figure 6

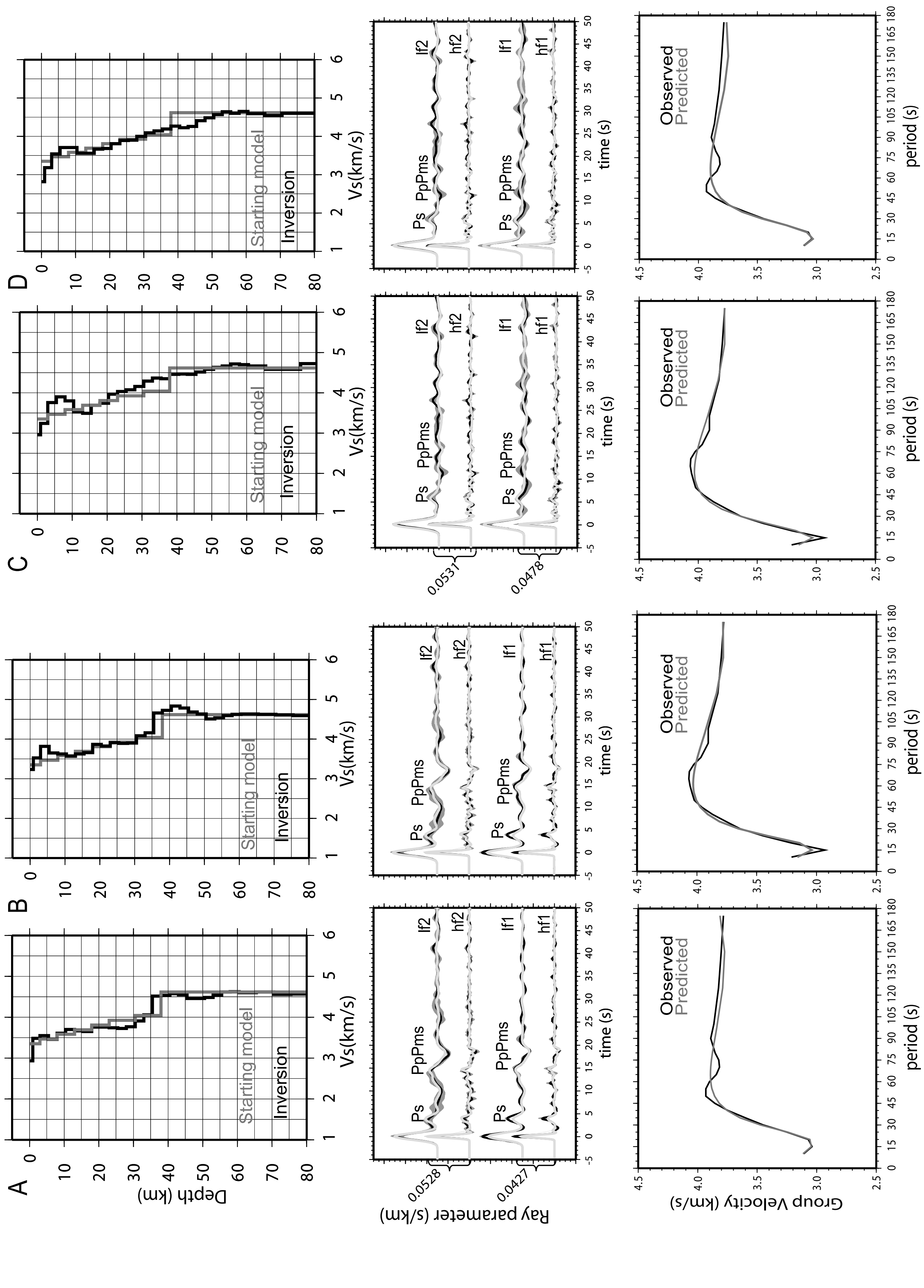
A
B
C
D
Depth (km)
Vs(km/s)
Starting model
Inversion
Ray parameter (s/km)
0.0528
0.0427
0.0531
0.0478
Ps
PpPms
lf2
hf2
lf1
hf1
time (s)
Group Velocity (km/s)
Observed
Predicted
period (s)

Figure 7

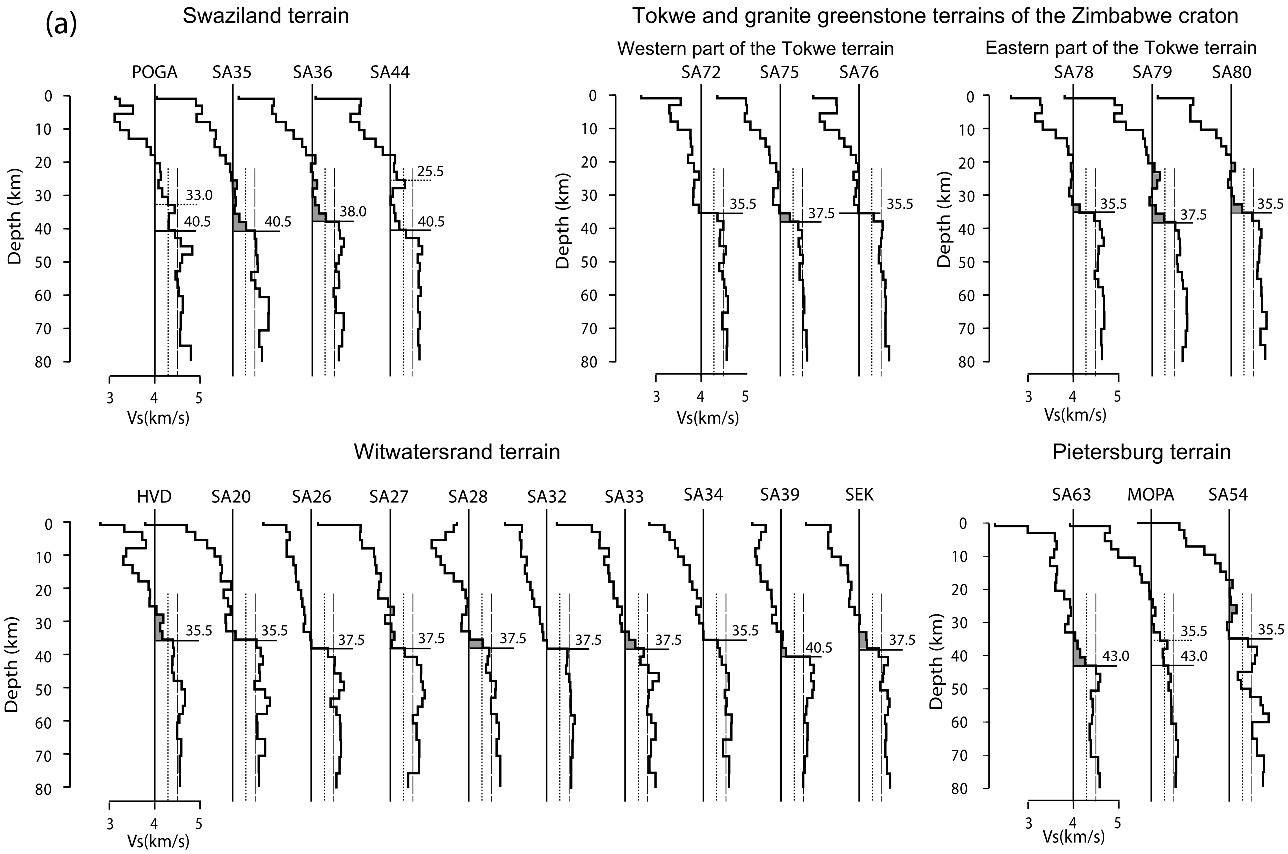

Figure 8. (a–d) Shear wave velocity profiles grouped by tectonic terrain. Moho depths are indicated with horizontal lines and numbers in km. Lower crustal layers with Vs $\geq$ 4.0 km/s are shaded, and reference lines at 4.0 km/s (solid), 4.3 km/s (dotted), and 4.5 km/s (dashed) are shown in each profile. See text for explanation of profiles where two horizontal lines (one dotted and one solid) are shown.

[31] Given these considerations, we place the overall uncertainty in the shear wave velocities at no more than 0.2 km/s for any given crustal layer in the model. This uncertainty in the shear wave velocity translates into an uncertainty of no more than 2 to 3 km in Moho depth for most stations where a velocity discontinuity can be seen between the crust and mantle, and no more than 5 km where a smoothly varying shear wave velocity profile is found, indicating a gradational Moho.

6. Results

[32] For twelve of the 101 stations, the inversions did not yield good fits to the receiver functions, and therefore, results for these stations are not presented or interpreted. The receiver functions are too noisy to obtain good waveform fits at stations SA01, SA02, SA03, SA58, SA69, SA82, SA139, SA155, CNG, while it is difficult to see a Moho Ps conversion on the receiver functions for stations SA07, SA08, SA12 (all in the NNB). The results for the remaining 89 stations are summarized in Figures 8, 9, 10, and 11.

[33] Figures 8a–8d show the shear wave velocity profiles grouped by tectonic terrain, and Table 2 provides a summary of key crustal parameters derived from these profiles. Crustal thickness beneath each station was determined by placing the Moho at the depth where the shear wave velocity exceeds 4.3 km/s. Shear wave velocity ranges for typical lower crustal lithologies obtained by using experimentally determined P wave velocities and Vp/Vs ratios [e.g., *Christensen and Mooney*, 1995; *Christensen*, 1996] show that shear wave velocities in the lower crust cannot

Figure 7. Analysis of uncertainties in the joint inversion results using two stations, BOSA and SA81, with different group velocity curves. (a) Results for BOSA using the group velocities for the location of BOSA from the revised *Pasyanos and Nyblade* [2007] model. (b) Same as Figure 7a but with the group velocities for the location of SA81 in the revised *Pasyanos and Nyblade* [2007] model. (c) Model results for SA81 using the group velocities for the location of SA81 from the revised *Pasyanos and Nyblade* [2007] model. (d) Same as Figure 7c but with the group velocities for the location of BOSA. The top plots show 1-D velocity models from the joint inversion using the receiver functions shown in the middle plots and the group velocities shown in the bottom plots. For the receiver functions, 1σ error bounds are shown with gray shading around the average observed receiver functions (black line) and the predicted receiver functions (light gray line). The high (hf1, hf2) and low (lf1, lf2) frequency receiver functions are grouped in different ray parameter bins.

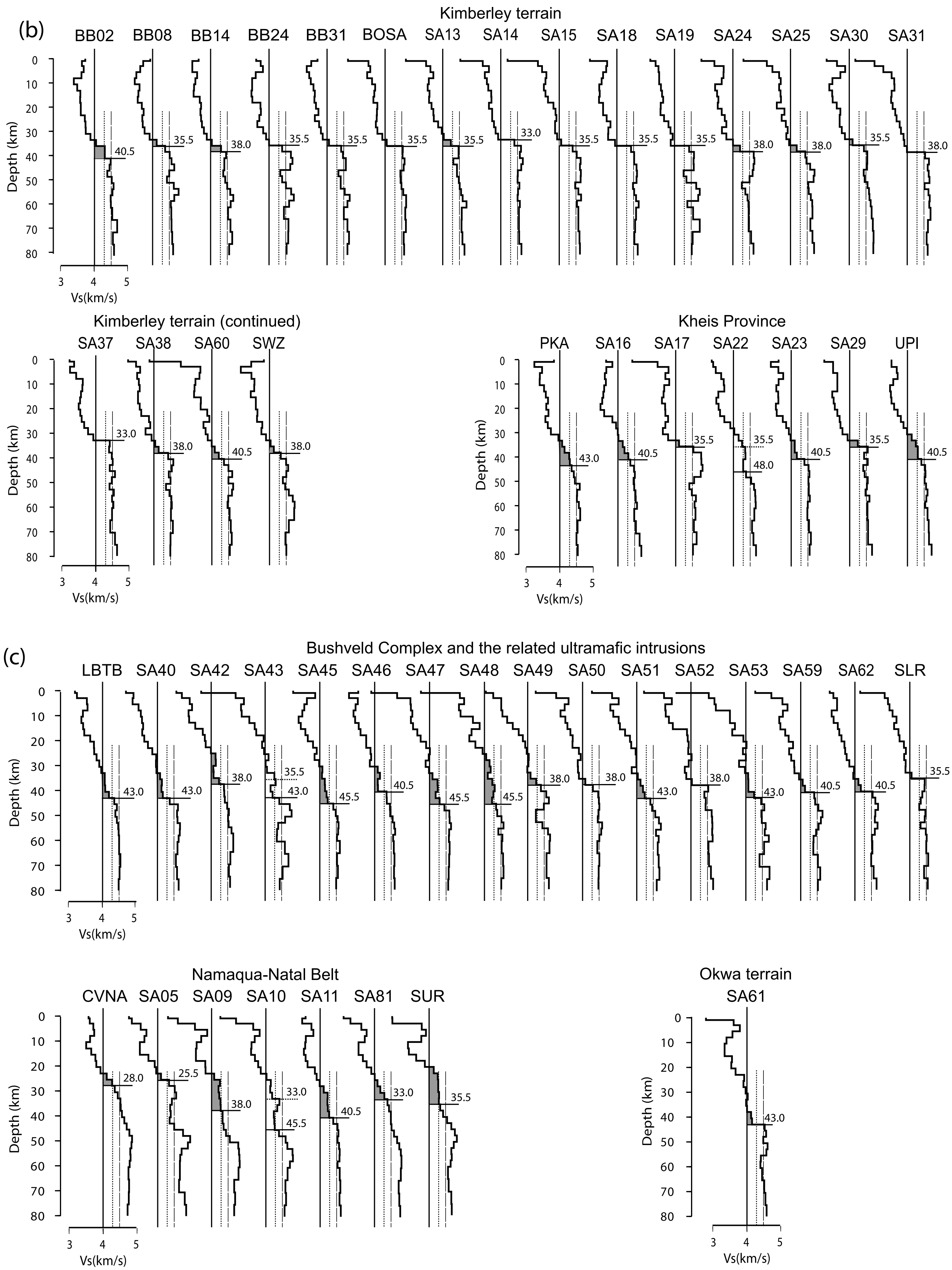

Figure 8. (continued)

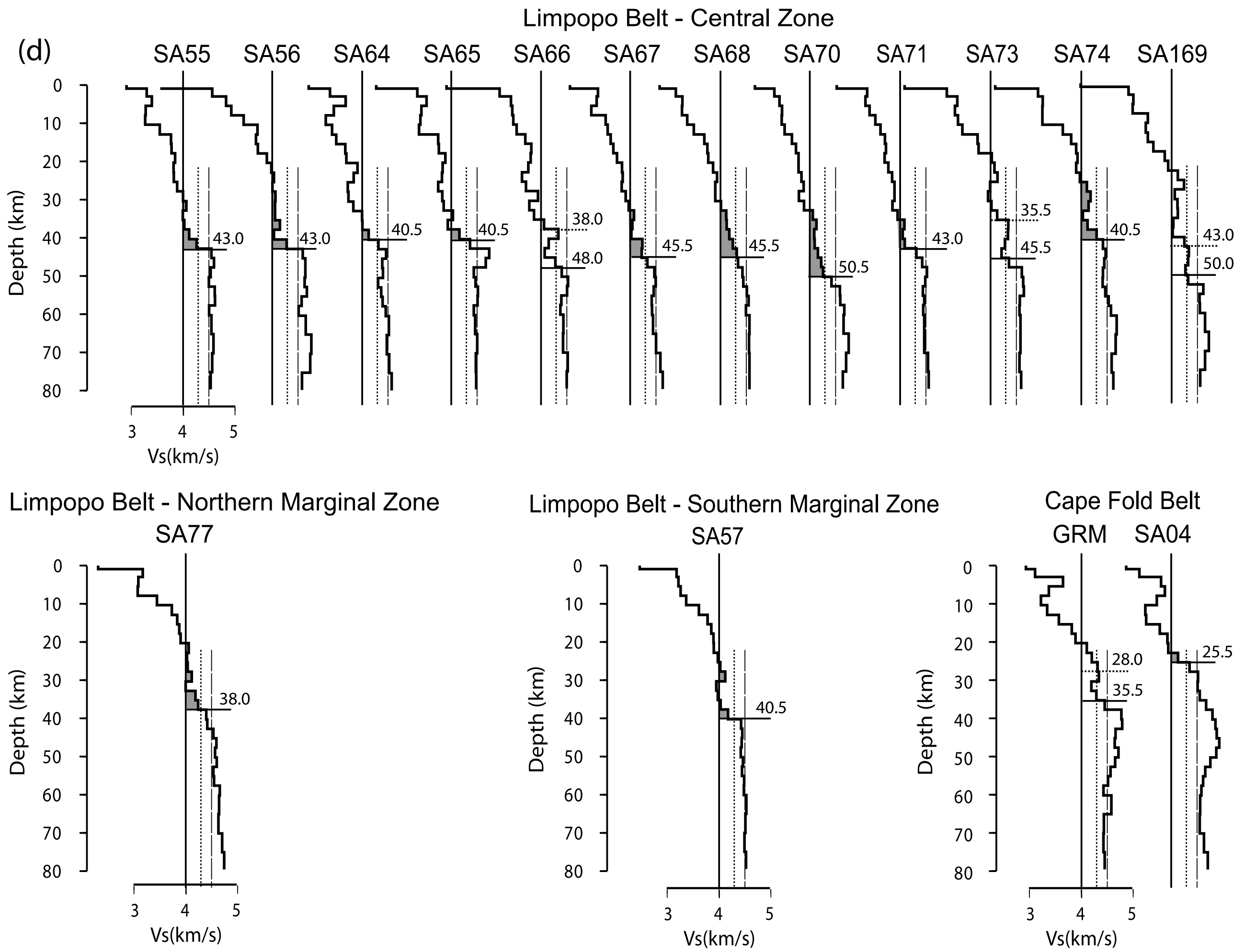

Figure 8. (continued)

be higher than 4.3 km/s. Therefore, we take shear wave velocities above 4.3 km/s to indicate the presence of lithologies with mantle compositions, and we place the Moho where the shear wave velocities exceed that value. For many stations, there is a significant increase in velocity at the depth at which the shear wave velocity exceeds 4.3 km/s, but for other stations the change in shear wave velocity is gradational. In addition, for 10 stations (SA10, SA22, SA43, SA44, SA66, SA73, SA169, GRM, MOPA, POGA) the velocity profiles show two depths where there is an increase in shear wave velocity above 4.3 km/s with a region of velocity less than 4.3 km/s in between. This high-low-high velocity structure is indicated in Figure 8 for the 10 stations by showing the first increase in velocity above 4.3 km/s with a dotted line and the second increase with a solid line. For these 10 stations, we do not attempt to define the Moho and therefore do not use them for further analysis.

[34] Within the reported uncertainties, we find a 1-to-1 correlation between our Moho estimates and those reported by *Nguuri et al.* [2001], *Nguuri* [2004] and *Nair et al.* [2006], except for a handful of stations, which are shown in Figure 9 with solid symbols. Five stations (SA05, SA09, SA49, SA81, SUR) lie more than 5 km above the 1-to-1 correlation line in Figure 9, where our estimates

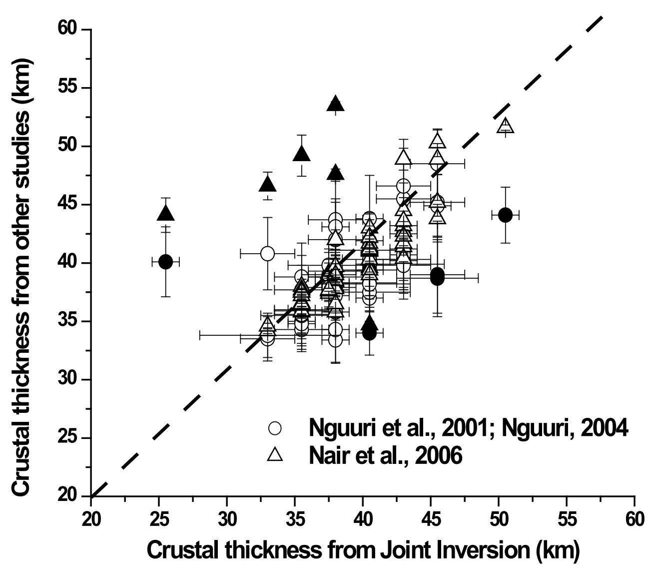

Figure 9. Comparison of crustal thickness estimates from this study with crustal thickness estimates from previous studies. The dashed line shows the 1-to-1 correlation, and the solid symbols show stations that do not fall close (≥5 km) to the 1-to-1 line.

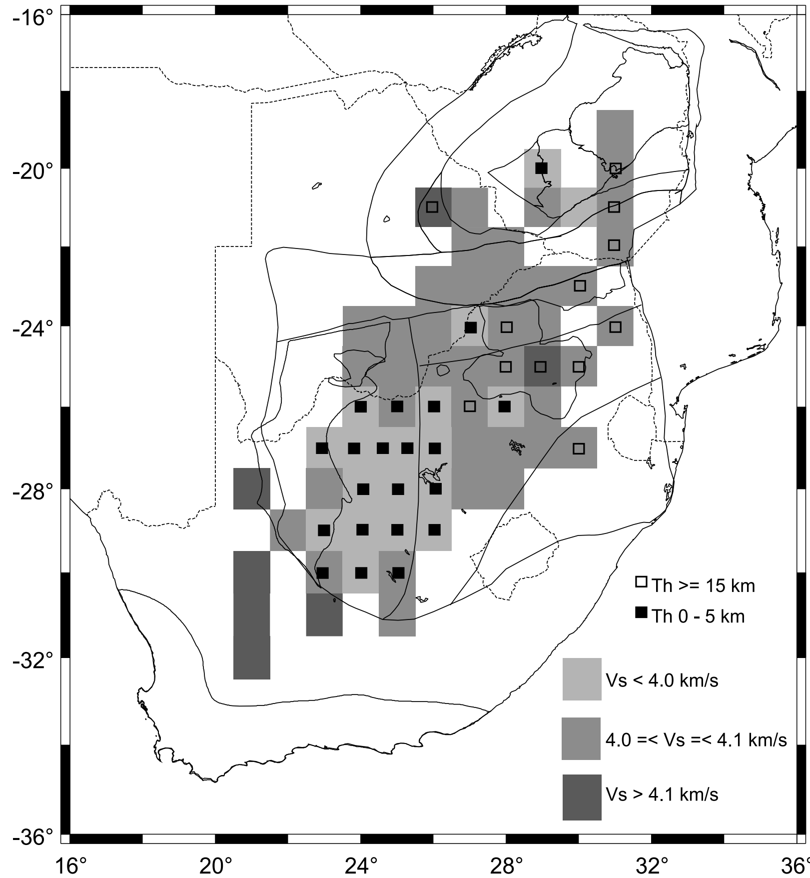

Figure 10. Map showing the average shear wave velocity below 30 km (gray shading) and the average total layer thickness with Vs $\geq$ 4.0 km/s (shown as open and solid squares and denoted as "Th") for 1 x 1 degree blocks. The blocks without symbols are areas where the average total layer thickness with Vs $\geq$ 4.0 km/s is between 5 and 15 km. Solid lines show the outlines of the tectonic terrains from Figure 1.

of Moho depth for these stations are less than those reported by *Nguuri et al.* [2001], *Nguuri* [2004] and *Nair et al.* [2006]. Four stations (SA16, SA47, SA48, SA70) lie more than 5 km below the 1-to-1 correlation line, where our estimates of Moho depth are greater than those reported by *Nguuri et al.* [2001], *Nguuri* [2004] and *Nair et al.* [2006]. The velocity profiles for these stations show complicated lowermost crustal structure commonly with a gradational Moho. We attribute the different Moho depth estimates for these stations to difficulty in identifying the crust-mantle boundary when the velocity structure across this boundary is gradational.

6.1. Lower Crustal Structure

[35] For most terrains, shear wave velocities reach 4.0 km/s or higher over a substantial part of the lower crust (Table 2). The Kimberley terrain and the western part of the Tokwe terrain, however, are different. In these terrains, mean velocities of $\leq$3.9 km/s occur in the lower part of the crust (Table 2). These terrains also have, on average, less than 5 km of high velocity (Vs $\geq$ 4.0 km/s) rock within the lower part of the crust.

[36] The variability in lower crustal structure is illustrated in Figures 10 and 11. In Figure 10, the spatial variability in lower crustal velocity structure is shown for 1 x 1 degree blocks. The mean shear wave velocity below 30 km depth is indicated with shaded boxes, and superimposed on the boxes are symbols showing the thickness of lower crustal layers with Vs $\geq$ 4.0 km/s. The anomalous nature of lower crustal structure in the Kimberley terrain and the western part of the Tokwe terrain is readily apparent. It can also be seen that the anomalous region of lower crustal structure extends beyond the Kimberley terrain into the western part of the Witwatersrand terrain and the eastern part of the Kheis Province. The lack of high velocity rock in the lower parts of the crust in these terrains can also be seen in Figure 8.

6.2. Upper Crustal Structure

[37] A high velocity zone in the upper crust at depths <15 km can be seen in the velocity models for a number of stations (Figure 8). The high velocity zones are isolated features seen on one or two stations in some terrains (e.g., station SA61 in the Okwa terrain), and given the resolution of the revised *Pasyanos and Nyblade* [2007] group velocity model, these isolated upper crustal high velocity zones might not be well imaged. However, for the NNB, a high velocity zone in the upper crust is found over an area wide enough to be resolved by the revised *Pasyanos and Nyblade* [2007] model (Figure 8c). Shear wave velocities within these zones are between 3.7 and 4.0 km/s, and decrease to

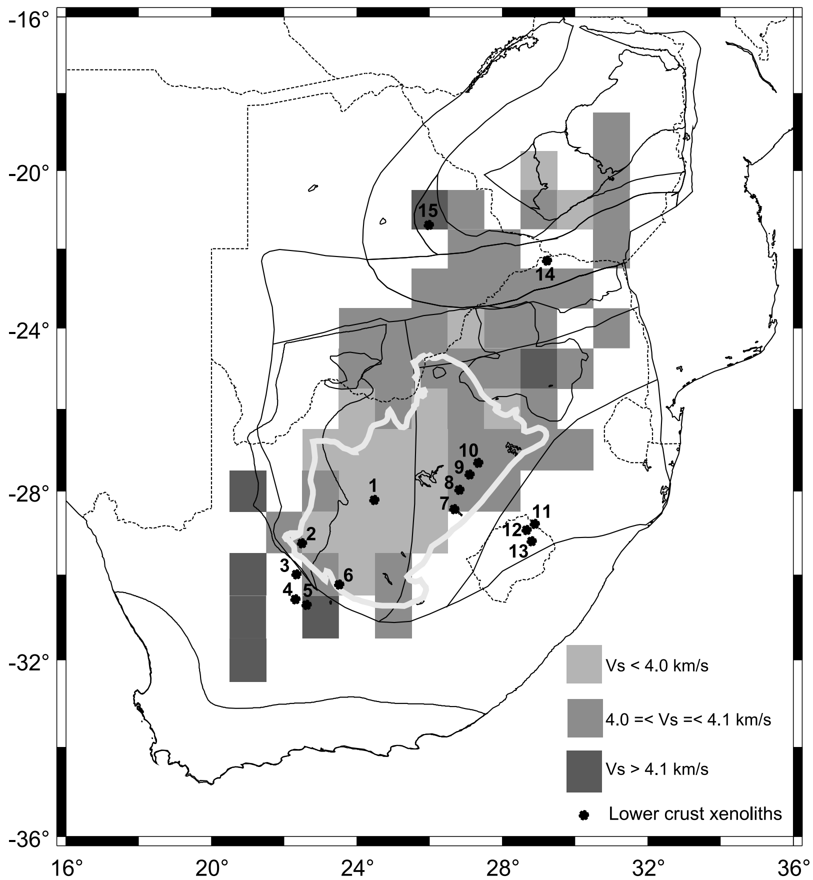

Figure 11. Map showing the average shear wave velocity below 30 km (gray shading), with distribution of the Ventersdorp supergroup (white line) taken from *van der Westhuizen et al.* [2006] and the location of lower crust xenoliths obtained from *Pretorius and Barton* [2003] and *Schmitz and Bowring* [2003a]. The number labels 1–15 represent the names of the kimberlites: 1, Newlands; 2, Markt; 3, Uintjiesberg; 4, Klipfontein-08; 5, Beyersfontein; 6, Lovedale; 7, Star Mine; 8, Kaalvallei; 9, Lace; 10, Voorspoed; 11, Mothae; 12, Letseng-la-Terae; 13, Matsoku; 14, Venetia Mine; and 15, Jwaneng. Terrain boundaries are the same as in Figure 1.

3.5–3.7 km/s below these zones, creating the appearance of a low velocity layer in the midcrust. However, it is the upper crustal velocities that are anomalous, not the midcrustal velocities.

6.3. Mantle Structure

[38] For most of the terrains within both the cratonic areas and mobile belts, the mean shear wave velocity from the Moho to depths of ~60 km is between 4.5 and 4.7 km/s (i.e., uppermost mantle; Table 2). We find little evidence for systematic differences in the uppermost mantle (i.e., the top 10–20 km of the mantle) velocities across southern Africa. As a result of using group velocities for periods >90 s from the Harvard model in the inversions to obtain a regionally representative upper mantle model, mantle structure below ~60–70 km is not sufficiently resolved to comment on variations in lithospheric thickness or sublithospheric mantle structure between terrains.

7. Discussion

[39] Because southern Africa has not experienced a major tectonothermal event since the Karoo flood basalt volcanism at c. 180 Ma, the variability found within the shear wave velocities at lower crustal depths most likely results from compositional differences rather than thermal ones. It is well established from laboratory studies that mafic lithologies commonly found in the continental crust, such as amphibolite, garnet-bearing and garnet-free mafic granulite, and mafic gneiss, have higher shear wave velocities (>3.9 km/s), while intermediate-to-felsic lithologies have lower shear wave velocities (<3.9 km/s) [e.g., *Holbrook et al.*, 1992; *Christensen and Mooney*, 1995; *Rudnick and Fountain*, 1995; *Rudnick and Gao*, 2003].

7.1. Interpretation of Higher Shear Wave Velocities in the Lower Crust

[40] We interpret the crustal layers in our models with shear wave velocities of 4.0 km/s or higher as consisting of predominantly mafic lithologies. *Rudnick and Fountain* [1995] and *Rudnick and Gao* [2003] argued that high velocity (Vp ~ 7.0 km/s, Vs ~ 4.0 km/s), mafic rock is characteristic of the lower crust in many Precambrian terrains globally. Thus, our interpretation is not unprecedented.

[41] *Rudnick and Gao* [2003] also suggest several explanations for the origin of mafic lower crust in Precambrian

Table 2. Summary of Crustal Structure by Geological Terrains Shown in Figures 8 and 10

Terrain	Average Moho Depth ± Standard Deviation (km)	Number of Stations Used	Uppermost Mantle Vs (km/s)	Average Crustal Vs	Average Vs Below 20 km Depth (km/s)	Average Vs Below 30 km Depth (km/s)	Average Thickness of Layers With $Vs \geq 4.0$ km/s (km)
Kaapvaal Craton							
Witwatersrand	37.2 ± 1.5	10	4.6	3.7	3.9	4.0	7
Swaziland	39.3 ± 1.8	2	4.6	3.7	4.0	4.1	14
Pietersburg	39.3 ± 5.3	2	4.5	3.6	4.0	4.0	12
Kimberley	36.6 ± 2.1	19	4.6	3.7	3.8	3.9	2
Zimbabwe Craton							
Western part of the Tokwe terrain	36.2 ± 1.2	3	4.5	3.6	3.9	3.9	4
Eastern part of the Tokwe terrain	36.2 ± 1.2	3	4.6	3.6	4.0	4.0	12
Bushveld Complex and the related ultramafic intrusions	41.2 ± 3.2	15	4.5	3.7	4.0	4.0	10
Namaqua-Natal Belt	33.4 ± 5.8	6	4.6	3.8	4.1	4.3	12
Limpopo Belt							
SMZ	40.5	1	4.5	3.7	4.0	4.1	15
CZ	43.6 ± 3.3	9	4.5	3.7	4.0	4.1	11
NMZ	38.0	1	4.6	3.7	4.1	4.1	15
Kheis Province	39.3 ± 3.1	6	4.6	3.7	3.9	4.1	7
Okwa terrain	43.0	1	4.5	3.7	3.9	4.0	13
Cape Fold Belt	25.5	1	4.7	3.7	4.0	-	-

terrains, such as basaltic underplating, magmatic intrusion, and tectonomagmatic processes responsible for the formation of Archaean crust. The mafic layer in the lower crust of the BC is likely caused by a combination of magmatic intrusion and underplating. It has been estimated that the total magma volume that has been added to the Bushveld crust is around 0.6×10^6 km^3 [*Von Gruenewaldt et al.*, 1985], thickening the crust by $\sim$5–10 km. The large (>10 km) thickness of mafic rock in the lower parts of the crust in the NNB, the CZ of the Limpopo Belt, parts of the Kheis Province and the CFB can be attributed to suture processes during the formation of these terrains. In Precambrian sutures elsewhere (e.g., the Superior Province [*Gibb et al.*, 1983], the Tanzania Craton [*Nyblade and Pollack*, 1992], the Yilgarn Craton [*Mathur*, 1974; *Wellmann*, 1978], the Indian shield [*Subrahmanyam*, 1978], the Mann shield [*Blot et al.*, 1962; *Louis*, 1978; *Black et al.*, 1979]), 5–10 km of crustal thickening is observed along with the presence of mafic units in a crust commonly affected by granulite facies metamorphism and extraction of a felsic partial melt component. Both the thicker crust and the large thickness of lower crust with high shear wave velocities found in the NNB, CZ, and Kheis Province is consistent with typical "suture" thickened crust found in other Precambrian terrains, and need not be viewed as anomalous.

[42] The mafic lower crust we find in the BC is consistent with Vp/Vs ratios of >1.76 as described by *Nguuri* [2004] and *Nair et al.* [2006] (Table 1). Similarly, the reported Vp/Vs ratios of 1.78 and 1.84 for the NNB and Limpopo Belt, respectively, are consistent with our findings (Table 1).

7.2. Interpretation of Lower Shear Wave Velocities in the Lower Crust

[43] Following the experimental studies of rock velocities discussed above, we interpret the lower shear wave velocities ($Vs \leq 3.9$ km/s) in the lower parts of the crust in several terrains to indicate the presence of predominantly intermediate-to-felsic lithologies. The lack of mafic material in the lower crust and the mean crustal thickness of 37 km for the Kimberley terrain are consistent with the findings by *Niu and James* [2002]. Our results indicate that the region of low shear wave velocities in the lower crust extends across much of the Kimberley terrain and into parts of the adjacent Kheis Province and Witwatersrand terrain (Figure 10). Low shear wave velocities in the lower crust also occur in the western part of the Tokwe terrain.

[44] To explain an intermediate-to-felsic composition for the lower crust in the Kimberley terrain, as well as the flat Moho that *Niu and James* [2002] observed, *James et al.* [2003] suggested that the crust could have been extensively melted during the Ventersdorp tectonomagmatic event at c. 2.7 Ga. However, it is not clear how melting of the lower crust during the Ventersdorp event would have resulted in the removal of the lower mafic crust unless accompanied by crustal thinning. Figure 11 shows the distribution of the Ventersdorp Supergroup superimposed on the shear wave velocity structure of the lower crust. Most of the areas underlain by intermediate-to-felsic lower crust in South Africa coincide with the region where Ventersdorp rocks have been preserved.

[45] Using seismic reflection profiles, *de Wit and Tinker* [2004] describe Ventersdorp age half graben systems

within the upper crust across the central Kimberley and Witwatersrand terrains. The half grabens are characterized by asymmetrical listric faults that trend east to southeast, and *de Wit and Tinker* [2004] argued that the listric faults are associated with thinning of underlying lower crust. Consequently, regions in the Kaapvaal Craton underlain by an intermediate-to-felsic lower crust may reflect areas where mafic lower crust was either thinned or removed during regional crustal thinning associated with the Ventersdorp event. A similar explanation could be invoked for the low shear wave velocities observed in the lower crust in the western part of the Tokwe terrain, which is overlain by 3.1–2.95 Ga transgressive passive margin and rift sequences [*Jelsma and Dirks*, 2002].

7.3. Crustal Xenoliths

[46] Lower crustal xenoliths in southern Africa are most commonly found within kimberlite pipes [e.g., *Dawson*, 1980; *Nixon*, 1987; *Schmitz and Bowring*, 2003a] (see numbers in Figure 11 for locations). Cratonic lower crustal granulite xenoliths have been described from the Kimberley region (location 1), NNB (locations 2, 3, 4, 5, 6), Free State province (locations 7, 8, 9, 10), northern Lesotho (locations 11, 12, 13) [*Schmitz and Bowring*, 2003a]. Off-craton and craton-margin xenoliths come from the CZ of the Limpopo Belt (location 14) [*Pretorius and Barton*, 2003] and the unexposed extension of the Magondi Belt in north central Botswana (location 15) [*Schmitz and Bowring*, 2003a].

[47] Xenoliths from kimberlite pipes [e.g., *Dawson*, 1980; *Nixon*, 1987; *Schmitz and Bowring*, 2003a] can be used as an independent check on the composition of the lithosphere through which the pipe ascended. In this way, suites of lower crustal xenoliths collected from kimberlite pipes in the Kaapvaal Craton and surrounding mobile belts [*Schmitz and Bowring*, 2003a; *Pretorius and Barton*, 2003] (Figure 11) can be used to confirm the presence or absence of mafic rocks in the lower crust.

[48] Lower crustal xenoliths from the Kimberley terrain are dominated by metapelite, and mafic rocks are absent [*Schmitz and Bowring*, 2003a]. In contrast, mafic granulite xenoliths are common at all of the other localities [*Dawson and Smith*, 1987; *Dawson et al.*, 1997; *Schmitz and Bowring*, 2003a, 2003b] (Figure 11), which is consistent with the variability in the shear wave velocity structure of the lower crust described in this study.

8. Summary

[49] To investigate details of lower crustal structure in southern Africa, we have jointly inverted receiver functions and Rayleigh wave group velocities for broadband seismic stations spanning the greater part of the exposed Precambrian shield of southern Africa. From the joint inversion, 1-D shear wave velocity profiles for the crust and uppermost mantle beneath 89 stations have been obtained.

[50] Within the reported uncertainties, we find a 1-to-1 correlation between our Moho depth estimates and those reported by previous studies [*Nguuri et al.*, 2001; *Nguuri*, 2004; *Nair et al.*, 2006]. The primary new observation that we make is that there is considerable variability in the velocity structure of the lower part of the crust across southern Africa. For most terrains, shear wave velocities reach 4.0 km/s or higher over a large part of the lower crust. In contrast, for much of the Kimberley terrain and adjacent parts of the Kheis Province and Witwatersrand terrain, as well as for the western part of the Tokwe terrain, mean shear wave velocities of $\leq$3.9 km/s characterize the lower part of the crust. The lower shear velocities in the lower crust of the Kimberley terrain are consistent with results from previous studies [*Niu and James*, 2002; *James et al.*, 2003].

[51] Our findings indicate that the lower crust across much of the southern African shield in both Archaean and Proterozoic terrains has a predominantly mafic composition, except for the southwest part of the Kaapvaal Craton and western part of the Zimbabwe Craton, where the lower crust is intermediate to felsic in composition. The mafic layer in the lower crust of the BC is likely caused by a combination of magmatic intrusion and underplating. The large thickness of high shear wave velocity lower crust found in the NNB, CZ, and Kheis Province are consistent with typical "suture" thickened crust found in Precambrian terrains globally.

[52] Most of the areas in the Kaapvaal Craton underlain by intermediate-to-felsic lower crust and a shallower Moho coincide with the region where Ventersdorp rocks have been preserved. This correlation supports the suggestion by *de Wit and Tinker* [2004] that extension along crustal-scale listric fault systems that were active during the Ventersdorp tectonomagmatic event at c. 2.7 Ga could have resulted in the attenuation and local removal of mafic lower crust. A similar explanation could be invoked for the low shear wave velocities observed in the lower crust in the western part of the Tokwe terrain, which is overlain by 3.1–2.95 Ga transgressive passive margin and rift sequences [*Jelsma and Dirks*, 2002]. The absence of mafic xenoliths in the Kimberley terrain and the presence of mafic xenoliths in the other terrains is consistent with the variability in the shear velocity structure of the lower crust found in this study.

[53] **Acknowledgments.** We would like to thank Charles Ammon, Mulugeta Dugda, and Yongcheol Park for assistance with computer codes, Magda Roos for help in digitizing terrain boundaries, and all those who assisted with the Southern African Seismic Experiment. Two anonymous reviewers and an Associate Editor provided comments that helped to improve this paper. E.K. would like to acknowledge support from the Council for Geoscience and the AfricaArray program. This research has been supported by the National Science Foundation (grants EAR 0440032 and OISE 0530062), the AfricaArray program and the South African National Research Foundation. This research was also performed under the auspices of the U.S. Department of Energy by Lawrence Livermore National Laboratory under contract DE-AC52-07NA27344. This is LLNL contribution LLNL-JRNL-408744.

References

Ammon, C. J., G. E. Randall, and G. Zandt (1990), On the nonuniqueness of receiver function inversions, *J. Geophys. Res.*, *95*, 15,303–15,318, doi:10.1029/JB095iB10p15303.

Barton, J. M., Jr., R. E. P. Fripp, P. Horrocks, and N. McLean (1979), The geology, age and tectonic setting of the Messina layered intrusion, Limpopo Mobile Belt, southern Africa, *Am. J. Sci.*, *279*, 1108–1134.

Berger, M., J. D. Kramers, and T. F. Nägler (1995), Geochemistry and geochronology of charno-enderbites in the Northern Marginal Zone of the Limpopo Belt, southern Africa and genetic models, *Schweiz. Mineral. Petrogr. Mitt.*, *75*, 17–42.

Berteussen, K. A. (1977), Moho depth determinations based on spectral ratio analysis, *Phys. Earth Planet. Inter.*, *31*, 313–326.

Black, R., R. Caby, A. Moussine-Pouchkine, J. M. Bertad, A. M. Boullier, J. Fabre, and A. Lesquer (1979), Evidence for late Precambrian plate tectonics in West Africa, *Nature*, *278*, 223–227, doi:10.1038/278223a0.

Bloch, S., A. L. Hales, and M. Landisman (1969), Velocities in the crust and upper mantle of southern Africa from multi-mode surface wave dispersion, *Bull. Seismol. Soc. Am.*, *59*, 1599–1629.

Blot, C., Y. Crenn, and R. Rechenmann (1962), Elements apportes par la gravimetrie a la connaissance de la tectonique profonde du Senegal, *C. R. Hebd. Seances Acad. Sci.*, *254*, 1131–1133.

Carlson, R. W., T. L. Grove, M. J. de Wit, and J. J. Gurney (1996), Program to study crust and mantle of the Archean Craton in southern Africa, *Eos Trans. AGU*, *77*(29), 273–277, doi:10.1029/96EO00194.

Cassidy, J. F. (1992), Numerical experiments in broad-band receiver function analysis, *Bull. Seismol. Soc. Am.*, *82*, 1453–1474.

Cawthorn, R. G., H. V. Eales, F. Walraven, R. Uken, and M. K. Watkeys (2006), The Bushveld complex, in *The Geology of South Africa*, edited by M. R. Johnson, C. R. Anhaeusser, and R. J. Thomas, pp. 261–281, Geol. Soc. of S. Afr., Johannesburg, South Africa.

Christensen, N. I. (1996), Poisson's ratio and crustal seismology, *J. Geophys. Res.*, *101*, 3139–3156, doi:10.1029/95JB03446.

Christensen, N. I., and W. D. Mooney (1995), Seismic velocity structure and composition of the continental crust: A global view, *J. Geophys. Res.*, *100*, 9761–9788, doi:10.1029/95JB00259.

Cornell, D. H., R. J. Thomas, H. F. G. Moen, D. L. Reid, J. M. Moore, and R. L. Gibson (2006), The Namaqua-Natal province, in *The Geology of South Africa*, edited by M. R. Johnson, C. R. Anhaeusser, and R. J. Thomas, pp. 325–379, Geol. Soc. of S. Afr., Johannesburg, South Africa.

Dawson, J. B. (1980), *Kimberlites and Their Xenoliths*, Springer, Berlin.

Dawson, J. B., and J. V. Smith (1987), Reduced sapphirine granulite xenoliths from the Lace kimberlite, South Africa: Implications for the deep structure of the Kaapvaal Craton, *Contrib. Mineral. Petrol.*, *95*, 376–383, doi:10.1007/BF00371851.

Dawson, J. B., S. L. Harley, R. L. Rudnick, and T. R. Irel (1997), Equilibration and reaction in Archaean quartz-sapphirine granulite xenoliths from the Lace kimberlite pipe, South Africa, *J. Metamorph. Geol.*, *15*, 253–266, doi:10.1111/j.1525-1314.1997.00017.x.

de Wit, M. J., and J. Tinker (2004), Crustal structures across the central Kaapvaal Craton from deep-seismic reflection data, *S. Afr. J. Geol.*, *107*, 185–206, doi:10.2113/107.1-2.185.

de Wit, M. J., C. Roering, R. J. Hart, R. A. Armstrong, C. E. J. Ronde, R. W. E. Green, M. Tredoux, E. Peberdy, and R. A. Hart (1992), Formation of an Archaean continent, *Nature*, *357*, 553–562, doi:10.1038/357553a0.

Dirks, P. H. G. M., and H. A. Jelsma (2002), Crust-mantle decoupling and the growth of the Archaean Zimbabwe Craton, *J. Afr. Earth Sci.*, *34*, 157–166, doi:10.1016/S0899-5362(02)00015-5.

Dugda, M. T., A. A. Nyblade, and J. Julia (2007), Thin lithosphere beneath the Ethiopian Plateau revealed by a joint inversion of Rayleigh wave group velocities and receiver functions, *J. Geophys. Res.*, *112*, B08305, doi:10.1029/2006JB004918.

Durrheim, R. J., and R. W. E. Green (1992), A seismic refraction investigation of the Archaean Kaapvaal Craton, South Africa, using the mine tremors as the energy source, *Geophys. J. Int.*, *108*, 812–832, doi:10.1111/j.1365-246X.1992.tb03472.x.

Dziewonski, A. M., and D. L. Anderson (1981), Preliminary reference Earth model, *Phys. Earth Planet. Inter.*, *25*, 297–356, doi:10.1016/0031-9201(81)90046-7.

Eglington, B. M., and R. A. Armstrong (2004), The Kaapvaal Craton and adjacent orogens, southern Africa: A geochronological database and overview of the geological development of the craton, *S. Afr. J. Geol.*, *107*, 13–32, doi:10.2113/107.1-2.13.

Gane, P. G., H. J. Logie, and J. H. Stephen (1949), Triggered telerecording seismic equipment, *Bull. Seismol. Soc. Am.*, *39*, 117–143.

Gane, P. G., A. R. Atkins, J. P. F. Sellschop, and P. Seligman (1956), Crustal structure in the Transvaal, *Bull. Seismol. Soc. Am.*, *46*, 293–316.

Gibb, R. A., M. D. Thomas, P. Lapointe, and M. Mukhopadhay (1983), Geophysics of proposed Proterozoic sutures in Canada, *Precambrian Res.*, *19*, 349–384, doi:10.1016/0301-9268(83)90021-9.

Green, R. W. E., and R. J. Durrheim (1990), A seismic refraction investigation of the Namaqualand metamorphic complex, South Africa, *J. Geophys. Res.*, *95*(B12), 19,927–19,932, doi:10.1029/JB095iB12p19927.

Gurrola, H., and J. B. Minster (1998), Thickness estimates of the upper-mantle transition zone from bootstrapped velocity spectrum stacks of receiver functions, *Geophys. J. Int.*, *133*, 31–43, doi:10.1046/j.1365-246X.1998.1331470.x.

Hales, A. L., and I. S. Sacks (1959), Evidence for an intermediate layer from crustal structure studies in the eastern Transvaal, *Geophys. J. R. Astron. Soc.*, *2*, 15–33.

Harvey, J. D., M. J. de Wit, J. Stankiewicz, and C. M. Doucouré (2001), Structural variations of the crust in the Southwestern Cape, deduced from seismic receiver functions, *S. Afr. J. Geol.*, *104*, 231–242, doi:10.2113/1040231.

Hatton, C. J., and J. K. Schweitzer (1995), Evidence for synchronous extrusive and intrusive Bushveld magmatism, *J. Afr. Earth Sci.*, *21*, 579–594, doi:10.1016/0899-5362(95)00103-4.

Holbrook, W. S., W. D. Mooney, and N. I. Christensen (1992), The seismic velocity structure of the deep continental crust, in *Continental Lower Crust*, edited by D. M. Fountain, R. Arculus, and R. W. Kay, chap. 1, pp. 1–43, Elsevier, Amsterdam.

James, D. E., F. Niu, and J. Rokosky (2003), Crustal structure of the Kaapvaal Craton and its significance for early crustal evolution, *Lithos*, *71*, 413–429, doi:10.1016/j.lithos.2003.07.009.

Jelsma, H. A., and P. H. G. M. Dirks (2002), Neoarchaean tectonic evolution of the Zimbabwe Craton, in *The Early Earth: Physical, Chemical, and Biological Development*, edited by C. M. R. Fowler, C. J. Ebinger, and C. J. Hawkesworth, *Geol. Soc. Spec. Publ.*, *199*, 183–211.

Johnson, M. R., C. R. Anhaeusser, and R. J. Thomas (Eds.) (2006), *The Geology of South Africa*, 691 pp., Geol. Soc. of S. Afr., Johannesburg, South Africa.

Julià, J. (2007), Constraining velocity and density contrasts across the crust-mantle boundary with receiver function amplitudes, *Geophys. J. Int.*, *171*, 286–301, doi:10.1111/j.1365-2966.2007.03502.x.

Julià, J., C. J. Ammon, R. B. Hermann, and A. M. Correig (2000), Joint inversion of receiver functions and surface-wave dispersion observations, *Geophys. J. Int.*, *143*, 99–112, doi:10.1046/j.1365-246x.2000.00217.x.

Julià, J., C. J. Ammon, and R. B. Hermann (2003), Lithospheric structure of the Arabian Shield from the joint inversion of receiver functions and surface-wave group velocities, *Tectonophysics*, *371*, 1–21, doi:10.1016/S0040-1951(03)00196-3.

Julià, J., C. J. Ammon, and A. A. Nyblade (2005), Evidence for mafic lower crust in Tanzania, East Africa from joint inversion of receiver functions and Rayleigh wave dispersion velocities, *Geophys. J. Int.*, *162*, 555–569, doi:10.1111/j.1365-246X.2005.02685.x.

Kramers, J. D., S. McCourt, and D. D. van Reenen (2006), The Limpopo Belt, in *The Geology of South Africa*, edited by M. R. Johnson, C. R. Anhaeusser, and R. J. Thomas, pp. 209–236, Geol. Soc. of S. Afr., Johannesburg, South Africa.

Kreissig, K., T. F. Nägler, J. D. Kramers, D. D. Van Reenen, and C. A. Smit (2000), An isotopic and geochemical study of the northern Kaapvaal Craton and the Southern Marginal Zone of the Limpopo Belt: Are they juxtaposed terrains?, *Lithos*, *50*, 1–25, doi:10.1016/S0024-4937(99)00037-7.

Kwadiba, M. T. O. G., C. Wright, E. M. Kgaswane, R. E. Simon, and T. K. Nguuri (2003), Pn arrivals and lateral variations of Moho geometry beneath the Kaapvaal Craton, *Lithos*, *71*, 393–411, doi:10.1016/j.lithos.2003.07.008.

Langston, C. A. (1979), Structure under Mount Rainier, Washington, inferred from teleseismic body waves, *J. Geophys. Res.*, *84*, 4749–4762, doi:10.1029/JB084iB09p04749.

Larson, E. W. F., and G. Ekström (2001), Global models of surface wave group velocity, *Pure Appl. Geophys.*, *158*(8), 1377–1400, doi:10.1007/PL00001226.

Li, A., and K. Burke (2006), Upper mantle structure of southern Africa from Rayleigh wave tomography, *J. Geophys. Res.*, *111*, B10303, doi:10.1029/2006JB004321.

Ligorría, J. P., and C. J. Ammon (1999), Iterative deconvolution and receiver function estimation, *Bull. Seismol. Soc. Am.*, *89*, 1359–1400.

Louis, P. (1978), Gravimetrie et geologie en Afrique occidentale et centrale, *Mem. BRGM*, *91*, 53–61.

Mathur, S. P. (1974), Crustal structure in southwestern Australia from seismic and gravity data, *Tectonophysics*, *24*, 151–182, doi:10.1016/0040-1951(74)90135-8.

McCourt, S., and R. A. Armstrong (1998), SIMS U-Pb zircon geochronology of granites from the Central Zone, Limpopo Belt, southern Africa: Implications for the age of the Limpopo Orogeny, *S. Afr. J. Geol.*, *101*, 329–338.

McCourt, S., P. Hilliard, R. A. Armstrong, and H. Munyanyiwa (2001), SHRIMP U-Pb zircon geochronology of the Hurungwe granite northwest Zimbabwe: Age constraints on the timing of the Magondi orogeny and implications for the correlation between the Kheis and Magondi belts, *S. Afr. J. Geol.*, *104*, 39–46, doi:10.2113/104.1.39.

Moen, H. F. G. (1999), The Kheis tectonic subprovince, southern Africa: A lithostratigraphic perspective, *S. Afr. J. Geol.*, *102*, 27–42.

Nair, S. K., S. S. Gao, K. H. Liu, and P. G. Silver (2006), Southern African crustal evolution and composition: Constraints from receiver function studies, *J. Geophys. Res.*, *111*, B02304, doi:10.1029/2005JB003802.

Newton, A. R., R. W. Shone, and P. W. K. Booth (2006), The Cape Fold Belt, in *The Geology of South Africa*, edited by M. R. Johnson, C. R. Anhaeusser, and R. J. Thomas, pp. 521–530, Geol. Soc. of S. Afr., Johannesburg, South Africa.

Nguuri, T. (2004), Crustal structure of the Kaapvaal Craton and surrounding mobile belts: Analysis of teleseismic P waveforms and surface wave inversions, Ph.D. dissertation, Univ. of the Witwatersrand, Johannesburg, South Africa.

Nguuri, T. K., J. Gore, D. E. James, S. J. Webb, C. Wright, T. G. Zengeni, O. Gwavava, J. A. Snoke, and Kaapvaal Seismic Group (2001), Crustal structure beneath southern Africa and its implications for the formation and evolution of the Kaapvaal and Zimbabwe cratons, *Geophys. Res. Lett.*, *28*(13), 2501–2504, doi:10.1029/2000GL012587.

Niu, F., and D. E. James (2002), Fine structure of the lowermost crust beneath the Kaapvaal Craton and its implications for crustal formation and evolution, *Earth Planet. Sci. Lett.*, *200*, 121–130, doi:10.1016/S0012-821X(02)00584-8.

Nixon, P. H. (1987), Kimberlitic xenoliths and their cratonic setting, in *Mantle Xenoliths*, edited by P. H. Nixon, pp. 215–239, John Wiley, Chichester, U. K.

Nyblade, A. A., and H. N. Pollack (1992), A gravity model for the lithosphere in western Kenya and northeastern Tanzania, *Tectonophysics*, *212*, 257–267, doi:10.1016/0040-1951(92)90294-G.

Owens, T. J., and G. Zandt (1985), The response of the continental crust-mantle boundary observed on broadband teleseismic receiver functions, *Geophys. Res. Lett.*, *12*, 705–708.

Pasyanos, M. E., and A. A. Nyblade (2007), A top to bottom lithospheric study of Africa and Arabia, *Tectonophysics*, *444*(1–4), 27–44, doi:10.1016/j.tecto.2007.07.008.

Pretorius, W., and J. M. Barton Jr. (2003), Measured and calculated compressional wave velocities of crustal and upper mantle rocks in the Central Zone of the Limpopo Belt, South Africa—Implications for lithospheric structure, *S. Afr. J. Geol.*, *106*, 205–212, doi:10.2113/106.2-3.205.

Qiu, X., K. Priestley, and D. McKenzie (1996), Average lithospheric structure of southern Africa, *Geophys. J. Int.*, *127*(3), 563–581, doi:10.1111/j.1365-246X.1996.tb04038.x.

Ransome, I. G. D., and M. J. de Wit (1992), Preliminary investigations into a microplate model for the South Western Cape, in *Inversion Tectonics of the Cape Fold Belt, Karoo and Cretaceous Basins of Southern Africa*, edited by M. J. de Wit and I. G. D. Ransome, pp. 257–266, A. A. Balkema, Rotterdam, Netherlands.

Rudnick, R. L., and D. M. Fountain (1995), Nature and composition of the continental crust: A lower crustal perspective, *Rev. Geophys.*, *33*(3), 267–309, doi:10.1029/95RG01302.

Rudnick, R. L., and S. Gao (2003), Composition of the continental crust, in *Treatise on Geochemistry*, vol. 3, *The Crust*, edited by H. D. Holland and K. K. Turekian, pp. 1–64, doi:10.1016/B0-08-043751-6/03016-4Elsevier, Amsterdam.

Schmitz, M. D., and S. A. Bowring (2003a), Constraints on the thermal evolution of continental lithosphere from U-Pb accessory mineral thermochronometry of lower crustal xenoliths, southern Africa, *Contrib. Mineral. Petrol.*, *144*, 592–618.

Schmitz, M. D., and S. A. Bowring (2003b), Ultrahigh-temperature metamorphism in the lower crust during Neoarchean Ventersdorp rifting and magmatism, Kaapvaal Craton, southern Africa, *Geol. Soc. Am. Bull.*, *115*, 533–548, doi:10.1130/0016-7606(2003)115<0533:UMITLC>2.0.CO;2.

Simon, R. E., C. Wright, E. M. Kgaswane, and M. T. O. Kwadiba (2002), The *P* wavespeed structure below and around the Kaapvaal Craton to depths of 800 km, from traveltimes and waveforms of local and regional earthquakes and mining-induced tremors, *Geophys. J. Int.*, *151*, 132–145, doi:10.1046/j.1365-246X.2002.01751.x.

South African Committee for Stratigraphy (1980), *Stratigraphy of South Africa. Part 1: Lithostratigraphy of the Republic of South Africa, South West Africa/Namibia, and the Republics of Bophuthatswana, Transkei, and Venda*, *Handb. Geol. Surv. S. Afr.*, vol. 8, 690 pp., Dep. of Miner. and Energy Affairs, Repub. of S. Afr., Pretoria, South Africa.

Stankiewicz, J., S. Chevrot, R. D. van der Hilst, and M. J. de Wit (2002), Crustal thickness, discontinuity depth, and upper mantle structure beneath southern Africa: Constraints from body wave conversions, *Phys. Earth Planet. Inter.*, *130*, 235–251, doi:10.1016/S0031-9201(02)00012-2.

Stowe, C. W. (1986), Synthesis and interpretation of structures along the north-eastern boundary of the Namaqua tectonic province, South Africa, *Trans. Geol. Soc. S. Afr.*, *89*, 185–198.

Stowe, C. W. (1989), Discussion on "The Proterozoic Magondi Belt in Zimbabwe—A review," *S. Afr. J. Geol.*, *92*, 69–71.

Subrahmanyam, C. (1978), On the relation of gravity anomalies to geotectonics of the Precambrian terrains of the South Indian shield, *J. Geol. Soc. India*, *19*, 251–263.

Thamm, A. G., and M. R. Johnson (2006), The Cape Supergroup, in *The Geology of South Africa*, edited by M. R. Johnson, C. R. Anhaeusser, and R. J. Thomas, pp. 443–460, Geol. Soc. of S. Afr., Johannesburg, South Africa.

van der Westhuizen, W. A., H. de Bruiyn, and P. G. Meintjes (2006), The Ventersdorp Supergroup, in *The Geology of South Africa*, edited by M. R. Johnson, C. R. Anhaeusser, and R. J. Thomas, pp. 187–208, Geol. Soc. of S. Afr., Johannesburg, South Africa.

Von Gruenewaldt, G., M. R. Sharpe, and C. J. Hatton (1985), The Bushveld complex: Introduction and review, *Econ. Geol.*, *80*, 803–812, doi:10.2113/gsecongeo.80.4.803.

Webb, S. J., R. G. Cawthorn, T. K. Nguuri, and D. E. James (2004), Gravity modeling of Bushveld complex connectivity supported by Southern African Seismic Experiment results, *S. Afr. J. Geol.*, *107*, 207–218, doi:10.2113/107.1-2.207.

Wellmann, P. (1978), Gravity evidence for abrupt changes in the mean crustal density at the junction of Australian crustal blocks, *Aust. Bur. Miner. Resour. Geol. Geophys. Bull.*, *3*, 153–162.

Willmore, P. L., A. L. Hales, and P. G. Gane (1952), A seismic investigation of crustal structure in the western Transvaal, *Bull. Seismol. Soc. Am.*, *42*, 53–80.

Wright, C., E. M. Kgaswane, M. T. O. Kwadiba, R. E. Simon, T. K. Nguuri, and R. McRae-Samuel (2003), South African seismicity, April 1997–April 1999, and regional variations in the crust and uppermost mantle of the Kaapvaal Craton, *Lithos*, *71*, 369–392, doi:10.1016/S0024-4937(03)00122-1.

Zhao, M., C. A. Langston, A. A. Nyblade, and T. J. Owens (1999), Upper mantle velocity structure beneath southern Africa from modeling regional seismic data, *J. Geophys. Res.*, *104*(B3), 4783–4794, doi:10.1029/1998JB900058.

P. H. G. M. Dirks, School of Earth and Environmental Sciences, James Cook University, Townsville, Qld 4811, Australia.

R. J. Durrheim, Council for Scientific and Industrial Research, corner of Rustenburg and Carlow Roads, Johannesburg 0001, South Africa.

J. Julià and A. A. Nyblade, Department of Geosciences, Pennsylvania State University, University Park, PA 16802, USA.

E. M. Kgaswane, Council for Geoscience, 280 Pretoria Rd., Private Bag X112, Pretoria 0001, South Africa. (ekgaswane@geoscience.org.za)

M. E. Pasyanos, Lawrence Livermore National Laboratory, 7000 East Ave., Livermore, CA 94550, USA.

Tectonophysics 554–557 (2012) 83–104

Contents lists available at SciVerse ScienceDirect

Tectonophysics

journal homepage: www.elsevier.com/locate/tecto

Shear wave velocity structure of the Bushveld Complex, South Africa

Eldridge M. Kgaswane [a,c,*], Andrew A. Nyblade [b], Raymond J. Durrheim [c,e], Jordi Julià [f], Paul H.G.M. Dirks [c,d], Susan J. Webb [c]

[a] Council for Geoscience, 280 Pretoria Road, Private Bag X112, Pretoria 0001, South Africa
[b] Department of Geosciences, Pennsylvania State University, University Park, PA, USA
[c] School of Geosciences, University of the Witwatersrand, Private Bag 3, Johannesburg 2050, South Africa
[d] School of Earth and Environmental Sciences, James Cook University, Townsville Qld 4811, Australia
[e] Council for Scientific and Industrial Research, cnr Rustenburg and Carlow Roads, Johannesburg, South Africa
[f] Departamento de Geofísica & Programa de Pós-Graduação em Geodinâmica e Geofísica, Universidade Federal do Rio Grando do Norte, Natal, Rio Grande do Norte, Brazil

ARTICLE INFO

Article history:
Received 27 September 2011
Received in revised form 4 May 2012
Accepted 3 June 2012
Available online 15 June 2012

Keywords:
Bushveld Complex
Continuous-sheet model
Dipping-sheet model
Joint inversion
Receiver functions
Rayleigh wave group velocities

ABSTRACT

The structure of the crust in the environs of the Bushveld Complex has been investigated by jointly inverting high-frequency teleseismic receiver functions and 2–60 s period Rayleigh wave group velocities for 16 broadband seismic stations located across the Bushveld Complex. Group velocities for 2–15 s periods were obtained from surface wave tomography using local and regional events, while group velocities for 20–60 s periods were taken from a published model. 1-D shear wave velocity models obtained for each station show the presence of thickened crust in the center of the Bushveld Complex and a region at the base of the crust where shear wave velocities exceed 4.0 km/s. The shear wave velocity models also suggest that velocities in some upper crustal layers may be as high as 3.7–3.8 km/s, consistent with the presence of mafic lithologies. These results favor a continuous-sheet model for the Bushveld Complex in which the outcropping mafic layers of the western and eastern limbs are continuous at depth beneath the center of the complex. However, detailed modeling of receiver functions at one station within the center of the complex indicates that the mafic layering may be locally disrupted due to thermal diapirism triggered by the emplacement of the Bushveld Complex or thermal and tectonic reactivation at a later time.

1. Introduction

The Bushveld Complex (BC; ~2.06 Ga) is one of the largest layered mafic igneous intrusions in the world, covering an area of ~66 000 km^2 within the northern Kaapvaal Craton, South Africa (Fig. 1a; e.g., Eglington and Armstrong, 2004; Walraven, 1997; Webb et al., 2004). It hosts the world's largest deposits of platinum group metals, as well as large reserves of chromium, titanium, vanadium, nickel and gold (e.g., Cawthorn et al., 2006). The BC, which intruded into the intracratonic sedimentary sequences of the Transvaal Supergroup (e.g., Cawthorn and Webb, 2001), can be divided into the Rooiberg Group (RG), the Rashoop Granophyre Suite (RGS), the Lebowa Granite Suite (LGS) and the Rustenburg Layered Suite (RLS; e.g., Cawthorn et al., 2006; Hatton and Schweitzer, 1995; South African Committee for Stratigraphy, 1980). Fig. 1 shows the distribution of the different lithologies around the BC. The mafic units of the RLS crop out in five geographically distinct areas, the Eastern Limb, the Western Limb, the Far Western Limb and the two Northern limbs (Fig. 1; e.g., Webb et al., 2004). A sixth limb, the Southeastern or Bethal Limb (Cawthorn and Webb, 2001), is buried under Karoo sediments. The BC is disrupted in several places by alkaline intrusions (Fig. 1).

The deep structure and emplacement history of the BC remain uncertain. The BC was initially described as an internally layered laccolithic (Jorissen, 1904; Mellor, 1906; Molengraaff, 1901) or lopolithic structure (e.g., Du Toit, 1954; Hall, 1932; Molengraaff, 1902), but gravity modeling by Cousins (1959) showed that a Bouguer gravity low associated with the central region of the BC was not consistent with these interpretations. Cousins (1959) suggested that the BC consisted of separate intrusive limbs, with each limb having its own magma feeder system. Cousins (1959) model underwent several refinements, resulting in a model with detached inward dipping bodies (e.g., the “dipping-sheet model”; Biesheuvel, 1970; Du Plessis and Kleywegt, 1987; Meyer and De Beer, 1987; Molyneux and Klinkert, 1978; Van der Merwe, 1976; Walraven and Darracott, 1976). Through additional modeling of gravity data, the “dipping-sheet model” was refined further by Meyer and De Beer (1987), who showed that the limbs could extend to depths of 15 km with no compensation at the Moho (Fig. 2a).

The gravity modeling by Meyer and De Beer (1987) was constrained by deep electrical soundings and resistivity observations, which indicated the presence of a conductive layer beneath the

* Corresponding author at: Council for Geoscience, Private Bag X112, Pretoria 0001, South Africa. Tel.: +27 12 841 1197; fax: +27 866788423.
E-mail address: ekgaswane@geoscience.org.za (E.M. Kgaswane).

0040-1951/$ – see front matter
doi:10.1016/j.tecto.2012.06.003

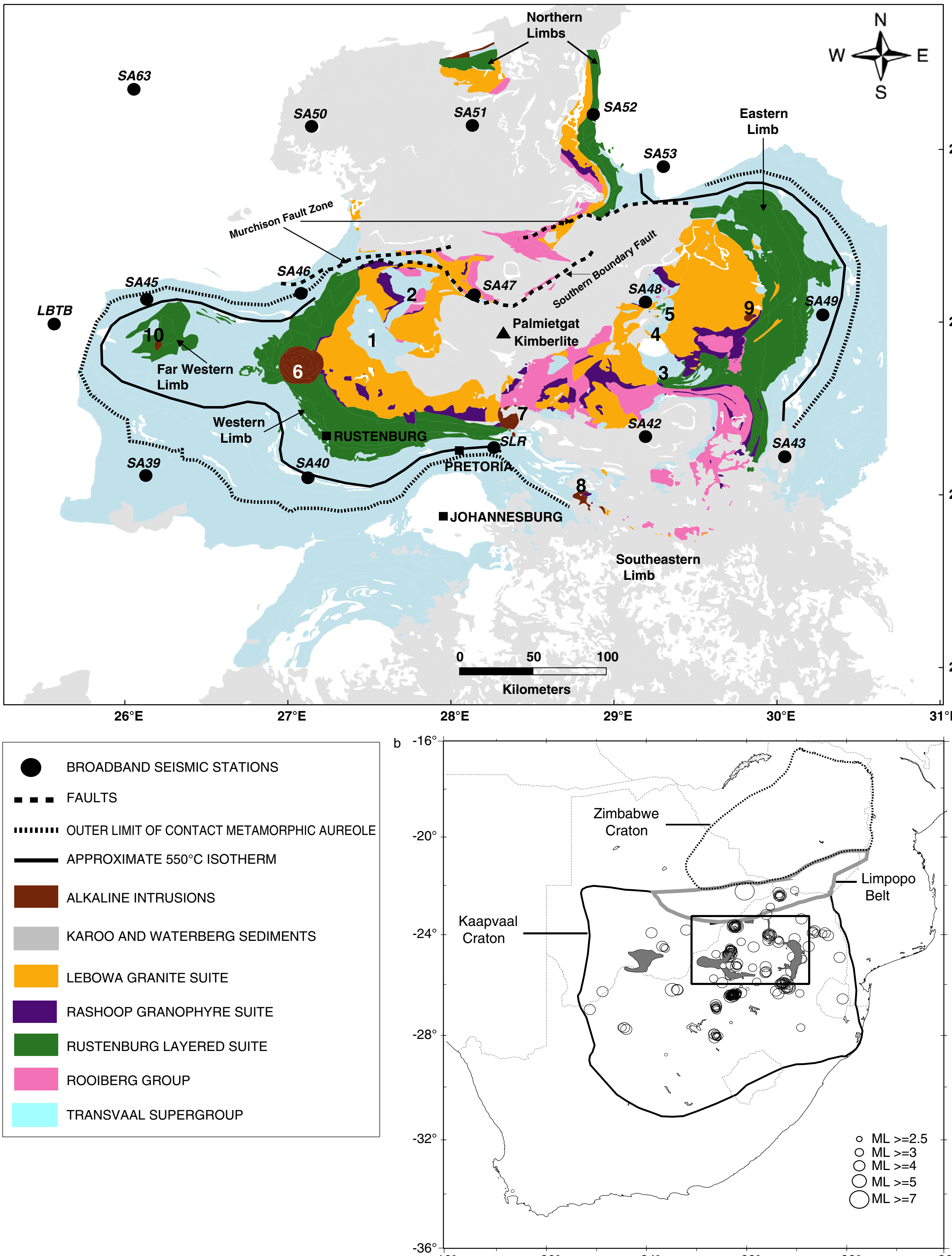
Northern Limbs
N
W
E
S
SA63
SA50
SA51
SA52
Eastern Limb
SA53
24°S
Murchison Fault Zone
Southern Boundary Fault
SA46
SA47
SA45
SA48
SA49
LBTB
2
1
5
4
9
10
Palmietgat Kimberlite
25°S
Far Western Limb
6
3
Western Limb
7
SA42
RUSTENBURG
SLR
SA43
SA39
SA40
PRETORIA
8
26°S
JOHANNESBURG
Southeastern Limb
0
50
100
Kilometers
27°S
26°E
27°E
28°E
29°E
30°E
31°E
BROADBAND SEISMIC STATIONS
FAULTS
OUTER LIMIT OF CONTACT METAMORPHIC AUREOLE
APPROXIMATE 550°C ISOTHERM
ALKALINE INTRUSIONS
KAROO AND WATERBERG SEDIMENTS
LEBOWA GRANITE SUITE
RASHOOP GRANOPHYRE SUITE
RUSTENBURG LAYERED SUITE
ROOIBERG GROUP
TRANSVAAL SUPERGROUP
b
-16°
-20°
-24°
-28°
-32°
-36°
Zimbabwe Craton
Limpopo Belt
Kaapvaal Craton
ML >=2.5
ML >=3
ML >=4
ML >=5
ML >=7
16°
20°
24°
28°
32°
36°

granites of the western and eastern limbs of the BC. Meyer and De Beer (1987) attributed this conductive layer to the Silverton shales of the Transvaal Supergroup. An alternative interpretation by Webb et al. (2004) of these resistivity observations based on drilling results of Walraven (1987) indicates that the conductive layer could be related to the rocks of the RLS.

More recent studies, based on geological observations and modeled gravity data, (Cawthorn and Webb, 2001; Cawthorn et al., 1998; Webb et al., 2004) have proposed the existence of continuous mafic layering at depth across the central region of the BC connecting the various limbs (Fig. 2b). In this model, hereinafter called the "continuous-sheet" model, the continuous mafic layering in the upper crust is isostatically compensated for by a depressed Moho, consistent with seismic constraints provided by receiver function studies (Kgaswane et al., 2009; Nair et al., 2006; Nguuri et al., 2001). The seismic velocity model of Nguuri et al. (2001) also shows a high shear wave velocity layer (Vs ~ 4.0 km/s) within the upper 10 km of the crust for one location near the center of the BC. Additional evidence supporting a model with continuous mafic layering under the center of the BC comes from mafic xenoliths found in the Palmietgat kimberlite pipe (Fig. 1; Webb et al., 2010).

The purpose of this paper is to use new seismic velocity models of the BC crust to evaluate the "dipping-sheet" and "continuous-sheet" models. The seismic velocity models are obtained by first measuring short-period Rayleigh wave group velocities using locally and regionally recorded seismic events, and then jointly inverting the group velocity measurements with high-frequency receiver functions. This study differs in two ways from the study by Kgaswane et al. (2009), which used a similar approach. Firstly, to improve constraints on the upper crustal velocity structure, we developed group velocity maps for short-period Rayleigh waves (2–15 s). Secondly, to improve resolution of fine-scale crustal structure, particularly in the upper crust, we used high-frequency ($f \leq 1.25$ Hz) receiver functions in the joint inversions with the group velocities. The study by Kgaswane et al. (2009) investigated the S-wave velocity structure of the crust in southern Africa by jointly inverting high- and low-frequency receiver functions with Rayleigh wave group velocity curves in the period range of 10–175 s. The results of this study provide better resolved shear wave velocity models for locations across the BC and yield new insights into the deep structure of the BC.

2. Data and methods

In this section, we first describe our Rayleigh wave tomography method to obtain group velocity maps for periods between 2 and 15 s. We follow this with a brief description of our methodology for computing receiver functions, and then explain how the two data sets have been jointly inverted.

2.1. Group velocity tomography

A total of 197 mining-related and regional tectonic earthquakes recorded by 45 broadband seismic stations were used for making Rayleigh wave group velocity measurements. The seismic events used have local magnitudes (ML) greater than 2.5 (Fig. 1b). An event list is provided as Supplemental material. Fig. 2c shows the location of the broadband seismic stations with respect to the outcrop pattern of the BC. Forty-three (43) of the stations belong to the Southern African Seismic Experiment (SASE) network (Carlson et al., 1996) and two of the stations belong to the Global Seismic Network (GSN) and South African National Seismograph Network (SANSN). Event catalogs (origin time, hypocenters and local magnitudes) were compiled from the earthquake bulletins published by the Council for Geoscience, by gold mines in the Witwatersrand Basin area and by the Incorporated Research Institutions for Seismology (IRIS). Mining-related earthquakes account for 81% of the total number of earthquakes used for the measurements, the majority of which originated within the gold mining districts of the Witwatersrand Basin.

To measure Rayleigh wave group velocities at each period, a code from Ammon (2001) was used based on multiple filter analysis (e.g., Claerbout, 1992; Dziewonski et al., 1969; Keilis-Borok, 1989; Levshin et al., 1992). The ray coverage is shown in Fig. 3, along with the total number of rays for each period. Ray coverage is greater at shorter periods (2–8 s) compared to longer periods (10–15 s). At each period the ensemble of measurements vary by no more than 0.1–0.2 km/s (see Supplemental material).

The group velocity measurements were inverted using a conjugate gradient algorithm (LSQR) based on the method by Paige and Saunders (1982). The LSQR algorithm solves the following equation:

$$\begin{bmatrix} A \\ \lambda \end{bmatrix} [x] = \begin{bmatrix} b \\ 0 \end{bmatrix} \tag{1}$$

where A represents a matrix of ray distances in each cell, x is a vector of group velocity perturbations or slownesses, b is a vector of group velocity travel-times (distance/group velocity) and λ is a Laplacian smoothing constraint. The choice of an optimal smoothing parameter was made by considering the trade-off between model smoothness and travel-time misfit. Fig. 4 shows the results for 2, 4 and 6 s periods. Trial-and-error inversions were performed using smoothing parameters in the range of 0–200, revealing that a smoothing parameter of 100 provides a good balance between data misfit and model smoothness at all periods. Therefore, a smoothing parameter of 100 was used for the group velocity inversions.

We evaluated the resolution of the group velocity tomography using checkerboard tests with 100 km and 125 km checkers (Fig. 5). The rectangles shown with dashed lines enclose the region with best resolution. The 100 × 100 km checkers are not as well recovered at any period compared to the 125 × 125 km checkers, indicating that velocity variations are not well resolved at scales less than ~125 km. In addition, at 12 and 15 s period, only velocity variations within the center of the BC can be resolved for the 125 × 125 km checkers.

The results of the group velocity tomography are shown in Fig. 6. Across the areas of the BC where velocity variations are best resolved, velocities at all periods vary between 2.8 and 3.2 km/s, but do not show a clear spatial correlation from one period to the next. We found group velocities at 10 and 15 s periods to be 10–30% greater than those reported by Pasyanos and Nyblade (2007) and used by Kgaswane et al. (2009). The ray path coverage reported by Pasyanos and Nyblade (2007) is limited at periods of 10 and 15 s compared to periods ≥20 s. Pasyanos and Nyblade (2007) did not report uncertainties at 10 and 15 s and Fig. 4 of Pasyanos and Nyblade (2007) shows uncertainties of less than 0.1 km/s for a period of 20 s. Pasyanos and Nyblade (2007) did not report group velocities for periods less than 10 s.

2.2. Receiver functions

A total of 17 stations, including LBTB and SLR (Fig. 1), fall within the area enclosed by the rectangles shown in Fig. 5. High quality

Fig. 1. a. Map of the Bushveld Complex (BC) showing simplified geology and its six limbs (lobes) — the Eastern, Western, Far Western, Southeastern and the two Northern limbs (map modified from the 1:250 000 geology map of South Africa). Numbers 1, 2, 3, 4 and 5 show the position of some of the domes, and numbers 6, 7, 8, 9 and 10 show the location of alkaline intrusions. The locations of the 16 seismic stations for which Vs models are reported are shown with the prefix "SA" followed by the station number. b. Map of southern Africa showing the locations of earthquakes (open circles) used in this study. The solid black rectangle encloses the study area. Outcrops of the BC are shown as gray polygons. The outlines of the Kaapvaal Craton, Limpopo Belt and the Zimbabwe Craton are shown in solid black, gray and dotted lines, respectively.

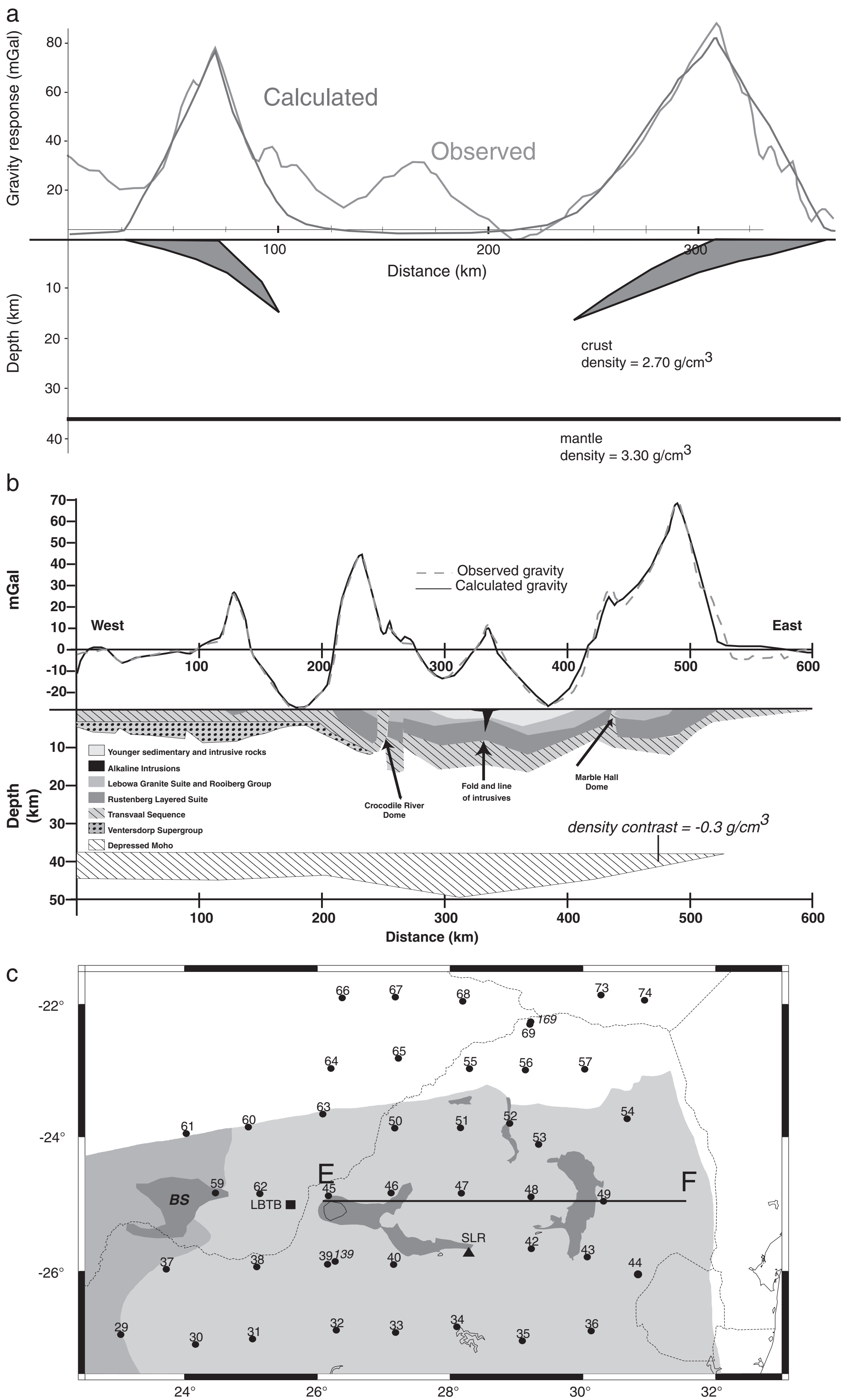
a
Gravity response (mGal)
Calculated
Observed
Distance (km)
Depth (km)
crust
density = 2.70 g/cm3
mantle
density = 3.30 g/cm3
b
mGal
Observed gravity
Calculated gravity
West
East
Younger sedimentary and intrusive rocks
Alkaline Intrusions
Lebowa Granite Suite and Rooiberg Group
Rustenberg Layered Suite
Transvaal Sequence
Ventersdorp Supergroup
Depressed Moho
Crocodile River Dome
Fold and line of intrusives
Marble Hall Dome
density contrast = -0.3 g/cm3
Depth (km)
Distance (km)
c
BS
LBTB
SLR
E
F
-22°
-24°
-26°
24°
26°
28°
30°
32°

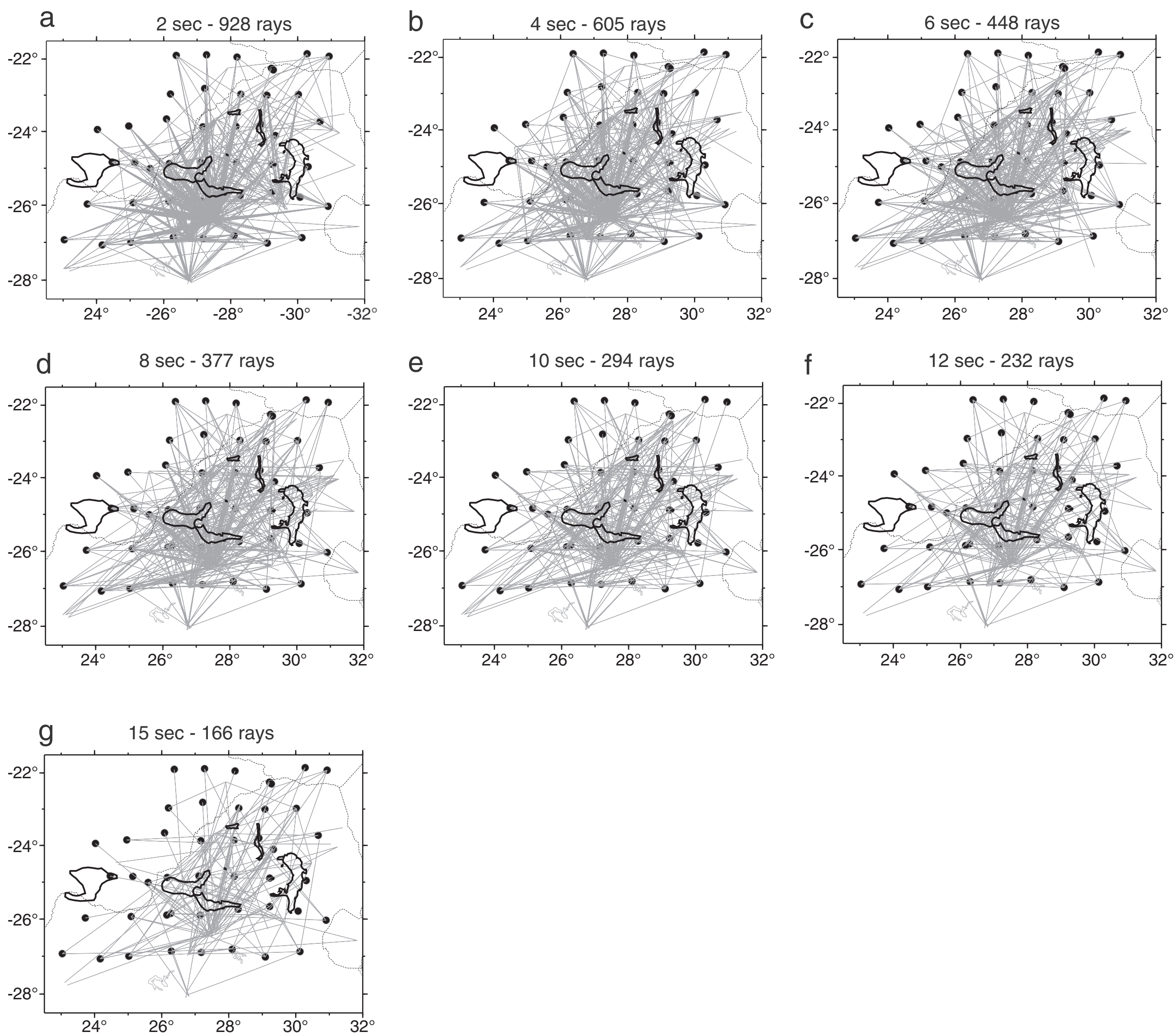

Fig. 3. Raypath maps for periods of 2, 4, 6, 8, 10, 12 and 15 s. Outlines of the BC outcrops are shown with solid black lines. The solid black circles show the position of the stations.

receiver functions were obtained for 16 of these stations (shown in Fig. 1). A total of 100 teleseismic earthquakes were used to compute receiver functions (see Supplemental material), many of them the same as used by Kgaswane et al. (2009).

Receiver functions were computed using the iterative time-domain deconvolution method of Ligorría and Ammon (1999). For each teleseismic event, receiver functions were computed at a frequency band of f ≤ 1.25 Hz (Gaussian bandwidth of 2.5 s) with a maximum number of 200 iterations. For each station, the receiver functions were binned in ray parameter groups from 0.04 to 0.049 s/km, 0.05 to 0.059 s/km, and 0.06 to 0.069 s/km, and also by backazimuth, and then stacked. The purpose of grouping the receiver functions according to ray parameter is to account for the phase move-out due to varying incidence angles (Cassidy, 1992; Gurrola and Minster, 1998). Fig. 7 shows examples of receiver functions for two stations, illustrating the quality of the data.

2.3. Joint inversion

The joint inversion of receiver functions and surface wave dispersion measurements yields 1-D Vs models of the structure beneath each recording station (Julià et al., 2000, 2003). The method used in this study employs a linearized inversion procedure that minimizes a weighted combination of the L2 norm of the vector residuals corresponding to each data set and a model roughness norm (Ammon et al., 1990). The weighting among the data sets is composed of normalization constants that are helpful in equalizing the contribution of each data set to the overall misfit of the objective function. Each data set is normalized by the number of data points, variances and an influence factor controlling the relative influence of each data set on the inverted 1-D Vs models (Julià et al., 2000). The model vector difference norm helps in stabilizing the inversion procedure by placing smoothness constraints on the resulting 1-D

Fig. 2. a. Meyer and De Beer (1987) gravity model. b. Webb et al. (2004) gravity model. The models in a) and b) have been reproduced from Webb et al. (2004). c. Locations of the SASE (solid circles), GSN (solid square) and SANSN (solid triangle) broadband stations within and surrounding the BC. The profile of the two gravity models is shown by the solid line EF. The area marked BS is the Molopo Farms Complex and represents one of the Bushveld satellites. The background gray-shaded regions show the Kaapvaal Craton. Terrain and political boundaries are shown by dashed black and gray lines, respectively.

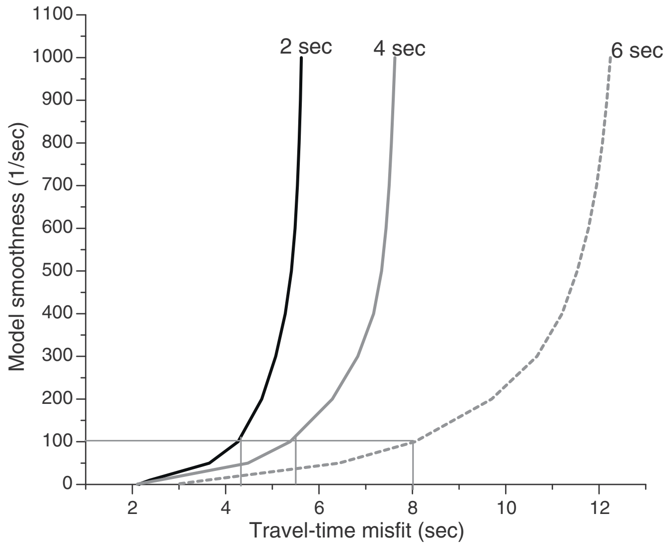

Fig. 4. Trade-off curves of smoothing versus travel-time misfit for periods of 2, 4 and 6 s.

depth-velocity profiles. The model difference norm corresponds to second order differences between adjacent layers (Ammon et al., 1990; Julià et al., 2000). The resulting Vs models are, therefore, a balance between fitting observations, model simplicity and a priori constraints (Julià et al., 2005).

Rayleigh wave group velocities obtained in this study from 2 to 15 s were combined with group velocities from 20 to 60 s from Pasyanos and Nyblade (2007) to create a composite dispersion curve for each station. The dispersion curves were smoothed with a 3-point running average prior to joint inversion with the receiver functions. For each inversion, the influence factor was set to 0.5 and no smoothing was applied, except for stations SA42, SA43 and SA53, for which smoothing parameters slightly greater than or equal to 0.1 were used. An influence factor of 0.5 equalizes the contribution of the combined misfit from each dataset. Fig. 8 shows trade-off curves of (i) waveform misfit versus model roughness and (ii) waveform misfit versus model smoothness for two stations, illustrating that using little, if any, smoothing is justified in the inversions.

The starting model used for the inversions is the PREM model (Dziewonski and Anderson, 1981) modified for continental structure above 60.5 km depth and further modified for the BC upper crust above 10 km depth (Figs. 9 and 10). The model parameterization

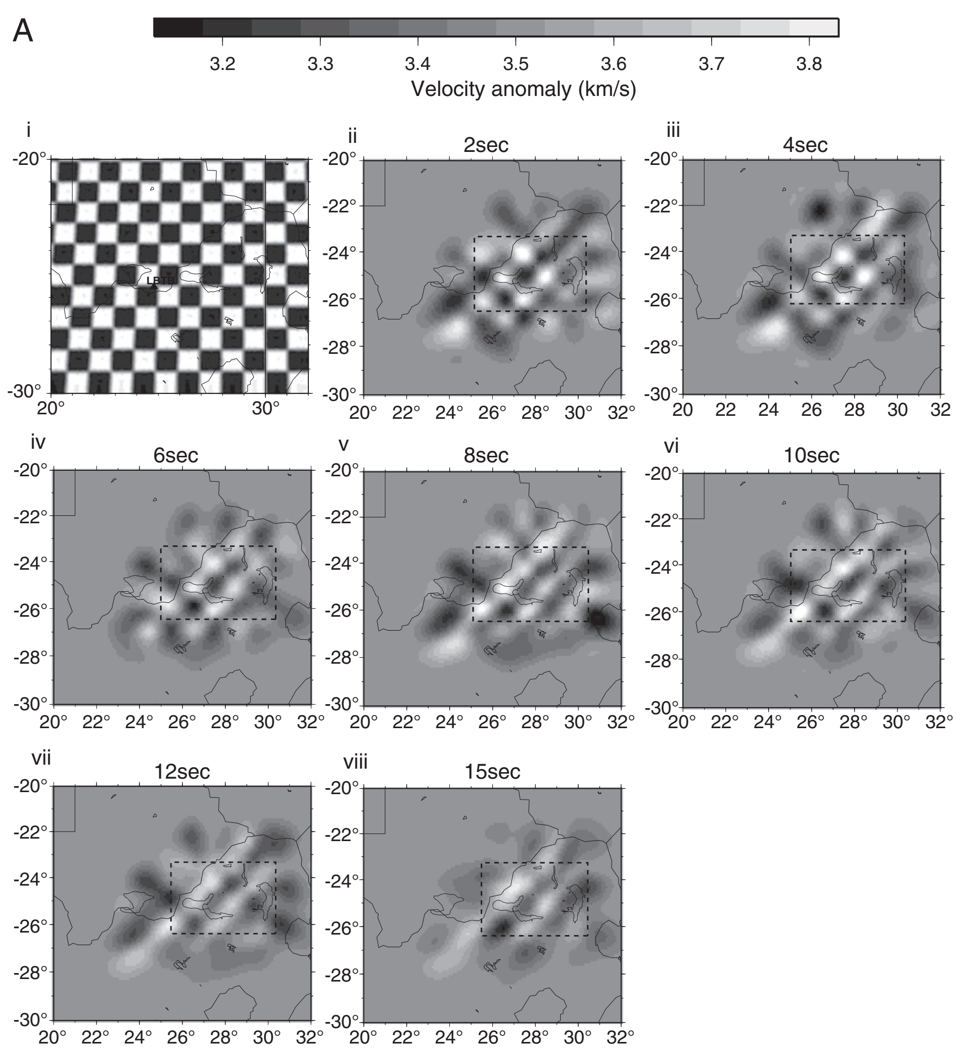

Fig. 5. Resolution tests a. Input (i) and output models (ii–viii) for 100 × 100 km checkers b. Input (i) and output models (ii–viii) for 125 × 125 km checkers. The dashed rectangles enclose the area of best resolution.

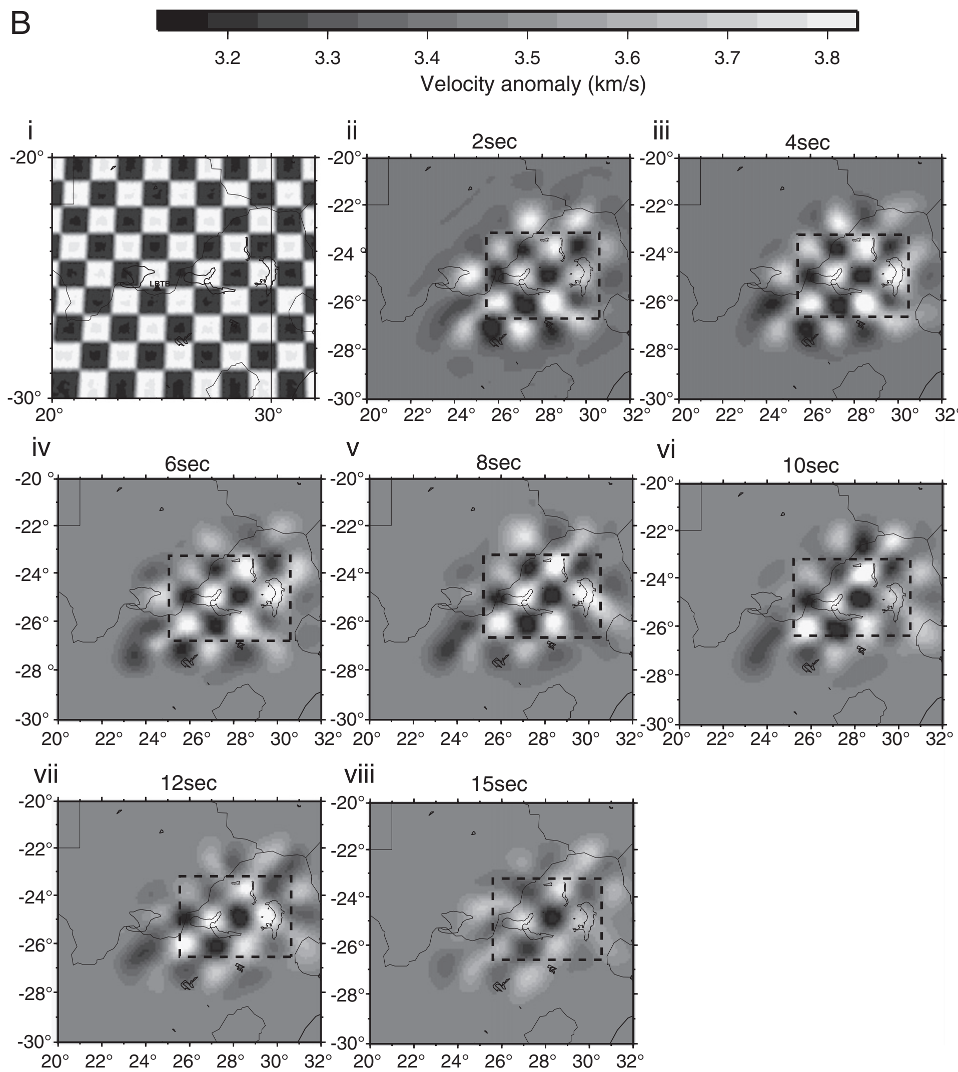

Fig. 5 (*continued*).

consisted of 1-km thick layers to a depth of 10 km, 2.5-km thick layers between depths of 10 to 47.5 km, 5-km thick layers between 47.5 and 242.5 km depth, and 17 to 40-km thick layers below 242.5 km depth. The importance of using 1 km thick layers to parameterize the model in the upper 10 km of the crust is illustrated in Fig. 9, where the fits to the data are compared for two models for station SA47, one with 1-km thick layers and the other with 2 km thick layers. The model with 1-km thick layers fits the receiver function stack better than the model with 2 km thick layers.

To estimate the uncertainties in our velocity model, we follow the approach developed by Julià et al. (2005) for their inversion method, which involves repeatedly performing the inversions using a range of inversion parameters. This may be viewed as an overly simplistic approach, but it is effective in developing a sense of the range of variation of the inverted parameters given the observations and the a priori constraints. As explained by Julià et al. (2000), more sophisticated and statistically rigorous approaches generally require that the observations meet desirable properties, such as being normally distributed, which in general are not satisfied by the data. By following the approach of Julià et al. (2005) of repeatedly performing the inversions with a range of inversion parameters, we obtain an uncertainty of approximately 0.1–0.2 km/s for the velocity in each layer, which translates into an uncertainty of ~2–3 km in the depth of any boundary observed in the model, such as the Moho.

2.3.1. Results

Fig. 10 shows the joint inversion results for all 16 stations, and crustal parameters used in the models are summarized in Table 1 and illustrated in Fig. 11. Many of the stations show a discontinuity where Vs increases from <4.3 km/s to >4.3 km/s, clearly delineating the Moho. For some stations, however, a velocity gradient is observed going from the lower crust into the upper mantle, and for those stations we have placed the Moho at the depth where Vs exceeds 4.3 km/s because velocities ≥ 4.3 km/s are indicative of mantle lithologies (Christensen, 1996; Christensen and Mooney, 1995). The crustal thicknesses obtained for all 16 stations are similar (i.e., within ~1–3 km) to those reported by Kgaswane et al. (2009).

Fig. 12 shows three profiles across the BC illustrating that the Moho reaches a maximum depth of 45 km in the center of the BC compared to ~37–38 km outside of the BC. In addition to ~5–8 km of crustal thickening, most stations within the BC record a high velocity layer with Vs ≥ 4.0 km/s in the lowermost crust (Table 1). For most of the stations, the thickness of this layer exceeds 5 km, but for a few stations (e.g., station SA50), it is less than 5 km thick.

The joint inversion yields an average Vs of 3.4–3.6 km/s for the crust above 10 km depth for most localities within the BC (Table 1), which is consistent with the upper crustal velocities reported by Yang et al. (2008). However, structural complexities affecting the layering within the upper crust can be inferred for some stations that

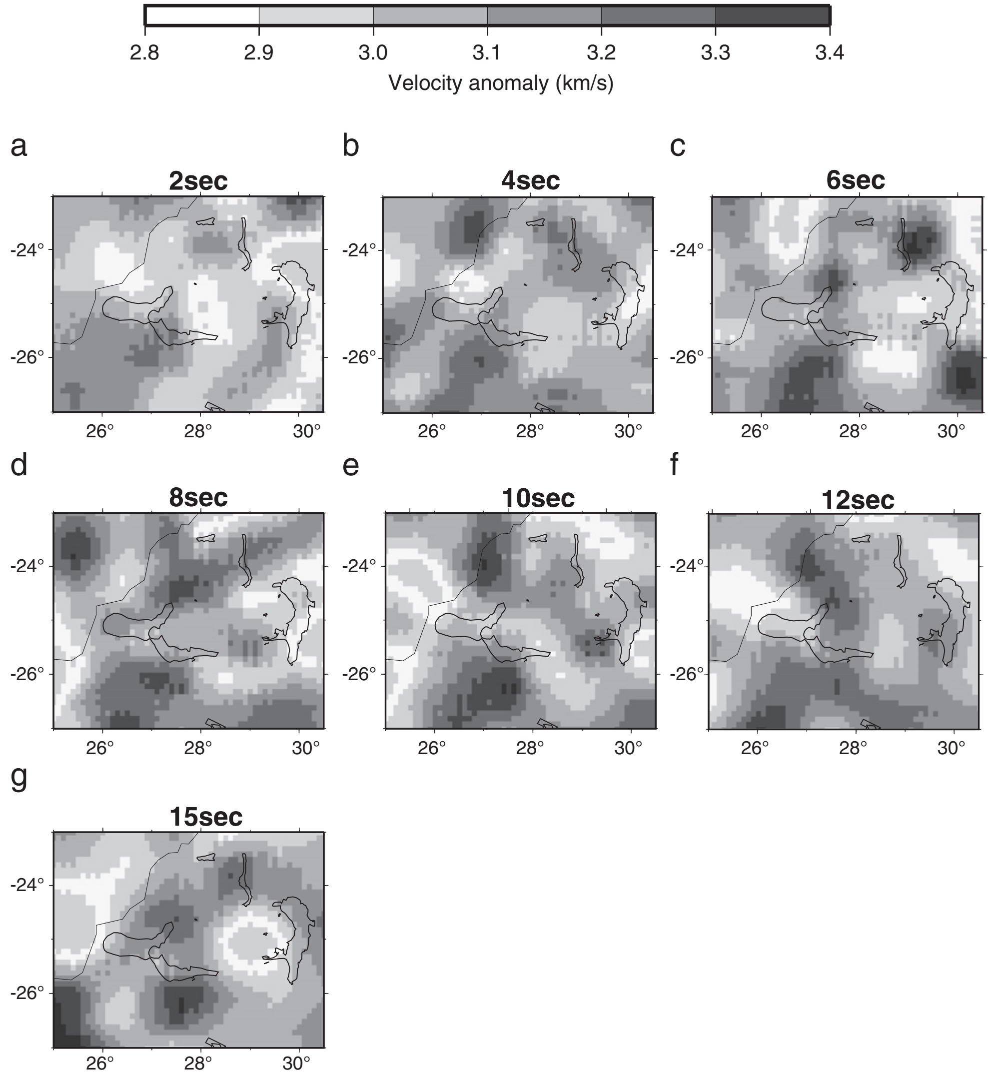

Fig. 6. Rayleigh wave group velocity maps at periods of 2, 4, 6, 8, 10, 12 and 15 s (a–g). The maps show the area within the dashed rectangle in Fig. 5.

record velocities as high as 3.7–3.8 km/s for layers that are only ±2 km thick (i.e., SA47, SA50 and SA53; Fig. 11). In addition, considerable variability in upper crustal structure can be seen for some stations as a function of backazimuth. Station SA47 is a good example, and we examine this variability in detail in Section 3.4.

3. Discussion

To summarize, the main findings of this study are: a) in the center of the BC the crust thickens to a depth of ~45 km (e.g., SA45, SA47, SA48) (Fig. 12) and a substantial portion of the lower crust (greater than 5 km thickness) across the BC consists of high velocity rock (Vs≥4.0 km/s) (Fig. 11), and b) for some stations velocities as high as 3.7–3.8 km/s are found in the upper crust (e.g., SA47, SA50, SA53). For interpreting our results, we convert Vs to density using the empirical Vs–density (ρ) relation from Christensen and Stanley (2003), which was formulated for both crustal and uppermost mantle lithologies at 200 MPa:

$$Vs = 0.0014\rho - 0.4019, \quad (2)$$

Using this equation, a lower crustal Vs of 4.0–4.3 km/s and an uppermost mantle Vs of 4.4–4.6 km/s, yields a density contrast for the crustal "root" of ~−0.2 to −0.3 g/cm^3. Using Eq. (2) and an average Vs of 3.4–3.6 km/s for the top 10 km of the crust, we obtain an average density for the upper crust of 2.7–2.9 g/cm^3. For upper crustal layers with Vs>3.6 km/s, we obtain densities>2.9 g/cm^3, which are consistent with the presence of mafic lithologies (Christensen and Stanley, 2003). These findings and density estimates can be used to evaluate the "dipping-sheet" and "continuous-sheet" models for the BC.

3.1. "Dipping-sheet" model

As discussed in the Introduction, the "dipping-sheet" model by Meyer and De Beer (1987) has a gap between the eastern and western limbs and no compensation at the Moho for the dense upper crustal layers (Fig. 2a). This model is not consistent with our findings of crustal thickening in the center of the BC, high Vs layers (Vs≥4.0 km/s) in the lowermost part of the crust (≥40 km), or high upper crustal densities beneath the center of the BC. Therefore, this model is not favored.

3.2. "Continuous-sheet" model

The "continuous-sheet" model by Webb et al. (2004) (Fig. 2b) proposes the presence of continuous mafic layering in the upper crust across the central region of the BC connecting the eastern and

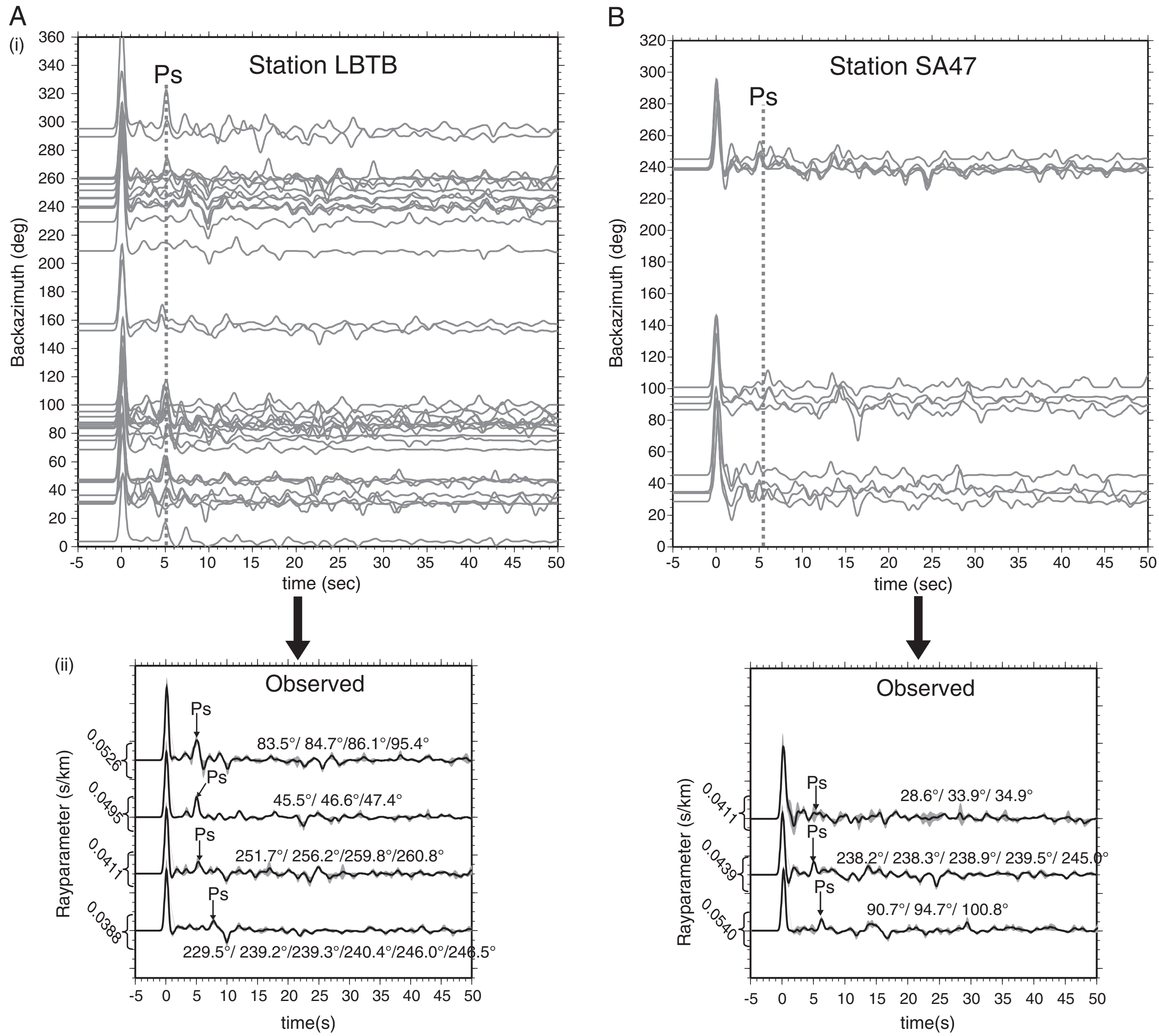

Fig. 7. Receiver functions at stations LBTB and SA47 (columns A and B, respectively). (i) Individual receiver functions for each station. The dashed gray lines show the theoretical arrival time of the Moho converted phase (Ps) for the crustal thicknesses and average crustal Vs for stations LBTB and SA47 reported in Table 1. The theoretical arrival times were computed using the joint inversion code and assuming the PREM model. (ii) Stacked receiver functions grouped according to ray parameter bins and backazimuth. The gray shading around the observed receiver functions shows 1σ error bounds.

western limbs of the BC. The model also includes isostatic compensation of the mafic layering by a thickened crust in the center of the BC, extending to a depth of ~50 km. In this model, a density contrast of 0.3 g/cm^3 for each of the upper crust mafic layers is used along with a density contrast of −0.3 g/cm^3 for the crustal root (>38 km depth).

Our results show that the crust has a thickness of ~45 km beneath the center of the BC (Fig. 12), consistent with, but somewhat thinner than, the lower crustal structure in the Webb et al. (2004) model. The Webb et al. (2004) model assumes an average density of 2.9 g/cm^3 for the structure above 10 km depth in the center of the BC, which is equivalent to a Vs of 3.65 km/s using the relation in Eq. (2). The Vs models (Figs. 10 and 11) for some stations show Vs > 3.65 km/s within upper crustal layers, as noted previously, and therefore our results are broadly consistent with the upper crustal structure in the Webb et al. (2004) model.

3.3. Refinement of the Webb et al. (2004) density model

Fig. 13 shows a revised density model that includes several adjustments to the Webb et al. (2004) model to make it consistent with our seismic models. Similar to Webb et al. (2004), a background density of 2.7 g/cm^3 was used for the bulk crust as well as the same density contrasts for the upper crustal layers (see Fig. 13). Based on the seismic results, we assume a density of 3.3–3.4 g/cm^3 for the uppermost mantle. For the crustal "root" (>37.5 km depth), a density contrast of −0.2 g/cm^3 was used instead of the −0.3 g/cm^3 density contrast used by Webb et al. (2004). After changing the structure and density of the crustal "root", we then adjusted the thickness of the upper crustal layers to obtain a good fit to the gravity data.

In the revised density model (Fig. 13), the mafic layering in the upper crust remains continuous across the BC with a maximum

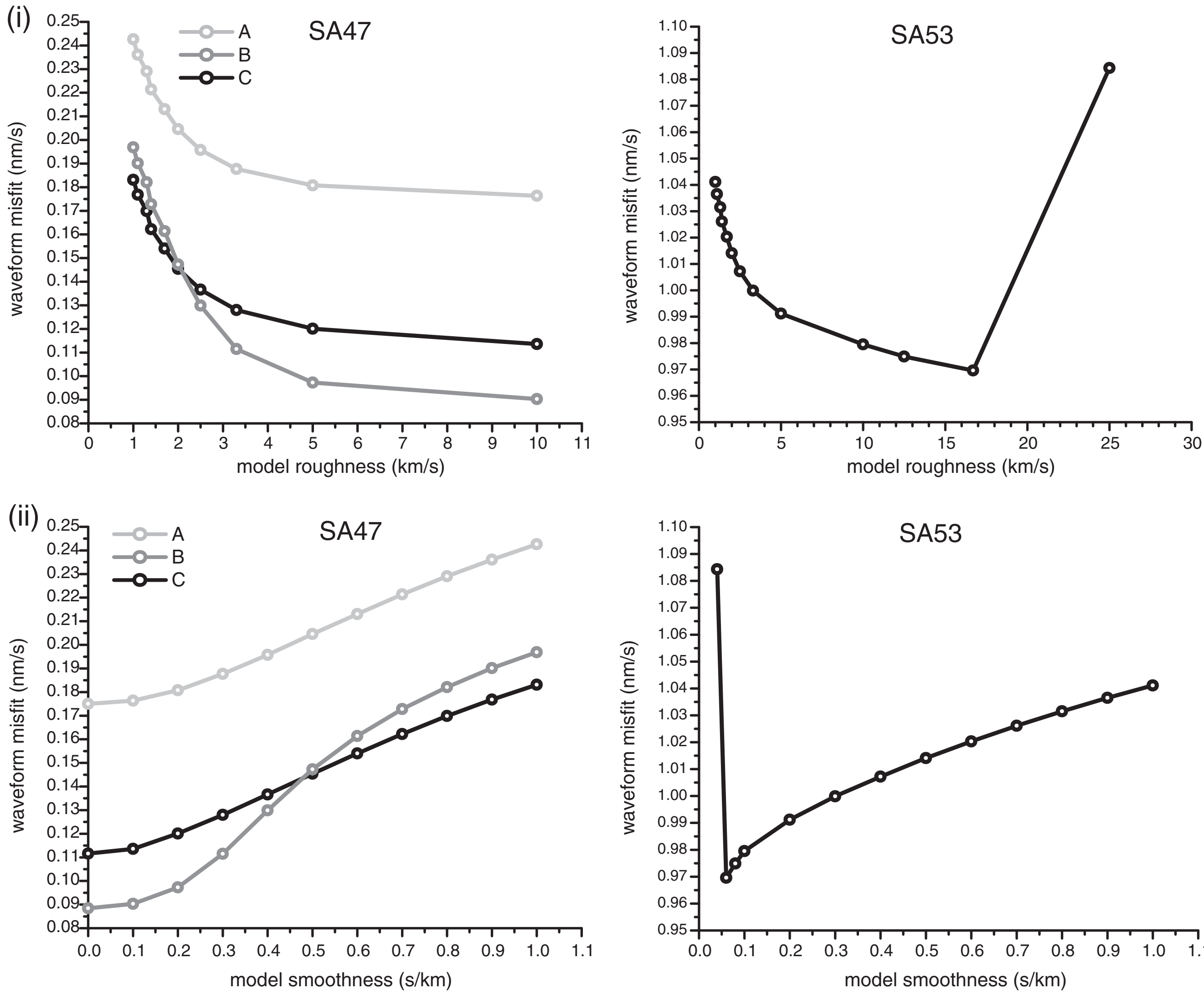

Fig. 8. Plots of waveform misfit as a function of model roughness and model smoothness (i and ii, respectively) for stations SA47 and SA53. Labels A, B, C for station SA47 refer to the three receiver function stacks for this station shown in Fig. 10.

thickness of 4–5 km, similar to Webb et al. (2004). However, the layers of the Transvaal Sequence and younger sediments in the center of the BC are somewhat thinner than those reported by Webb et al. (2004). This illustrates that to accommodate the difference in crustal thickness between the Webb et al. (2004) model and our seismic results, only minor adjustments are required to the Webb et al. (2004) model.

3.4. Structural complexity in the upper crust

Although our results are in general agreement with Webb et al. (2004) suggesting the presence of mafic lithologies beneath the center of the BC, our results also indicate that there is a considerable structural complexity within the upper crust, much more than is shown in either the Webb et al. (2004) model or in Fig. 13. We illustrate this by carefully examining the receiver functions for station SA47, which is located near the center of the BC (Fig. 1). The geology immediately around station SA47 is shown in Fig. 14. Plotted on this figure are average Ps conversion points at 5 km depth for the three receiver function stacks for SA47 shown in Fig. 10. The Vs profile for SA47 at backazimuth (a) in Fig. 11 corresponds to the conversion point at A in Fig. 14, and similarly the Vs profiles at backazimuths (b) and (c) correspond to conversion points B and C, respectively. Fig. 14 shows an overthrust just to the south of station SA47, resulting in a complicated anticlinal structure with the receiver functions likely sampling different lithologies (i.e., granites, sandstones, quartzites) depending on backazimuth and depth.

In Fig. 15, the three receiver function stacks for SA47 are modeled to ascertain the effect of upper crustal structure on the waveforms. The synthetic receiver functions in the first column of Fig. 15 were obtained from the joint inversion, whereas those in the second and third columns were generated using a code based on a reflection matrix method by Kennett (1983). For reference, the first column of receiver functions shows the fit between observed and synthetic receiver functions for the models obtained from the joint inversion. The first prominent phase after the direct P arrival within the first 2 s is labeled P1, and is the primary arrival resulting from upper crustal structure. There is a considerable variability in this phase between the three receiver function stacks. For stack (a), the phase is characterized by a large down-swing with a peak amplitude at 1.8 s. For stack (b), the phase is characterized by a large down-swing with a peak amplitude at 1.0 s. And for stack (c), the phase is characterized by a small down-swing with a peak amplitude around 1.7 s. The Ps conversion from the Moho is also labeled on each stack.

In the second column, we show synthetic receiver functions for a velocity model that contains the velocity layering in the upper

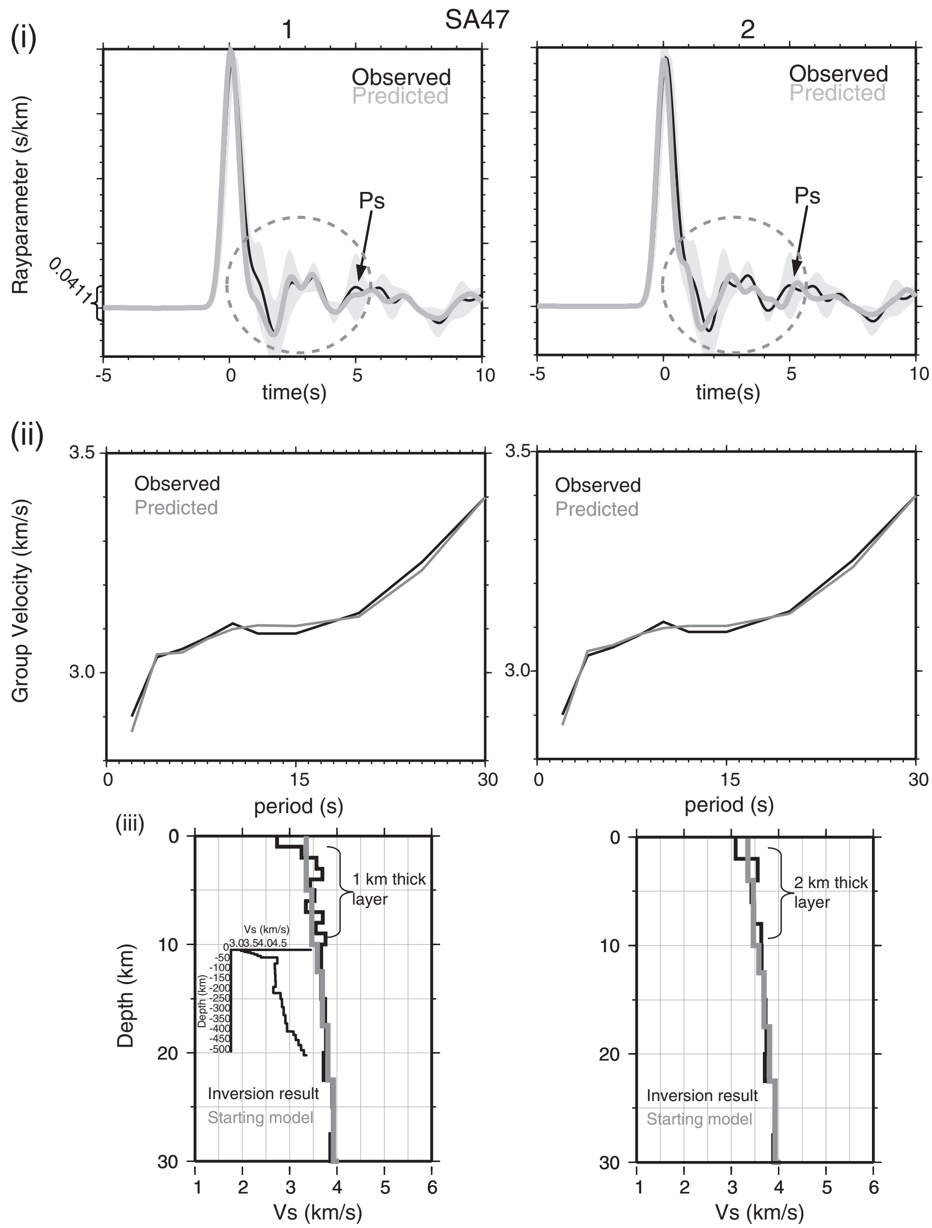

Fig. 9. Diagram for station SA47 illustrating the improved fit to the receiver functions by using 1 km thick layers (column 1) in the top 10 km of the model versus 2 km thick layers (column 2). The Ps conversion from the Moho is labeled "Ps", and the gray shading around the observed receiver function shows 1σ error bounds.

10 km of the crust from the joint inversion models (shown at far left in Fig. 15), and a half space beneath it with a velocity of 3.6 km/s. A comparison between the synthetic and actual receiver functions illustrates that the P1 phase does indeed originate from structure (i.e. thrusted zone) within the top 10 km of the crust.

To isolate which layers within the top 10 km of the crust influence the P1 phase the most, in the third column we show two synthetic receiver functions with altered upper crustal layering (structure below 10 km is the same as in the joint inversion models). In the first one (dotted line), the low velocity layer in the top 1 km of the model is removed (i.e., the topmost velocity is increased to the velocity in the layer just below it). A comparison of the receiver function fits shows that the earlier arriving P1 phase in stack (b) is changed significantly (effectively removed), but the fits for stacks (a) and (c) are essentially unchanged, indicating that the later arriving P1 phases in those stacks might be influenced by deeper structure. In the second case (gray line), the velocity structure in the top 10 km is set to a uniform 3.4 km/s, thus removing all of the higher velocity layering in the top 10 km of the crust seen in the joint inversion models. Even though the velocity models (gray lines) in the third column have been set to a uniform 3.4 km/s in the top 10 km of the crust, the corresponding receiver functions are different because of influences from structures below 10 km depth. In this case, the P1 phase in stacks (a) and (c) is significantly altered, indicating that the higher velocity layering between 1 and 10 km depth in the joint inversion model is required to fit the P1 phase.

Our modeling shows that the receiver function stacks from two of the three backazimuths (stacks a and c) require higher velocity layers (i.e., Vs of 3.7–3.8 km/s) in the upper crust to obtain a good fit, as compared to stack (b). These results suggest that the mafic layering may be better developed to the east and northeast of station SA47 than to the southwest, and hence the upper crustal structure is not as uniform as illustrated by the gravity models (Fig. 13 and Webb et al., 2004). The non-uniformity could potentially be a characteristic of much of the central areas of the BC. The non-uniformity could either be entirely or partially associated with the diapirism and metamorphism and associated structural complexity triggered by the emplacement of the BC (Uken and Watkeys, 1997).

Fig. 1 shows the position of some of the domes associated with diapirism triggered by high thermal gradients at the base of the BC. According to Uken and Watkeys (1997), the domes were produced by gravitational loading and heating of the sedimentary rocks of the Transvaal Supergroup below the floor of the BC. For areas where temperatures were above 550 °C, these floor rocks became unstable and diapirically rose into the overlying units of the RLS. Although the domes are best exposed towards the margins of the BC, as shown in Fig. 1, the diapirism of floor rocks into the overlying RLS could be widespread across the center of the BC, assuming that diapirism was generally driven by thermal destabilization of low density rocks of the Transvaal Sequence (Uken and Watkeys, 1997).

Thermally-driven diapirism as proposed by Uken and Watkeys (1997) may not be the only source of structural complexity affecting the BC. Field, petrographic and $^{40}Ar/^{39}Ar$ data presented by Alexandre et al. (2006, 2007) for Pretoria Group rocks (west of Pretoria) strongly support a ~2040 Ma episode of intracratonic crustal shortening marked by folding, thrusting and lower greenschist facies metamorphism best observed in the broad area between Pretoria, the village of Magaliesburg, and the Cradle of Humankind (cf. Andreoli, 1988a, 1988b). Further evidence for this so-called “Transvaalide” tectonic–metamorphic event, tentatively linked to coeval reactivation of the Central Zone in the Limpopo Belt, was also identified in the Malip River–Pilgrim's Rest areas, close to the NE and E margin of the BC respectively (cf. Alexandre et al., 2006; Harley and Charlesworth, 1994).

4. Summary

The 1-D shear wave velocity models have been obtained for the BC crust by jointly inverting high-frequency receiver functions and Rayleigh wave group velocities for 16 broadband seismic stations spanning the BC. The 1-D shear wave velocity models show that, 1) there is ~5–8 km crustal thickening beneath the center of the BC, 2) shear wave velocities reach 4.0 km/s or higher over a significant portion of the lower crust, and 3) there are upper crustal layers beneath the center of the BC with shear wave velocities high enough (Vs > 3.65 km/s) to indicate the presence of mafic lithologies. These findings are consistent with the “continuous-sheet” model (e.g., Webb et al., 2004) for the BC. However, detailed modeling of receiver function stacks for station SA47 in the center of the BC shows that the upper crustal structure varies considerably around the station, indicating that the structure of the BC at depth is locally complicated. This inhomogeneity

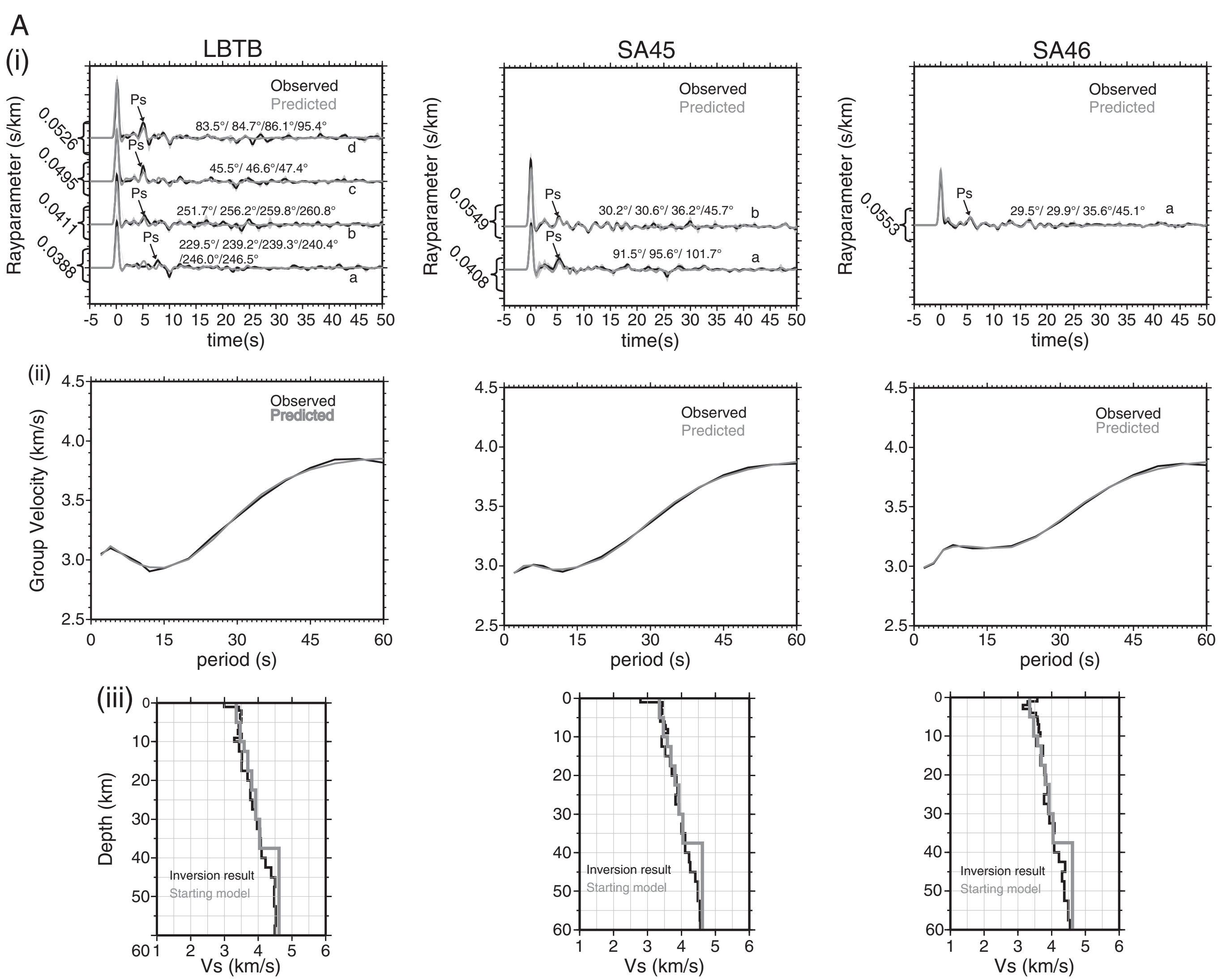

Fig. 10. Joint inversion results for the 16 stations (i) Observed (black curves) and predicted (gray curves) receiver functions with 1σ error bounds shown with gray shading around the observed receiver functions. The backazimuths of the receiver functions within each stack are shown on top. (ii) Observed (black curves) and predicted (gray curves) group velocities. (iii) Shear wave velocity models obtained from the joint inversion.

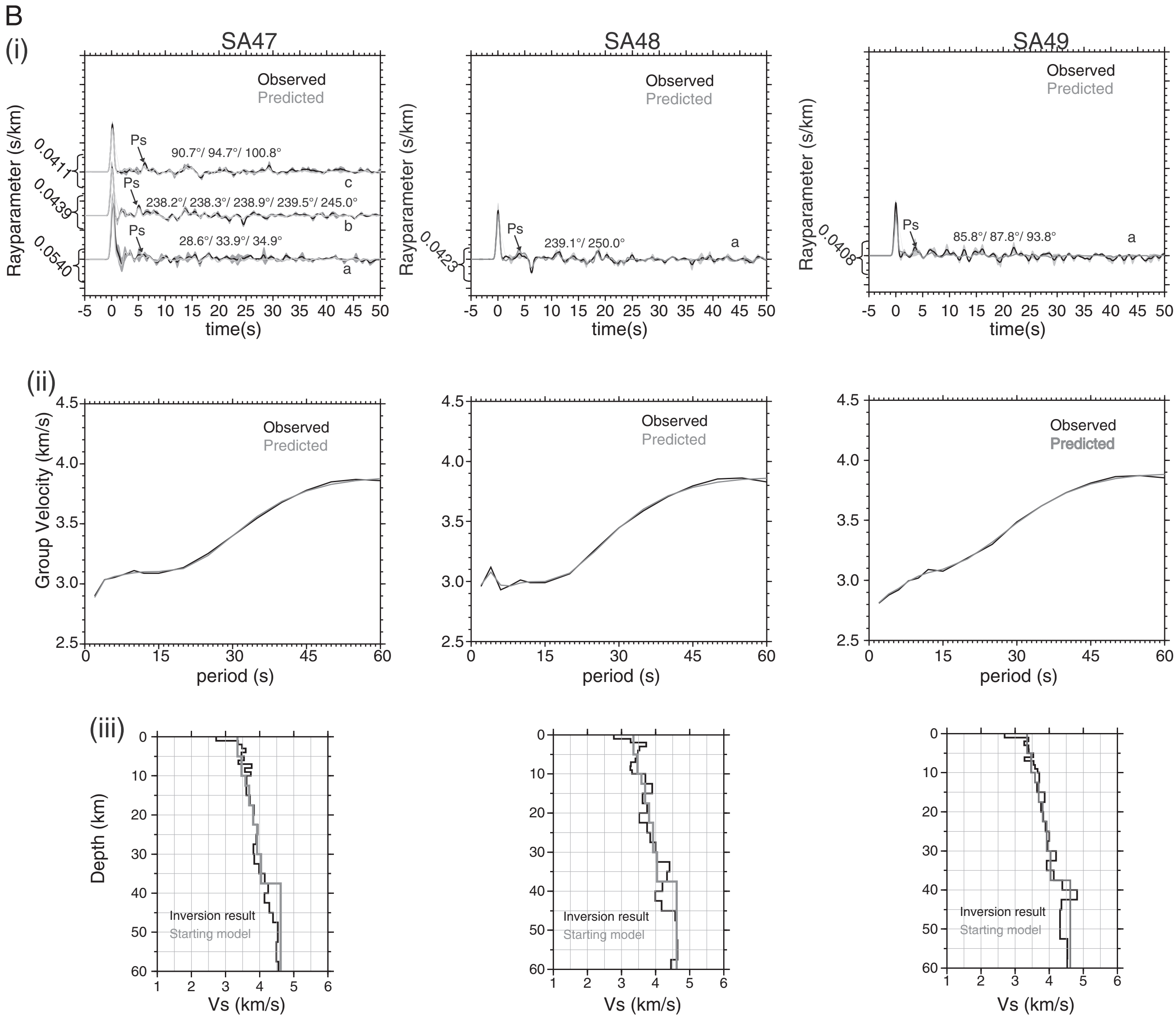

Fig. 10 (*continued*).

may be the result of thermal diapirism triggered by the emplacement of the BC at ~2060 Ma, or thermal and tectonic reactivation produced by a ~2040 Ma intraplate event.

Supplementary data to this article can be found online at http://dx.doi.org/10.1016/j.tecto.2012.06.003.

Acknowledgments

We would like to thank Charles Ammon for the use of his inversion code, Yongcheol Park for assistance with the computer codes, Tarzan Kwadiba for the additional catalog of earthquakes used for the group velocity measurements and all those who assisted with the Southern African Seismic Experiment. Discussions with Marco Andreoli have provided further clarity to the interpretation of the results of this study. Two anonymous reviewers provided comments that helped to improve this manuscript. E.K. would like to acknowledge support from the Council for Geoscience and the AfricaArray program and R.J.D. acknowledges support from the DST/NRF South African Research Chair program. This research has been supported by the National Science Foundation (grants EAR 0440032 and OISE 0530062), the AfricaArray program and the South African National Research Foundation.

References

Alexandre, P., Andreoli, M.A.G., Jamison, A., Gibson, R.L., 2006. ^{40}Ar/^{39}Ar age constraints on low-grade metamorphism and cleavage development in the Transvaal Supergroup (Central Kaapvaal craton, South Africa): implications for the tectonic setting of the Bushveld igneous complex. South African Journal of Geology 109, 393–410.

Alexandre, P., Andreoli, M.A.G., Jamison, A., Gibson, R.L., 2007. Response to the comment by Reimold et al. on ^{40}Ar/^{39}Ar age constraints on low-grade metamorphism and cleavage development in the Transvaal Supergroup (central Kaapvaal Craton, South Africa): implications for the tectonic setting of the Bushveld Igneous Complex (South African Journal of Geology, 109, 393–410), by Alexandre et al. (2006). South African Journal of Geology 110, 160–162.

Ammon, C.J., 2001. Notes on Seismic Surface-Wave Processing, Part 1, Group Velocity EstimationSaint Louis University, version 3.9.0. , http://eqseis.geosc.psu.edu/~cammon2001.

Ammon, C.J., Randall, G.E., Zandt, G., 1990. On the nonuniqueness of receiver function inversions. Journal of Geophysical Research 95, 15303–15318, http://dx.doi.org/10.1029/JB095Ib10p15303.

Andreoli, M.A.G., 1988a. The discovery of a hidden and strange African orogeny: the Transvaalide Fold Belt. Tectonic Division, Geol. Soc. S. Africa, Abstracts Vol. 4th Annual Conference, Silverton, 25 February 1988, pp. 1–2.

Andreoli, M.A.G., 1988b. Evidence for thrust tectonics in the Transvaal Sequence based on geophysical profiles. Ext. Abstracts Geocongress'88, Geol Soc. S. Afr., Durban, South Africa, pp. 3–6.

Biesheuvel, K., 1970. An interpretation of a gravimetric survey in the area west of Pilanesburg in the western Transvaal. Geological Society of South Africa, Special Publications 1, 266–282.

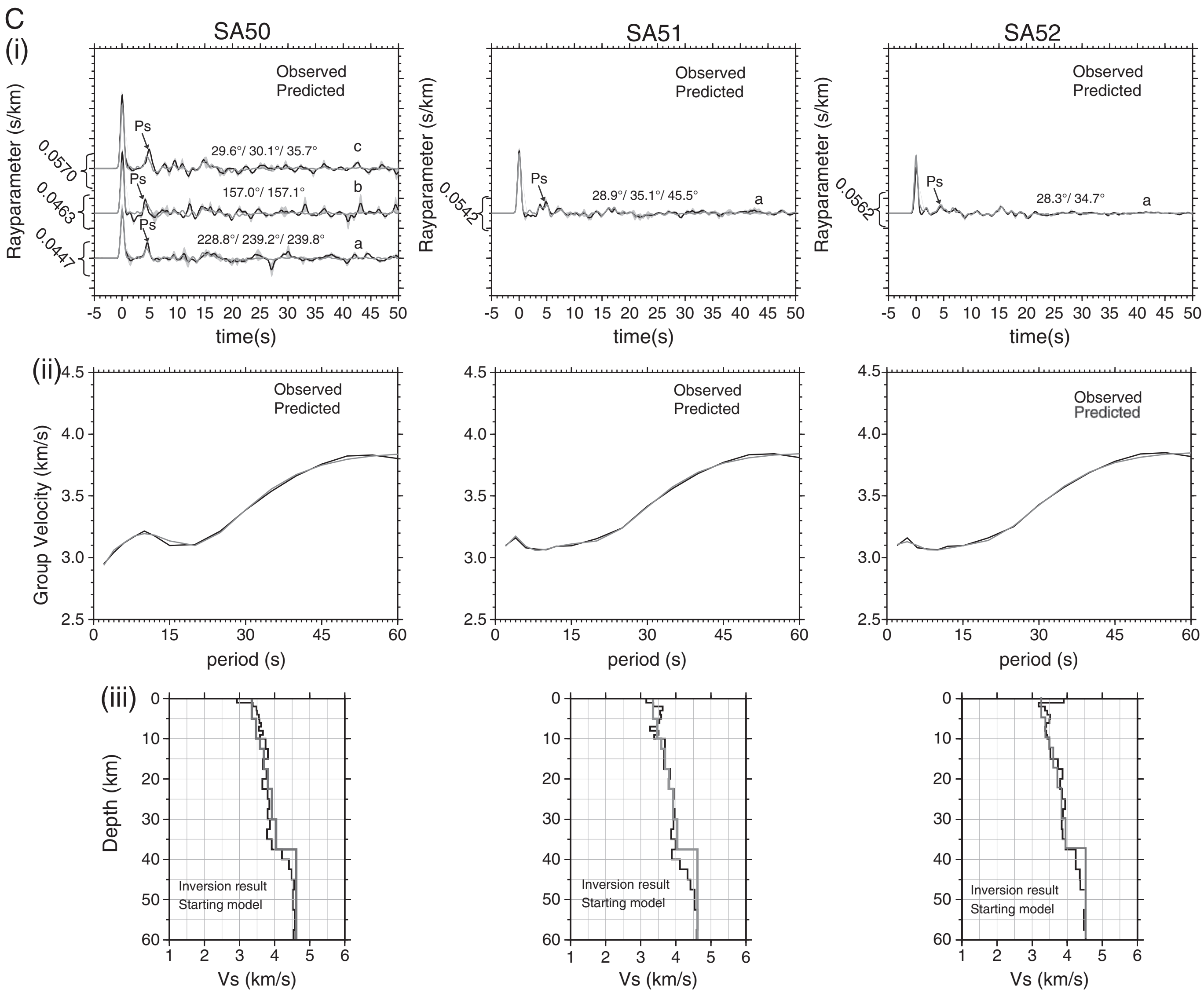

Fig. 10 (*continued*).

Carlson, R.W., Grove, T.L., De Wit, M.J., Gurney, J.J., 1996. Program to study crust and mantle of the Archean Craton in southern Africa. EOS, Transactions, American Geophysical Union 77 (29), 273–277, http://dx.doi.org/10.1029/96EO00194.

Cassidy, J.F., 1992. Numerical experiments in broad-band receiver function analysis. Bulletin of the Seismological Society of America 82, 1453–1474.

Cawthorn, R.G., Webb, S.J., 2001. Connectivity between the western and eastern limbs of the Bushveld Complex. Tectonophysics 300, 195–2009.

Cawthorn, R.G., Cooper, G.R.J., Webb, S.J., 1998. Connectivity between the western and eastern limbs of the Bushveld Complex. South African Journal of Geology 101, 291–298.

Cawthorn, R.G., Eales, H.V., Walraven, F., Uken, R., Watkeys, M.K., 2006. The Bushveld Complex. In: Johnson, M.R., Anhaeusser, C.R., Thomas, R.J. (Eds.), The Geology of South Africa. : Geological Society of South Africa. Johannesburg/Council for Geoscience, Pretoria, pp. 261–281.

Christensen, N.I., 1996. Poisson's ratio and crustal seismology. Journal of Geophysical Research 101, 3139–3156.

Christensen, N.I., Mooney, W.D., 1995. Seismic velocity structure and composition of the continental crust: a global view. Journal of Geophysical Research 100, 9761–9788.

Christensen, N.I., Stanley, D., 2003. Seismic velocities and densities. In: Lee, W.H.K., Kanamori, H., Jennings, P.C., Kisslinger, C. (Eds.), International Handbook of Earthquake and Engineering, 81B, pp. 1587–1594.

Claerbout, J.F., 1992. Earth Soundings Analysis: Processing Versus Inversion. Blackwell Scientific Publications, Boston, MA. 304 pages.

Cousins, C.A., 1959. The structure of the mafic portion of the Bushveld Igneous Complex. Transactions of the Geological Society of South Africa 62, 179–189.

Du Plessis, A., Kleywegt, R.J., 1987. A dipping sheet model for the mafic lobes of the Bushveld Complex. South African Journal of Geology 90, 1–6.

Du Toit, A.L., 1954. The Geology of South Africa. Oliver and Boyd, Edinburgh, U.K. 539 pp.

Dziewonski, A.M., Anderson, D.L., 1981. Preliminary reference Earth model. Physics of the Earth Planetary Interiors 25, S.297–S.356.

Dziewonski, A., Bloch, S., Landisman, L., 1969. A technique for the analysis of transient seismic signals. Bulletin of the Seismological Society of America 59, 427–444.

Eglington, B.M., Armstrong, R.A., 2004. The Kaapvaal Craton and adjacent orogens, southern Africa: a geochronological database and overview of the geological development of the Craton. South African Journal of Geology 107, 13–32.

Gurrola, H., Minster, J.B., 1998. Thickness estimates of the uppermantle transition zone from bootstrapped velocity spectrum stacks of receiver functions. Geophysical Journal International 133, 31–43, http://dx.doi.org/10.1046/j.1365-246X.1998.1331470.x.

Hall, A.L., 1932. The Bushveld Igneous Complex of the central Transvaal. South African Geological Survey Memoir, 28. Pretoria, 560 pp.

Harley, M., Charlesworth, E.G., 1994. Structural development and controls to epigenetic, mesothermal gold mineralization in the Sabie–Pilgrim's Rest goldfield, eastern Transvaal, South Africa. Exploration and Mining Geology 3, 231–246.

Hatton, C.J., Schweitzer, J.K., 1995. Evidence for synchronous extrusive and intrusive Bushveld magmatism. Journal of African Earth Sciences 21, 579–594.

Jorissen, 1904. On the occurrence of the Dolomite and Chert Series in the Rustenburg district. Transvaal Geological Society of South Africa 7, 30–38.

Julià, J., Ammon, C.J., Hermann, R.B., Correig, A.M., 2000. Joint inversion of receiver functions and surface-wave dispersion observations. Geophysical Journal International 143, 99–112.

Julià, J., Ammon, C.J., Hermann, R.B., 2003. Lithospheric structure of the Arabian Shield from the joint inversion of receiver functions and surface-wave group velocities. Tectonophysics 371, 1–21.

Julià, J., Ammon, C.J., Nyblade, A.A., 2005. Evidence for mafic lower crust in Tanzania, East Africa from joint inversion of receiver functions and Rayleigh wave dispersion velocities. Geophysical Journal International 162, 555–569.

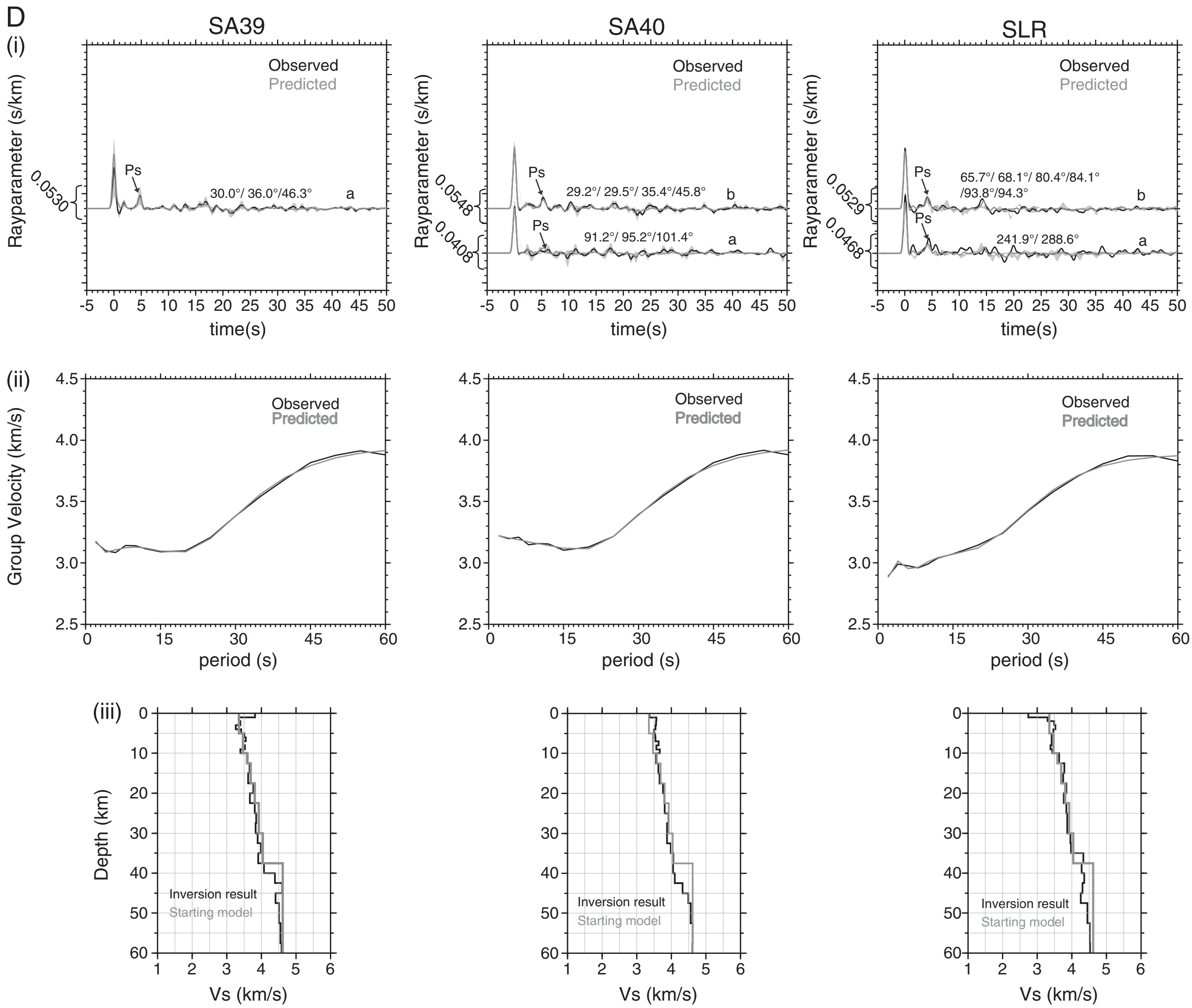

Fig. 10 (*continued*).

Keilis-Borok, V.I., 1989. Seismic Surface Waves in a Laterally Inhomogeneous Earth. Kluwer Academic Publishers, Dordrecht.

Kennett, B.L.N., 1983. Seismic Wave Propagation in Stratified Media. Cambridge University Press, Cambridge.

Kgaswane, E.M., Nyblade, A.A., Julià, J., Dirks, P.H.G.M., Durrheim, R.J., Pasyanos, M.E., 2009. Shear wave velocity structure of the lower crust in southern Africa: evidence for compositional heterogeneity within Archaean and Proterozoic terrains. Journal of Geophysical Research 114, B12304, http://dx.doi.org/10.1029/2008JB006217.

Levshin, A., Ratnikova, L., Berger, J., 1992. Peculiarities of surface-wave propagation across central Asia. Bulletin of the Seismological Society of America 82, 2464–2493.

Ligorría, J.P., Ammon, C.J., 1999. Iterative deconvolution and receiver function estimation. Bulletin of the Seismological Society of America 89, 1359–1400.

Mellor, E.T., 1906. The geology of the central portion of the Middelburg district. Annual Report of the Geological Survey of Transvaal 55–71.

Meyer, R., De Beer, J.H., 1987. Structure of the Bushveld Complex from resistivity measurements. Nature 325, 610–612.

Molengraaff, G.A.F., 1901. Geologie de la Republique S. Africaine. Bulletin of the Geological Society of France 1, 13–92.

Molengraaff, G.A.F., 1902. Vice President's address. Transvaal Geological Society of South Africa 5, 69–75.

Molyneux, T.G., Klinkert, P.S., 1978. A structural interpretation of part of the eastern mafic lobe of the Bushveld Complex and its surrounds. Transactions of the Geological Society of South Africa 81, 359–368.

Nair, S.K., Gao, S.S., Kelly, H.L., Silver, P.G., 2006. Southern African crustal evolution and composition: constraints from receiver function studies. Journal of Geophysical Research 111, B02304, http://dx.doi.org/10.1029/2005JB003802.

Nguuri, T.K., Gore, J., James, D.E., Webb, S.J., Wright, C., Zengeni, T.G., Gwavava, O., Snoke, J.A., Kaapvaal Seismic Group, 2001. Crustal structure beneath southern Africa and its implications for the formation and evolution of the Kaapvaal and Zimbabwe Cratons. Geophysical Research Letters 28 (13), 2501–2504.

Paige, C.C., Saunders, M.A., 1982. LSQR: an algorithm for sparse linear equations and sparse least squares. ACM Transactions on Mathematical Software 8 (1), 43–71, http://dx.doi.org/10.1145/355984.355989.

Pasyanos, M.E., Nyblade, A.A., 2007. A top to bottom lithospheric study of Africa and Arabia. Tectonophysics 444 (1–4), 27–44.

South African Committee for Stratigraphy, 1980. Stratigraphy of South Africa. Part 1 (Kent, L.E., Comp.), Lithostratigraphy of the Republic of South Africa, South West Africa/Namibia, and the Republics of Bophuthatswana, Transkei and Venda: Handbook of Geological Survey of South Africa, 8. 690 pp.

Uken, R., Watkeys, M.K., 1997. Diapirism initiated by the Bushveld Complex, South Africa. Geology 25, 723–726.

Van der Merwe, M.J., 1976. The layered sequence of the Potgietersrus limb of the Bushveld Complex. Economic Geology 71, 1337–1351.

Walraven, F., 1987. Geochronological and isotopic studies of Bushveld Complex rocks from the Fairfield borehole at Moloto, northeast of Pretoria. South African Journal of Geology 90, 352–360.

Walraven, F., 1997. Geochronology of the Rooiberg Group, Transvaal Supergroup, South Africa. Economic Geology Research Unit, University of the Witwatersrand, Johannesburg, South Africa, Information Circular, 316. 21 pp.

Walraven, F., Darracott, B.W., 1976. Quantitative interpretation of a gravity profile across the western Bushveld Complex. Transaction of the Geological Society of South Africa 79, 22–26.

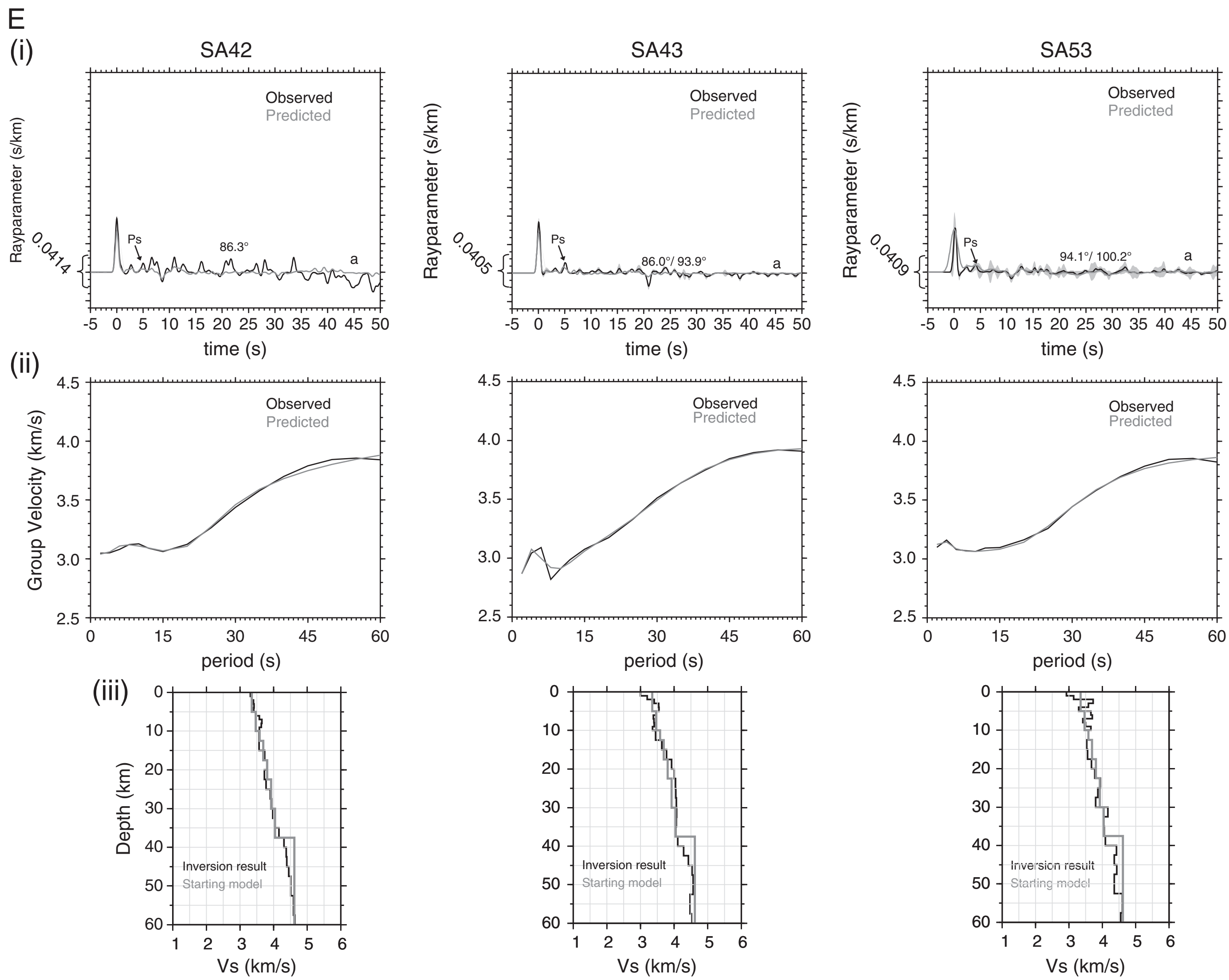

Fig. 10 (*continued*).

Webb, S.J., Cawthorn, R.G., Nguuri, T.K., James, D.E., 2004. Gravity modelling of Bushveld Complex connectivity supported by Southern African Seismic Experiment results. South African Journal of Geology 107, 207–218.

Webb, S.J., Ashwal, L.D., Cawthorn, R.G., 2010. Continuity between eastern and western Bushveld Complex, South Africa, confirmed by xenoliths from kimberlite. Contributions to Mineralogy and Petrology 162, 101–107, http://dx.doi.org/10.1007/s00410-010-0586-z.

Yang, Y., Li, A., Ritzwoller, M.H., 2008. Crustal and uppermost mantle structure in southern Africa revealed from ambient noise and teleseismic tomography. Geophysical Journal International 174, 235–248, http://dx.doi.org/10.1111/j.1365-246X.2008.03779x.

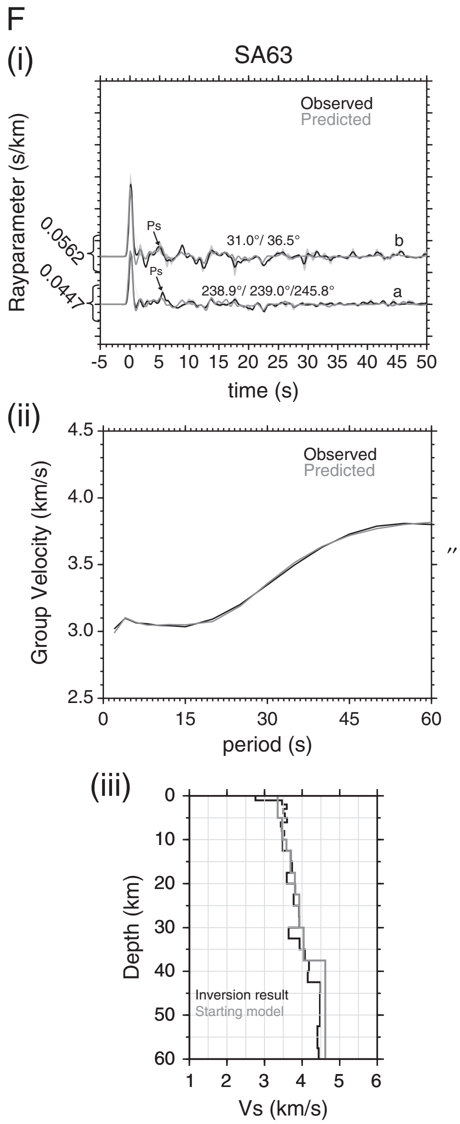

Fig. 10 (*continued*).

Table 1
Summary of crustal parameters.

Station	Back-azimuth (deg)	Vs (1–5 km depth) $\pm$ Std. deviation (km/s)	Vs (6–10 km depth) $\pm$ Std. deviation (km/s)	Vs below 30 km depth $\pm$ Std. deviation (km/s)	Crustal thickness (km)	Thickness of layers with Vs $\geq$ 4.0 km/s (km)	Average Vs (1–10 km depth) (km/s) $\pm$ Std. deviation (km/s)	Average Vs below 30 km depth (km/s) $\pm$ Std. deviation (km/s)	Average Crustal thickness (km)	Average Thickness of layers with Vs $\geq$ 4.0 km/s (km)
LBTB	46.5°	3.5 $\pm$ 0.0	3.5 $\pm$ 0.1	4.1 $\pm$ 0.0	42.5	15	3.5 $\pm$ 0.1	4.1 $\pm$ 0.1	42.5	11
	87.4°	3.5 $\pm$ 0.1	3.5 $\pm$ 0.1	4.1 $\pm$ 0.1	42.5	10				
	240.2°	3.5 $\pm$ 0.1	3.5 $\pm$ 0.1	4.0 $\pm$ 0.1	40.0	10				
	257.1°	3.5 $\pm$ 0.1	3.4 $\pm$ 0.1	4.0 $\pm$ 0.1	40.0	10				
SA39	37.4°	3.4 $\pm$ 0.1	3.5 $\pm$ 0.1	4.0 $\pm$ 0.1	40.0	5	3.5 $\pm$ 0.1	4.0 $\pm$ 0.1	40.0	5
SA40	35.0°	3.5 $\pm$ 0.0	3.6 $\pm$ 0.0	4.0 $\pm$ 0.1	45.0	15	3.6 $\pm$ 0.1	4.0 $\pm$ 0.2	42.5	12
	95.9°	3.6 $\pm$ 0.1	3.6 $\pm$ 0.1	4.0 $\pm$ 0.2	42.5	8				
SA42	86.3°	3.4 $\pm$ 0.0	3.6 $\pm$ 0.0	4.1 $\pm$ 0.1	40.0	13	3.5 $\pm$ 0.1	4.1 $\pm$ 0.1	40.0	13
SA43	90.0°	3.4 $\pm$ 0.2	3.4 $\pm$ 0.0	4.1 $\pm$ 0.1	42.5	10	3.4 $\pm$ 0.1	4.1 $\pm$ 0.1	42.5	23
SA45	35.7°	3.4 $\pm$ 0.0	3.5 $\pm$ 0.1	4.1 $\pm$ 0.1	42.5	13	3.5 $\pm$ 0.1	4.1 $\pm$ 0.0	45.0	15
	96.3°	3.4 $\pm$ 0.0	3.5 $\pm$ 0.1	4.1 $\pm$ 0.1	45.5	16				
SA46	35.0°	3.3 $\pm$ 0.1	3.6 $\pm$ 0.0	4.1 $\pm$ 0.1	42.5	10	3.5 $\pm$ 0.1	4.1 $\pm$ 0.1	42.5	10
SA47	32.5°	3.5 $\pm$ 0.2	3.6 $\pm$ 0.2	4.1 $\pm$ 0.1	45.0	13	3.6 $\pm$ 0.2	4.1 $\pm$ 0.1	45.0	11
	95.4°	3.5 $\pm$ 0.1	3.6 $\pm$ 0.2	–	–	–				
	240.0°	3.5 $\pm$ 0.0	3.6 $\pm$ 0.1	4.0 $\pm$ 0.2	42.5	8				
SA48	244.6°	3.5 $\pm$ 0.1	3.3 $\pm$ 0.1	4.2 $\pm$ 0.1	45.0	18	3.4 $\pm$ 0.1	4.2 $\pm$ 0.1	45.0	18
SA49	89.1°	3.3 $\pm$ 0.1	3.5 $\pm$ 0.1	4.1 $\pm$ 0.1	37.5	10	3.4 $\pm$ 0.1	4.1 $\pm$ 0.1	37.5	10
SA50	31.8°	3.5 $\pm$ 0.1	3.6 $\pm$ 0.1	3.9 $\pm$ 0.2	40.0	5	3.6 $\pm$ 0.1	3.9 $\pm$ 0.1	40.0	4
	157.1°	3.5 $\pm$ 0.1	3.6 $\pm$ 0.1	3.8 $\pm$ 0.1	37.5	0				
	235.9°	3.4 $\pm$ 0.1	3.6 $\pm$ 0.1	3.9 $\pm$ 0.1	40.0	3				
SA51	36.5°	3.3 $\pm$ 0.1	3.4 $\pm$ 0.1	4.0 $\pm$ 0.1	42.5	8	3.4 $\pm$ 0.1	4.0 $\pm$ 0.1	42.5	8
SA52	31.5°	3.4 $\pm$ 0.1	3.4 $\pm$ 0.0	4.0 $\pm$ 0.2	37.5	6	3.4 $\pm$ 0.1	4.0 $\pm$ 0.2	37.5	6
SA53	97.2°	3.5 $\pm$ 0.1	3.5 $\pm$ 0.3	4.1 $\pm$ 0.1	40.0	10	3.5 $\pm$ 0.1	4.1 $\pm$ 0.1	40.0	10
SA63	33.8°	3.5 $\pm$ 0.1	3.5 $\pm$ 0.1	4.0 $\pm$ 0.3	42.5	10	3.5 $\pm$ 0.1	4.0 $\pm$ 0.2	42.5	9
	241.2°	3.6 $\pm$ 0.0	3.5 $\pm$ 0.1	4.0 $\pm$ 0.1	42.5	8				
SLR	81.1°	3.5 $\pm$ 0.2	3.4 $\pm$ 0.2	3.9 $\pm$ 0.1	37.5	3	3.5 $\pm$ 0.2	3.9 $\pm$ 0.1	35.0	3
	265.3°	3.5 $\pm$ 0.2	3.4 $\pm$ 0.1	3.9 $\pm$ 0.1	35.0	3				

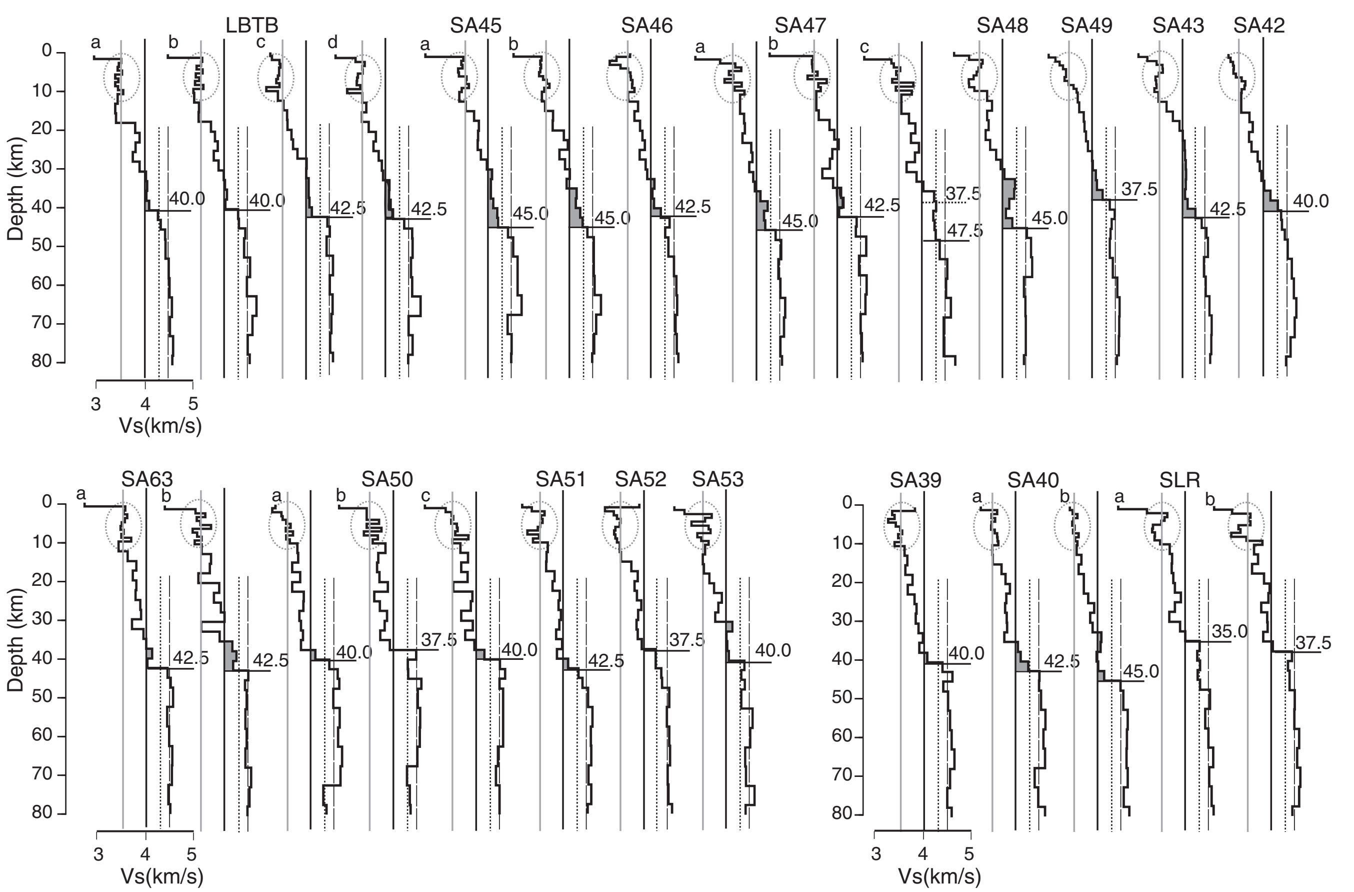

Fig. 11. A compilation of shear wave velocity profiles from joint inversion results showing Moho depths and details of the velocity structure in the upper and lower parts of the crust. The letters on top of each profile correspond to the letters on the receiver function stacks as shown in Fig. 10. The dashed ellipses enclose an area of the upper crust from 0 to 10 km depth. Crustal thicknesses are indicated with horizontal lines and numbers in km. Lower crustal layers with Vs $\geq$ 4.0 km/s are shaded, and reference lines at 3.5 km/s (gray solid), 4.0 km/s (black solid), 4.3 km/s (dotted) and 4.5 km/s (dashed) are shown on each profile.

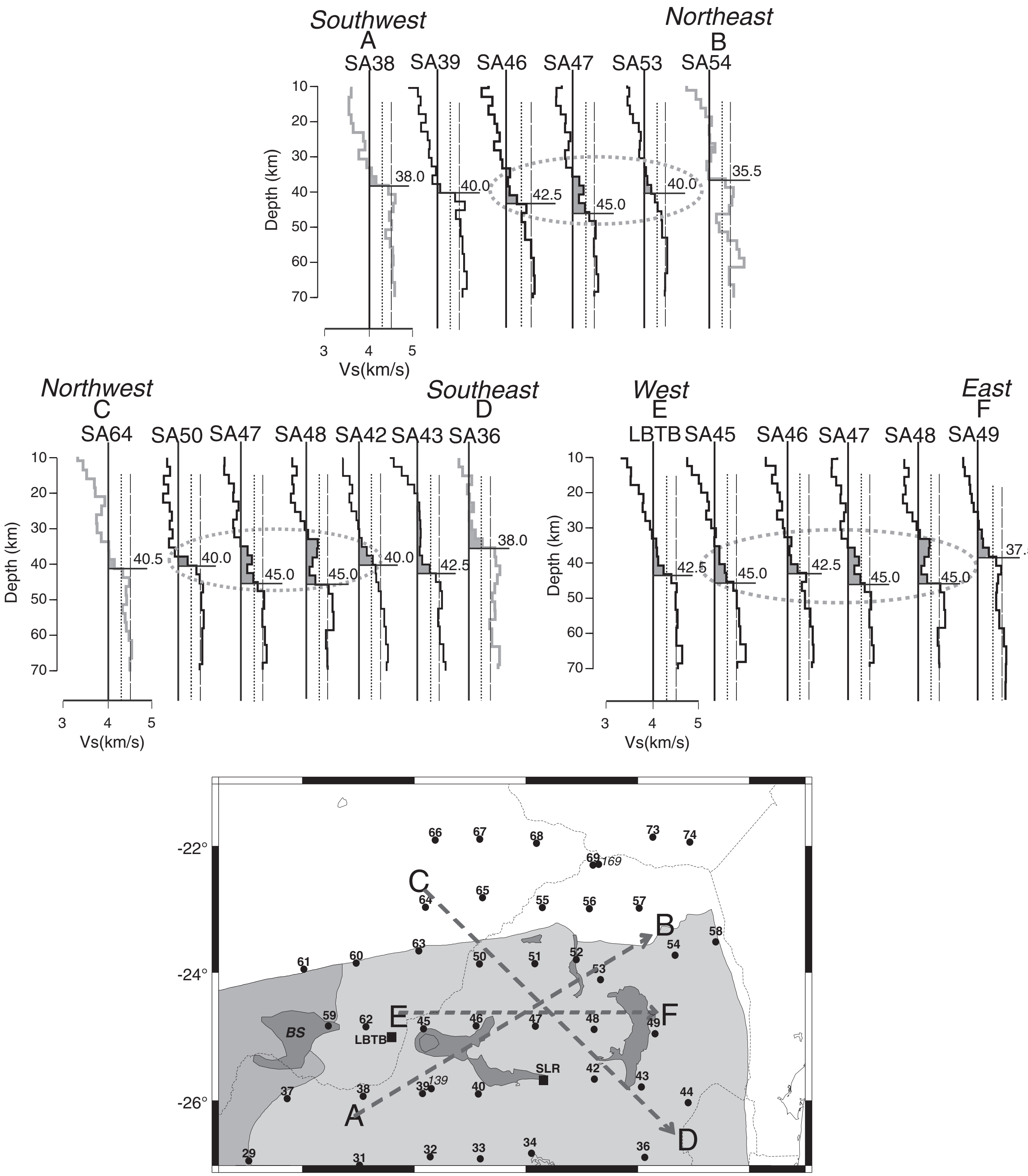

Fig. 12. Cross-section of the crust across the BC from southwest to northeast (AB), northwest to southeast (CD), and west to east (EF). The shear wave profiles in gray are from Kgaswane et al. (2009). The map shows the location of the profiles (dotted lines) and station locations. The gray shading is the same as in Fig. 2c.

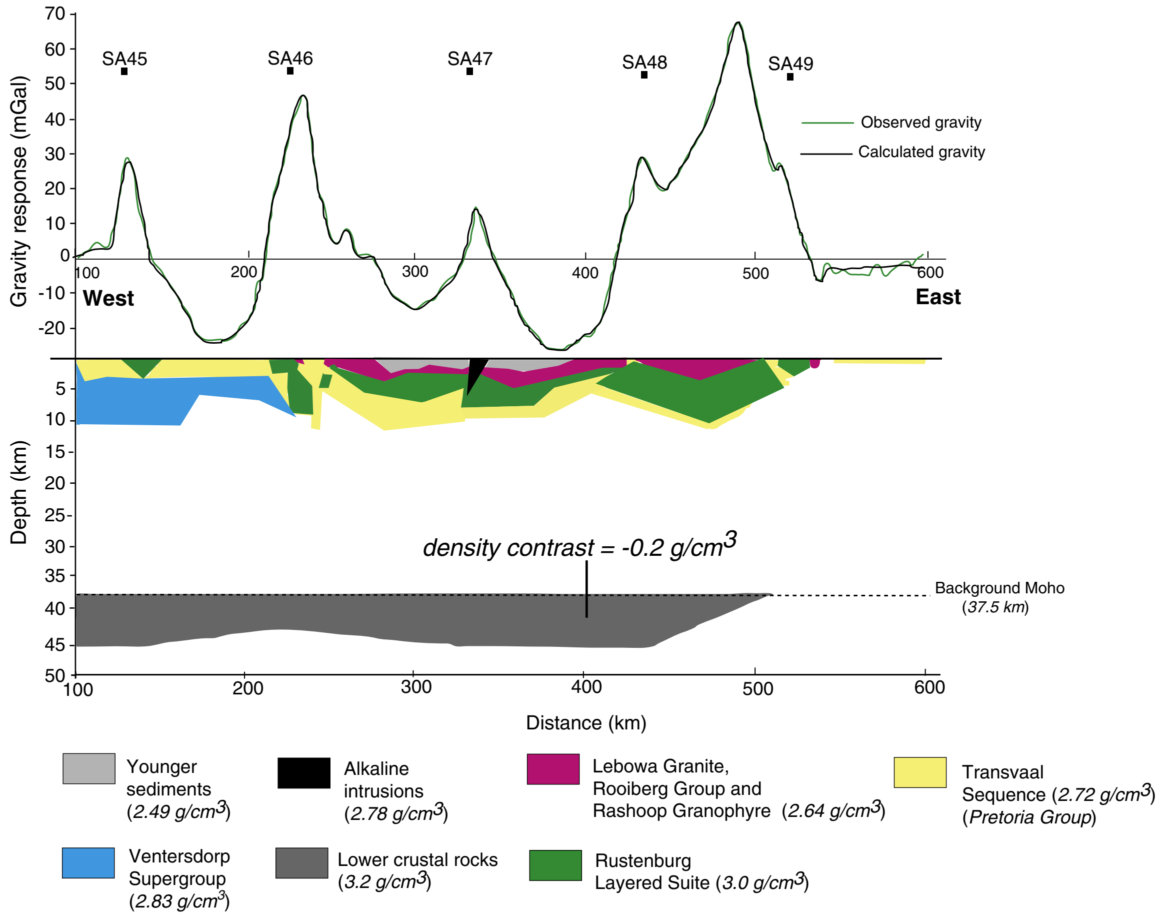

Fig. 13. Revised Webb et al. (2004) density model based on the Vs models for the five seismic stations indicated. The densities (inside brackets in the legend) for the different crustal layers are taken from Webb et al., 2004.

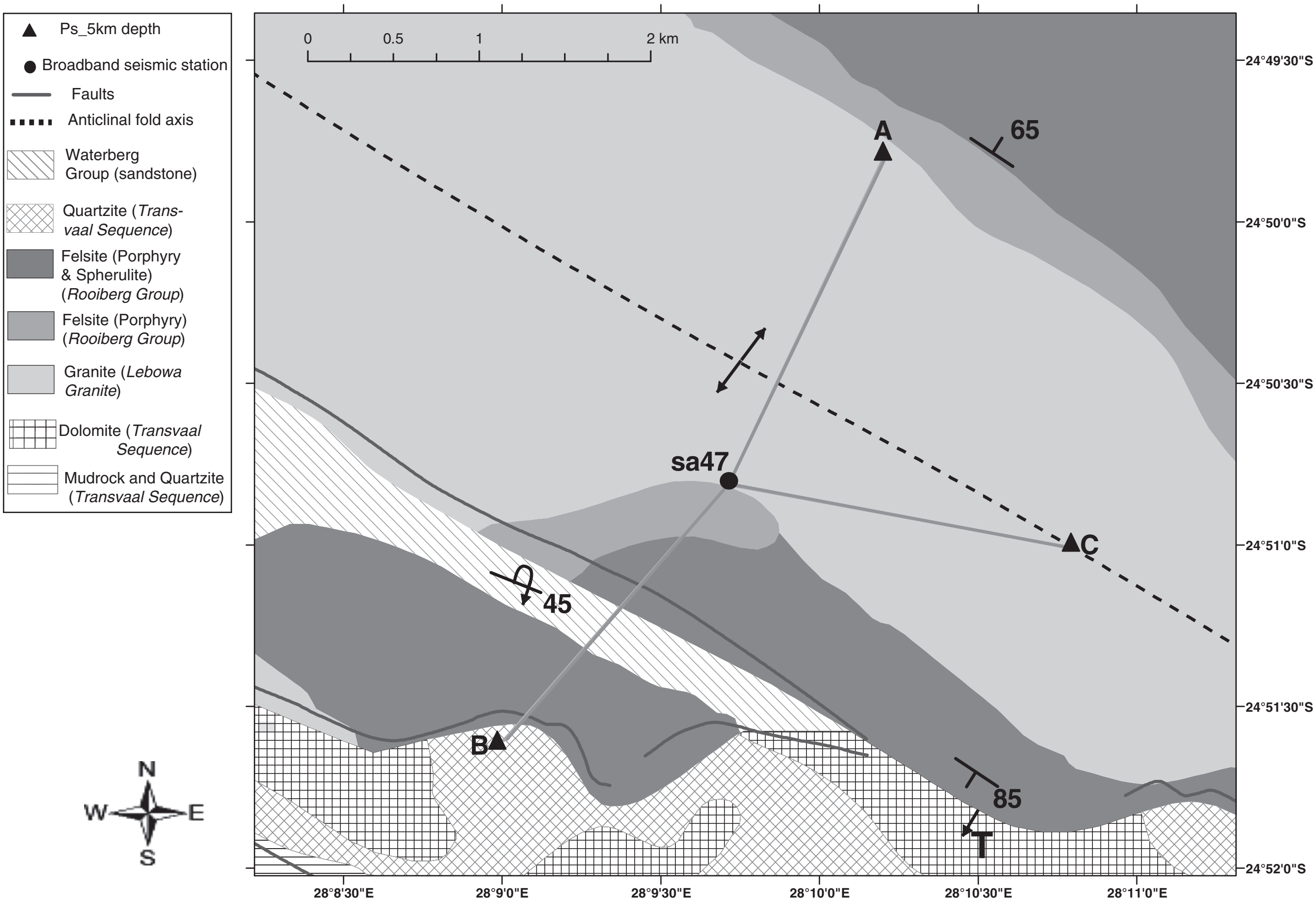

Fig. 14. Map of the local surface geology around station SA47 showing the Ps conversion points and structural relationships of the different sequences (map modified from the 1:250 000 geology map of South Africa).

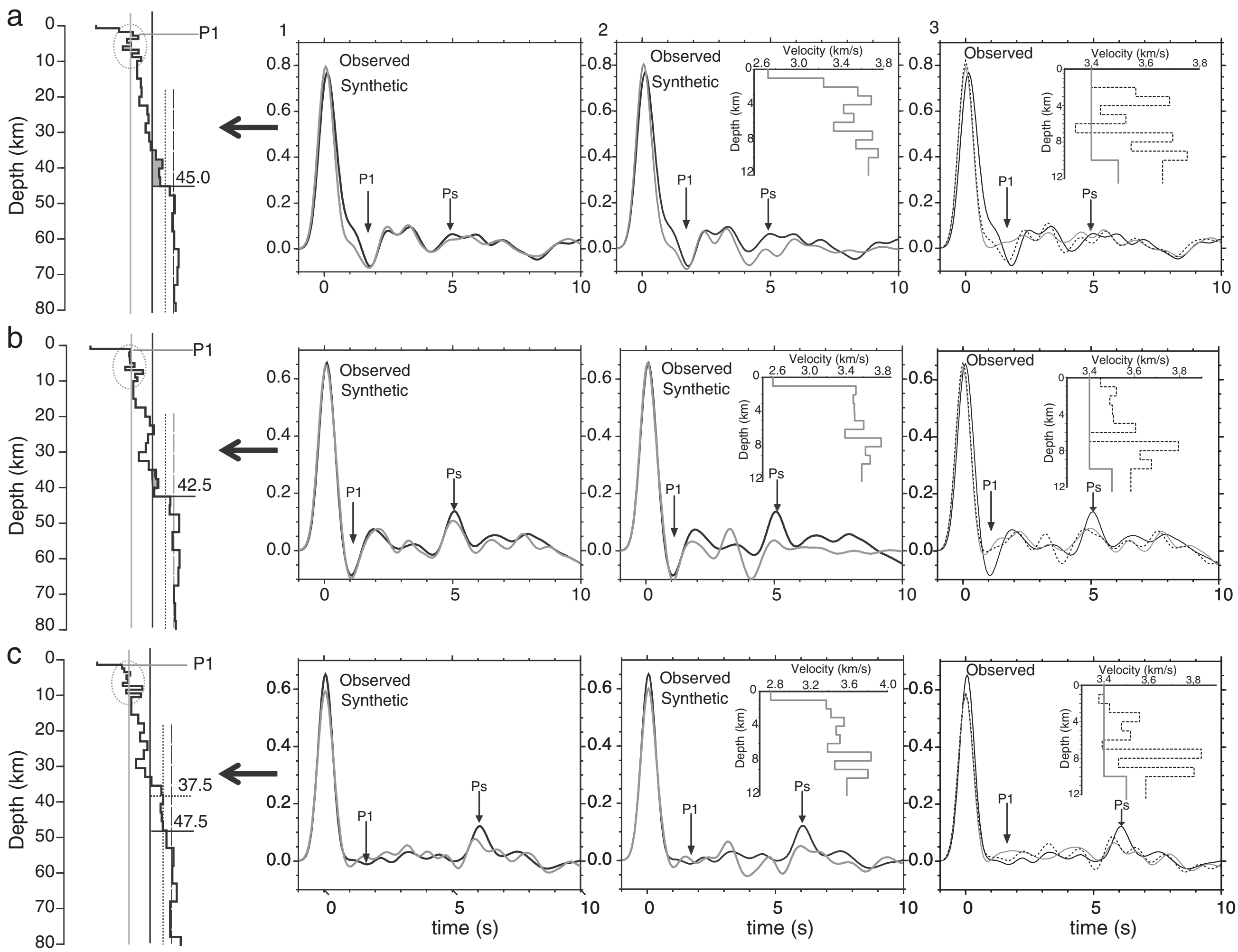

Fig. 15. Modeling results of the three receiver function stacks for station SA47 (a, b, and c). See text for an explanation of each panel.